University of Groningen

The influence of conjugation in molecular tunneling junctions and nanofabrication

Zhang, Yanxi

Publication date:
2018

The Influence of Conjugation in Molecular Tunneling Junctions and Nanofabrication

Yanxi Zhang

The Influence of Conjugation in Molecular Tunneling Junctions and Nanofabrication

Yanxi Zhang
University of Groningen, The Netherlands

European
Research
Council

An electronic version of this dissertation is available at
http://www.rug.nl/research/portal.

university of
groningen

faculty of science
and engineering

university of
groningen

The Influence of Conjugation in Molecular Tunneling Junctions and Nanofabrication

PhD Thesis

to obtain the degree of PhD at the
University of Groningen
on the authority of the
Rector Magnificus Prof. dr. E. Sterken
and in accordance with
the decision by the College of Deans.

This thesis will be defended in public on

Friday 26 October 2018 at 12.45 hours

by

Yanxi Zhang

born on 5 February 1988
in Fujian, China

Supervisors

Prof. R.C. Chiechi
Prof. J.C. Hummelen

Assessment committee

Prof. W. Hong
Prof. M. S. Pchenitchnikov
Prof. E. van der Giessen

To my dear parents and supervisors

Contents

1

INTRODUCTION

1

1.1. MOLECULAR ELECTRONICS AND MOLECULAR JUNCTIONS

The invention of the transistor, which is the crucial component of modern electronics, opened the door to the information era for just as the light bulb illuminated the path in the darkness. The first transistor was invented by Bell Labs in 1947, followed by the first integrated circuit by Texas Instruments in 1958 and the first microprocessor, by Intel, in 1971. Since then, the semiconductor industry has kept roughly doubling the density of Si transistors on a chip every two years, as predicted by Moore's Law. Researchers are constantly trying to scale down the size of the transistor and put more of them into integrated circuits. Nowadays we can fit about a billion transistors on a single chip. The release of the 7-nm node FinFET devices is expected soon, followed by continued efforts to pursue 5-nm node devices. However, there is a limit in the downscaling of the transistor. It is tremendously expensive to fabricate sub-10nm transistors, and Si semiconductor technology is likely to encounter implacable physical limits sooner or later.[1] Back in the 1970s, scientists had foreseen some of these difficulties, predicting an eventual end to Moore's Law. Instead of using top-down fabrication techniques, they proposed solutions that use bottom-up approaches where one single atom or molecule defines the active layer of the electronics. The breadth of accessible organic molecular structures, the most versatile method of arranging atoms, provides numerous opportunities to modulate the electrical properties of bottom-up devices. In fact, the idea of molecular electronics originated from the past demands and predictions in the development of modern electronics.

Molecular junctions are central to the field of Molecular Electronics (ME), which we define as research concerning the flow of electricity end-to-end through individual molecules. And the dominant mechanism of charge-transport is tunneling. All molecular junctions have at least two contacts, which we denote as a bottom electrode (or substrate) and a top-contact, regardless of the actual orientation of the electrodes (Figure 1.1). The bottom-electrode is almost always a metal (in particular Au or Ag), but the composition of the top-contact varies.

There are two principle aims in ME: i) to study and model the mechanisms of charge-transport through individual molecules and ii) to control the flow of electricity through molecular junctions. In general terms, these two goals divide physicists and chemists working in this field. Complex, top-down spectroscopic tools, like break junction techniques, are necessary to study charge-transport at a level of detail needed to develop robust theoretical descriptions and models, which is the domain of Physics. Controlling the flow of electricity through molecules is more application/phenomena driven and relies on synthetic chemistry to tailor molecules to affect the flow of electricity through them, thus it is the domain of Chemistry. Furthermore, complex molecules and ensembles add unwanted complexity to research that seeks to find the most fundamental principles involved in transport, while ensembles of tailored molecules are ideal for physical-organic studies to establish structure-function relationships. Thus, the complexity of top-down spectroscopic tools is not at all limiting to research in Physics, but Chemistry requires facile, high-throughput techniques for forming molecular junctions that get out of the way of synthetic and physical-organic studies.

To differentiate the various types of contacts that can occur between molecules and electrodes, we use "//" to denote van der Waals (physisorbed) interface, "/" to denote
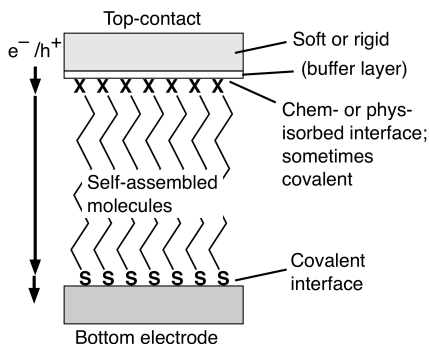
Figure 1.1 A schematic of a bottom-up molecular junction comprising a top-contact (electrode) and bottom electrode separated by self-assembled molecules that define the distance between the two electrodes. The top-contact can be either rigid (e.g., Au) or soft (e.g., Hg) and may be separated from the molecular layer by a buffer layer (e.g., a conjugated polymer or the native oxide of the top-contact). "S" means the sulfur atom and "X" means the substituents.

covalent (chemisorbed) interface, and "-" to denote a covalent interaction.

1.2. LARGE AREA MOLECULAR JUNCTIONS COMPRISING SELF-ASSEMBLED MONOLAYERS (SAMS)

Almost all bottom-up techniques rely on SAMs because they provide an intrinsic interface between macro and nano by assembling into 2D structures. These monolayers form at fluid/solid interfaces at which molecules spontaneously arrange themselves to minimize the surface free-energy of the system and, in doing so, form ordered ensembles of molecules. All SAMs are self-organized, but not all self-organized monolayers are SAMs. There are two basic categories of self-assembly: dynamic, out-of-equilibrium and static, equilibrium assembly. Dynamic self-assembly requires the dissipation of energy in order to remain out of equilibrium and is not generally relevant to SAMs.[2] Static self-assembly may require energy to overcome kinetic barriers (activation energy), but the systems are at thermodynamic equilibrium when assembled; crystallization is an example of static self-assembly, as are SAMs.[3] A system can only undergo self-assembly when it forms by a collection of weak, reversible interactions that balance attractive and repulsive forces. Such systems are capable of self-repair, are responsive to changes in their environments, and can undergo exchange. Self-organized monolayers, such as silanes on glass (SiO_2) or alkenes/alkynes on silicon (Si-H) can be highly ordered, but are very sensitive to the conditions under which they are formed and cannot self-repair. They are also thermodynamically stable indefinitely due to the anchoring of molecules by covalent bonds. By contrast, SAMs are only stable when they are physically prevented from equilibrating with the surrounding medium, e.g., by encapsulation; however, they are capable of self-repair and exchange and are not particularly sensitive to the conditions under which they are formed.[4]

Self-assembled monolayers of alkanethiolates on noble metals are particularly in-

sensitive to parameters such as concentration and solvent, form in minutes, and tolerate a wide variety of head-groups. Although they form covalent metal-sulfur bonds, they also induce reversible metal-metal bonds and therefore benefit from the selectivity of covalent bonds, but are self-assembled. These properties make them well suited to physical-organic studies and the formation of bottom-up molecular junctions because high-quality SAMs are easy to form reproducibly.[5] This facile property of alkanethiols has lead to the to mistaken assumption that all that is required to form a SAM is a thiol and a gold substrate; however, consideration of the mechanism of assembly must be taken into account when using molecules with multiple, strong surface interactions such as dithiols and conjugated molecules. Akkerman et al. used data from molecular junctions to show that the conditions of dithiols must be optimized to avoid backbiting, which creates thin spots, and multilayer formation, which creates thick spots.[6] Valkeneir et al. showed that conjugated "molecular wire" dithiols are extremely sensitive to the base used to deprotect them during the formation of SAMs.[7] They used a combination of spectroscopies to determine that strong bases lead to molecule lying down on the surface and that importantly, these lying-down structures still yielded cogent data in molecular junctions; reasonable electrical data alone are not evidence of well-ordered SAMs in molecular junctions. Thus, it is extremely important that the structure of a SAM be determined unambiguously when investigating a new molecule in a bottom-up junction. It is because SAMs of alkanethiols on Au and Ag form reproducibly and are extremely well characterized that they are used so widely in bottom-up molecular junctions, including "benchmarking" a new method for forming top-contacts; they are the physical equivalent of a model organism.

The first report of the measurement of current through a molecular junction was likely Mann and Kuhn in 1971.[8] Although these researchers formed Langmuir-Blodgett films and not SAMs, they investigated tunneling charge-transport through monolayers of fatty acids using a variety of top-contacts, most notably Hg. The main conclusion of that paper was that the rectangular tunneling-barrier model was valid for tunneling through molecular junctions, which they showed by varying the work functions of the electrodes and by the length-dependence of the tunneling currents. Three years later, Aviram and Ratner predicted that a donor-bridge-acceptor molecule—an electron-rich and an electron-poor π-system separated by a rigid σ-framework—between symmetrical metallic electrodes would rectify (tunneling) current.[9] That paper is widely cited as the motivation for research into ME because it captured both essential elements; the physics of tunneling charge-transport and the chemistry of synthesizing realistic, functional molecules. These two papers are also representative of the two most common theoretical approaches that exist today.

The rectangular tunneling-barrier model that is most commonly used today is Simmons' approximation, which provides a description for current (I) or current density (J) as a function of potential (V) based on the "barrier height" (ϕ), the distance between the electrodes (d).[10] The simplified Simmons equation is given in Eq. 1.1, which captures the distance dependence of tunneling currents where d is the distance between the electrodes, β is the characteristic tunneling decay parameter, and J_0 is the theoretical value of J when $d = 0$. And Eq. 1.2 defines (β) in terms of (ϕ). This form of Simmons' approximation is useful because it separates most of the experimental uncertainties of the

electrode/molecule contact into the pre-exponential factor, J_0, and captures the contribution of the specific molecules being observed as the parameter, β. Moreover, the distance (hence β) can be expressed in any unit, including N_c, the number of carbons in the molecular backbones, which accounts for systems in which the exact length of the molecule, for example, sandwiched between electrodes, is not known. The only requirement for determining these parameters (directly and experimentally) is that a series of at least three similar molecules of different lengths be measured such that β and J_0 can be determined from the slope and Y-intercept of plots of ln(J) vs d. Since the value of β depends on ϕ, it discriminates between aliphatic systems with large HOMO/LUMO gaps (i.e., no density of states near E_f) and conjugated systems where E_f comes into resonance with the HOMO or LUMO at lower potentials. Thus, this simple form of Simmons' approximation is an ideal probe for systematic synthetic alterations and is widely used by chemists. It does not, however, provide much mechanistic detail.

$$J = J_0 e^{-\beta d} = J_0 10^{-\beta d/2.303} \tag{1.1}$$

$$\beta = \frac{4\pi}{h} \sqrt{2m\phi} \tag{1.2}$$

In 2006, Beebe et al. observed that the minima of Fowler-Nordheim plots, ln($I \cdot V^{-2}$) vs. V^{-1}, of J/V data from tunneling junctions comprising SAMs correlated well to E_f-E_{HOMO}.[11] The initial interpretation of this finding was that this minimum, V_{trans}, correlated to a change in mechanism from tunneling to field-emission (Fowler-Nordheim tunneling) that occurs when the tunneling barrier is distorted sufficiently to create accessible states in the gap. This interpretation was later refuted by Huisman et al.[12] in what can be considered the epoch of an explosion of theoretical studies trying to ascertain the meaning of V_{trans}. Experimentally—and of relevance to experimentalists—V_{trans} has become an important tool for probing the energies of molecular orbitals at voltages that are compatible with tunneling junctions. For example, ϕ may be as high as 4 eV for alkanethiols on Au electrodes, but V_{trans} is closer to 1.25 V.[13] Thus, directly observing ϕ would require a bias of ~4 V, which is sufficient to collapse a SAM-based junction, but V_{trans} can be observed at ~1 V. Moreover, V_{trans} is determined by simply re-plotting I/V (or J/V) data; no additional experiments or measurements are required.[14] There are, of course, much more complex theoretical interpretations of molecular tunneling data. However, β, J_0 and, V_{trans} are the most relevant and commonly used in bottom-up tunneling junctions because they are comparable between disparate experimental setups, easy to obtain from simple I/V measurements, and their interpretation–particularly in a physical-organic context–is straightforward.

1.3. SOFT, CONFORMAL TOP-CONTACTS

1.3.1. HG-DROP JUNCTIONS

Although Mann et al. used Hg as a top-contact in their study in 1971, the modern use of Hg top-contacts has its roots in electrochemistry, where Hg drops are used as conformal, self-regenerating working and counter electrodes.[15–17] Majda and Slowinsky used this approach to study tunneling charge transport through SAMs sandwiched between two

drops of Hg controlled by a micromanipulator.[18–20] Since simply exposing the surface of Hg to a solution of alkanethiols is enough to form a pinhole-free SAM, the experimental setup is remarkably simple; extrude two drops of Hg in an electrolyte solution containing alkanethiols and then bring them together until they "twitch." Rather than the two drops coalescing, this twitch is the sign that the SAMs on the surface of each Hg drop have come into contact.

These junctions usually comprised bi-layers, Hg-SAM//SAM-Hg, because both Hg-drops were exposed to the same thiol solution. However, York et al.[20] used the Hg-drop technique to measure the distance dependence of series of Hg-SAM//SAM-Hg, and Hg-SAM//Hg junctions. They were able to capture a single SAM between the drops of Hg by holding one at a negative potential sufficient to desorb negatively charged thiolates while bringing the two drops into contact. From these data they extracted values of J_0 and β and characterized the influence of the Van der Waals interface between the two SAMs, which had surprisingly little influence; β=1.06 ± 0.04 N_c^{-1} for monolayers and 1.02 ± 0.07 N_c^{-1} for bilayers. They determined that the CH_3//CH_3 interface between the SAMs was considerably better coupled than the CH_3//Hg interface. This result is demonstrative of the utility of measurements of β and of the straightforward nature of the rectangular barrier model, which treats only the coupling of the two electrodes and not the coupling between the atoms comprising the molecules in the junction. It also illustrates the sensitivity afforded by physical-organic studies in a simple testbed; comparing the electronic coupling between a CH_3//CH_3 and a metal//CH_3 interface would otherwise be non-trivial.

A limitation of the Hg-drop technique employed by Majda and Slowinksy is that it requires two Hg drops to be brought into contact using a somewhat specialized apparatus. Although a simple experimental platform, there are practical drawbacks including the fragility of the junctions. Most notably, however, is that SAMs on Hg are more useful for spectroscopic studies than for potential molecular-electronic devices. Instead, SAMs on rigid metal electrodes are more relevant for potential technological applications.

A simple variation of the Hg-drop technique is to form a SAM on a surface (usually Ag) and then to bring a drop of Hg into contact with that surface.[21–26] This approach allows the measurement of "real" SAMs in the sense that they are formed on a solid metal electrode material, the topology of which profoundly influences the structure and properties of the SAM. Measurements can be performed on several different spots, and through the collection of statistically significant amounts of data, a picture can be constructed that encompasses all of the defects that are inherent in SAMs on solid metal surfaces. Measurements with Hg drops were facile enough that values of β were determined from a range of laboratories on a range of different SAMs, which enabled a consensus to be determined for what β should be for SAMs of alkanethiolates.

The conformal nature of liquid Hg, coupled with its ability to form amalgams with noble metals, makes Hg particularly sensitive to the defects in SAMs that are induced by solid metal electrodes (e.g., step edges and grain boundaries). A pinhole or "thin spot" in a SAM can induce the catastrophic failure of an Hg-drop. A very effective method for mitigating the catastrophic failure of Hg-drop junctions is to use substrates prepared by template stripping,[27–38] which creates smooth metal surfaces by templating them against smooth surfaces. A template stripping method that is particularly useful for Hg-

drop junctions was introduced by Weiss et al.[39] in which a thin film of Au or Ag is deposited onto a silicon wafer and a substrate is glued to the film. Just before forming a SAM, the substrate (usually glass) is peeled from the wafer, exposing the buried metal surface. Self-assembled monolayers grown on these ultra-smooth surfaces have fewer (substrate-induced) defects in them. Because tunneling currents depend exponentially on d (Eq. 2), randomly distributed defects give rise to log-normal distributions in J, the spread of which reflects the density of defects in the SAM. Thus, J/V data obtained from Hg-drop tunneling junctions comprising SAMs on template-stripped metals show markedly narrower distributions as is shown in Figure 1.2. We abbreviate template-stripped metals with the superscript "TS," e.g., Au^{TS}.
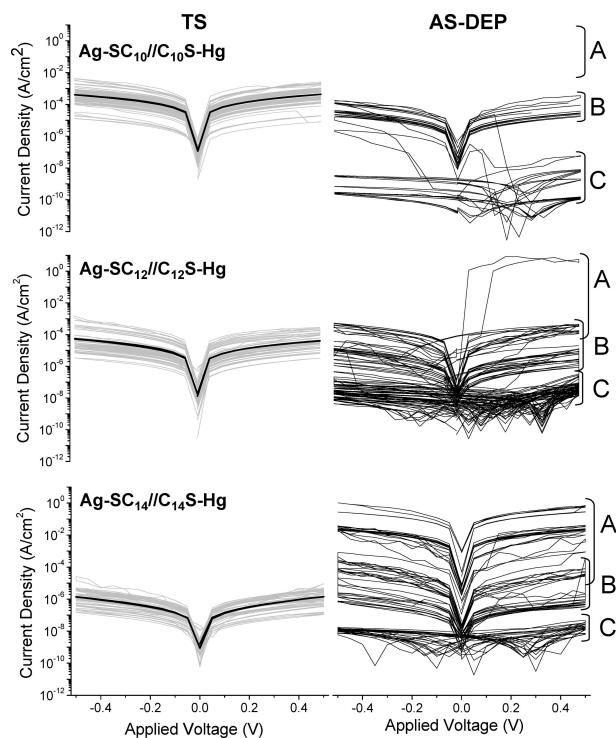
Figure 1.2 (Left) Plots of the average J/V curves (log-mean, bold black lines) and all J/V curves (light gray lines) measured on the TS junctions Ag-SC_n//C_nS-Hg (n = 10, 12, 14), except for the initial traces that had a current density several orders of magnitude below the remaining traces, and traces directly preceding and following amalgamation. (Right) The same set of traces for the corresponding junction using vacuum-deposited silver. (No averages were calculated for these data.) The designations "A", "B", and "C" refer to different tranches of conductivity. Reprinted with permission from from reference [27]. Copyright 2007 American Chemical Society.

As useful as Hg is as a top-contact, it has some severe limitations, the most obvious of which is the toxicity of Hg. While not so much an issue for small, laboratory-scale work, it precludes the commercialization of Hg-drops and limits their use in chemical education. A more subtle drawback is the combination of its chemical and rheological properties. Noble metals are, by far, the most common substrates for the formation of SAMs and Hg

readily forms amalgams with these metals. Combined with the fact that Hg is a New-tonian fluid, Hg top-contacts have a very low tolerance for pinholes and "thin" defects in SAMs, which tend to precipitate the catastrophic failure of metal/SAM//Hg junctions when the Hg dissolves the bottom-electrode. This low tolerance for defects and pinholes leads to "high-J filtering," in which the system self-selects for molecular junctions that do not comprise these types of defects, while tolerating other defects. Measurements with Hg top-contacts usually require a solvent bath containing free thiols in order to repair pinholes continuously (i.e., by self-assembly). "Thick" defects occur most com-monly when the solvent becomes trapped between the Hg and the SAM. In principle it is expelled by electrostatic pressure that is caused by biasing the two electrodes for meas-urement, but "low-J" traces are common in Hg-drop measurements. Thus the resulting data are biased both by self-selection and by how the measurements are performed; e.g., how many J/V traces are acquired before forming a new junction, how many total junc-tions are measured, and if shorts and low-J traces are discarded.

1.3.2. EUTECTIC GALLIUM INDIUM (EGAIN)

In 2008, Chiechi et al. introduced eutectic Ga-In (25% In, 75% Ga, etc.; "EGaIn") as a top-contact to replace Hg.[40] EGaIn is a liquid metal at room temperature, but it lacks some of the key drawbacks of Hg; it does not readily alloy with noble metals (because of the presence of a self-limiting oxide), it is a non-Newtonian fluid, and it is non-toxic. These properties obviate the need for solvent baths completely—EGaIn measurements are per-formed under ambient conditions—and lead to more stable junctions of (much) smal-ler area than Hg. Most of the useful properties of EGaIn are driven by the self-limiting Ga_2O_3 skin, which forms spontaneously in air. This oxide imparts a non-Newtonian, shear-yielding behavior to EGaIn that allows it to retain non-Newtonian shapes such as the sharp tips used to form molecular junctions. Thus, we describe EGaIn junctions as EGaIn/Ga_2O_3//SAM-Metal.

The formation of an EGaIn/Ga_2O_3//SAM/Au^{TS} junction is shown in Figure 1.3. A small drop of EGaIn is extruded from a 15 μL syringe with a blunt, metal needle onto a metal surface, to which it adheres. The syringe is raised slowly such that the EGaIn is stretched between the syringe and the drop stuck to the surface, forming an hourglass shape. At a critical radius, the EGaIn severs into two parts, one adhered to the syringe, and one adhered to the surface. However, due to the shear-yielding behavior of EGaIn, it does not return to a spherical shape (as would, for example, Hg or water) because there is no longer any shear stress acting on it. The tip is then brought into contact with a SAM using a micromanipulator or linear piezo stepper motor. Contact is observable as the joining of the tip with its mirror image. The diameter of the tip is remarkably consistent at ~25 μm because it is defined by the rheological properties of EGaIn, however, the exact diameter is somewhat dependent on the speed at which the syringe is raised.

The utility of EGaIn is that bottom-up molecular junctions can be formed quickly and easily, with minimal equipment. Thus, EGaIn is a "bench top" tool that is accessible to chemists. This is an important feature because it removes a common bottleneck in ME research; synthetic chemists must invest time synthesizing molecules and are therefore reliant on collaborations to perform the often-complex measurements and/or device fabrication. And physicists tend to prefer working with familiar, well-behaved molecules

rather than spending time learning the nuances of a new molecular motif. Thus, EGaIn allows chemists to measure molecules directly, working out the exact protocols for forming dense SAMs and screening molecules for potentially interesting properties that can later be expounded on with more complex and laborious spectroscopies.
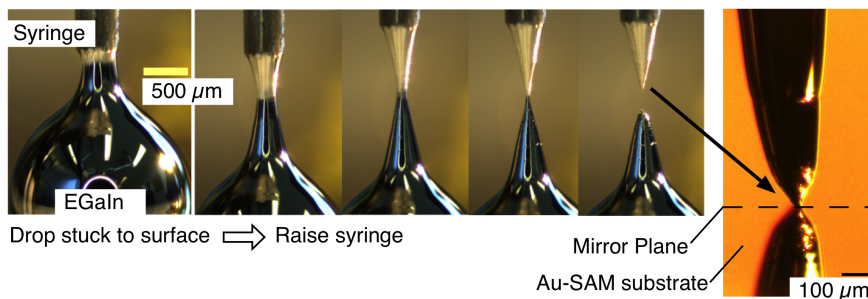
Figure 1.3 Optical micrographs of the formation of an EGaIn tip and an EGaIn/Ga_2O_3//SAM/Au junction. Left to right: a sacrificial drop of EGaIn is extruded from a syringe and stuck to a surface. The syringe is raised forming an hourglass shape between the syringe and the sacrificial drop. The EGaIn separates into two parts, with a sharp tip adhered to the end of the syringe. This tip is then brought into contact with a SAM to form a bottom-up molecular junction.

The influence of Ga_2O_3

The Ga_2O_3 skin that imparts useful properties to EGaIn also adds the complexity of two additional interfaces to what is otherwise a metal/molecule/metal junction; EGaIn/Ga_2O_3 and Ga_2O_3//SAM. Cademartiri et al. determined the composition of the oxide skin using X-ray photoelectron spectroscopy (XPS) and observed that the composition and thickness do not change when the tip is deformed (e.g., by forming a molecular junction).[41] They used angle-resolved XPS (ARXPS) and time-of-flight secondary ion mass spectrometry (ToF-SIMS) to determine the thickness of the Ga_2O_3 skin, finding an average thickness of 0.7 nm; however, they observed that there were regions of micron-thick threads of Ga_2O_3 all over the surface. The authors could not determine if these threads were formed during characterization (e.g., when the EGaIn was frozen) or if the corrugated topology of the EGaIn/Ga_2O_3 was innate and therefore present in molecular junctions. They also observed the presence of surreptitious adsorbates, mostly fatty acids, distributed on the surface of the oxide. These features are captured in Figure 1.4 along with a depiction of a SAM that captures the topology that is present at length scales commensurate with the size of EGaIn/Ga_2O_3//SAM/Metal junctions. From this "messy" picture, it is rather remarkable that EGaIn forms molecular junctions at all. The authors addressed this point by considering molecular junctions as a collection of resistors in series and parallel, concluding that transport through the SAM dominates the electrical properties because of the relatively high electrical resistance of SAMs compared to the common defects.

The overarching conclusion of Cademartiri et al. is essentially that the oxide does not significantly impact the properties of molecular junctions and that its influence is constant. Reus et al. concluded that "The SAM, not the electrodes, dominates charge

Figure 1.4 A schematic of an EGaIn/Ga$_2$O$_3$//SAM/Ag^{TS} junction showing the structure and dimensions of the oxide and the common features found in SAMs on Ag^{TS} and on the surface of Ga$_2$O$_3$. Reprinted with permission from reference [41]. Copyright 2012 American Chemical Society.
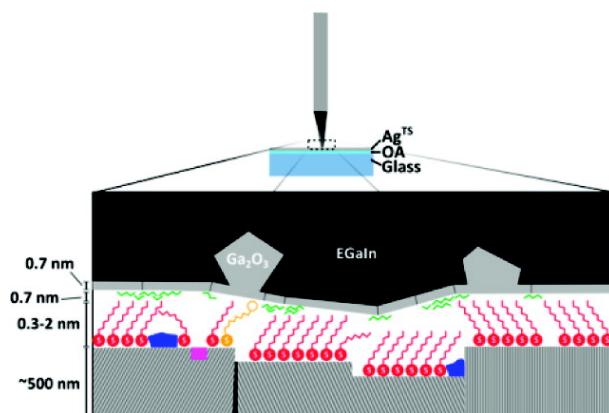
transport in metal/monolayer//Ga$_2$O$_3$/Gallium-Indium eutectic junctions" by comparing the rectification (which is discussed below) of SAMs incorporating molecules with HOMO/LUMO levels close to E_f in EGaIn/Ga$_2$O$_3$//SAM/Ag^{TS} junctions.[42] They reached this conclusion based on the observation that the direction and magnitude of rectification depended on the functionality of the SAM at the EGaIn/Ga$_2$O$_3$//SAM interface; ferrocenes rectified negatively and strongly, quinones rectified positively and weakly, and methyl and carboxylic acid groups did not rectify. This observation was explained by involvement of the HOMO of ferrocene and the LUMO of the quinone moieties interacting with E_f of Ag^{TS} and was shown to be statistically significant. Thus, the tunneling of charges through EGaIn/Ga$_2$O$_3$//SAM junctions necessarily involves the electronic states of the SAM and, therefore, is not simply an artifact of the thin oxide layer.

Yoon et al. made the curious observation that, with the exception of rectification, the functional groups at the EGaIn/Ga$_2$O$_3$//SAM interface do not influence the rate of tunneling.[43, 44] They screened numerous functional groups attached to n-alkanes and aliphatic amides in which the amides where buried in the SAM (thus not altering the tunneling properties compared to n-alkanes[45]) including polar groups, coordinating groups, aromatic groups, and bulky ring structures. Plots of log(J) at $\pm$ 0.5 V versus molecular length, shown in Figure 1.5, were linear an did not differ by functional group—only the thickness of the head groups mattered. This observation is counterintuitive given the nature of Ga$_2$O$_3$, which presents an active surface and possibly dangling hydroxyls (e.g., by hydrolysis in air). One would expect that carboxylic acids and pyridines would ionize at the interface, affecting the transport properties, particularly given that the anchoring and head groups affect tunneling properties significantly in other metal/molecule/metal junctions.[46, 47] These experiments highlight the utility of a bench top tool such as EGaIn for physical-organic studies; a completely counterintuitive result can be rigorously proven experimentally by collecting statistically significant data on large series of molecules directly and quickly. They also reveal an important aspect of the Ga$_2$O$_3$ layer, which is that it chemically isolates the bulk Ga-In from the SAM while leaving them elec-

trically coupled.
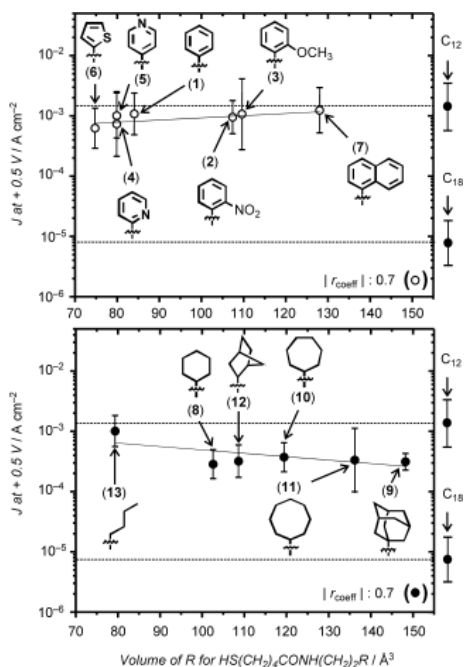
Figure 1.5 Plots of current densities of SAMs with various head groups and two calibration standard alkanethiols, 1-dodecanethiol (HS$-$(CH$_2$)$_{11}$CH$_3$, C12) and 1-octadecanethiol (HS$-$(CH$_2$)$_{17}$CH$_3$, C18), as a function of volume of the corresponding aromatic and aliphatic tail group (R for HS(CH$_2$)$_4$CONH(CH$_2$)$_2$R). The dashed lines represent the tunneling current for the calibration standards (C12 and C18 alkane-thiols), and the solid lines are linear squares fits. The molecular structures shown are those of the tail groups R. The r_{coeff} is a correlation coefficient for each scatterplot. The molecular volumes of the tail groups were calculated from the Molinspiration Property Calculation Service at http://www.molinspiration.com. ○: aromatic moieties, •: aliphatic moieties Reprinted with permission from reference [43]. Copyright 2012, Wiley-VCH.

Dickey et al. leveraged the non-Newtonian rheology of EGaIn to form stable structures in microfluidic channels.[48] This property is a direct result of the shear-yielding properties of EGaIn (and is therefore a consequence of the oxide), as liquid metals tend to have very high surface free energies (surface tensions), meaning that they will normally retract spontaneously from microfluidic channels to minimize their surface area. They authors demonstrated this property by placing drops of either EGaIn or Hg over the inlets of microfluidic channels and then filling them by applying a vacuum. When the vacuum was removed, the Hg spontaneously and quickly withdrew from the channels, while EGaIn remained in the channels indefinitely.[49–52] Nijhuis et al. used EGaIn in microfluidic channels to form EGaIn/Ga$_2$O$_3$//SAM/Ag^{TS} junctions by placing the microfluidic channel perpendicular to an array of thin Ag^{TS} strips.[53] The SAMs incorporated ferrocene terminal groups, which posses a HOMO that is accessible by both Ag^{TS} and EGaIn, separated by aliphatic tails that create a tunneling junction. This experimental setup enabled variable-temperature measurements and the construction of Arrhenius plots from which the authors were able to differentiate the contributions of hopping

11

and tunneling and the activation energy of the hopping processes across a bias window. These experiments extended the utility of EGaIn into variable-temperature studies without sacrificing the simplicity of EGaIn-based junction. The microfluidic devices were constructed using soft lithography.

RECTIFICATION

Since the seminal paper of Aviram and Ratner predicted the possibility of rectification in tunneling junctions,[9] the observation of rectification has been, at the very least, much more complicated to observe experimentally than was expected. EGaIn-based rectifiers have proven to be particularly robust and reproducible and have demonstrated the usefulness of rectification as a tool for probing the properties of molecular junctions. Rectification is when an electrical circuit exhibits different resistance at positive and negative bias and is defined as R = $|J(–)/J(+)|$ (or its reciprocal) at a particularly value of V. For the purposes of this discussion, we will define a negative rectification as a circuit that is less resistive at negative bias and vice versa (formally R does not have a sign). Nijhuis et al. first observed negative rectification of R=1.0 x 10^2 in SAMs of alkane-thiolates terminated by ferrocenes in EGaIn/Ga_2O_3//SAM/Ag^{TS} junctions.[54, 55] They showed that the ferrocenes were densely packed by measuring the peak-broadening of the ferrocene oxidation peak by cyclic voltammetry (CV) as compared to SAMs diluted with n-alkanethiolates. This is an important property for rectification because disorder introduces leakage currents (shunts) from non-rectifying thin spots that reduce R.[56]

Nerngchamnong et al. probed the influence of Van der Waals forces on the rectification properties of ferrocene-terminated SAMs.[57] By taking advantage of the odd-even effect present in the alkane tails, they were able to show that the magnitude of R depended not just on the presence or absence of ferrocenes, but also on their packing density and orientation with respect to EGaIn. This study is not only important for understanding the origins of rectification in ferrocene-containing SAMs, but also adds detail to the ongoing efforts to understand the Ga_2O_3//SAM interface. Although insensitive to a wide variety of functional groups that would otherwise be expected to interact chemically with an oxide, the interface is apparently quite sensitive to the proximity of ferrocenes; subtle changes to the Van der Walls interactions in the SAM that disturb the tight, upright packing of these SAMs dramatically influences R and the stability/yield of junctions.

UNDERSTANDING β AND J_0

The spread in the values of J measured for any SAM-based molecular junction may be influenced by other parameters, but will always include the influence of defects in the monolayer. Thus, EGaIn junctions show a log-normal distribution of J due to the random distribution of defects. With few exceptions (which are discussed below) all EGaIn molecular junctions are measured on Au^{TS} or Ag^{TS}, but template-stripping only lessens the density of defects as compared to vacuum-deposited films, it does not eliminate them completely. Given the popularity of the simplified Simmons' approximation and the numerous reports of values of β and J_0, these two values remain indispensable, even when more advanced theories are invoked. Thus, it is important to understand how to derive them properly and how to interpret the distributions of J to extract meaningful data. Reus et al. performed a detailed statistical analysis on data obtained

from EGaIn junctions comprising SAMs of alkanethiolates.[58] They reiterate that J varies log-normal and therefore the most meaningful analysis is a fit to a normal distribution. Mean values derived from Gaussian fits are, for example, significantly less sensitive to outliers—thin and thick-area defects—and even shorts than medians or arithmetic means as is shown in Figure 1.6. The error expressed in J/V plots derived from Gaussian means therefore corresponds to the variance of the distribution of values of J. This analysis imparts greater meaning to the error bars because they represent the confidence—the probability that a subsequent value will fall inside the error bounds—rather than instrument or measurement error. In addition, plots of $\ln(J)$ vs length can be plotted with confidence bands, providing a more detailed insight into the ranges of β and J_0. Thus, a relatively simple and straightforward analysis can be used to extract meaningful parameters from high throughput physical-organic studies. Importantly, this statistical method does not require any "pruning" or selection of data, which removes a potential source of bias.
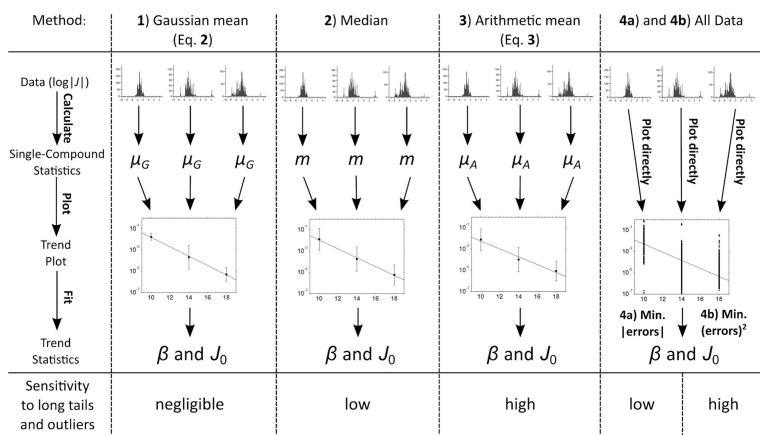
Figure 1.6 Schematic of the four methods of analyzing charge transport discussed in this paper. Methods 1–3 use the data (samples of $\log|J|$) to calculate single-compound statistics; plotting those statistics, and fitting the plots, yields trend statistics. For Method 1, μG is the Gaussian mean; for Method 2, m is the median; and for Method 3, μA is the arithmetic mean. Methods 4a and 4b proceed directly to plotting and fitting the raw data to determine trend statistics. The bottom row gives the sensitivity of each method to common deviations of $\log|J|$ from normality (long tails and outliers). Reprinted with permission from reference [58]. Copyright 2012 American Chemical Society.

A very nice example of the level of detail present in J/V data generated from EGaIn junctions was the observation of an odd-even effect by Thuo et al.[59] The odd-even effect in SAMs of alkanethiolates arises from the slightly different packing of alkanethiols with odd and even numbers of carbons that influences how the terminal methyl groups are presented at the surface. This difference manifests itself in a variety of ways, including a measureable difference in contact angles and values of β. The odd-even effect, in general, is found throughout natural and artificial systems; we direct the reader to a comprehensive review on the topic.[60] Thuo et al. measured SAMs of alkanethiolates from n=8-17 in EGaIn/Ga_2O_3//$CH_3(CH_2)_n$S/Ag^{TS} junctions. When plotted together, the odds and evens are not immediately distinguishable, but from the Gaussian means, the

authors were able to determined that $\beta_{\text{odd}} = 1.15 \pm 0.07$ and $\beta_{\text{even}} = 1.02 \pm 0.09 \ N_c^{-1}$ and that SAMs of alkanethiolates with even numbers of carbons gave higher values of J than odd numbers. Importantly, they observed that the confidence bands of the linear fits from which these values were derived did not overlap in the region in which the SAMs were measured, but did overlap closer to the Y-intercept, thus J_0 for the two series could not be differentiated (or claimed to be equal). The authors also directly confronted the question of what a "simple" technique is. This term is used subjectively and is frequently abused, particularly in the realm of bottom-up and top-down nanofabrication and ME. They compared the data acquired from one experienced user to those collected from a variety of users with varying levels of experience, including complete beginners. These data yielded $\beta_{\text{odd}} = 1.19 \pm 0.08$ and $\beta_{even} = 1.04 \pm 0.06 \ N_c^{-1}$, a negligible difference from the experienced user, particularly given the spread in values of β reported for SAMs of alkanethiolates by a variety of methods. There are two reasons for this observation: i) EGaIn measurements require no special training and are, therefore, simple by the most general definition and ii) because the values are derived from Gaussian fits, the mean is not strongly influenced by outliers. Thus, provided the sample size is adequate to build a log-normal distribution, EGaIn is simple in the sense that it is easy to collect "real" data and not artifacts of the experimental technique.

There are two outstanding issues with J_0: i) it is difficult to measure accurately because it is derived from the Y-intercept of plots of d $\gg$ 0 and ii) its physical meaning is not well understood. The latter problem would be helped tremendously by a solution to the former problem. Simeone et al. addressed this problem by measuring J_0 directly.[61] Typically, SAMs of n-alkanethiolates comprising fewer than about eight carbons are difficult or impossible to measure in bottom-up molecular junctions because they are disordered and liquid-like. At the extremes, the precursor thiols are also volatile liquids or gasses at room temperature. Simeone et al. solved the latter problem by forming SAMs slowly via the hydrolysis of their salts by suspending paper soaked in aqueous solutions of the salts over Ag^{TS} substrates submerged in toluene. Remarkably, the yield of non-shorting EGaIn/Ga_2O_3//$C_nH_{2n+2}S$/Au^{TS} junctions was ~90% for n=0-18. This observation was explained by the authors as (at least partially) the result of the way in which they formed tips of EGaIn. Frequently, when the EGaIn tip severs from the sacrificial drop, a macroscopic "whisker" is formed at the tip. This whisker is then pressed back into the bulk when the tip is brought into contact with the SAM; however, it is likely that the surface topology of the tip either comprises more of these whiskers or ripples that are trapped as the shear stress falls below the critical yield threshold. Thus, the authors pushed the tip back into the sacrificial drop to remove the visible whisker and then pressed the tip against a polished Si wafer to flatten it out. While one does have to be careful not to conflate the yield of working junctions with the presence of densely-packed, ordered SAMs,[53] the observation of a distance-dependence all the way to d=0 is remarkable by itself, let alone the high yields.

Simeone et al. determined $\log|J_0| = 3.6 \pm 0.3$ ($J_0 = A\,cm^{-2}$); however, this value assumes an accurate determination of the contact area, which is highly unlikely given the topology of EGaIn observed by Cademartiri et al.[41] Thus, they measured a substrate with a known specific resistance (Fe_2O_3/Fe) and, by comparison to Hg and measurements of the resistivity of Ga_2O_3 on highly ordered pyrolytic graphite (HOPG), they de-

termined that the actual contact area was about 1,000x smaller than previously estimated. They then constructed a plot comprising values of log(J) and β of various different (bottom-up and top-down) junctions to find consensus values, dividing the data into rough contacts, smooth contacts, and single molecule measurements. Correcting the EGaIn data for contact area lead to a value of J that was in excellent agreement with measurements from smooth contacts. It remains to be seen if this correction is valid for all measurements using EGaIn, but the data so far are compelling. Simeone et al. also make a more controversial claim: that the structure of the SAM does not play a significant role in the magnitude of J. They make no claims about other observables, e.g., R or V_{trans}, however, this claim directly refutes Levine et al., who observed the influence of disorder in shorter SAMs of n-alkylphosphonates on Al/Al$_2$O$_3$ in J and β.[62] One possible reason for this discrepancy is that monolayers of phosphonates on metal oxides are probably self-organized and not self-assembled because they form irreversible covalent interactions (and is why that work is not discussed further in this mini-review.) In either case, more work is needed to determine the role of disorder on tunneling charge transport in molecular junctions unambiguously.

Uncovering new phenomena

The aforementioned studies focused primarily on elucidating known properties and phenomenon in EGaIn/Ga$_2$O$_3$//CH$_3$(CH$_2$)nS/Ag^{TS} junctions and in doing so demonstrating the utility of EGaIn. Fracasso et al. used EGaIn to observe quantum interference experimentally in EGaIn/Ga$_2$O$_3$//SAM/Au^{Mica} (Au^{Mica}≡gold-on-mica).[63] The phenomenon of quantum interference can be understood by the conjugation patterns of benzene; meta substituents are not connected by alternating single and double bonds—they are cross-conjugated—and therefore communicate only through the σ framework of the ring. Para substituents, however, are linearly conjugated and therefore are strongly electronically linked through resonance structures of π the system. Theorists had predicted a similar effect in tunneling junctions; cross-conjugated molecules should exhibit a lower rate of tunneling (i.e., be less conductive) than linearly conjugated molecules of the same length. Observing this phenomenon experimentally, however, proved difficult, requiring a close collaboration between synthetic chemists to design and synthesize the molecules and physicists to perform the measurements.

One of the principle advantages of EGaIn is that it is a bench top tool that is accessible to chemists. Fracasso et al. leveraged this accessibility to perform measurements on three molecules that they synthesized and characterized, which are shown in Figure 1.7. The molecules were of the same length, comprising either a cross-conjugated, linearly-conjugated, or non-conjugated core. The conjugation patterns differed only at the 9,10 positions of anthracene moieties, allowing the observation of the influence of conjugation patterns to be separated from length and the specifics of the packing of the SAMs.[7] They observed a difference in J of 1-2 orders of magnitude; the linearly-conjugated core was more conductive that the cross- or non-conjugated cores. Due to the incompatibility of template-stripped surfaces with the organic solvents necessary to dissolve the anthracene moieties, the measurements were performed on Au^{Mica} surfaces. While excellent for small-area studies by scanning tunneling microscopy (STM), mica surfaces comprise numerous step-edges and a much higher RMS roughness than Au^{TS}. This roughness lowered the yields of working junctions and complicated Gaussian fits

somewhat. However, the authors observed that the distribution of $\log(J)$ for the linearly-conjugated (and most conductive) SAM was truncated. Thus, a fit to the truncated data revealed a value of J that was higher than what could actually be observed experimentally. Interestingly, the cut-off value was very similar to the highest value of J measured for d=0 by Simeone et al.[59] The results of Fracasso et al. were later corroborated in CP-AFM junctions.[64] In that case, synthetic chemists were able to address an outstanding problem in ME synthetically and perform measurements using EGaIn which were later confirmed by physicists using more time-consuming and laborious techniques; this is the appropriate model for research in ME and highlights the increasingly important role of EGaIn in the field.
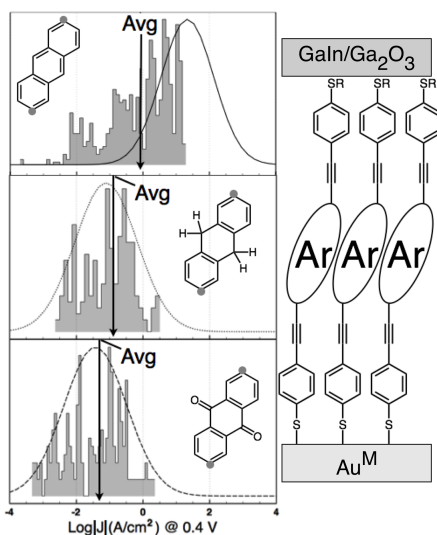

Figure 1.7 A schematic of the tunneling junctions (right; not to scale) of gold-on-mica supporting SAMs of thiolated arylethynylenes with cores (left; shown in the plots) of anthracene (linear-conjugation), 9,10-anthraquinone (cross-conjugation), or 9,10-dihydroanthracene (broken-conjugation) connected at the 2,6 positions (indicated with grey circles). The plots on the left are histograms of $\log|J|$ at 400 mV showing the difference in conductivities and the truncated Gaussian of the anthracene moiety. Reprinted with permission from reference [63]. Copyright 2011 American Chemical Society.

The first measurements of V_{trans} using EGaIn were reported by Ricœur et al.[65] They found that, for n-alkanes, $V_{\text{trans}} \sim 0.3\,\text{V}$, which could not be explained by the offsets between E_f and the HOMO or LUMO of the molecules. The authors concluded that it was the offset between the LUMO of the alkanethiolates and the band structure of Ga_2O_3 that dominated V_{trans}, meaning that this useful parameter was inaccessible via EGaIn. Fracasso et al. measured V_{trans} for a series of phenylenes bearing alkanethiol tails and a homologous series bearing a terminal p-pyridine shown in Figure 9.[66] They observed $0.27 < V_{\text{trans}} < 0.64$ and correlated these values to E_f-E_{HOMO} using density functional theory (DFT). The key to this observation was the consideration of the difference in dipole moments between the phyenylene and pyridine head groups; the latter induced a shift in vacuum level at the interface, producing a commensurate shift in V_{trans}. This obser-

vation was validated by a correlation between the measured work function of the SAMs on Au^{TS} and V_{trans}. The authors conclude that Ricœur et al. were probably correct, but only because the HOMO and LUMO levels of alkanes are so far removed from E_f for Hg, EGaIn, Au, and Ag that the band structure of Ga_2O_3 dominates V_{trans}. For conjugated molecules, where the HOMO is readily accessible, V_{trans} is dominated by E_f-E_{HOMO}.

Thus far six SAMs with accessible HOMO levels have been measured: i) ferrocene-terminated SAMs, ii) anthracene moieties, iii) phenylene/pyridyl SAMs, iv) Ru "tripod" complexes[67], v) quinone-terminated SAMs[42] and vi) biphenylthiolates.[68] In all cases interesting and/or new phenomena were uncovered; rectification, quantum interference, dipole-induced influences on the tunneling properties, rectification, inverse rectification, and torsional-angle dependent tunneling, respectively. In the ten years between the first publication of EGaIn tunneling junctions, $EGaIn/Ga_2O_3//SAM/Metal$ junctions have proven a valuable tool in ME for the formation of bottom-up molecular junctions. It has, in essence, picked up where Hg-drops left off, offering a more robust measurement platform that is simple to setup, learn, and use.
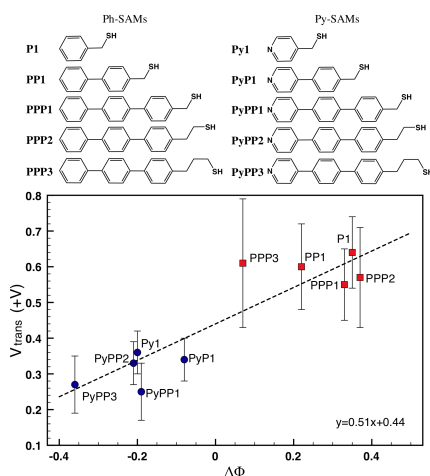
Figure 1.8 Plots of V_{trans} (from $EGaIn/Ga_2O_3/SAM/Au^{TS}$ junctions) vs. the measured shift in work function (ϕ) for SAMs of the molecules pictured above in. The Py-SAMs (blue circles) and Ph-SAMs (red squares) cluster around different values of V_{trans}, which is influenced by the dipole-induced shift in work function (vacuum level) caused by the SAMs. Reprinted with permission from reference [66]. Copyright 2013 American Chemical Society.

1.4. RIGID CONTACTS TOWARD SOLID STATE DEVICES

The ideal contacts for forming bottom-up molecular junctions are rigid metal electrodes. The direct contact of molecules to a metal simplifies the junctions both experimentally and theoretically and it is difficult to imagine a commercialized ME-based device with liquid metal contacts. The mechanical stability of molecules is, however, generally not sufficient to withstand most conventional methods for installing metallic top-contacts.

1

Thus, metal/molecule/metal junctions are typically restricted to top-down spectroscopies such as STM break junctions and CP-AFM. There are, however, approaches to installing metals as top-contacts non-destructively while preserving the key feature of bottom-up fabrication; that the molecules themselves form the smallest dimensions of the device.

1.4.1. CONJUGATED POLYMER CONTACTS

The most well known example of a conjugated polymer contact is in the "large-area molecular junctions" developed by Akkerman et al.[6, 69, 70] The conducting polymer blend used in these devices is poly(3,4-ethylenedioxythiophene):poly(4-styrenesulphonic acid) (PEDOT:PSS), which is spin-coated from an aqueous suspension on top of SAMs of alkanethiolates on gold. The contact area is defined by micron-sized pores that are formed by photolithography on Au structures supported by a silicon wafer. Large-area molecular junctions use some top-down methods, but in this case it advantageous, as the smallest dimension of the device is still defined by the SAM, but the devices are fabricated in parallel on silicon wafers making them compatible with modern microelectronics. These junctions have been reviewed recently and therefore will be discussed only briefly.[71]

The key feature of the PEDOT:PSS buffer layer is that prevents parasitic currents and electrical shorts between the top metal electrode and bottom metal electrode that would otherwise occur by the penetration of metal atoms into the SAMs upon deposition of the Au top electrode. Since the interface with the SAM is actually PEDOT:PSS, it is difficult to characterize them as having rigid or soft contacts, but the top-most electrode is vacuum-deposited Au. Large-area molecular junctions exhibit excellent stability and yields close to 100% and are therefore one of very few examples of actual ME devices. Akkerman et al. observed no significant deterioration after 888 days in ambient conditions up to 50 °C.[72] Unlike Hg//polymer//SAM/Metal junctions fabricated by Milani et al., which use Poly(2-methoxy-5-(2'-ethylhexyloxy)-1,4"-phenylenevinylene) (MEH-PPV) in its undoped, semiconducting state, the PEDOT in PEDOT:PSS is in its doped, metallic state and is therefore more conductive; however, the resistivity of bulk PEDOT:PSS films is still high enough to contribute to the total resistivity of Au//PEDOT:PSS/SAM/Au junctions.[73] Kronemeijer et al. quantified this observation, concluding that Au//PEDOT:-PSS cannot be regarded as a simple metallic electrode and that the resistance of a molecular junction does in fact depend on the bulk conductivity of PEDOT:PSS.[74] Wang et al. observed that the electrical properties of large-area junctions are also influenced by the morphology of the PEDOT:PSS films and by thermal treatment.[75] Thus, Au//PEDOT:-PSS//SAM/Au junctions share the same complexity as EGaIn/Ga_2O_3//SAM/Metal junctions in that the buffer layer (PEDOT:PSS or Ga_2O_3) has a profound influence on the transport properties and must therefore be studied, understood, and controlled. However, unlike EGaIn, larger-area junctions are not a particularly good platform for physical-organic studies because the influence of PEDOT:PSS—which is hundreds of times thicker than the SAM—is much more pronounced than the influence of Ga_2O_3. They are, instead, much better suited for device applications and integration into circuits. For example, for flexible molecular electronic devices[76] and optical switching.[77]

1.4.2. Nanoskiving

An emerging bottom-up technique utilizes a form of edge lithography developed by Whitesides and co-workers known as nanoskiving. It combines the deposition of thin film with the mechanical sectioning of thin films embedded in a polymer matrix via ultramicrotomy.[78–80] It involves three major steps: i) depositing a thin metallic, semi-conducting, or polymeric film onto a substrate; ii) embedding the film in an epoxy or thiol-ene polymer block;[81] and iii) sectioning the block into slabs using an ultramic-rotome, which is pictured in Figure 1.9. The operation is based on the controlled mechanical advance of a sample arm that holds the sample to be sectioned. The topography of the original substrate, the thickness of the deposited film, and the thickness of the sections cut by the ultramicrotome determine the three dimensions of the nanostructures. Compared to conventional methods of nanofabrication, nanoskiving is cheap and simple, requiring no special associated tools and clean rooms.[82] In principle, nanoskiving does not even require electricity, as the ultramicrotome can be operated by hand.

Xu et al. reported the first use of nanoskiving for the fabrication of nanostructures including arrays of Au "nanoband" electrodes, frequency-selective surface-plasmonic Au nanowires, high aspect ratio Au nanostructures, large-area optical structures at mid-IR wavelengths, and stacking of multilayer structures on planes and curved surfaces.[83–87] Lipomi et al. developed methods for using nanoskiving to generate more complex nanostructures of relevance to metamaterials over areas of 1 mm^2.[88]

The key step of nanoskiving is mechanical, making it compatible with soft materials such as conjugated polymers that would not survive conventional photolithography.[89, 90] By co-embedding nickel within the slabs, the sections can be placed and oriented magnetically.[91] These two features make nanoskiving particularly attractive for ME, as a wide variety of electrodes, metallic and polymeric, can be investigated and, in principle, devices can be aligned magnetically and wired together. Crystalline Au can also be used, which should greatly reduce the density of defects in SAMs.[92] Individually addressable parallel nanowire electrodes with 30 nm spacing, which is approaching molecular length scales, were easily fabricated by nanoskiving.[93]

Pourhossein et al. scaled the gap-size of nanoskived, electrically addressable Au electrodes to < 3 nm—well within the length-scale of molecules—by using self-assembled monolayers as templates.[94] These junctions are bottom-up, but use rigid metal contacts, affording a resolution of metal nanogaps as small as 2.5 Å (a C-C bond). Figure 1.10 shows the resulting SAM-templated addressable nanogap (STAN) electrodes and the process of the fabrication of STAN electrodes. Once a block is prepared for nanoskiving, hundreds of thousands of STAN electrodes can be generated, on demand, at a rate of about one per second. All three dimensions of the STANs can be controlled, and they can be placed onto almost any substrate. These Au/SAM/Au^{TS} junctions are directly electrically addressable by applying silver paste under a light microscope by hand; no probe stations or further lithography are required. Length-dependent electrical measurements on alkanedithiols yielded $\beta = 0.75$ Å^{-1} (Figure 1.11). Thus, STAN electrodes offer an exceedingly simple platform for directly fabricating tunneling junctions comprising SAMs that pack densely enough to withstand the deposition of gold. While electrical shorts do form, it is unlikely that they are captured by the 50-100 nm-thick sections used to form STANs. Moreover, when defects are encountered in a block, they can be trimmed and
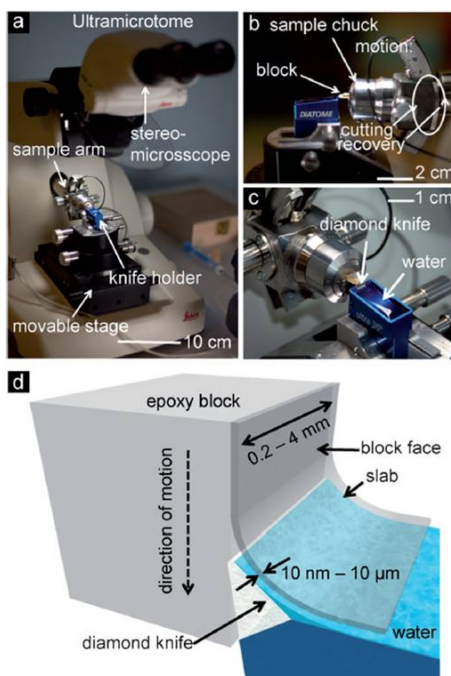
Figure 1.9 Photographs and schematic drawings of the tools of ultramicrotomy and nanoskiving. a) A photograph of a Leica UC6 ultramicrotome. b) A side view of the sample chuck and knife holder. c) A top view of the single-crystalline diamond blade and the water-filled trough. d) A schematic drawing of the sectioning process. The block contacts the diamond knife, and the slab slides onto the surface of water. The cutting process repeats until the user stops the ultramicrotome or the embedded material is consumed. The water supports the slabs until the user collects them. Reprinted with permission from reference [79]. Copyright 2011, Wiley-VCH.

discarded. Nanoskiving and STAN electrodes are still quite new to ME, but they offer a unique combination of addressability and simple, bottom-up fabrication.

When discussing the broad, interdisciplinary field of ME, it is important to draw a clear distinction between spectroscopic tools and devices. The former give insights into the basic physics of tunneling phenomena through organic molecules, while the latter addresses the decades old question of whether or not molecules can be used to circumvent the limitations of top-down lithography in modern electronics. If ME is realized as a viable technology, it will almost certainly be based on this principle of bottom-up fabrication. There are many approaches to fabricating such devices, some are focused on parallel fabrication and integrating molecular junctions into existing fab technologies, while others are focused on reproducibility and physical-organic studies.

Although many challenges remain in the fabrication of molecular junctions, the future of ME lies in chemistry. There is still work to be done to separate the influences of the individual molecules from those of the supramolecular assembly and the substrate,[95] but transport through SAMs of alkanethiolates is well understood and, importantly, the data and fabrication techniques are sufficiently reproducible. The realization of ME as a technology, however, will involve gating, switching, and sensing, all of which require
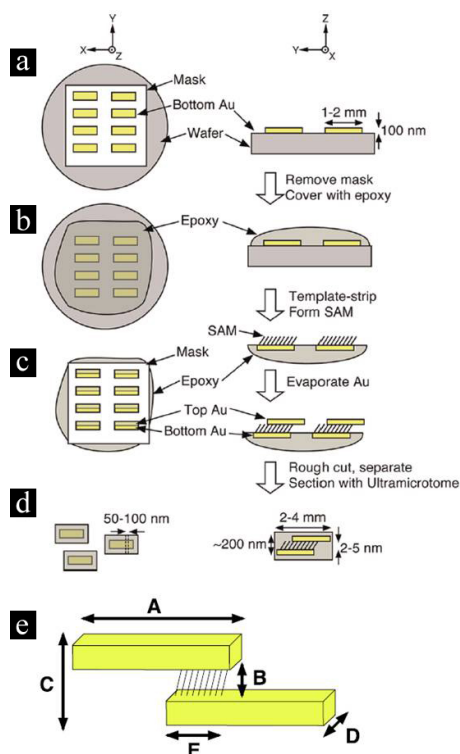
Figure 1.10 Schematics of the fabrication and dimensions of STAN electrodes. a) A 100 nm-thick layer of gold is deposited through a Teflon shadow mask onto a fluorinated silicon wafer via thermal evaporation to produce an array of mm-sized rectangles. b) The mask is removed and the gold features covered in epoxy. After the epoxy cures, it is separated from the wafer such that the gold features remain adhered to epoxy. A SAM is then formed on the newly exposed gold surfaces. c) The Teflon mask is placed over the SAM-covered gold features with an offset of 250-500 μm and another 100 nm-thick layer of gold is deposited. d) The mask is removed and the gold/SAM/gold features are separated by rough-cutting the epoxy with a jeweller's saw. The features are then embedded in epoxy and sectioned with an ultramicrotome. e) A schematic of the dimensions of the STAN electrodes showing how each dimension is defined. Reprinted with permission from reference [94]. Copyright 2012 American Chemical Society.

enormous synthetic efforts to design and synthesize functional molecules that can self-assemble into systems robust enough for the bottom-up fabrication of two- and three-terminal junctions. Simple, bench top molecular junctions such as those incorporating EGaIn are necessary to catalyze this work, while robust, addressable devices such as large-area molecular junctions are necessary to push ME out of academic labs an into industry, though this transition may take several more decades.
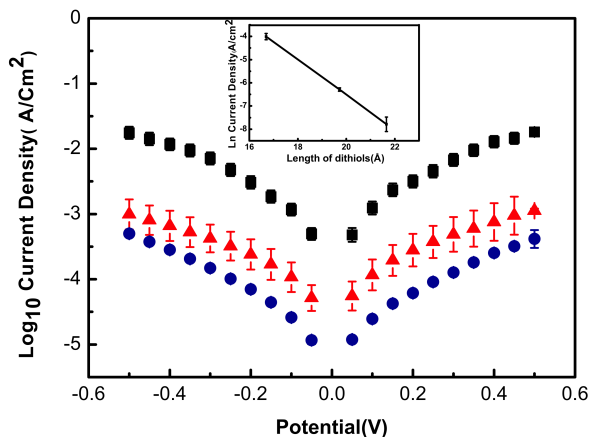
Figure 1.11 Log current-density versus potential plots for STAN electrodes fabricated from three different dithiols; SC12S (black squares), SC14S (red triangles), and SC16S (blue circles). The inset is a plot of $\ln(J)$ versus length (Å) showing a linear fit ($R^2 = 0.99$) with a slope corresponding to β=0.75 Å^{-1} (0.94 N_c^{-1}). Reprinted with permission from reference [94]. Copyright 2012 American Chemical Society.

1.5. THESIS OUTLINE

In **Chapter 2**, we studied the mechanical and electrical properties of self-assembled monolayers (SAMs) comprising 4-([2,2':5',2":5",2"'-quaterthiophen]-5-yl)butane-1-thiol (**T4C4**) using conducting probe AFM (CP-AFM) and eutectic Ga-In (EGaIn) top-contacts. We found that **T4C4** is more mechanically robust than decanethiol. And we used density functional theory (DFT) calculations and transition voltage spectroscopy to figure out that at high pressures the resistance of **T4C4** begins to change due to the force-induced changes to the electronic structure of the thiophene rings rather than the physical structure of the SAM. Further, we correlated the increased mechanical stability of **T4C4** to higher breakdown voltages, comparing to alkanes, in large-area junctions using EGaIn top-contacts, which suggests the electrostatic pressure results in the breakdown of molecular tunneling junctions instead of electrochemical instability.

In **Chapter 3**, we synthesized three benzodithiophenes based molecular wires; one linearly-conjugated, one cross-conjugated and one cross-conjugated quinone. We designed these benzodithiophene derivatives to isolate the effects of bond topology from that of quinone functional groups in quantum interference. We compared the charge transport of the benzodithiophenes derivatives to a well-known anthraquinone in large area molecular junctions comprising self-assembled monolayers (SAMs) using two different techniques: eutectic Ga-In (EGaIn) and conducting probe AFM (CP-AFM). We showed that the presence of an interference feature and its position could be controlled independently by manipulating bond topology and electronegativity using density functional theory and transition voltage spectroscopy. We found that the quinones suppress tunneling transport further than cross-conjugation alone and switch the mechanism from tunneling mediated by occupied states to tunneling mediated by unoccupied states.

In **Chapter 4**, we fabricated SAM-templated addressable nanogap electrodes (STANs) using nanoskiving. We used SAMs of molecules with different terminal groups and different metal electrodes to construct the molecular junctions. We also tried to manufacture the sub-10 nm nanogaps defined by the reduced graphene oxide (rGO), and gate them using ionic liquid as the dielectric layers. We discussed the fabrication, the results, and the remaining challenges.

In **Chapter 5**, we used nanoskiving to prepare Au nanowires (Au NWs) and placed them in the center of the microfluidic channels, where the rate of the flow is highest. We can fabricate free-standing Au NWs simply using nanoskiving without the need for the complicated, conventional lithographic techniques. We demonstrated two applications of the suspended Au NWs in the microfluidic channels: One acts as a hot-wire anemometer that measures the flow by a change in resistance across the Au nanowire. And the other is that stretching DNA molecules in the stream to visualize them by single-molecule fluorescence imaging. We eliminated the background noise from nonspecific binding by forming a curtain of DNA attached to a suspended nanowire. Moreover, the DNA, attached to the suspended nanowire, extends further at lower rates of the flow, comparing to those directly bind to the bottom of the microfluidic channel. Because the DNA is positioned in the center of the channel where the rate of the flow is highest.

1

BIBLIOGRAPHY

[1] Editorial. Moore's deviation. *Nat. Nanotech.*, 12:1105, 2017.

[2] Marcin Fialkowski, Kyle J M Bishop, Rafal Klajn, Stoyan K Smoukov, Christopher J Campbell, and Bartosz A Grzybowski. Principles and Implementations of Dissipative (Dynamic) Self-Assembly. *The Journal of Physical Chemistry B*, 110(6):2482–2496, 2006.

[3] George M Whitesides and Mila Boncheva. Beyond molecules: Self-assembly of mesoscopic and macroscopic components. *Proceedings of the National Academy of Sciences*, 99(8):4769–4774, 2002.

[4] Colin D Bain, E Barry Troughton, Yu Tai Tao, Joseph Evall, George M Whitesides, and Ralph G Nuzzo. Formation of monolayer films by the spontaneous assembly of organic thiols from solution onto gold. *Journal of the American Chemical Society*, 111(1):321–335, 1989.

[5] J Christopher Love, Lara a Estroff, Jennah K Kriebel, Ralph G Nuzzo, and George M Whitesides. Self-assembled monolayers of thiolates on metals as a form of nanotechnology.. *Chemical Reviews*, 105(4):1103–1170, 2005.

[6] Hylke B Akkerman, Paul W M Blom, Dago M de Leeuw, and Bert de Boer. Towards molecular electronics with large-area molecular junctions. *Nature*, 441(7089):69–72, 2006.

[7] Hennie Valkenier, Everardus H Huisman, Paul a van Hal, Dago M de Leeuw, Ryan C Chiechi, and Jan C Hummelen. Formation of high-quality self-assembled monolayers of conjugated dithiols on gold: base matters. *Journal of the American Chemical Society*, 133(13):4930–4939, 2011.

[8] Bernhard Mann and Hans Kuhn. Tunneling through Fatty Acid Salt Monolayers. *Journal of Applied Physics*, 42(11), 1971.

[9] Arieh Aviram and Mark A Ratner. Molecular rectifiers. *Chemical Physics Letters*, 29 (2):277–283, 1974.

[10] John G. Simmons. Generalized Formula for the Electric Tunnel Effect between Similar Electrodes Separated by a Thin Insulating Film. *Journal of Applied Physics*, 34 (6):1793, 1963.

[11] Jeremy Beebe, BongSoo Kim, J. Gadzuk, C. Daniel Frisbie, and James Kushmerick. Transition from Direct Tunneling to Field Emission in Metal-Molecule-Metal Junctions. *Physical Review Letters*, 97(2):026801, 2006.

[12] Everardus H Huisman, Constant M Guedon, Bart J van Wees, and Sense Jan van der Molen. Interpretation of Transition Voltage Spectroscopy. *Nano Letters*, 9(11):3909–3913, 2009.

[13] Jeremy M Beebe, BongSoo Kim, C Daniel Frisbie, and James G Kushmerick. Measuring Relative Barrier Heights in Molecular Electronic Junctions with Transition Voltage Spectroscopy. *ACS Nano*, 2(5):827–832, 2008.

[14] BongSoo Kim, Seong Ho Choi, X.-Y. Zhu, and C Daniel Frisbie. Molecular Tunnel Junctions Based on π-Conjugated Oligoacene Thiols and Dithiols between Ag, Au, and Pt Contacts: Effect of Surface Linking Group and Metal Work Function. *Journal of the American Chemical Society*, 133(49):19864–19877, 2011.

[15] Krzysztof Slowinski, Richard V Chamberlain, Renata Bilewicz, and Marcin Majda. Evidence for Inefficient Chain-to-Chain Coupling in Electron Tunneling through Liquid Alkanethiol Monolayer Films on Mercury. *Journal of the American Chemical Society*, 118(19):4709–4710, 1996.

[16] Krzysztof Slowinski, Richard V Chamberlain, Cary J Miller, and Marcin Majda. Through-Bond and Chain-to-Chain Coupling. Two Pathways in Electron Tunneling through Liquid Alkanethiol Monolayers on Mercury Electrodes. *Journal of the American Chemical Society*, 119(49):11910–11919, 1997.

[17] Krzysztof Slowinski, Katarzyna U. Slowinska, and Marcin Majda. Electron Tunneling Across Hexadecanethiolate Monolayers on Mercury Electrodes: Reorganization Energy, Structure, and Permeability of the Alkane/Water Interface. *The Journal of Physical Chemistry B*, 103(40):8544–8551, 1999.

[18] Krzysztof Slowinski, Harold K Y Fong, and Marcin Majda. Mercury-Mercury Tunneling Junctions. 1. Electron Tunneling Across Symmetric and Asymmetric Alkanethiolate Bilayers. *Journal of the American Chemical Society*, 121(31):7257–7261, 1999.

[19] Krzysztof Slowinski and Marcin Majda. Mercury–mercury tunneling junctions: Part II. Structure and stability of symmetric alkanethiolate bilayers and their effect on the rate of electron tunneling. *Journal of Electroanalytical Chemistry*, 491(1–2):139–147, 2000.

[20] Roger L York, Phuong T Nguyen, and Krzysztof Slowinski. Long-Range Electron Transfer through Monolayers and Bilayers of Alkanethiols in Electrochemically Controlled Hg-Hg Tunneling Junctions. *Journal of the American Chemical Society*, 125(19):5948–5953, 2003.

[21] R Erik Holmlin, Rainer Haag, Michael L Chabinyc, Rustem F Ismagilov, Adam E Cohen, Andreas Terfort, Maria Anita Rampi, and George M Whitesides. Electron Transport through Thin Organic Films in Metal-Insulator-Metal Junctions Based on Self-Assembled Monolayers. *Journal of the American Chemical Society*, 123(21):5075–5085, 2001.

[22] Rainer Haag, Maria Anita Rampi, R Erik Holmlin, and George M Whitesides. Electrical Breakdown of Aliphatic and Aromatic Self-Assembled Monolayers Used as Nanometer-Thick Organic Dielectrics. *Journal of the American Chemical Society*, 121(34):7895–7906, 1999.

1

[23] Michael L Chabinyc, Xiaoxi Chen, R Erik Holmlin, Heiko Jacobs, Hjalti Skulason, C Daniel Frisbie, Vladimiro Mujica, Mark A Ratner, Maria Anita Rampi, and George M Whitesides. Molecular Rectification in a Metal-Insulator-Metal Junction Based on Self-Assembled Monolayers. *Journal of the American Chemical Society*, 124(39):11730–11736, 2002.

[24] Christian Grave, Elizabeth Tran, Paolo Samorì, George M Whitesides, and Maria A Rampi. Correlating electrical properties and molecular structure of SAMs organized between two metal surfaces. *Synthetic Metals*, 147(1–3):11–18, 2004.

[25] E. Tran, M. Duati, V. Ferri, K. Müllen, M. Zharnikov, G. M. Whitesides, and M. a. Rampi. Experimental Approaches for Controlling Current Flowing through Metal–Molecule–Metal Junctions. *Advanced Materials*, 18(10):1323–1328, 2006.

[26] Felice Carlo Simeone and Maria Anita Rampi. Test-beds for Molecular Electronics: Metal–Molecules–Metal Junctions Based on Hg Electrodes. *CHIMIA International Journal for Chemistry*, 64(6):362–369, 2010.

[27] Emily A Weiss, Ryan C Chiechi, George K Kaufman, Jennah K Kriebel, Zhefeng Li, Marco Duati, Maria A Rampi, and George M Whitesides. Influence of Defects on the Electrical Characteristics of Mercury-Drop Junctions: Self-Assembled Monolayers of n-Alkanethiolates on Rough and Smooth Silver. *Journal of the American Chemical Society*, 129(14):4336–4349, 2007.

[28] Martin Hegner, Peter Wagner, and Giorgio Semenza. Ultralarge atomically flat template-stripped Au surfaces for scanning probe microscopy. *Surface Science Letters*, 291(1-2):A562, 1993.

[29] Peter Wagner, Martin Hegner, Hans-Joachim Guentherodt, and Giorgio Semenza. Formation and in Situ Modification of Monolayers Chemisorbed on Ultraflat Template-Stripped Gold Surfaces. *Langmuir*, 11(10):3867–3875, 1995.

[30] P Samorí, J Diebel, H Löwe, and J P Rabe. Template-Stripped Gold Supported on Ni as a Substrate for SAMs. *Langmuir*, 15(7):2592–2594, 1999.

[31] Thomas Ederth. Template-stripped gold surfaces with 0.4-nm rms roughness suitable for force measurements: Application to the Casimir force in the 20-100 nm range. *Phys. Rev. A*, 62(6):62104, 2000.

[32] J Diebel, H Löwe, P Samorí, and J P Rabe. Fabrication of large-scale ultra-smooth metal surfaces by a replica technique. *Applied Physics A*, 73(3):273–279, 2001.

[33] Renate Naumann, Stefan M Schiller, Frank Giess, Bernd Grohe, Keith B Hartman, Iris Kärcher, Ingo Köper, Jörn Lübben, Krasimir Vasilev, and Wolfgang Knoll. Tethered Lipid Bilayers on Ultraflat Gold Surfaces. *Langmuir*, 19(13):5435–5443, 2003.

[34] Pooja Gupta, Katja Loos, Alexander Korniakov, Chiara Spagnoli, Mary Cowman, and Abraham Ulman. Facile route to ultraflat SAM-protected gold surfaces by "amphiphile splitting". *Angew. Chem. Int. Ed.*, 43(4):520–523, 2004.

[35] Regina Ragan, Doug Ohlberg, Jason J Blackstock, Sehun Kim, and R Stanley Williams. Atomic Surface Structure of UHV-Prepared Template-Stripped Platinum and Single-Crystal Platinum(111). *The Journal of Physical Chemistry B*, 108(52):20187–20192, 2004.

[36] Dejian Zhou, Andreas Bruckbauer, Matthew Batchelor, Dae-Joon Kang, Chris Abell, and David Klenerman. Influence of the Foundation Layer on the Layer-by-Layer Assembly of Poly-l-lysine and Poly(styrenesulfonate) and Its Usage in the Fabrication of 3D Microscale Features. *Langmuir*, 20(21):9089–9094, 2004.

[37] Vincent B Engelkes, Jeremy M Beebe, and C Daniel Frisbie. Analysis of the Causes of Variance in Resistance Measurements on Metal-Molecule-Metal Junctions Formed by Conducting-Probe Atomic Force Microscopy. *The Journal of Physical Chemistry B*, 109(35):16801–16810, 2005.

[38] Lizhong He, Joseph W F Robertson, Jing Li, Iris Kärcher, Stefan M Schiller, Wolfgang Knoll, and Renate Naumann. Tethered Bilayer Lipid Membranes Based on Monolayers of Thiolipids Mixed with a Complementary Dilution Molecule. 1. Incorporation of Channel Peptides. *Langmuir*, 21(25):11666–11672, 2005.

[39] Emily A Weiss, George K Kaufman, Jennah K Kriebel, Zhefeng Li, Richard Schalek, and George M Whitesides. Si/SiO2-Templated Formation of Ultraflat Metal Surfaces on Glass, Polymer, and Solder Supports: Their Use as Substrates for Self-Assembled Monolayers. *Langmuir*, 23(19):9686–9694, 2007.

[40] Ryan C. Chiechi, Emily A. Weiss, Michael D. Dickey, and George M. Whitesides. Eutectic Gallium–Indium (EGaIn): A Moldable Liquid Metal for Electrical Characterization of Self-Assembled Monolayers. *Angewandte Chemie International Edition*, 47(1):142–144, 2008.

[41] Ludovico Cademartiri, Martin M Thuo, Christian A Nijhuis, William F Reus, Simon Tricard, Jabulani R Barber, Rana N S Sodhi, Peter Brodersen, Choongik Kim, Ryan C Chiechi, and George M Whitesides. Electrical Resistance of AgTS-S(CH2)n-1CH3//Ga2O3/EGaIn Tunneling Junctions. *The Journal of Physical Chemistry C*, 116(20):10848–10860, 2012.

[42] William F Reus, Martin M Thuo, Nathan D Shapiro, Christian A Nijhuis, and George M Whitesides. The SAM, Not the Electrodes, Dominates Charge Transport in Metal-Monolayer//Ga2O3/Gallium–Indium Eutectic Junctions. *ACS Nano*, 6(6):4806–4822, 2012.

[43] Hyo Jae Yoon, Nathan D Shapiro, Kyeng Min Park, Martin M Thuo, Siowling Soh, and George M Whitesides. The rate of charge tunneling through self-assembled monolayers is insensitive to many functional group substitutions. *Angewandte Chemie International Edition*, 51(19):4658–4661, 2012.

[44] Hyo Jae Yoon, Carleen M Bowers, Mostafa Baghbanzadeh, George M Whitesides, Nathan D Shapiro, Kyeng Min Park, Martin M Thuo, and Siowling Soh. The Rate of

Charge Tunneling Is Insensitive to Polar Terminal Groups in Self-Assembled Monolayers in AgTSS(CH2)nM(CH2)mT//Ga2O3/EGaIn Junctions. *Journal of the American Chemical Society*, 136(1):16–19, 2013.

[45] Martin M Thuo, William F Reus, Felice C Simeone, Choongik Kim, Michael D Schulz, Hyo Jae Yoon, and George M Whitesides. Replacing -CH_2CH_2- with -CONH- Does Not Significantly Change Rates of Charge Transport through AgTS-SAM//Ga_2O_3/EGaIn Junctions. *Journal of the American Chemical Society*, 134(26): 10876–10884, 2012.

[46] BongSoo Kim, Jeremy M Beebe, Yongseok Jun, X-Y Zhu, and C Daniel Frisbie. Correlation between HOMO alignment and contact resistance in molecular junctions: aromatic thiols versus aromatic isocyanides. *Journal of the American Chemical Society*, 128(15):4970–4971, 2006.

[47] Vincent B Engelkes, Jeremy M Beebe, and C Daniel Frisbie. Length-Dependent Transport in Molecular Junctions Based on SAMs of Alkanethiols and Alkanedithiols: Effect of Metal Work Function and Applied Bias on Tunneling Efficiency and Contact Resistance. *Journal of the American Chemical Society*, 126(43):14287–14296, 2004.

[48] Michael D Dickey, Ryan C Chiechi, Ryan J Larsen, Emily A Weiss, David A Weitz, and George M Whitesides. Eutectic Gallium-Indium (EGaIn): A Liquid Metal Alloy for the Formation of Stable Structures in Microchannels at Room Temperature. *Advanced Functional Materials*, 18(7):1097–1104, 2008. .

[49] Ryan J Larsen, Michael D Dickey, George M Whitesides, and David A Weitz. Viscoelastic properties of oxide-coated liquid metals. *Journal of Rheology (1978-present)*, 53(6), 2009.

[50] M R Khan, G J Hayes, S Zhang, M D Dickey, and G Lazzi. A Pressure Responsive Fluidic Microstrip Open Stub Resonator Using a Liquid Metal Alloy, 2012.

[51] Brad L. Cumby, Gerard J. Hayes, Michael D. Dickey, Ryan S. Justice, Christopher E. Tabor, and Jason C. Heikenfeld. Reconfigurable liquid metal circuits by Laplace pressure shaping. *Applied Physics Letters*, 101(17):174102, 2012.

[52] Mohammed G. Mohammed and Michael D. Dickey. Strain-controlled diffraction of light from stretchable liquid metal micro-components. *Sensors and Actuators A: Physical*, 193:246–250, 2013.

[53] Christian a Nijhuis, William F Reus, Jabulani R Barber, Michael D Dickey, and George M Whitesides. Charge transport and rectification in arrays of SAM-based tunneling junctions. *Nano letters*, 10(9):3611–3619, 2010.

[54] Christian A Nijhuis, William F Reus, and George M Whitesides. Molecular Rectification in Metal-SAM-Metal Oxide-Metal Junctions. *Journal of the American Chemical Society*, 131(49):17814–17827, 2009.

[55] Christian A Nijhuis, William F Reus, and George M Whitesides. Mechanism of Rectification in Tunneling Junctions Based on Molecules with Asymmetric Potential Drops. *Journal of the American Chemical Society*, 132(51):18386–18401, 2010.

[56] Li Jiang, Li Yuan, Liang Cao, and Christian A Nijhuis. Controlling Leakage Currents: The Role of the Binding Group and Purity of the Precursors for Self-Assembled Monolayers in the Performance of Molecular Diodes. *Journal of the American Chemical Society*, 136:1982–1991, 2014.

[57] Nisachol Nerngchamnong, Li Yuan, Dong-Chen Qi, Jiang Li, Damien Thompson, and Christian a Nijhuis. The role of van der Waals forces in the performance of molecular diodes. *Nature nanotechnology*, 8(2):113–118, 2013.

[58] William F. Reus, Christian a. Nijhuis, Jabulani R. Barber, Martin M. Thuo, Simon Tricard, and George M. Whitesides. Statistical Tools for Analyzing Measurements of Charge Transport. *The Journal of Physical Chemistry C*, 116(11):6714–6733, 2012.

[59] Martin M Thuo, William F Reus, Christian A Nijhuis, Jabulani R Barber, Choongik Kim, Michael D Schulz, and George M Whitesides. Odd-Even Effects in Charge Transport across Self-Assembled Monolayers. *Journal of the American Chemical Society*, 133(9):2962–2975, 2011.

[60] Feng Tao and Steven L Bernasek. Understanding Odd-Even Effects in Organic Self-Assembled Monolayers. *Chemical Reviews*, 107(5):1408–1453, 2007.

[61] Felice C Simeone, Hyo Jae Yoon, Martin M Thuo, Jabulani R Barber, Barbara Smith, and George M Whitesides. Defining the Value of Injection Current and Effective Electrical Contact Area for EGaIn-Based Molecular Tunneling Junctions. *Journal of the American Chemical Society*, 135(48):18131–18144, 2013.

[62] Igal Levine, Stephanie M Weber, Yishay Feldman, Tatyana Bendikov, Hagai Cohen, David Cahen, and Ayelet Vilan. Molecular Length, Monolayer Density, and Charge Transport: Lessons from Al–AlOx/Alkyl–Phosphonate/Hg Junctions. *Langmuir*, 28 (1):404–415, 2011.

[63] Davide Fracasso, Hennie Valkenier, Jan C Hummelen, Gemma C Solomon, and Ryan C Chiechi. Evidence for quantum interference in SAMs of arylethynylene thiolates in tunneling junctions with eutectic Ga-In (EGaIn) top-contacts. *Journal of the American Chemical Society*, 133(24):9556–9563, 2011.

[64] Constant M Guedon, Hennie Valkenier, Troels Markussen, Kristian S Thygesen, Jan C Hummelen, and Sense Jan van der Molen. Observation of quantum interference in molecular charge transport. *Nat Nano*, 7(5):305–309, 2012.

[65] Guillaume Ricœur, Stéphane Lenfant, David Guérin, and Dominique Vuillaume. Molecule/Electrode Interface Energetics in Molecular Junction: A "Transition Voltage Spectroscopy" Study. *The Journal of Physical Chemistry C*, 116(39):20722–20730, 2012.

1

[66] Davide Fracasso, Mutlu Iskender Muglali, Michael Rohwerder, Andreas Terfort, and Ryan C Chiechi. Influence of an Atom in EGaIn/Ga2O3 Tunneling Junctions Comprising Self-Assembled Monolayers. *The Journal of Physical Chemistry C*, 117(21): 11367–11376, 2013.

[67] Srinidhi Ramachandra, Klaus C Schuermann, Fabio Edafe, Peter Belser, Christian a Nijhuis, William F Reus, George M Whitesides, and Luisa De Cola. Luminescent ruthenium tripod complexes: properties in solution and on conductive surfaces. *Inorganic chemistry*, 50(5):1581–1591, 2011.

[68] Appan Merari Masillamani, Núria Crivillers, Emanuele Orgiu, Jürgen Rotzler, David Bossert, Ramakrishnappa Thippeswamy, Michael Zharnikov, Marcel Mayor, and Paolo Samorì. Multiscale charge injection and transport properties in self-assembled monolayers of biphenyl thiols with varying torsion angles. *Chemistry (Weinheim an der Bergstrasse, Germany)*, 18(33):10335–10347, 2012.

[69] Hylke B. Akkerman, Auke J. Kronemeijer, Paul A. van Hal, Dago M. de Leeuw, Paul W. M. Blom, and Bert de Boer. Self-Assembled-Monolayer Formation of Long Alkanedithiols in Molecular Junctions. *Small*, 4(1):100–104, 2008.

[70] Hylke B Akkerman, Ronald C G Naber, Bert Jongbloed, Paul A van Hal, Paul W M Blom, Dago M de Leeuw, and Bert de Boer. Electron tunneling through alkanedithiol self-assembled monolayers in large-area molecular junctions. *Proceedings of the National Academy of Sciences*, 104(27):11161–11166, 2007.

[71] Hylke B Akkerman and Bert de Boer. Electrical conduction through single molecules and self-assembled monolayers. *Journal of Physics: Condensed Matter*, 20 (1):013001, 2008.

[72] Hylke B Akkerman, Auke J Kronemeijer, Jan Harkema, Paul A van Hal, Edsger C P Smits, Dago M de Leeuw, and Paul W M Blom. Stability of large-area molecular junctions. *Organic Electronics*, 11(1):146–149, 2010.

[73] Federico Milani, Christian Grave, Violetta Ferri, Paolo Samorì, and Maria Anita Rampi. Ultrathin π-Conjugated Polymer Films for Simple Fabrication of Large-Area Molecular Junctions. *ChemPhysChem*, 8(4):515–518, 2007.

[74] Auke J Kronemeijer, Ilias Katsouras, Eek H Huisman, Paul a van Hal, Tom C T Geuns, Paul W M Blom, and Dago M de Leeuw. Universal scaling of the charge transport in large-area molecular junctions. *Small (Weinheim an der Bergstrasse, Germany)*, 7(11):1593–1598, 2011.

[75] Gunuk Wang, Seok-In Na, Tae-Wook Kim, Yonghun Kim, Sungjun Park, and Takhee Lee. Effect of PEDOT:PSS–molecule interface on the charge transport characteristics of the large-area molecular electronic junctions. *Organic Electronics*, 13(5): 771–777, 2012.

[76] Sungjun Park, Gunuk Wang, Byungjin Cho, Yonghun Kim, Sunghoon Song, Yongsung Ji, Myung-Han Yoon, and Takhee Lee. Flexible molecular-scale electronic devices. *Nature nanotechnology*, 7(7):438–442, 2012.

[77] Kronemeijer Auke J., Akkerman Hylke B., Kudernac Tibor, van Wees Bart J., Feringa Ben L., Blom Paul W M., and de Boer Bert. Reversible Conductance Switching in Molecular Devices. *Advanced Materials*, 20(8):1467–1473, 2008.

[78] Qiaobing Xu, Robert M Rioux, Michael D Dickey, and George M Whitesides. Nanoskiving: a new method to produce arrays of nanostructures. *Accounts of chemical research*, 41(12):1566–1577, 2008.

[79] Darren J Lipomi, Ramses V Martinez, and George M Whitesides. Use of Thin Sectioning (Nanoskiving) to Fabricate Nanostructures for Electronic and Optical Applications. *Angewandte Chemie International Edition*, 50(37):8566–8583, 2011.

[80] Darren J Lipomi, Ramses V Martinez, Robert M Rioux, Ludovico Cademartiri, William F Reus, and George M Whitesides. Survey of materials for nanoskiving and influence of the cutting process on the nanostructures produced. *ACS applied materials & interfaces*, 2(9):2503–2514, 2010.

[81] Robin L. Mays, Parisa Pourhossein, Dhanalekshmi Savithri, Jan Genzer, Ryan C. Chiechi, and Michael D. Dickey. Thiol-containing polymeric embedding materials for nanoskiving. *Journal of Materials Chemistry C*, 1(1):121, 2013.

[82] Benjamin J Wiley, Dong Qin, and Younan Xia. Nanofabrication at high throughput and low cost. *ACS nano*, 4(7):3554–3559, 2010.

[83] Qiaobing Xu, Byron D Gates, and George M Whitesides. Fabrication of metal structures with nanometer-scale lateral dimensions by sectioning using a microtome. *Journal of the American Chemical Society*, 126(5):1332–1333, 2004.

[84] Qiaobing Xu, Raquel Perez-Castillejos, Zhefeng Li, and George M Whitesides. Fabrication of high-aspect-ratio metallic nanostructures using nanoskiving. *Nano letters*, 6(9):2163–2165, 2006.

[85] Qiaobing Xu, Jiming Bao, Federico Capasso, and George M Whitesides. Surface plasmon resonances of free-standing gold nanowires fabricated by nanoskiving. *Angewandte Chemie International Edition*, 45(22):3631–3635, 2006.

[86] Qiaobing Xu, Robert M Rioux, and George M Whitesides. Fabrication of complex metallic nanostructures by nanoskiving. *ACS nano*, 1(3):215–227, 2007.

[87] Qiaobing Xu, Jiming Bao, Robert M Rioux, Raquel Perez-Castillejos, Federico Capasso, and George M Whitesides. Fabrication of large-area patterned nanostructures for optical applications by nanoskiving. *Nano letters*, 7(9):2800–2805, 2007.

[88] Darren J Lipomi, Mikhail A Kats, Philseok Kim, Sung H Kang, Joanna Aizenberg, Federico Capasso, and George M Whitesides. Fabrication and Replication of Arrays of Single- or Multicomponent Nanostructures by Replica Molding and Mechanical Sectioning. *ACS Nano*, 4(7):4017–4026, 2010.

1

[89] Darren J Lipomi, Ryan C Chiechi, Michael D Dickey, and George M Whitesides. Fabrication of conjugated polymer nanowires by edge lithography. *Nano letters*, 8(7): 2100–2105, 2008.

[90] Darren J. Lipomi, Ryan C. Chiechi, William F. Reus, and George M. Whitesides. Laterally Ordered Bulk Heterojunction of Conjugated Polymers: Nanoskiving a Jelly Roll. *Advanced Functional Materials*, 18(21):3469–3477, 2008.

[91] Darren J Lipomi, Filip Ilievski, Benjamin J Wiley, Parag B Deotare, Marko Loncar, and George M Whitesides. Integrated fabrication and magnetic positioning of metallic and polymeric nanowires embedded in thin epoxy slabs. *ACS nano*, 3 (10):3315–3325, 2009.

[92] Benjamin J Wiley, Darren J Lipomi, Jiming Bao, Federico Capasso, and George M Whitesides. Fabrication of surface plasmon resonators by nanoskiving single-crystalline gold microplates. *Nano letters*, 8(9):3023–3028, 2008.

[93] Michael D Dickey, Darren J Lipomi, Paul J Bracher, and George M Whitesides. Electrically addressable parallel nanowires with 30 nm spacing from micromolding and nanoskiving. *Nano letters*, 8(12):4568–4573, 2008.

[94] Parisa Pourhossein and Ryan C Chiechi. Directly addressable sub-3 nm gold nanogaps fabricated by Nanoskiving using self-assembled monolayers as templates. *ACS nano*, 6(6):5566–5573, 2012.

[95] Li Yuan, Li Jiang, Bo Zhang, and Christian A Nijhuis. Dependency of the Tunneling Decay Coefficient in Molecular Tunneling Junctions on the Topography of the Bottom Electrodes. *Angewandte Chemie International Edition*, 53(13):3377–3381, 2014.

2

MECHANICALLY AND ELECTRICALLY ROBUST SELF-ASSEMBLED MONOLAYERS FOR LARGE-AREA TUNNELING JUNCTIONS

2

Abstract: *Ín this chapter, we examines the relationship between mechanical deformation
and the electronic properties of self-assembled monolayers (SAMs) of the oligothiophene
4-([2,2':5',2":5",2'''-quaterthiophen]-5-yl)butane-1-thiol (T4C4) in tunneling junctions us-
ing conductive probe atomic force microscopy (CP-AFM) and Eutectic Ga-In (EGaIn). We
compared shifts in conductivity, transition voltages of T4C4 with increasing AFM tip load-
ing force to alkanethiolates. While these shifts result from an increasing tilt angle from
penetration of the SAM by the AFM tip for the latter, we ascribe them to distortions of
the π system present in T4C4, which is more mechanically robust than alkanethiolates of
comparable length; SAMs comprising T4C4 shows about five times higher Young's mod-
ulus than alkanethiolates. Density functional theory calculations confirm that mechan-
ical deformations shift the barrier height due to changes in the frontier orbitals caused
by small rearrangements to the conformation of the quaterthiophene moiety. The mech-
anical robustness of T4C4 manifests as an increased tolerance to high bias in large-area
EGaIn junctions suggesting that electrostatic pressure plays a significant role in the short-
ing of molecular junctions at high bias.*
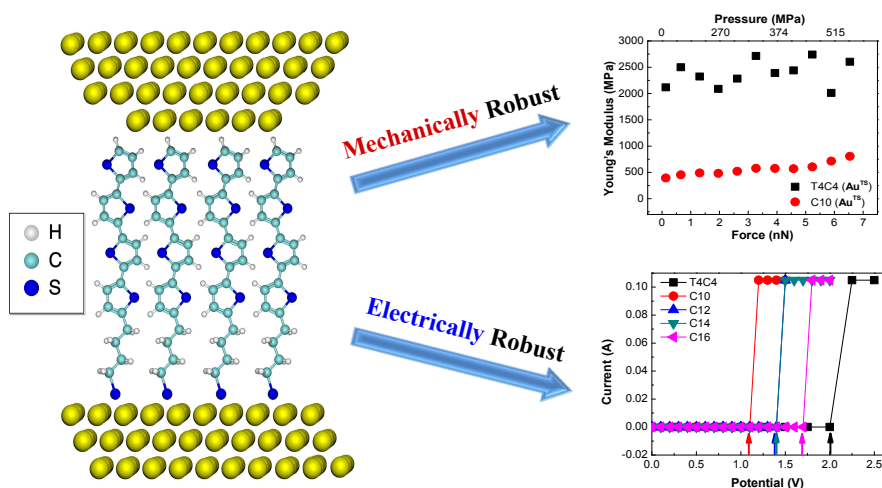
2.1. INTRODUCTION

Emerging challenges in Information Technology are driving research into new computer architectures and circuit designs[1] that require new materials and concepts in nano-electronics. Molecular Electronics, specifically tunneling junctions comprising discrete molecules, are well suited to address these challenges[2, 3] because they control charge-transport directly at the quantum level, however, it remains impractical to integrate single-molecule junctions[4, 5] into devices. Bottom-up junctions comprising self-assembled monolayers[6–8] (SAMs,) on the other hand, can already be incorporated into wafer-scale fabrication processes[9] and diode logic circuits.[10] When molecules pack into a SAM, collective effects, such as the overlap of interacting electronic states and charges, give rise to new properties that affect tunneling charge-transport significantly as compared to single-molecule junctions.[11–14] In addition to electronic and electrostatic effects, SAMs exhibit mechanical properties derived from the interactions between individual molecules, which play a critical role in the tolerance of SAMs towards particular top-contacts and, ultimately, technological applications. Small changes in the conformation of a molecule or ensemble of molecules (*e.g.*, in a SAM) between two electrodes can have dramatic effects on conductance by altering electronic states in the metal/molecule/metal junction.[12, 15] Large-area junctions are typically constructed using SAMs of molecules with anchoring groups such as thiols that drive self-assembly into ordered structures that impose fixed conformations. The effects of these conformations and their relationship to the bulk mechanical properties of the SAM can not be ignored, particularly for π-conjugated molecules, since intermolecular interactions affect charge transport via electrostatic effects and because both hopping and tunneling charge-transport are sensitive to electronic delocalization, which is maximized in co-planar conformations. Establishing a structure-function relationship between mechanical deformation and electrostatics in SAMs of π-conjugated molecules is, therefore, important fundamentally and for the potential for exploitation in molecular-scale devices that are sensitive to force/pressure/deformation.

Conductive probe atomic force microscopy (CP-AFM) is capable of characterizing the electrical properties of SAMs while varying the loading force applied to a probe tip that doubles as a top-contact. Changes in the resistances of SAMs of alkanethiolates with applied force have been ascribed to changes in the tilt angle of the alkane chains.[16–20] Transition voltage spectroscopy (TVS) indicates that the transition voltage V_{trans} shifts to a lower bias with increasing force (*i.e.*, as the tilt angle increases).[19, 20] This observation implies a decrease in barrier height of molecular junctions because V_{trans} is proportional to the energy offset between the Fermi level E_F and the highest-occupied molecular state.[21] If there are more subtle influences to the electrostatics of the junctions from bond distortions they are masked by the larger effect of the tilt angle increasing as the tip penetrates the SAM, which is stabilized only by relatively weak intermolecular dispersion forces. The mechanical properties of SAMs of π-conjugated molecules have not been similarly investigated. Thus, we synthesized 4-([2,2':5',2":5",2"'-quaterthiophen]-5-yl)butane-1-thiol (T4C4), a molecule containing both a flexible butanethiol chain to facilitate the formation of a densely-packed monolayer and a rigid quarterthiophene to impart mechanical stability through relatively strong π-π interactions. The molecular structure and the geometry of a CP-AFM junction are shown in Figure 2.1. We stud-

ied the mechanical and electrical properties of SAMs of T4C4 using CP-AFM and density functional theory (DFT). They are quantitatively more robust than SAMs of alkanethiolates, but the electrostatics of the junction respond to small distortions of the π-system. This robustness translates into junctions that are capable of withstanding larger bias windows than alkanethiolates in large-area junctions using eutectic Ga-In (EGaIn) top-contacts.[22]
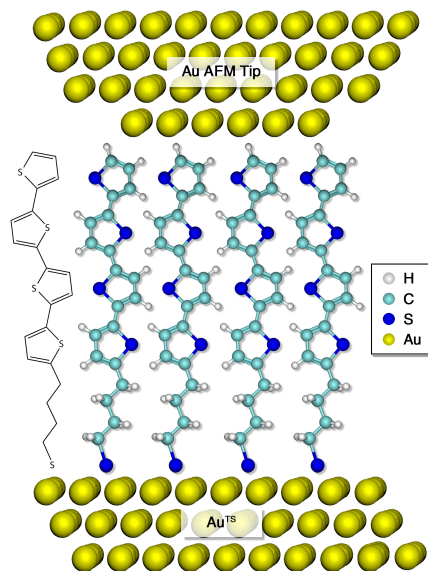

Figure 2.1 Representative schematic of molecular junction comprising T4C4 with a Au coated CP-AFM tip as top electrode and template-stripped Au as bottom electrode.

2.2. RESULTS AND DISCUSSION

Oligothiophenes can form densely-packed SAMs.[23–25] For comparison to previously reported mechanical studies, we used decanethiol (C10). We chose C10 specifically because the properties of SAMs of C10 have been studied extensively by CP-AFM.[16, 26, 27] We prepared both template-stripped gold (Au^{TS}) and silver (Ag^{TS}) ultra-smooth electrodes following literature procedures template-stripping.[28] These substrates are particularly well suited to large-area junctions[29].

2.2.1. CP-AFM MEASUREMENTS

We formed metal-molecule-metal junctions by placing the gold coated CP-AFM tip (denoted as Au^{AFM}) with spring constant of $0.35\,\text{Nm}^{-1}$ and nominal radius of 30 nm in a stationary point contact with the SAM under a controlled tip loading force, which translates into an applied pressure that depends on the radius of the tip; CP-AFM tips are larger than ordinary Si_3N_4 tips due to the additional metallic layers. We refer to the

molecular junctions as Au^{TS}/SAM//Au^{AFM}, where '/' and '//' denote a covalent inter-face and a van der Waals contact, respectively. We measured the I-V characteristics of Au^{TS}/C10//Au^{AFM} and Au^{TS}/T4C4//Au^{AFM} junctions at low applied forces, which we define as 25 nN or less. Characteristic data are shown in Figure 2.2 for C10 and T4C4. (The I-V curves for C10 at and above 25 nN shorted when bias was applied and are, therefore, omitted from the figure.) The I-V characteristics of C10 were sufficiently sim-ilar to published data to validate our measurement technique.[16–20] The I-V curves of T4C4 did not change at low forces (Figure 2.2A), passing approximately 10 nA at 1 V. The I-V curves of C10, however, varied by about a factor of two, passing approximately 200 nA at 1 V with a force of 10 nN and 100 nA at 1.4 nN. We were only able to measure T4C4 to ±1 V without saturating the current amplifier, while we were able to measure C10 to ±1.5 V using the low-gain amplifier because the absolute current in the intermediate-bias regime (*i.e.*, where the I-V dependence becomes exponential) increases more slowly for C10 than for T4C4. To verify the reproducibility of the data in Figure 2.2, we per-formed a statistical analysis by constructing histograms of I at ±1 V (Figures 2.15 and 2.16) and fitting them to Gaussian distributions. The data points with error bars are the peak and standard deviations, respectively, derived from such histograms.

The I-V curves of T4C4 are sigmoidal, passing nearly invariant, low current in the lin-ear, low-bias regime (below 0.5 V) and increasing dramatically in the exponential, inter-mediate-bias regime, which is consistent for π-conjugated (or σ-π) 'molecular wire' mole-cules.[30]. The I-V curves of C10 are sigmoidal, but increase throughout the low-bias regime, which is consistent for alkanethiols.[16, 31] The evolution of the I-V curves with increasing loading force can be caused by any combination of three factors; 1) the mo-lecular tilt increases; 2) molecules in the SAM are deformed; and 3) the contact area increases. As mentioned above, the response of C10 is attributed mainly to the tilt angle, but T4C4 showed no change at forces up to 30 nN as can be seen in Figure 2.3. (Note that the dependence of pressure on loading force is non-linear due to the dependence of contact-area on force, thus, the values across the top X-axis are only meant to show the range of pressures experienced by the SAM; see Experimental section for details.) This semi-log scale plot compresses the data somewhat, but there is still a clear, increas-ing trend for C10 that is absent for T4C4 even up to 30 nN (*i.e.*, three times the loading force). At high force (30 nN to 150 nN) the conductivity of T4C4 begins to increase, but C10 either shorts or saturates the current amplifier (both manifest as hitting the compli-ance limit) above 10 nN (Figure 2.14). Thus, we measured SAMs of dodecanethiol (C12) in Ag^{TS}/C12//Au^{AFM} and Ag^{TS}/C12//EGaIn junctions in order to compare the effects at high forces. We switched to Ag^{TS} substrates for C12 to facilitate comparisons to literat-ure reports for EGaIn, for which Ag^{TS} is the preferred substrate as described below.[32–34] We also measured Ag^{TS}/T4C4//Au^{AFM} and Ag^{TS}/T4C4//EGaIn junctions for compar-ison. The increase in current of Ag^{TS}/C12//Au^{AFM} as a function of loading force is even more dramatic than Au^{TS}/C10//Au^{AFM} and Ag^{TS}/C10//Au^{AFM}, spanning three orders of magnitude up to 150 nN; see Figures 2.17 and 2.18.

2.2.2. MECHANICAL PROPERTIES

In addition to I-V measurements via CP-AFM, we measured the mechanical properties of SAMs of T4C4 and C10 on Au^{TS} using PeakForce QNM® AFM. Figure 2.4A shows the

2

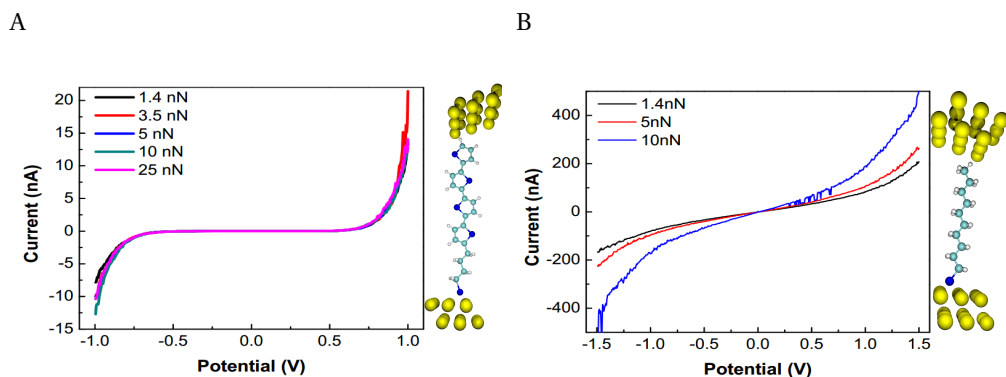A   B

Figure 2.2 A) *I-V* plots of T4C4 with different forces: black for 1.4 nN, red for 3.5 nN, blue for 5 nN, dark cyan for 10 nN, pink for 25 nN. B) *I-V* plots of C10 with different forces: black for 1.4 nN, red for 5 nN, blue for 10 nN. Both SAMs were measured on Au^{TS} substrates by CP-AFM.
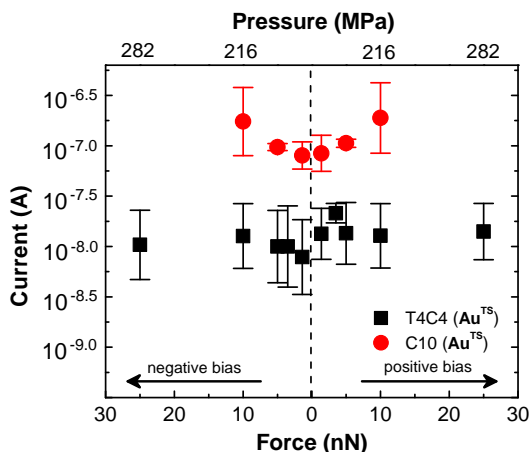

Figure 2.3 Current at 1.0 V versus loading force on Au^{TS} plots: dark squares for T4C4, red circles for C10. Each data point is the peak of Gaussian fit to a histogram of I at that value of V. The error bars are standard deviations. The values listed on the top X-axis are the pressures calculated explicitly for the corresponding values of force on the bottom X-axis.

deformation as a function of loading force up to 7 nN. To enable a comparison between these data and CP-AFM data, we estimated the pressure applied to the SAM by considering the loading force and the radius of the tip (see Experimental section Table 2.8). At loading forces below 3 nN the magnitudes and slopes are similar, but above 3 nN the displacement of T4C4 begins to level off at approximately 0.8 nm while C10 continues to increase. We hypothesize that the inflection point in the T4C4 curve is caused by compression/deformation of the butyl tail, which deforms at lower loading force than the quarterthiophene unit (but similar to C10). Figure 2.4B shows the Derjaguin-Muller-Toporov(DMT) Young's modulus (stiffness in the elastic region) over the same range of

loading force.[35] (There are no error bars because the Young's modulus was calculated from the average deformation of each force load using the DMT model.) The difference is unambiguous; the modulus of T4C4 is five times higher than C10, indicating that SAMs of T4C4 are considerably stiffer than SAMs of C10. Our measured values for C10 are also in good agreement with the moduli for SAMs of alkanethiolates reported previously; 280 MPa for octanethiol (C8) and 860 MPa for C12.[36] From the electrical and mechanical measurements, we conclude that SAMs of T4C4 are more mechanically robust than C10, which translates into more stable conductance across a wider range of loading force; however, conductance alone does not provide much insight into the electrostatics of the junctions or address the question of why the I-V characteristics of T4C4 are stable despite deforming considerably at low loading forces.
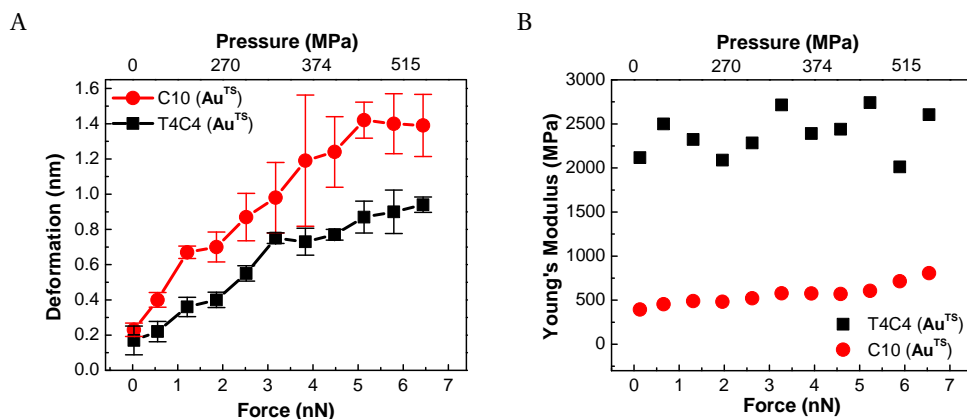

Figure 2.4 A) Deformation of SAMs on Au^{TS}: black squares for T4C4, red circles of C10. The error bars are standard deviations. B) Young's modulus of SAMs: black squares for T4C4, red circles of C10. The values listed on the top X-axis are the pressures calculated explicitly for the corresponding values of force on the bottom X-axis.

2.2.3. Transition Voltage Spectroscopy

Transition Voltage Spectroscopy (TVS) is a useful tool to gain insights into the electrostatics of molecular junctions by providing an indirect measure of ϕ, the offset between E_F and the frontier orbital that participates most strongly in tunneling transport (the highest-occupied state for both C10 and T4C4, *i.e.*, hole transport). The transition voltage V_{trans} corresponds to the transition from Ohmic, low-bias conduction to exponential/hyperlinear conduction at intermediate bias, which can be estimated by re-plotting the I-V curves and looking for minimums. The value of V_{trans} is proportional to the height of the tunneling barrier imposed by ϕ. Shifts in V_{trans}, therefore, reveal changes to ϕ, which is a function of the electrostatics (*i.e.*, level-alignment) near E_F. These shifts can occur independently of changes in conductance, either because they are below the threshold for detection or are offset by other changes, for example, the barrier width, which is related to the distance between the electrodes and, therefore, decreases as the SAM deforms. To compute V_{trans}, we plotted $\ln(IV^{-2})$ vs. V^{-1} using the peaks of Gaussian fits of histo-

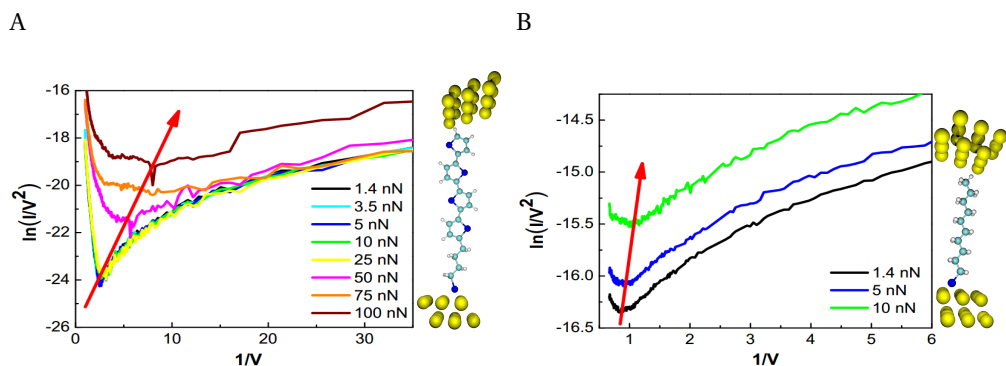A   B

Figure 2.5 Transition voltage spectroscopy of $Au^{TS}/SAM//Au$ junctions versus loading force from the peaks of Gaussian fits obtained by CP-AFM at each loading force. A) T4C4, 200 traces at each loading force. B) C10, 30 traces at each loading force. The equivalent pressures for each force are shown in Table 2.1.

grams of I for each value of V at different loading forces (200 traces for T4C4 and 30 for C10) and recorded the center of the dips in the plots. These data are plotted in Figure 2.5 and summarized in Table 2.1. At loading forces above 75 nN the dips were not very pronounced, but they were well-resolved at all other forces, revealing clear differences between T4C4 and C10.

Table 2.1 Measured values of V_{trans}^+ at different loading forces

Pressure (MPa)	Force (nN)	V_{trans}^+ (V)	
		T4C4	**C10**
163.12	**1.4**	0.4	1.20
177.35	**3.5**	0.4	-
186.94	**5.0**	0.4	1.10
215.93	**10**	0.38	0.95
282.28	**25**	0.34	-
352.43	**50**	0.18	-
396.49	**75**	0.14	-
426.72	**100**	0.13	-

The trend for C10 shown in Figure 2.5B and Table 2.1 is in excellent agreement with literature values; V_{trans}^+ (V_{trans} at positive bias) decreases from a maximum of 1.20 V to 0.95 V, a change of approximately 20 %. Table 2.2 compares literature values of V_{trans}^+ for C10, C12 and C8 at low loading force to our value for C10; these values, which are typically 1.10 V to 1.40 V for alkanethiols, are also in excellent agreement.[27, 37] Because V_{trans} is proportional to ϕ and E_F is invariant (*i.e.*, the value for Au^{TS},) V_{trans} is almost always smaller for π-conjugated molecules than for alkanethiols by virtue of the fact that the HOMO tends to lie closer to E_F.[38, 39] Indeed, V_{trans}^+ for T4C4 is about one-third the value of C10. Moreover, it decreases from 0.4 V to 0.13 V, a change of approximately 70 % over a range of 1.4 nN to 100 nN. From 1.4 nN to 10 nN, the range over which C10 could

be measured, T4C4 only changes by approximately 5 %, compared to 20 % for C10. Thus, the changes in conductance in both SAMs correspond to a lowering of the barrier height, but it requires about one order of magnitude more loading force to induce a change in T4C4 as compared to C10. Given the substantial differences in chemical structure and mechanical properties, it is unlikely that the cause of the shifts in V_{trans} are the same for T4C4 as they are for C10 (*i.e.,* increased tilt angle).

Table 2.2 Comparison of V_{trans}^{+} of alkanethiols on Au substrate at low loading forces to literature values

	V_{trans}^{+} (V)		
	C8	**C10**	**C12**
This work	-	1.20	-
Ref. 27	1.28	1.27	1.20
Ref. 37	1.21	-	1.33

2.2.4. DFT CALCULATIONS

For insights into the electrostatics of SAMs of T4C4 under deformation, we constructed model junctions and computed their properties using DFT. The model junctions consist of single molecules spanning two clusters of Au atoms; these are not meant as direct simulations of Au$^{\text{TS}}$/SAM//Au junctions, rather, they are computationally accessible models from which we can compute trends to compare to experimental data. First, we optimized the geometry of the molecule in the gas-phase using B3LYP/6-311G*. Given the co-planar geometry of the quarterthiophene moiety and the tendency for alkanes to adopt a trans-extended conformation in SAMs, this geometry is a reasonable approximation for T4C4 in a SAM. Second, we attached a cluster of Au at a hollow site via the thiol anchor on one end and positioned an identical cluster above the terminal thiophene ring/methyl group at the other end. (The Au-S and Au-thiophene distances do have a small effect on the computed electrostatics, but they are kept constant across all calculations such that the effect is constant.)

Finally, we computed point energies using B3LYP/LANL2DZ for the molecule before and after attaching the metal electrodes to compare the orbital energies and isoplots of the molecule in gas phase and in the model junctions, respectively. To model the deformation of the SAM, we distorted the T4C4 molecules in the model junctions systematically either by hand or by using displacements predicted from frequency calculations. The figure of merit of these calculations is the offset between the metal Fermi level and the highest-occupied π-state (HOPS) of T4C4 (E_{F}-E_{HOPS}), which is a direct approximation of ϕ and, therefore, will vary accordingly with V_{trans}. Because these are Gaussian (*i.e.,* discrete, aperiodic) calculations the 'HOMO' corresponds to E_{F}, thus we locate the HOPS by comparing the model junction to the gas-phase calculation. Figure 2.19 shows isoplots of the HOPS for T4C4 and the highest-occupied σ-state (HOSS) for C10 obtained using this method.

We estimated E_{F}-E_{HOPS} of SAMs of T4C4 on Au$^{\text{TS}}$ and Ag$^{\text{TS}}$ experimentally from ultraviolet photoelectron spectroscopy (UPS) data according to Reference 39 (Table 2.3). To relate the DFT calculations to experimental data, we computed E_{F}-E_{HOPS} using the value of E_{F} from UPS and the value of E_{HOPS} from DFT of the minimized geometry of

T4C4 in a model Au/T4C4/Au junction. This method produced excellent agreement for E_F-E_{HOPS} between UPS and DFT.

Table 2.3 Energy levels determined by UPS

	$HOPS$ (eV)		E_F-E_{HOPS} (eV)	
	center	**onset**	**center**	**onset**
T4C4 on Au	−5.42	−4.88	1.23	0.68
T4C4 on Ag	−5.25	−4.71	1.31	0.77

Figure 2.6 shows E_F-E_{HOPS} of model junction as a function of in-plane bending. Unsurprisingly, there is hardly any effect on C10, however, the response of T4C4 is nonlinear, increasing at first and then rapidly decreasing. The initial increase is due to the decrease in orbital overlap in the π-system, which lowers the energy of the HOPS (the total energy still increases). It is not clear why E_F-E_{HOPS} then decreases, but since we did not observe any increase in V_{trans} experimentally, we conclude that in-plane bending (a relatively high-energy deformation, particularly in a SAM) does not play a large role in the mechanical deformation of SAMs of T4C4; we cannot exclude its contribution to C10, however. The exact bond angles of each conformation are shown in Figure 2.20 and Tables 2.9 and 2.10.

In-plane bending is a relatively high-energy process. Deformations in which atoms are allowed to displace along all vibrational vectors are generally lower-energy processes, but are more difficult to rationalize because it translates a compressive force (from the AFM tip) into motion in all directions within a SAM. Nonetheless, molecules of T4C4 stretched and compressed along these vectors show a linear response of E_F-E_{HOPS} as a function of relative displacement as is shown in Figure 2.7. This response (as we go from 'stretched' to 'compressed' forms) also correctly predicts the direction of change in V_{trans}. Given the high Young's modulus and relatively small tip displacement, we hypothesize that the shifts in V_{trans} for Au^{TS}/T4C4//Au junctions are, therefore, the result of compressing molecules of T4C4 along displacement vectors corresponding to vibrational modes that are allowed by the constraints of the SAM. This is a very different mechanism from that of C10 and provides a coherent explanation for the change in conductance that occurs at high loading forces. Other bending and twisting modes yielded either no change or an increase in V_{trans}; see Figures 2.21 and 2.22.

2.2.5. Stability of Large-Area Junctions

The studies enumerated above probe areas on the order of tens of nm^2 to give insight into the bulk mechanical properties of a SAM (*e.g.,* stiffness,) however, the electrical properties that SAMs exhibit in large-area junctions include the influence of defects (*e.g.,* local disorder) driven by inhomogeneities in the substrate, chemical impurities and grain boundaries.[28, 40–42] Shorter alkanethiols exhibit more resilience to defects because they are more liquid-like;[43] however, when a voltage is applied to a large-area junction, a substantial electrostatic pressure develops that can deform and induce the reorganization[44] in which case the stiffness of longer alkyl chains is advantageous. We hypothesize that there is, therefore, a relationship between the mechanical stability of a
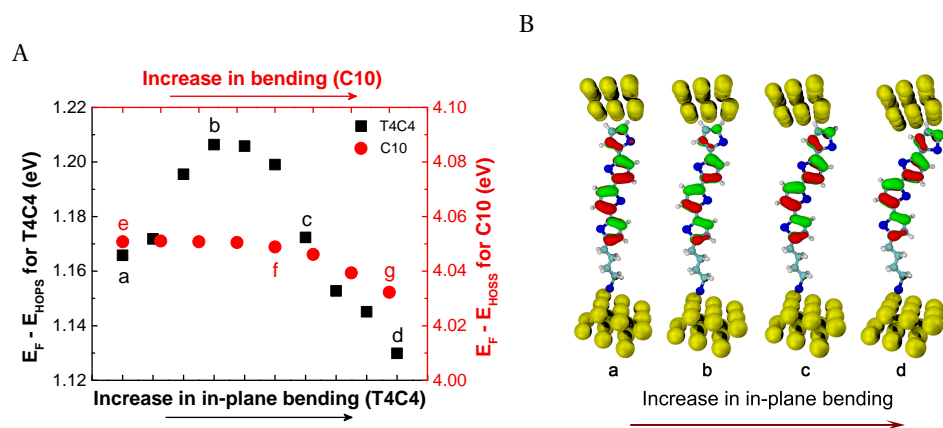
Figure 2.6 (A) Shift in the energy of E_F-E_{HOPS} of Au^{TS}/SAM//Au model junctions with the increased in-plane bending of the T4C4 molecules (black squares), and E_F-E_{HOSS} with the increased bending of C10 alkanethiol molecules (red dots), relative to their equilibrium geometries. The labeled data points (a, b, c and d) correspond to the energies of the T4C4 geometries showed in the bottom schematic (B). The first points a and e correspond to optimized geometries of T4C4 and C10 molecules, respectively. The geometries corresponding to the data points e, f, and g and further details are given in the Experimental section. The E_F of Au electrodes was set to –4.20 eV for these plots from the UPS measurements.

SAM and its breakdown voltage; SAMs that can withstand higher electrostatic pressures should form large-area tunneling junctions that resist shorting at high bias. There is no consensus on the mechanism of failure of large-area junctions at high bias, which could be 1) entirely a function of the ability of a SAM to resist penetration by the top-contact, 2) the migration of metal atoms from the bottom-contact, *e.g.*, the formation of filaments of Au, 3) electrochemical instability or 4) some combination of the three. A clear correlation between breakdown voltage and the mechanical robustness of T4C4 would imply that mechanism 1 is dominant because the electrochemical window of T4C4 is much smaller than that of an alkanethiol. Extending the potential window in which a SAM can operate in a large-area junction is particularly relevant to molecule diodes[45] such as SAMs incorporating ferrocenyl,[46, 47] bipyridyl[48, 49], pyrimydyl,[14] fullerene[50] moieties because the degree of rectification tends to scale with bias and they function under bias in integrated circuits.[10]

To investigate the influence of mechanical stability on breakdown voltages in large-area molecular junctions, we formed Ag^{TS}/SAM//EGaIn junctions[22] of T4C4, C12, tetradecanethiol (C14) and hexadecanethiol (C16). As mentioned above, we chose Ag^{TS} because it is the most commonly reported substrate for EGaIn top-contacts. We swept junctions of each SAM through increasing bias windows and recorded the frequency of shorts, defined by the sudden increase in current to the compliance limit of the instrument. Figure 2.8A shows representative *I-V* plots (on a linear scale) revealing a clear trend of increasing breakdown potential: T4C4 > C16 > C14 ≈ C12 > C10. Figure 2.8B shows the percent-yield of non-shorting junctions scanned from ±1V, ±1.5V, ±2V and ±2.5V (see Table 2.7 for details). All SAMs shorted 100 % of the time at ±2.5V, but only

2

A

B
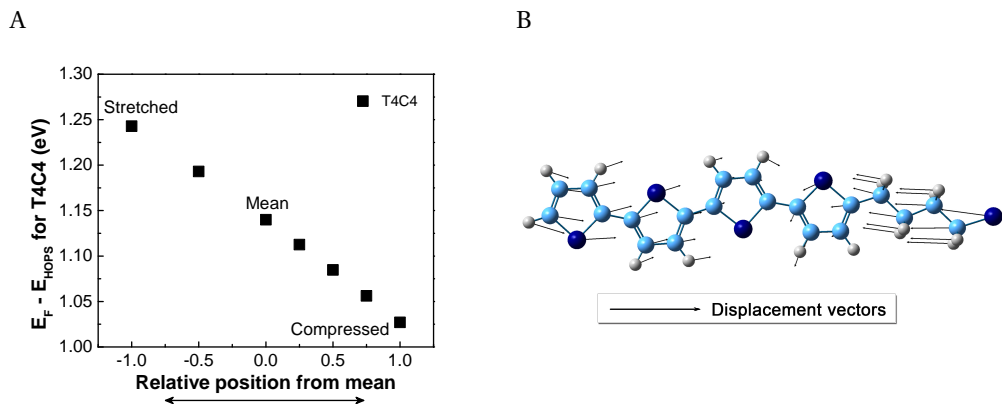
Figure 2.7 (A) Shift in the energy of E_F-E_{HOPS} of Au^{TS}/T4C4//Au model junctions as a function of the displacement of atoms along vibrational vectors from frequency calculations. The points on X-axis span from -1 (fully stretched geometry) to $+1$ (fully compressed geometry), where 0 corresponds to the equilibrium geometry. (B) The arrows represent the displacement vectors of individual atoms as they vibrate. The E_F of Au electrodes was set to -4.20 eV for these plots from the UPS measurements.

A

B
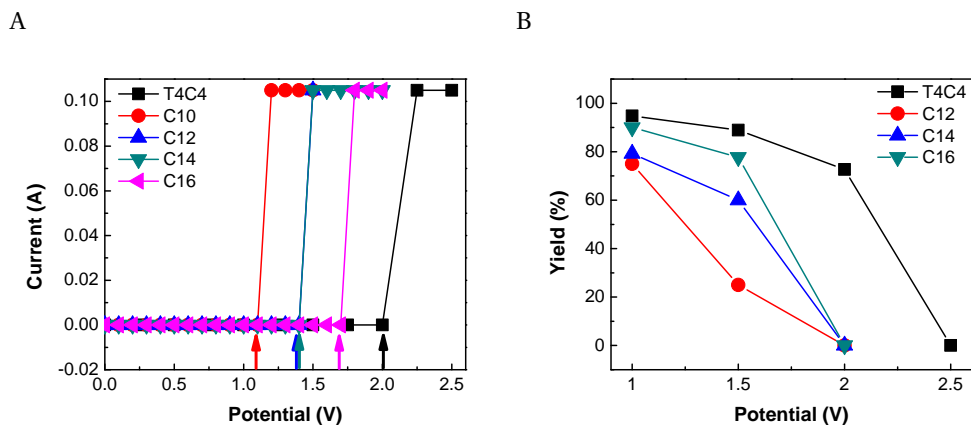
Figure 2.8 A) Representative I-V plots show the breakdown voltage of Ag^{TS}/SAM//EGaIn junctions comprising T4C4, C10, C12, C14 and C16. B) Yield of non-shorting junctions as a function of potential window.

20 % of junctions comprising T4C4 shorted at ±2 V, whereas 100 % of junctions comprising C12, C14 and C16 shorted. At ±1 V and ±1.5 V there is a clear trend of increasing percentage of shorts: C12 > C14 > C16 > T4C4. This trend supports the hypothesis that the primary mode of failure of these Ag^{TS}/SAM//EGaIn junctions is mechanical failure due to electrostatic pressure from the applied bias; the mechanical robustness of SAMs of alkanethiolates scales with chain-length, but T4C4 is considerably more robust than a SAM of alkanethiolates of any number of carbons up to at least C16.

2.3. CONCLUSION

Technological applications of Molecular Electronics in the medium-term will almost certainly utilize SAMs; they simplify fabrication and large-area junctions, in particular, can already be incorporated into integrated circuits and wafer-scale manufacturing processes. The usefulness of molecular tunneling junctions derives from the non-linear dependence of I-V characteristics on the conformation and electronic structure of the molecules. However, the I-V properties of bottom-up junctions comprising SAMs are affected by mechanical force. For SAMs of alkanethiolates, mechanical forces disturb the packing of the SAM, causing tilt angles to increase. We have shown that the electronic structure of π-conjugated molecules (*i.e.*, the electrostatics of the junction) is also directly affected by mechanical force. Thus, it is important to develop an understanding of this relationship and relate it to molecular structure such that the mechanical properties of a SAM and how a tunneling junction responds to forces can be tailored synthetically both to increase the robustness and stability of junctions and to develop devices that respond to mechanical inputs.

We have shown that SAMs of a σ-π molecule designed to maximize intermolecular interactions, T4C4, are significantly more mechanically robust than SAMs of alkanethiolates. Self-assembled monolayers of T4C4 undergo less deformation as a function of loading force by AFM and the Young's modulus is approximately five times higher. At relatively low loading forces, tunneling junctions comprising SAMs of T4C4 show no changes in conductance or values of V_{trans}; SAMs of C10 show significant changes. At higher loading forces than SAMs of C10 are capable of withstanding, junctions comprising T4C4 begin to show differences. Our DFT calculations suggest that these changes are due to force-induced distortions of the π-system and not, as is the case for C10, a change in tilt angle; the AFM tip does not penetrate SAMs of T4C4 as it does C10. The mechanical stability of T4C4 translates into a higher breakdown potential in large-area tunneling junctions with EGaIn top-contacts. This observation suggests that electrostatic pressure plays a significant role in the shorting of molecular tunneling junctions at high bias; SAMs of T4C4 are more mechanically robust than SAMs of alkanethiolates, but T4C4 is significantly less electrochemically stable than an alkanethiol. Our results demonstrate that it is possible to design molecules that maximize mechanical properties and breakdown voltages in large-area tunneling junctions comprising SAMs.

2.4. EXPERIMENTAL

2.4.1. GENERAL

1-decanethiol (C10), 1-dodecanethiol (C12), 1-tetradecanethiol (C14) and 1-hexadecanethiol (C16) were obtained from Sigma-Aldrich and were purified by column chromatography (silica, hexane) and further stored in nitrogen-flushed vials and in the dark. n-butyllithium (1.6 M in hexanes), 1,4-Dibromobutane, Potassium thioacetate were purchased from Acros Organics and used directly. 2,2':5',2":5",2"'-quaterthiophene was provided by Prof. Jan C. Hummelen and confirmed with NMR.

2.4.2. Synthesis of T4C4

The systhesis of T4C4 follows the reported method[6, 51] with some modifications. n-butyllithium in hexane (1.6 mol/L, 1.25 mL, 2 mmol) was slowly added to a solution of 2,2':5',2":5",2"'-quaterthiophene (0.5 g, 1.51 mmol) in dry THF (100 mL) at -78 °C under nitrogen atmosphere (quaterthiophene can not dissolve in THF completely, because of its poor solubility). The solution was stirred for 10 min at -78 °C and then warm to room temperature. In a seperate flask, a solution of 1,4-dibromobutane (4.5 g, 20.8 mmol) in dry THF (50 mL) was heated to 50 °C. The lithiated thiophene was slowly added to the 1,4-dibromobutane solution with the use of dropping funnel under nitrogen flow, and stirred for 3 h at 50 °C. The reaction was then washed with aqueous ammonium chloride(100 mL). The product was extracted with dichloromethane, washed with water and dried over Na_2SO_4. The crude product was washed with heptane, diethyl ether, yielding 0.3 g mixture which was used directly in the next step. 0.3 g mixture was dissolved in 100 mL dry THF and then excess amount of potassium thioacetate (3.49 g) was added. The mixed solution was heated to reflux over night under nitrogen flow and was monitored by TLC (Dichloromethane:Hexane=1:1 in vol). After the removal of THF, the product was dissolved in dichloromethane, washed with water three times and dried over Na_2SO_4. The crude product was purified using column chromatography, using a silica support and first using 1:10 (volume) dichloromethane in hexane as eluent, then 1:5 (volume) dichloromethane in hexane, finally 1:1 (volume) dichloromethane in hexane, yielding 0.200 g of orange solid of (4-([2,2':5',2":5",2"'-quaterthiophen]-5-yl)butyl) ethanethioate (**2**). ^{1}H NMR (400 MHz, $CDCl_3$, δ ppm): δ 7.22 (dd, J_1 = 5.1 Hz, J_2 = 1.1 Hz, 1H), 7.17 (dd, J_1 = 3.6 Hz, J_2 = 1.1 Hz, 1H), 7.09-6.97 (m, 6H), 6.69 (d, J = 3.6 Hz, 1H), 2.91 (t, J = 7.1 Hz, 2H), 2.82 (t, J = 7.4 Hz, 2H), 2.33 (s, 3H), 1.78-1.73 (m, 2H), 1.70-1.63 (m, 2H).

0.1g of (4-([2,2':5',2":5",2"'-quaterthiophen]-5-yl)butyl) ethanethioate (**2**) was dissolved in 70 mL ethanol and 30 mL Toluene. After purging with N_2 for 0.5h, 1 mL 37% HCl was added dropwise. The solution was refluxed over night under the protection of nitrogen flow. The solvent then was evporated under reduced pressure. The crude product was purified using column chromatography, using a silica support and first 1:20 (volume) dichloromethane in hexane as eluent, then 1:5 (volume) dichloromethane in hexane, finally 1:1 (volume) dichloromethane in hexane, yielding 45 mg of orange solid of 4-([2,2':5',2":5",2"'-quaterthiophen]-5-yl)butane-1-thiol. ^{1}H NMR (400 MHz, $CDCl_3$, δ ppm): δ 7.22 (dd, J_1 = 5.1 Hz, J_2 = 0.7 Hz, 1H), 7.18 (dd, 3.6, 0.7 Hz, 1H), 7.11-6.95 (m, 6H), 6.70 (d, J = 3.4 Hz, 1H), 2.82 (t, J = 7.3 Hz, 2H), 2.57 (q, J = 7.2 Hz, 2H), 1.85-1.75 (m, 2H), 1.75-1.63 (m, 2H), 1.36 (t, J = 7.8 Hz, 1H). ^{13}C NMR (100 MHz, $CDCl_3$): δ 144.68, 137.07, 136.73, 136.12, 135.97, 135.27, 134.68, 127.89, 125.14, 124.50, 124.35, 124.20, 124.07, 123.69, 123.45, 33.24, 30.17, 29.61, 24.35. FTMS (ESI+) calculated for $C_{20}H_{19}S_5^+$ (($C_{20}H_{18}S_5$+H)$^+$) 419.00848 found 419.00802

2.4.3. The Formation of Self-assembled Monolayers (SAMs)

The formation of SAMs follows the reported methods.[33] The Ag and Au substrates were prepared by Template Stripping (TS) described in details elsewhere.[28] 200 nm of Ag (99.99%) and 100 nm of Au (99.99 %) were deposited by thermal deposition at 10^{-7} mbar onto a 3" Silicon wafer (without adhesion layer). Glass substrates (1 cm × 1 cm) were glued onto deposited metal by using UV-curable Optical Adhesive (Norland 61) with 300s
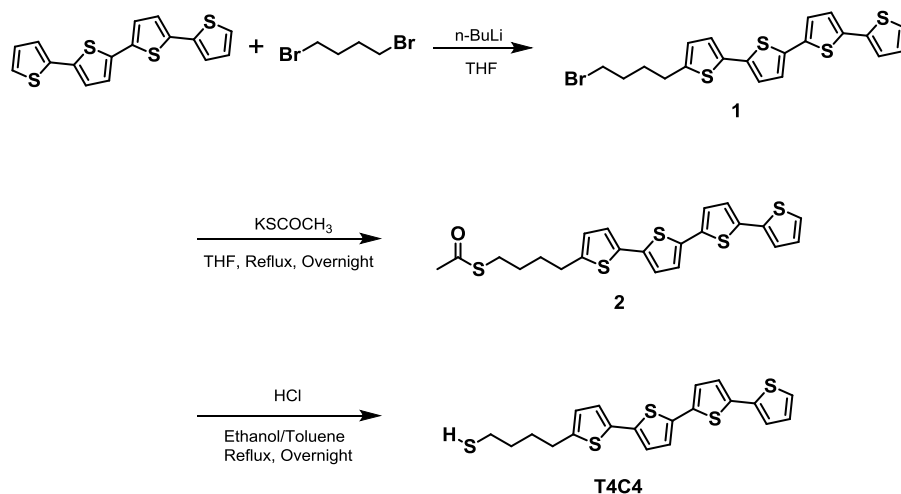
Figure 2.9 Synthetic route of T4C4

exposure of UV. All samples were made by incubation of freshly cleaved silver and gold substrates into either 3 mM solution of the corresponding n-alkanethiols (n = 10, 12, 14, 16) in ethanol or 0.5 mM solution of T4C4 in toluene at room temperature and kept inside a nitrogen flow box (in which the O_2 was below 3 % and the humidity was below 10 %) for 3h. Then the substrates of alkanethiols and T4C4 were rinsed by ethanol and toluene respectively and dried gently by N_2. Prior to forming the SAMs, the solution was degassed by bubbling N_2 for at least 20 minutes and all solution were kept under N_2 atmosphere to prevent oxidation of thiol and Ag substrates.

2.4.4. The Characterization of Self-assembled Monolayers (SAMs)

The SAMs were characterized by Water Contact Angles, Ellipsometry and Ultraviolet Photoelectron Spectroscopy (UPS).

Water Contact Angle

Contact Angles were measured under ambient conditions on a SCA20 Dataphysics instrument with software version 3.60.2. Equilibrium contact angles were obtained by applying 3 μL water droplets on SAMs using the sessile drop method. The contact angles were measured at two samples, three different locations on each surface and the results were averaged with the standard deviation as the error bar.

2
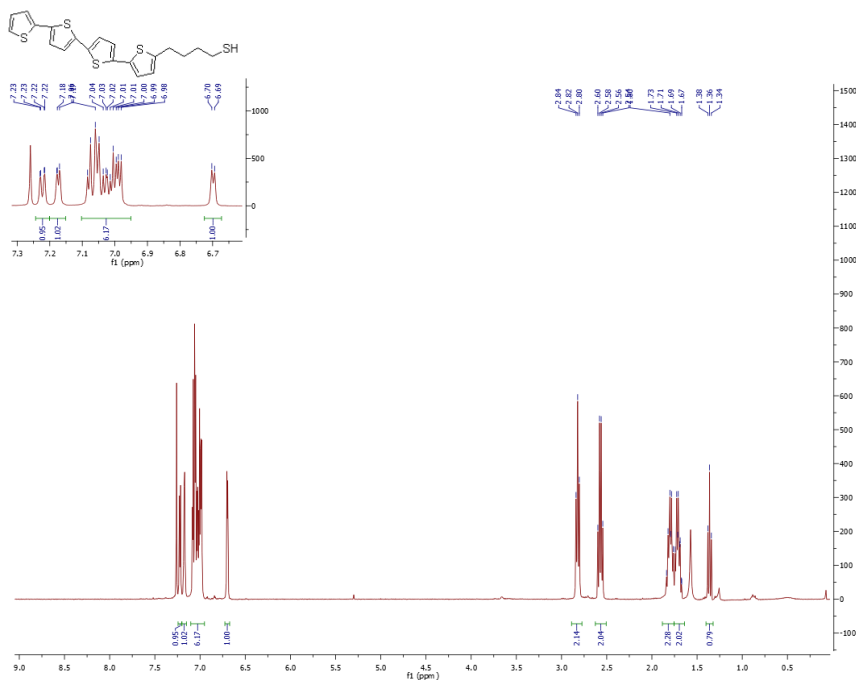
Figure 2.10 ^{1}H NMR spectrum of T4C4

Table 2.4 Table of water contact angle of substrates and modified with T4C4

	Water Contact Angle [°]
Au	53.93 ± 3.38
Au modified with T4C4	61.13 ± 3.73
Ag	28.20 ± 2.82
Ag modified with T4C4	76.67 ± 0.55

ELLIPSOMETRY

The ellipsometry measurements were carried on a V-Vase Rotating Analyzer equipped with a HS-190 monochromator ellipsometer from J.A. Woollam Co., Inc. in air. A two-layer model consisting of a bottom Au or Ag layer, for which optical constants were calculated from freshly prepared template stripped Au or Ag surfaces, and a Cauchy layer was used for the fit of the measurements on the SAMs.[52] A chosen value of n=1.55[23] and k=0 at all wavelengths (i.e. Cauchy parameter A=1.55, B=C=0) was used to fit the thickness. For every SAM we measured six different spots in total (three spots of each sample and two samples) and reported the thicknesses as the average with the standard deviation as the error bar.
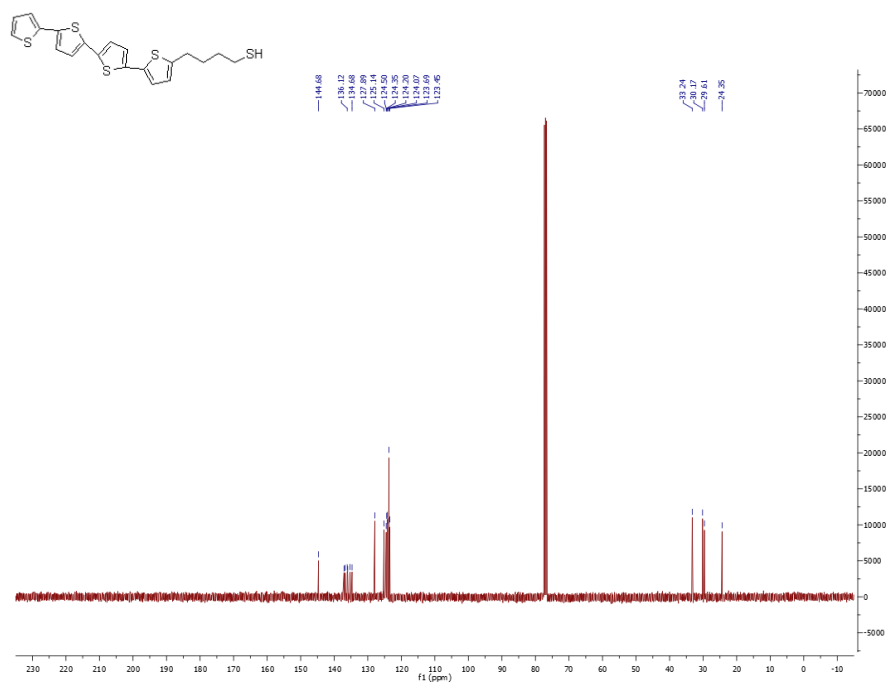
Figure 2.11 ^{13}C NMR spectrum of T4C4

Table 2.5 Table of thickness of SAMs of T4C4 measured by ellipsometry

	Thickness [Å]	**Theoretical Molecular length** [Å]
T4C4 on Au	12.88 ± 0.01	21.34
T4C4 on Ag	22.81 ± 1.46	21.34

ULTRAVIOLET PHOTOELECTRON SPECTROSCOPY (UPS)

UPS measurements were performed using a VG microtech clam 100 spectrometer and an ultraviolet (He I, 21.2 eV) light source. Samples of SAMs were prepared as described in the Experimental and quickly transferred into the entry lock of the vacuum system. The base pressure of the measurement chamber was $<5 \times 10^{-9}$ mbar. A bias of -4 V was applied to the sample holder to obtain the secondary electron cut-off (SEC). HOMO onsets and centers were found by fitting multiple Gaussian functions

$$He^{-\frac{(x-\mu)^2}{2\sigma^2}}$$

to the spectra. The onset for the HOMOs is found at $\mu + 2\sigma$ for the peak corresponding to the HOMO. The vacuum levels for the two samples are found by adding 21.2 eV to the SEC. The binding energy scale is in reference to these vacuum levels.

2.4.5. CURRENT-VOLTAGE MEASUREMENTS

A

B

C
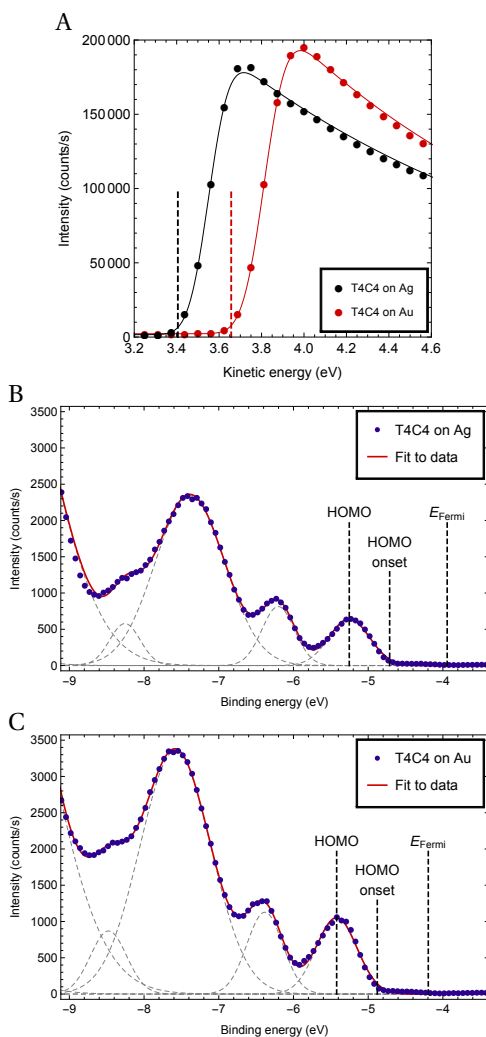
Figure 2.12 UPS spectra of T4C4 on Au^{TS} and Ag^{TS}. A) Low kinetic energy side of the spectrum where the SEC is determined. B&C) Low binding energy region of the spectra of T4C4 on Ag^{TS} and Au^{TS} respectively. Dashed lines indicate the HOMO center, HOMO onset, and the Fermi level. The Fermi levels are determined by UPS measurements on samples of bare Au^{TS} and Ag^{TS}.

CP-AFM

I-V measurements were performed on a Bruker AFM Multimode MMAFM-2 equipped with a Peak Force TUNA Application Module (Bruker). The SAMs were contacted with an Au-coated silicon nitride tip with a nominal radius of 30 nm (NPG-10, Bruker, tip A: resonant frequency: 65 kHz, spring constant: 0.35 N/m; tip B: resonant frequency: 23 kHz, spring constant: 0.12 N/m; tip D: resonant frequency: 18 kHz, spring constant: 0.06 N/m. Tip A was chosen in this work) in TUNA mode. The AFM tip was grounded and

for all loading forces, T4C4 on Au^{TS} were biased from -1.0 V to $+1.0$ V and from $+1.0$ V to -1.0 V while C10 on were biased from -1.5 V to $+1.5$ V and from $+1.5$ V to -1.5 V on Au^{TS} to record the I-V curves: a max of 10 trace/re-trace cycles per junction were performed and the top electrode was removed from SAMs between junctions. Between different samples a new tip was used. The total number of I-V traces recorded by CP-AFM is summarized in Table 2.6. It is difficult to determine V_{trans} for an individual I-V trace due to the inherent noise in the raw data. The peaks of Gaussian fits of histograms of I for each value of V at different loading forces obtained by CP-AFM were plotted and transformed into axes of $\ln(I/V^2)$ versus $1/V$. The position of the V_{trans} was determined manually by the center of the dips in the plots.

Table 2.6 Summary of number of I-V traces recorded by CP-AFM in this work

	Force (nN)	**Traces**		**Force** (nN)	**Traces**
T4C4(Au)	1.4	202	**C10(Au)**	1.4	30
	3.5	198		5	30
	5	200		10	30
	10	179			
	25	156			
	50	200			
	75	198			
	100	198			
T4C4(Ag)	2	52	**C10(Ag)**	1.4	21
	25	51		5	10
	50	52		10	20
	75	54		25	21
	100	51		50	20
	125	47	**C12(Ag)**	2	35
	150	81		25	48
				50	48
				75	49
				100	74
				125	37
				150	48

EGAIN

The electrical measurement with the EGaIn, as well as sample preparation and handling, was performed in the nitrogen flow box in which O_2 was maintained below 3 % and the humidity was kept below 10 %. At least two samples were examined for each molecule. The potential windows include: 1) 0 V→ 1 V→ −1 V→ 0 V, steps of 0.05 V; 2) 0 V→ 1.5 V→ −1.5 V→ 0 V, steps of 0.1 V; 3) 0 V→ 2 V→ −2 V→ 0 V, steps of 0.1 V; 4) 0 V→ 2.5 V→ −2.5 V→ 0 V, steps of 0.25 V. 20 trace/re-trace cycles were measured for each junction and shorts occur during the cycles is counted for the failure of junction. The statistics of the stability test on EGaIn junctions are summarized in Table 2.7. Figure 2.13 shows the plots of J/V curves for Ag^{TS}**SAMs**\\EGaIn Junctions comprising **T4C4, C12, C14, C16**.
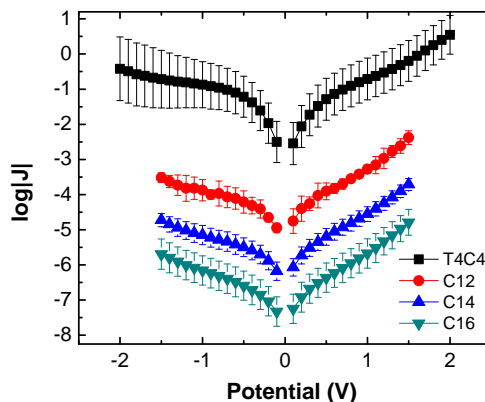
Figure 2.13 Plots of $log|J|$ (the units of J are $A\,cm^{-2}$) *versus* V for SAMs using EGaIn top-contacts (Ag^{TS}**SAMs**\\EGaIn): black squares for T4C4, red circles for C12, blue up-triangle for C14, dark cyan down-triangle for C16. Each datapoint is the mean from a Gaussian fit to a histogram of $log|J|$ for that value of V and the error bars are the 95 % confidence intervals of the fit.

I-V DATA PROCESSING:

Data were acquired as described above and then parsed in a "hands-off" manner using Scientific Python to produce histograms of I for each value of V and the associated Gaussian fits (using a least-squares fitting routine).

The *I-V* curve of **T4C4** (Au^{TS}**T4C4**\\CP-AFM) in all range of loading forces (from 1.4 nN to 100 nN) is shown in Figure 2.14A and current of **T4C4** and **C10** at +1.0 V(positive bias) or -1.0 V(negative bias) versus loading force is shown in Figure 2.14B.

Figure 2.17 and Figure 2.18 show the results of CP-AFM *I-V* characterization on Ag^{TS} substrate. C12 on Ag^{TS}, the samples were biased from −2 V to +2 V and from +2 V to −2 V and C10, T4C4 on Ag^{TS}, the samples were biased from −1.5 V to +1.5 V and from +1.5 V to −1.5 V.

Table 2.7 Table of Yield of SAMs on Ag^{TS} at different voltages

	Voltage	Total Junctions	Working	Short	Yield
T4C4	**1.0V**	58	55	3	94.83%
	1.5V	9	8	1	88.9%
	2.0V	11	8	3	72.7%
	2.5V	10	0	10	0%
C12	**1.0V**	36	27	9	75%
	1.5V	8	2	6	25%
	2.0V	8	0	8	0%
C14	**1.0V**	24	19	5	79.2%
	1.5V	20	12	8	60%
	2.0V	10	0	10	0%
C16	**1.0V**	10	9	1	90%
	1.5V	9	7	2	77.7%
	2.0V	10	0	10	0%
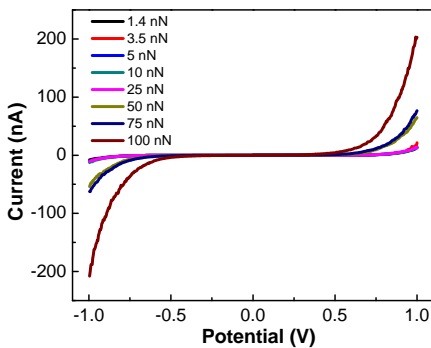
A   B
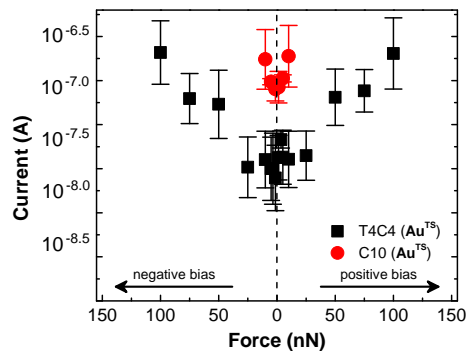
Figure 2.14 A) I-V plots of **T4C4** on Au^{TS} (Au^{TS}**T4C4**\\CP-AFM) with different forces from 1.4 nN to 100 nN. B) Semi-log plot of current of **T4C4** (black square) and **C10** (red circle) on Au^{TS} at +1.0 V(positive bias) or -1.0 V(negative bias) versus loading force.

2.4.6. PEAKFORCE QNM

Measurements of Young's modulus were performed on a Bruker AFM Multimode MMAFM-2. The SAMs were contacted with a silicon nitride tip with a nominal radius of 2 nm (ScanAsyst-Air, Bruker, resonant frequency: 70 kHz, spring constant: 0.4N/m) in Peak-Force QNM$^{®}$ mode. The deflection sensitivity, spring constant of the cantilever and tip radius were calibrated both before and after the measurement. Deflection sensitivity was calibrated by measuring 5 force curves on fused silica sample provided by Bruker and taking the average of the results. Spring constant was calibrated by thermal tune before and after the measurements. Tip radius was calibrated before and after the measurements using scanning electron microscope (SEM). Deformation under each force
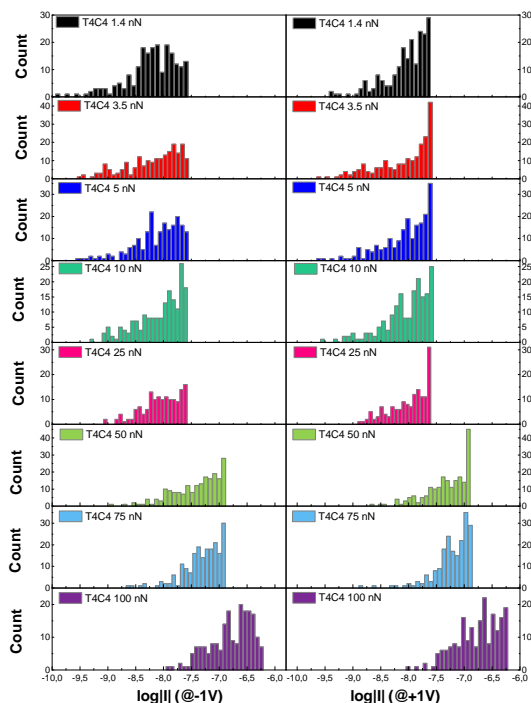
Figure 2.15 Histogram of T4C4 on Au^{TS} (Au^{TS}**T4C4**\\CP-AFM) at different forces: Left panel is log of current at -1 V (Top to bottom starting from 1.4 nN to 100 nN) and right panel is log of current at +1 V (Top to bottom starting from 1.4 nN to 100 nN)

load was measured from 5 spots of the sample and averaged. Samples were scanned in ScanAsyst Mode for selecting a region where dust particles or other contaminants were not present. Deformation of the sample were measured under a loading force ranging from 0.13 nN to 19.62 nN over 5 positions and later used to calculate Young's modulus from DMT model in Nanoscope Analysis (Bruker). Young's modulus was calculated by DMT model from the averaged deformation of each force load. The contact area of Au tip is calculated based on reported work[19], in which the radius of the contact area between the Au AFM tip and C10 SAM changes linearly with the loading force as shown in equation 1.

$$A = 1.70F + 100.8 \tag{2.1}$$

in which A is the contact area (nm^2) between the AFM tip and the SAM, F (nN) is the load force. Then the pressure can be calculated from load force divided by contact area.

In the case of Si$_3$N$_4$ tip, the part where the tip is in contact with the SAM is considered as a spherical cap, the deformation h is the height of the cap and the radius of the tip is the radius of the sphere R. We simplified the contact area between the AFM tip and the SAM as the projection of the spherical cap on the plane of the SAM. Then the contact area can be calculated by

$$A = \pi[R^2 - (R - h)^2] \tag{2.2}$$
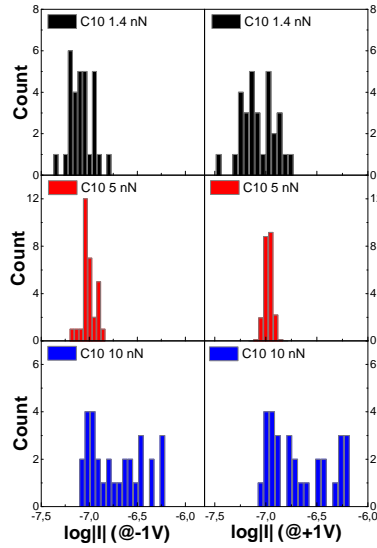
Figure 2.16 Histogram of C10 on Au^{TS} (Au^{TS}**C10**\\CP-AFM): Left panel is log of current at -1 V (Top to bottom starting from 1.4 nN to 10 nN) and right panel is log of current at +1 V (Top to bottom starting from 1.4 nN to 10 nN)

A
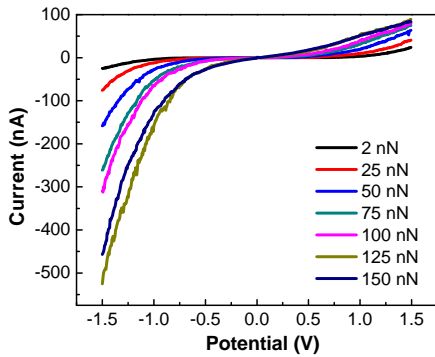
B
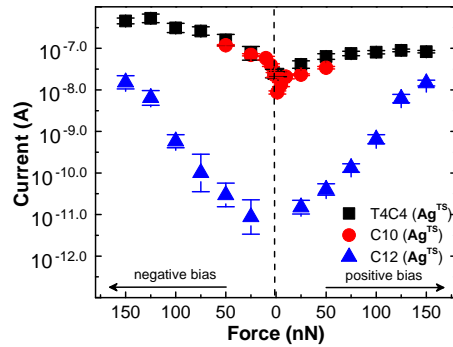
Figure 2.17 A) *I-V* plots of **T4C4** on Ag^{TS} (Ag^{TS}**T4C4**\\CP-AFM) with different forces from 2 nN to 150 nN. B) Plot of logI of T4C4 (black square) and C10 (red circle) on Ag^{TS} at +1.5 V(positive bias) or -1.5 V(negative bias) versus loading force.

Similar to the case of Au tip, the pressure is then calculated from load force divided by contact area.

2

A
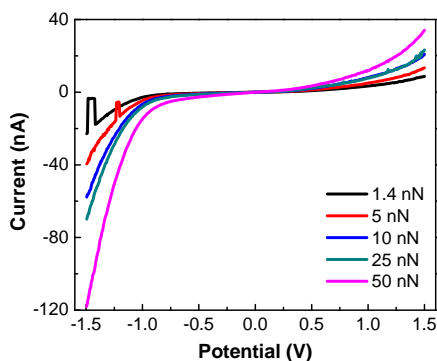
B
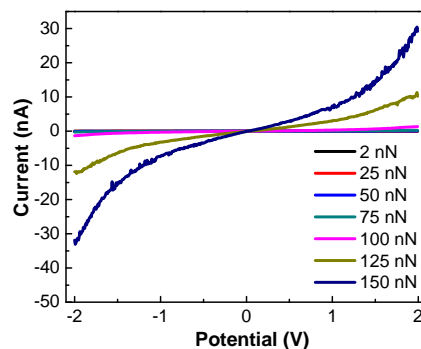
Figure 2.18 A) *I-V* plots of **C10** on Ag^{TS} (Ag^{TS}**C10**\\CP-AFM) with different forces from 1.4 nN to 50 nN. B) *I-V* plots of **C12** on Ag^{TS} (Ag^{TS}**C12**\\CP-AFM) with different forces from 2 nN to 150 nN.

Table 2.8 Summary of different Load Forces, Contact Areas and Pressures by AFM Tip in this work

	Loading Force (nN)	**Contact Area** (nm^2)	**Applied Pressure** (MPa)
Au tip	**1.4**	103.17	163.12
	3.5	106.74	177.35
	5	109.28	186.94
	10	117.77	215.93
	25	143.23	282.28
	50	185.65	352.43
	75	228.08	396.49
	100	270.51	426.72
Si$_3$N$_4$ tip	**0.13**	2.72	48.11
	0.65	4.52	144.64
	1.31	7.01	186.99
	1.96	7.25	270.22
	2.62	8.55	306.41
	3.27	9.29	351.87
	3.93	10.50	374.29
	4.58	10.75	426.19
	5.23	11.50	454.64
	5.89	11.43	515.33
	6.54	11.39	574.11

2.4.7. DFT CALCULATIONS

All calculations were performed using Gaussian 09 software. Structures were first minimized by B3LYP/6-311G*; then, the single-point energies were computed by B3LYP/LANL2DZ. Single-molecule junctions were constructed by attaching the minimized structures to 17- or 18-atom Au(111) clusters via the terminal sulfur atoms at hexagonal close-

pack hollow sites at a distance of 1.75 Å from the center of the hollow site. To calculate the energy difference E_F - E_{HOPS} and E_F - E_{HOSS}, the value of E_F for Au electrodes was taken to be –4.2 eV from the UPS measurements.

This section lays out the details on how the geometries of T4C4 and C10 molecules were altered to induce different systematic deformation in the molecules. The section focuses on establishing the hypothesis that only specific kind of deformations (or their cumulative effect) in the molecules will yield a decreasing trend in the energy barrier (E_F - E_{HOPS}), as observed experimentally for V_{trans} under application of force (Table 2.1).

2.4.8. IN-PLANE BENDING:

The simulation results for the energy shift trend (E_F - E_{HOPS}) were obtained after the bending of T4C4 molecules in the plane of conjugation of the four thiophene rings. Similarly for the C10 molecule, the bending was induced by simultaneous decrease and increase in the alternate C-C-C bond angles. Fig. 2.19 shows a schematic of different geometries that correspond to the particular data labels (a - d for T4C4; e - g for C10) in the Fig. 2.6 of the main text. Then in Fig. 2.20, the schematic shows the exact bond angles that were changed, followed by their exact values in Table 2.9 and Table 2.10 for T4C4 and C10, respectively.
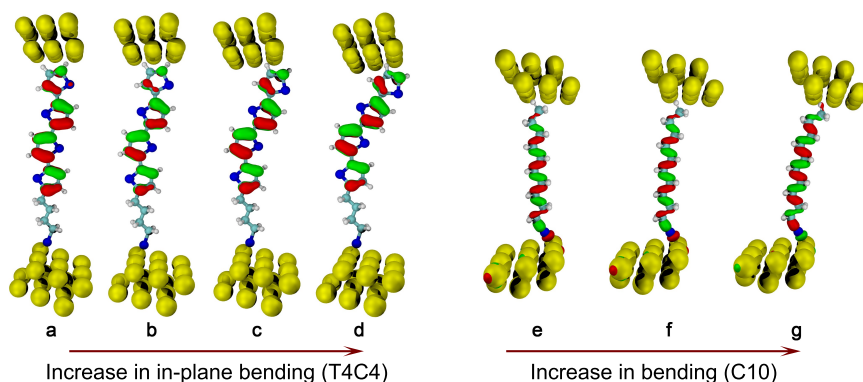
Figure 2.19 Schematics showing the geometries of the T4C4 (left) and C10 (right) molecules, for the corresponding data points labelled in Fig. 2.6(A) in the DFT calculations section.
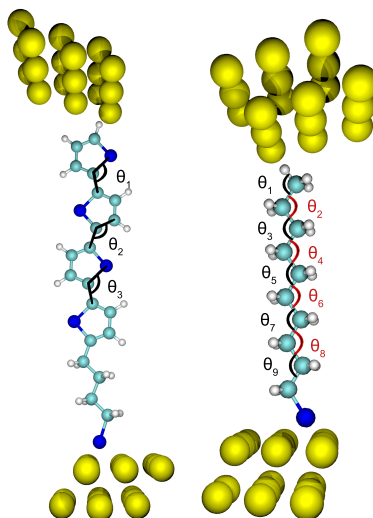
Figure 2.20 Schematics showing the different bond angles were altered to introduce in-plane bend in the T4C4 (left) and C10 (right) molecules in the gaussian software, for Fig. 2.6(A). The values by which different angles were systematically altered are presented in the Table 2.9 and Table 2.10 for T4C4 and C10 molecules, respectively.

No.	labelled data point	$\Delta\theta 1$ [°]	$\Delta\theta 2$ [°]	$\Delta\theta 3$ [°]
1	a	0	0	0
2		-5	0	0
3		-5	-5	0
4	b	-5	-5	-5
5		-10	- 5	-5
5		-10	-10	-5
6	c	-10	-10	-10
7		-15	-10	-10
8		-15	-15	-10
9	d	-20	-15	-10

Table 2.9 Table of the values by which respective angles were changed to bend the T4C4 molecule in the plane of conjugation. The '-' signs mean that the respective angles are decreased by that particular value. The data points labelled a, b, c and d in Fig. 2.6(A) are mentioned in the table.

In the Fig. 2.21 and Fig. 2.7, we present two systematic deformations: first by increasing the ring-torsion, and second by studying the out-of-plane vibration mode. We show that these two deformations that were introduced in the T4C4 molecules did not result in a decrease in the energy barrier (E_{F} - E_{HOPS}). The fact that different deformations produce different energy shift trends, builds a strong argument in the favour of our hypothesis: that it is not just tilting of the molecules in the SAM, but a complicated change in the conformation of the molecules upon application of pressure on the SAMs

No.	labelled data point	$\Delta\theta1$	$\Delta\theta2$	$\Delta\theta3$	$\Delta\theta4$	$\Delta\theta5$	$\Delta\theta6$	$\Delta\theta7$	$\Delta\theta8$	$\Delta\theta9$
1	e	0	0	0	0	0	0	0	0	0
2		2	0	0	0	0	0	0	0	0
3		2	-2	2	0	0	0	0	0	0
4		2	-2	2	-2	2	0	0	0	0
5	f	2	-2	2	-2	2	-2	2	0	0
5		2	-2	2	-2	2	-2	2	-2	2
6		5	-5	2	-2	2	-2	2	-2	2
7	g	5	-5	5	-5	2	-2	2	-2	2

Table 2.10 Table of the values by which respective angles were changed to systematically bend the C10 molecules. The '+' and '-' signs represent increase and decrease in the corresponding angles, respectively, resulting in a particular way of deforming, specifically bending, of the C10 molecules. The units of the angles reported here are degrees.

that produces the increasing trend in V_{trans} obtained experimentally.

2.4.9. RING TORSIONAL ANGLES:

The gas-phase DFT optimized structure of the T4C4 molecules have the four thiophene rings tilted slightly out of the plane of conjugation (approx. 18 degrees). This is to compensate for the H - H steric repulsion while still maintaining the extended conjugation between the four rings. However, it is also known that these molecules pack in a planar geometry when they form SAMs. So, starting from a planar geometry, we begin by increasing the simultaneous ring torsional angles between the four thiophene rings, as shown in Fig. 2.21. The exact values of the increase in the torsional angle ($\Delta\theta$) for each data point in Fig. 2.21 are tabulated in table 2.11.

The increasing trend of the energy barrier with increasing ring torsional angle is opposite to the trend of V_{trans} observed experimentally. Thus, we can assume that the experimentally observed trend in V_{trans} is probably not due to the deformation in the ring torsional angles.

Data point	$\Delta\theta$ [°]
1	0
2	5
3	10
4	15
5	18
6	23
7	28
8	33

Table 2.11 The value of torsional angles for the corresponding data points in Fig. 2.21.

2
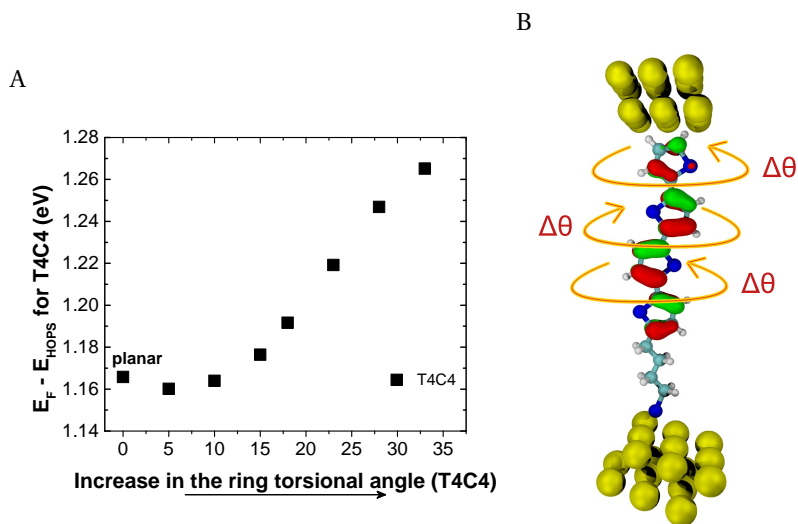
Figure 2.21 (left) Shift in the energy difference E_F-E_{HOPS} of Au^{TS}/SAM//Au model junctions with the increased torsional bending of the rings in T4C4 molecules, relative to the equilibrium geometry. The first point correspond to the optimized planar geometry of T4C4. (right) The schematic explains how the torsional angles between the consecutive thiophene rings were alternatively increased to skew them out of the plane of conjugation. The torsional angle values corresponding to all the data points in the left figure are given in the table 2.11. The E_F of Au electrodes was set to -4.20 eV for these plots from the UPS measurements.

2.4.10. OUT-OF-PLANE VIBRATION MODE:

Atoms of T4C4 molecule were displaced systematically along the displacement vectors corresponding to the out-of-plane ring vibration mode. Differently from the trend in Fig. 2.7, the energy shift (E_F - E_{HOPS}) doesn't show any significant variation. This systematic study also validates our hypothesis: that not all kind of deformations yield the same trend as obtained experimentally for V_{trans}, rather it has to be a cumulative effect of a certain kind of deformations.

2.4.11. C10 BENDING:

As another control simulation on C10 alkane molecules, the molecule was bent in the same direction, but by different amounts than in Fig. 2.6(A) of the main text. The bond angle values are summarised in Table 2.12, and the exact bond angles shown in the schematic in Fig. 2.20. The energy shift (E_F - E_{HOPS}) in Fig. 2.23 is consistent with Fig. 2.6(A) in showing no significant variation over the same range of energy values.

A

B
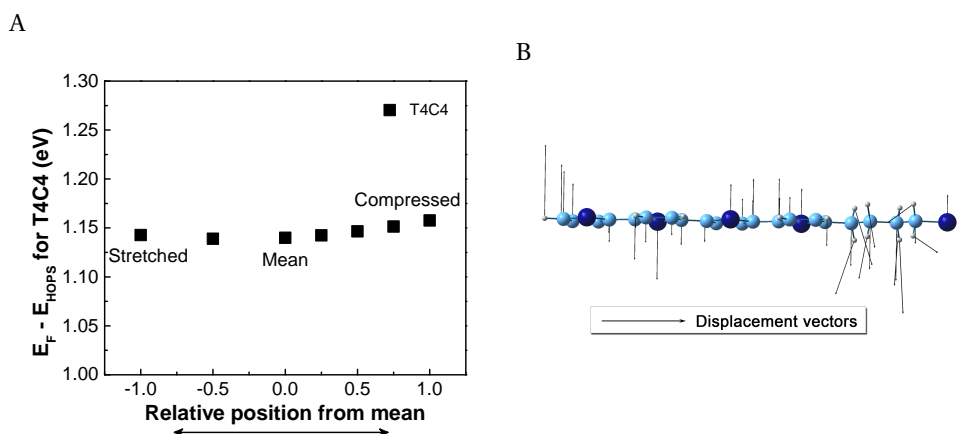
Figure 2.22 A) Shift in the energy of E_F-E_{HOPS} of Au^{TS}/T4C4//Au model junctions as a function of the displacement of atoms along vibrational vectors from out-of-plane frequency mode. The points on X-axis span from -1 (bent-out one side of the plane) to $+1$ (bent-out the other side of the plane), where 0 corresponds to the equilibrium geometry. The arrows in the figure on the right represent the displacement vectors of individual atoms. The E_F of Au electrodes was set to –4.20 eV for these plots from the UPS measurements.
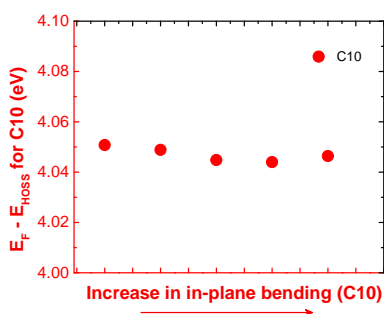
Figure 2.23 The shift in the energy barrier between the fermi level of Au electrode and the HOSS (Highest Occupied Sigma State) of the C10 molecule with the increase in the in-plane bending mode. The values by which different bond angles were altered are presented in the Table 2.12.

Data point	$\Delta\theta1$	$\Delta\theta2$	$\Delta\theta3$	$\Delta\theta4$	$\Delta\theta5$	$\Delta\theta6$	$\Delta\theta7$	$\Delta\theta8$	$\Delta\theta9$
1	0	0	0	0	0	0	0	0	0
2	1	-1	1	-1	1	-1	1	-1	1
3	2	-2	2	-2	2	-2	2	-2	2
4	4	-4	4	-4	4	-4	4	-4	4
5	6	-6	6	-6	6	-6	6	-6	6

Table 2.12 Table of the values by which respective angles were changed to bend the C10 molecules. The $'+'$ and $'-'$ signs represent the respective increase and decrease in the corresponding angles. This shows how the different angles were systematically increased or decreased to result in a particular way of deforming, specifically bending, of the C10 molecule. The units of the angles reported here are degrees

BIBLIOGRAPHY

[1] Robert F. Service. The brain chip. *Science*, 345(6197):614–616, 2014. ISSN 0036-8075.

[2] Dong Xiang, Xiaolong Wang, Chuancheng Jia, Takhee Lee, and Xuefeng Guo. Molecular-scale electronics: From concept to function. *Chem. Rev.*, 116(7):4318–4440, 2016.

[3] Gunuk Wang, Yonghun Kim, Seok-In Na, Yung Ho Kahng, Jamin Ku, Sungjun Park, Yun Hee Jang, Dong-Yu Kim, and Takhee Lee. Investigation of the transition voltage spectra of molecular junctions considering frontier molecular orbitals and the asymmetric coupling effect. *J. Phys. Chem. C*, 115(36):17979–17985, 2011.

[4] X D Cui, a Primak, X Zarate, J Tomfohr, O F Sankey, a L Moore, T a Moore, D Gust, G Harris, and S M Lindsay. Reproducible measurement of single-molecule conductivity. *Science*, 294(5542):571–574, 2001.

[5] N J Tao. Electron transport in molecular junctions. *Nat. Nanotech.*, 1(3):173–181, 2006.

[6] Hylke B Akkerman, Paul W M Blom, Dago M de Leeuw, and Bert de Boer. Towards molecular electronics with large-area molecular junctions. *Nature*, 441(7089):69–72, 2006.

[7] Gunuk Wang, Yonghun Kim, Minhyeok Choe, Tae-Wook Kim, and Takhee Lee. A new approach for molecular electronic junctions with a multilayer graphene electrode. *Adv. Mater.*, 23(6):755–760, 2011.

[8] Yanxi Zhang, Zhiyuan Zhao, Davide Fracasso, and Ryan C. Chiechi. Bottom-up molecular tunneling junctions formed by self-assembly. *Is. J. Chem.*, 54(5-6):513–533, 2014.

[9] Paul A van Hal, Edsger C P Smits, Tom C T Geuns, Hylke B Akkerman, Bianca C De Brito, Stefano Perissinotto, Guglielmo Lanzani, Auke J Kronemeijer, Victor Geskin, Jerome Cornil, Paul W M Blom, Bert de Boer, and Dago M de Leeuw. Upscaling, integration and electrical characterization of molecular junctions. *Nat. Nanotech.*, 3(12):749–754, 2008.

[10] Albert Wan, C S Suchand Sangeeth, Lejia Wang, Li Yuan, Li Jiang, and Christian Albertus Nijhuis. Arrays of high quality sam-based junctions and their application in molecular diode based logic. *Nanoscale*, 7(46):19547–19556, 2015.

[11] Andrii Kovalchuk, Tarek Abu-Husein, Davide Fracasso, David A Egger, Egbert Zojer, Michael Zharnikov, Andreas Terfort, and Ryan C Chiechi. Transition voltages respond to synthetic reorientation of embedded dipoles in self-assembled monolayers. *Chem. Sci.*, 7(1):781–787, 2016.

[12] Marco Carlotti, Andrii Kovalchuk, Tobias Wächter, Xinkai Qiu, Michael Zharnikov, and Ryan C. Chiechi. Conformation-driven quantum interference effects mediated by through-space conjugation in self-assembled monolayers. *Nat. Commun.*, 7: 13904, 2016.

2

[13] Nisachol Nerngchamnong, Li Yuan, Dong-Chen Qi, Jiang Li, Damien Thompson, and Christian A Nijhuis. The role of van der waals forces in the performance of molecular diodes. *Nat. Nanotech.*, 8(2):113–118, 2013.

[14] Andrii Kovalchuk, David A Egger, Tarek Abu-Husein, Egbert Zojer, Andreas Terfort, and Ryan C Chiechi. Dipole-induced asymmetric conduction in tunneling junctions comprising self-assembled monolayers. *Rsc Advances*, 6(73):69479–69483, 2016.

[15] Latha Venkataraman, Jennifer E. Klare, Colin Nuckolls, Mark S. Hybertsen, and Michael L. Steigerwald. Dependence of single-molecule junction conductance on molecular conformation. *Nature*, 442(7105):904–907, 2006. .

[16] D J Wold and C D Frisbie. Fabrication and characterization of metal-molecule-metal junctions by conducting probe atomic force microscopy. *J. Am. Chem. Soc.*, 123(23):5549–5556, 2001.

[17] Hyunwook Song, Hyoyoung Lee, and Takhee Lee. Intermolecular chain-to-chain tunneling in metal-alkanethiol-metal junctions. *J. Am. Chem. Soc.*, 129(13):3806–3807, 2007.

[18] Yabing Qi, Imma Ratera, Jeong Y. Park, Paul D. Ashby, Su Ying Quek, J. B. Neaton, and Miquel Salmeron. Mechanical and charge transport properties of alkanethiol self-assembled monolayers on a au(111) surface: The role of molecular tilt. *Langmuir*, 24(111):2219–2223, 2008. doi: 10.1021/la703147q.

[19] Gunuk Wang, Tae-Wook Kim, Gunho Jo, and Takhee Lee. Enhancement of field emission transport by molecular tilt configuration in metal-molecule-metal junctions. *J. Am. Chem. Soc.*, 131(16):5980–5985, 2009.

[20] K Smaali, S Desbief, G Foti, T Frederiksen, D Sanchez-Portal, A Arnau, J P Nys, P Leclere, D Vuillaume, and N Clement. On the mechanical and electronic properties of thiolated gold nanocrystals. *Nanoscale*, 7(5):1809–1819, 2015.

[21] Jeremy M. Beebe, BongSoo Kim, J. W. Gadzuk, C. Daniel Frisbie, and James G. Kushmerick. Transition from direct tunneling to field emission in metal-molecule-metal junctions. *Phys. Rev. Lett.*, 97:026801, 2006.

[22] Ryan C Chiechi, Emily A Weiss, Michael D Dickey, and George M Whitesides. Eutectic gallium–indium (egain): A moldable liquid metal for electrical characterization of self-assembled monolayers. *Angew. Chem.*, 120(1):148–150, 2008.

[23] Bert De Boer, Hong Meng, Dmitrii F. Perepichka, Jie Zheng, Martin M. Frank, Yves J. Chabal, and Zhenan Bao. Synthesis and characterization of conjugated mono- and dithiol oligomers and characterization of their self-assembled monolayers. *Langmuir*, 19(24):4272–4284, 2003.

[24] B. Liedberg, Z. Yang, I. Engquist, M. Wirde, U. Gelius, G. Götz, P. Bäuerle, R.-M. Rummel, Ch. Ziegler, and W. Göpel. Self-assembly of α-functionalized terthiophenes on gold. *J. Phys. Chem. B*, 101(97):5951–5962, 1997.

[25] Hiroyuki S Kato, Yoshinari Murakami, Yoshiaki Kiriyama, Riyo Saitoh, Takahiro Ueba, Takashi Yamada, Yutaka Ie, Yoshio Aso, and Toshiaki Munakata. Decay of the exciton in quaterthiophene-terminated alkanethiolate self-assembled monolayers on au(111). *J. Phys. Chem. C*, 119(111):7400–7407, 2015.

[26] Jeremy M Beebe, Vincent B Engelkes, Larry L Miller, and C Daniel Frisbie. Contact resistance in metal-molecule-metal junctions based on aliphatic sams: effects of surface linker and metal work function. *J. Am. Chem. Soc.*, 124(38):11268–11269, 2002.

[27] Jeremy M Beebe, BongSoo Kim, C Daniel Frisbie, and James G Kushmerick. Measuring relative barrier heights in molecular electronic junctions with transition voltage spectroscopy. *ACS Nano*, 2(5):827–832, 2008.

[28] Emily A Weiss, George K Kaufman, Jennah K Kriebel, Zhefeng Li, Richard Schalek, and George M Whitesides. Si/sio2-templated formation of ultraflat metal surfaces on glass, polymer, and solder supports: Their use as substrates for self-assembled monolayers. *Langmuir*, 23(19):9686–9694, 2007.

[29] Emily A. Weiss, Ryan C. Chiechi, George K. Kaufman, Jennah K. Kriebel, Zhefeng Li, Marco Duati, Maria A. Rampi, and George M. Whitesides. Influence of defects on the electrical characteristics of Mercury-Drop junctions: Self-Assembled monolayers of N-Alkanethiolates on rough and smooth silver. *J. Am. Chem. Soc.*, 129(14): 4336–4349, 2007.

[30] Seong Ho Choi, Chad Risko, M Carmen Ruiz Delgado, BongSoo Kim, Jean-Luc Brédas, and C Daniel Frisbie. Transition from tunneling to hopping transport in long, conjugated oligo-imine wires connected to metals. *J. Am. Chem. Soc.*, 132(12):4358–4368, 2010.

[31] Dong Xiang, Yi Zhang, Feliks Pyatkov, Andreas Offenhäusser, and Dirk Mayer. Gap size dependent transition from direct tunneling to field emission in single molecule junctions. *Chem. Comm.*, 47:4760–4762, 2011.

[32] Felice C Simeone, Hyo Jae Yoon, Martin M Thuo, Jabulani R Barber, Barbara Smith, and George M Whitesides. Defining the Value of Injection Current and Effective Electrical Contact Area for EGaIn-Based Molecular Tunneling Junctions. *J. Am. Chem. Soc.*, 135(48):18131–18144, 2013.

[33] Li Jiang, C S Suchand Sangeeth, and Christian A Nijhuis. The origin of the odd–even effect in the tunneling rates across egain junctions with self-assembled monolayers (sams) of n-alkanethiolates. *J. Am. Chem. Soc.*, 137(33):10659–10667, 2015.

[34] Marco Carlotti, Maarten Degen, Yanxi Zhang, and Ryan C Chiechi. Pronounced environmental effects on injection currents in egain tunneling junctions comprising self-assembled monolayers. *J. Phys. Chem. C*, 120(36):20437–20445, 2016.

[35] Maxim E Dokukin and Igor Sokolov. Quantitative Mapping of the Elastic Modulus of Soft Materials with HarmoniX and PeakForce QNM AFM Modes. *Langmuir*, 28 (46):16060–16071, 2012.

[36] Frank W DelRio, Cherno Jaye, Daniel A Fischer, and Robert F Cook. Elastic and adhesive properties of alkanethiol self-assembled monolayers on gold. *Appl. Phys. Lett.*, 94(13):131909, 2009.

[37] Guillaume Ricœur, Stéphane Lenfant, David Guérin, and Dominique Vuillaume. Molecule/electrode interface energetics in molecular junction: A "transition voltage spectroscopy" study. *J. Phys. Chem. C*, 116(39):20722–20730, 2012.

[38] Zuoti Xie, Ioan Bâldea, Christopher E. Smith, Yanfei Wu, and C. Daniel Frisbie. Experimental and theoretical analysis of nanotransport in oligophenylene dithiol junctions as a function of molecular length and contact work function. *ACS Nano*, 9(8):8022–8036, 2015.

[39] BongSoo Kim, Seong Ho Choi, X.-Y. Zhu, and C Daniel Frisbie. Molecular tunnel junctions based on π-conjugated oligoacene thiols and dithiols between ag, au, and pt contacts: Effect of surface linking group and metal work function. *J. Am. Chem. Soc.*, 133(49):19864–19877, 2011.

[40] Krzysztof Slowinski, Richard V Chamberlain, Cary J Miller, and Marcin Majda. Through-bond and chain-to-chain coupling. two pathways in electron tunneling through liquid alkanethiol monolayers on mercury electrodes. *J. Am. Chem. Soc.*, 119(49):11910–11919, 1997.

[41] J C Love, L A Estroff, J K Kriebel, R G Nuzzo, and George M Whitesides. Self-assembled monolayers of thiolates on metals as a form of nanotechnology. *Chem. Rev.*, 105(4):1103–1169, 2005.

[42] Li Jiang, C S Suchand Sangeeth, Albert Wan, Ayelet Vilan, and Christian Albertus Nijhuis. Defect scaling with contact area in egain-based junctions: Impact on quality, joule heating, and apparent injection current. *J. Phys. Chem. C*, 119(2):960–969, 2015.

[43] Li Jiang, C S Suchand Sangeeth, Li Yuan, Damien Thompson, and Christian Albertus Nijhuis. One-nanometer thin monolayers remove the deleterious effect of substrate defects in molecular tunnel junctions. *Nano letters*, pages 6643—-6649, 2015.

[44] K Slowinski and M Majda. Mercury-mercury tunneling junctions - part ii. structure and stability of symmetric alkanethiolate bilayers and their effect on the rate of electron tunneling. *J. Electroanal. Chem.*, 491(1-2):139–147, 2000.

[45] Christian Albertus Nijhuis, William F Reus, Adam C Siegel, and George M Whitesides. A molecular half-wave rectifier. *J. Am. Chem. Soc.*, 133(39):15397–15411, 2011.

[46] Christian Albertus Nijhuis, William F Reus, and George M Whitesides. Molecular rectification in metal-sam-metal oxide-metal junctions. *J. Am. Chem. Soc.*, 131(49):17814–17827, 2009.

[47] Li Yuan, Rochus Breuer, Li Jiang, Michael Schmittel, and Christian Albertus Nijhuis. A molecular diode with a statistically robust rectification ratio of three orders of magnitude. *Nano letters*, 15(8):5506–5512, 2015.

[48] Hyo Jae Yoon, Kung Ching Liao, Matthew R Lockett, Sen Wai Kwok, Mostafa Baghbanzadeh, and George M Whitesides. Rectification in tunneling junctions: 2,2'-bipyridyl-terminated n-alkanethiolates. *J. Am. Chem. Soc.*, 136(49):17155–17162, 2014.

[49] Gyu Don Kong, Miso Kim, Soo Jin Cho, and Hyo Jae Yoon. Gradients of rectification: Tuning molecular electronic devices by the controlled use of different-sized diluents in heterogeneous self-assembled monolayers. *Angew. Chem.*, 55(35):10307–10311, 2016.

[50] Li Qiu, Yanxi Zhang, Theodorus Leonardus Krijger, Xinkai Qiu, Patrick van 't Hof, Jan Cornelis Hummelen, and Ryan Chiechi. Rectification of current responds to incorporation of fullerenes into mixed-monolayers of alkanethiolates in tunneling junctions. *Chem. Sci.*, 8(3):2365–2372, 2017.

[51] W J E Beek and R a J Janssen. Spacer length dependence of photoinduced electron transfer in heterosupramolecular assemblies of tio2 nanoparticles and terthiophene. *J. Mat. Chem.*, 14:2795–2800, 2004.

[52] Hennie Valkenier, Everardus H. Huisman, Paul A. van Hal, Dago M. de Leeuw, Ryan C. Chiechi, and Jan C. Hummelen. Formation of high-quality self-assembled monolayers of conjugated dithiols on gold: Base matters. *J. Am. Chem. Soc.*, 133 (13):4930–4939, 2011.

3

Controlling Quantum Interference in Tunneling Junctions Comprising Self-assembled Monolayers via Bond Topology and Functional Groups

3

Abstract: *Quantum interference effects (QI) are of interest in nano-scale devices based on molecular tunneling junctions because they can affect conductance exponentially through minor structural changes. However, their utilization requires the prediction and deterministic control over the position and magnitude of QI features, which remains a significant challenge. In this context, we designed and synthesized three benzodithiophenes based molecular wires; one linearly-conjugated, one cross-conjugated and one cross-conjugated quinone. Using EGaIn and CP-AFM, we compared them to a well-known anthraquinone in molecular junctions comprising self-assembled monolayers. By combining density functional theory and transition voltage spectroscopy, we show that the presence of an interference feature and its position can be controlled independently by manipulating bond topology and electronegativity. This is the first study to separate these two parameters experimentally, demonstrating that the conductance of a tunneling junction depends on the position and depth of a QI feature, both of which can be controlled synthetically.*
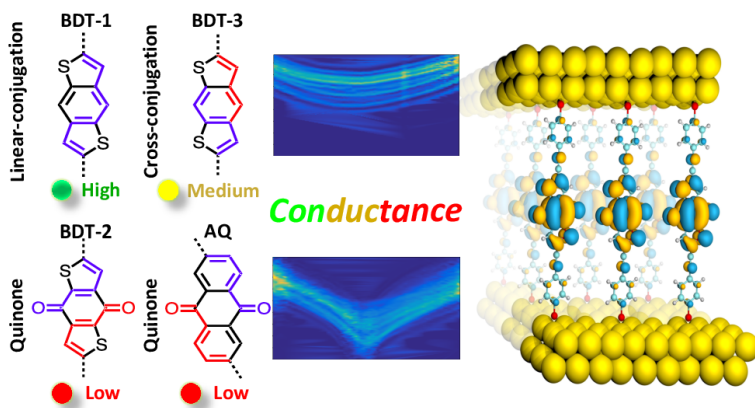
3.1. Introduction

Molecular electronics is concerned with the transport of charge through molecules spanning two electrodes,[1] the fabrication of which is a challenging area of nanotechnology.-[2–4] In such junctions, π-conjugated molecules influence transport more than a simple, rectangular tunneling barrier; when a tunneling electron traverses the region of space occupied by orbitals localized on these molecules, its wave function can undergo constructive or destructive interference, enhancing or suppressing conductance. When the presence of different pathways in molecular system affects conductance, it is typically described as quantum interference (QI),[5] which was originally adapted from Aharonov-Bohm effect[6] to substituted benzenes.[7, 8] The concept "quantum interference effect transistor" was also proposed using meta-benzene structures for device application.[9] Solomon et al. further refined the concept in the context of Molecular Electronics where it is now well established that destructive QI leads to lower conductance in tunneling junctions. [10–15] We previously demonstrated QI in SAM-based junctions using a series of compounds based on an anthracene core; **AC**, which is linearly-conjugated; **AQ**, which is cross-conjugated via a quinone moiety; and **AH**, in which the conjugation is interrupted by saturated methylene bridges (Figure 3.1).[16] Subsequent studies verified these findings in a variety of experimental platforms and a consensus emerged that, provided the destructive QI feature (anti-resonances in transmission) is sufficiently close to the Fermi level, E_F, cross-conjugation leads to QI.[17–24] However, experimental studies on conjugation patterns other than **AC**/**AQ** are currently limited to ring substitutions such as *meta*-substituted phenyl rings,[25–32] or varied connectivities in azulene,[33–35] which differ fundamentally[5, 11, 36–38] from cross-conjugated bond topologies[23, 39, 40] because they change tunneling pathways, molecular-lengths and bond topology simultaneously (Table 3.1). Isolating these variables is however important because the only primary observable is conductance, which varies exponentially with molecular length. More recent work has focused on "gating" QI effects by controlling the alignment of π-systems through-space[37, 41, 42] and affecting the orbital symmetry of aromatic rings with heteroatoms.[43–45] These studies exclusively study the effects of the presence and absence of QI features; to date—and despite recent efforts[46]—the specific effects of bond topology and electronegativity on the depth and position of QI features have not been isolated experimentally.

To address this issue, we designed and synthesized the series of benzodithiophene derivatives (**BDT-**n); benzo[1,2-b:4,5-b']dithiophene (**BDT-**1, linearly conjugated), benzo-[1,2-b:4,5-b']dithiophene-4,8-dione (**BDT-**2, cross-conjugated with quinone), and benzo-[1,2-b:5,4-b']dithiophene (**BDT-**3, cross-conjugated and an isomer of **BDT-**1). These compounds separate the influence of cross-conjugation (bond topology) from that of the electron-withdrawing effects of the quinone functionality while controlling for molecular formula and length. We investigated the charge transport properties of these molecules in tunneling junctions comprising self-assembled monolayers (SAMs), which are relevant for solid-state molecular-electronic devices.[47–49] Through a combination of density functional theory (DFT) and transition voltage spectroscopy (TVS) we show that cross-conjugation produces QI features near occupied molecular states and that the position and depth of the QI feature is strongly influenced by the strongly electron-withdrawing quinone functionality, which places these features near unoccupied states
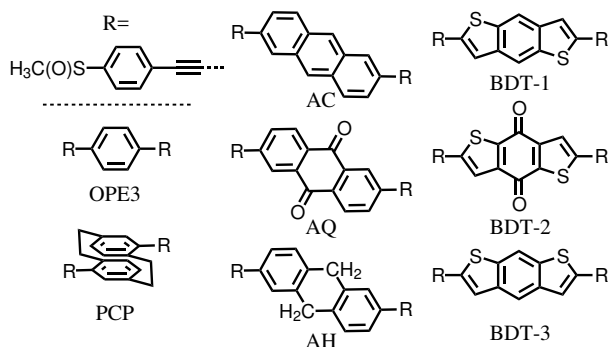
Figure 3.1 Structures and labels for all compounds mentioned in this chapter.

while simultaneously bringing those states close to E_F. Thus, by controlling bond topology and electronegativity separately, the conductance can be tuned independently of length and connectivity via the relative positions of the QI features and molecular states and not just the presence or absence of such features.

Table 3.1 Summary of compounds reported to exhibit quantum interference experimentally.

Compound	Technique	Reference
BDT-2,3	EGaIn	This work
AQ	EGaIn, CP-AFM, MC/STM-BJ, e-Carbon	16–19, 58
AH	EGaIn,MCBJ	41, 59
PCP	EGaIn,STM	41, 42
Azulene	STM-BJ,MCBJ	33, 35
m-benzene/fluorene	MC/STM-BJ	25–32, 60

3.2. RESULTS AND DISCUSSION

To isolate molecular effects on transport, it is important to control for changes to the width of the tunneling barrier which, in SAMs, is typically defined by the end-to-end lengths of the molecules. Conductance G generally varies exponentially with the barrier-width d such that $G = G_0 \exp(-\beta d)$, where G_0 is the theoretical value of G when $d = 0$, and β is the tunneling decay coefficient. Since β depends on the positions of molecular states relative to E_F and we are comparing compounds with very different redox potentials (orbital energies) we can only ascribe changes to G if d is invariant across the series. Furthermore, to isolate the variable of bond topology experimentally, the electronic properties of the linear- and cross-conjugated compounds must be nearly identical. Figure 3.2a shows the structures of the **BDT-***n* series and **AQ**; the "arms" are linearly-conjugated phenylacetylenes (highlighted in the light blue background) and the cores (Ar, highlighted in the brown background) are substituted by the structures indicated. The variation in the end-to-end lengths of these compounds is within 1 Å and the linear- and cross-conjugated compounds **BDT-**1 and **BDT-**3 differ only by the relative

position of sulfur atoms; they have the same molecular formula. The synthesis, full characterization and a detailed discussion of their properties are included in Experimental section. Note that we include **AQ** in the series as a benchmark for destructive QI effects.
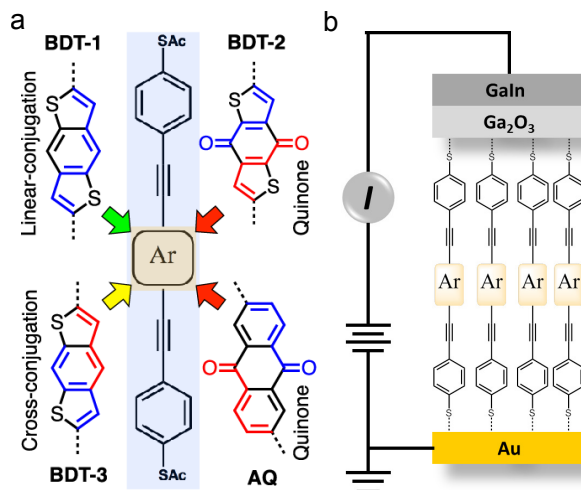
Figure 3.2 (a) Structures of **BDT**-1, **BDT**-2 and **BDT**-3 with linearly and cross-conjugated pathways of the cores drawn in blue and red, respectively. The phenylacetylene arms (highlighted in blue) are linearly conjugated. **BDT**-1 is linearly-conjugated, **BDT**-2 contains a cross-conjugation imposed by the central quinone ring analogous to **AQ** and **BDT**-3 is similarly cross-conjugated, but the cross-conjugation separating the two linearly-conjugated pathways arises from the positions of the sulfur atoms relative to the central phenyl ring (there are no exocyclic bonds). (b) Schematic of Au/SAM//EGaIn junction ("/" and "//" denote a covalent and van der Waals interfaces, respectively).

We measured tunneling charge transport through metal-molecule-metal junctions comprising **BDT**-1, **BDT**-2, **BDT**-3 and **AQ** using conformal eutectic Ga-In (EGaIn) contacts as top electrodes.[50] We utilized an established procedure of the *in situ* deprotection of thioacetates[41, 51] to form well-defined SAMs on Au substrates; these substrates served then as bottom electrodes. We refer to the assembled junctions as Au/SAM//EGaIn where "/" and "//" denote a covalent and van der Waals interfaces, respectively. The geometry of the EGaIn junctions is shown in Figure 3.2b. To verify that the structural similarities of the compounds carry over into the self-assembly process, we characterized the SAMs of **BDT**-*n* by several complementary techniques, including (high-resolution) X-ray photoelectron spectroscopy (HRXPS/XPS) and angle-resolved near-edge X-ray absorption fine structure spectroscopy (NEXAFS). These data are discussed in detail in the Experimental section and summarized in Table 3.2. The characterization of SAMs of **AQ** is reported elsewhere.[16, 41] The XPS and NEXAFS data suggest that the molecules in the **BDT**-*n* SAMs are assembled upright with the tilt angle of approximately 35°. The molecules are packed densely on the order of 10^{14} molecules per cm^2 as are similar conjugated molecular-wire compounds.[41]

Figure 3.3a shows the current-density versus voltage (J/V) curves for the **BDT**-*n* series and **AQ** using EGaIn top contacts. **BDT**-1 is the most conductive across the entire bias window. The conductance of linearly-conjugated **BDT**-1 and **AC** (Figure 3.1; a linearly-

Table 3.2 Summary of the properties of SAMs of **BDT-***n* and Au/**BDT-***n*//EGaIn junctions.

Compound	BDT-1	BDT-2	BDT-3	C18 reference
XPS thickness (Å)	17 ± 3	18 ± 4	19 ± 4	n.d.
HRXPS thickness (Å)	19.81 ± 0.40	22.30 ± 0.45	17.17 ± 0.34	20.9
Averaged XPS thickness (Å)	18.4	20.2	18.4	n.d.
Water contact angle (°)	68.3 ± 4.8	65.8 ± 4.0	62.8 ± 4.6	104.2 ± 2.2
Density (10^{14} molecules per cm^2)	2.05	3.30	2.33	4.63
Area per molecule ($Å^2$)	48.8 ± 2	30.3 ± 2	43.0 ± 2	21.6
$\log|J|$@0.5 V ($A\,cm^{-2}$)	-2.34 ± 0.17	-4.09 ± 0.23	-3.53 ± 0.20	-4.96 ± 0.87[41]
Yield of working junctions (%)	88.9	93.8	84.2	79[41]
Num. working EGaIn junctions	32	30	32	28[41]
Total J/V traces	643	626	666	280[41]

conjugated analog of **AQ**), are almost identical (Figure 3.26), meaning that the low-bias conductivity and/or values of *J* are directly comparable between the **AC**/**AQ** and **BDT-***n* series. As expected, the cross-conjugated **BDT-**2, **BDT-**3 and **AQ** are all less conductive than **BDT-**1 (and **AC**). The low-bias conductivity (from the Ohmic region, –0.1 V to 0.1 V) of the quinones (**BDT-**2 and **AQ**), however, is even more suppressed than the cross-conjugated **BDT-**3, while the magnitudes of *J* for **BDT-**2, **BDT-**3 and **AQ** are similar beyond –0.5 V. We observed similar behavior in QI mediated by through-space conjugation in which the compound with an interference feature very close to E_F exhibited a sharp rise in *J*, eventually crossing *J/V* curve of the compound with a feature further from E_F.[41] This observation suggests that, as the junction is biased, the transmission probability "climbs" the interference feature rapidly, bringing highly transmissive conduction channels into the bias window at sufficiently low values of *V* to meet and exceed the total transmission of the compound for which the interference feature is far from E_F at zero bias. Further discussion on the asymmetry of J/V curves is included in the Experimental.

To better compare the conductance of the molecules, we calculated the low-bias conductivities and normalized them to **BDT-**1. These values are plotted in Figure 3.3b, showing that cross-conjugation lowers the conductance of **BDT-**3 by an order of magnitude compared to **BDT-**1 and the quinone functionality of **BDT-**2 and **AQ** lowers it by two orders of magnitude, in agreement with the analogous behavior of **AC** and **AQ**. [20] To control for large-area effects (*e.g.*, if there are defects in the SAM), we measured **BDT-***n* series by conducting-probe atomic force microscopy (CP-AFM) with Au electrodes and found the same trend: **BDT-**1 > **BDT-**3 > **BDT-**2, however, a direct comparison of low-bias conductivities was precluded by the extremely high resistance of **BDT-**2 and **AQ** at low bias. These data are discussed in detail in the Experimental section. Thus, we conclude that quinones suppress conductance more than cross-conjugation alone, irrespective of the measurement/device platform.

For insight into the shapes of the *J/V* curves and the conductance, we simulated the transmission spectra, $T(E)$ vs. $E-E_F$ (E_F value of –4.3 eV, see Experimental section), of the **BDT-***n* series using density functional theory (DFT) and compared the resulting curves with **AQ** (Figure 3.4). These calculations, which are discussed in more detail in the Computational Methodology section of the Experimental section, simulate the
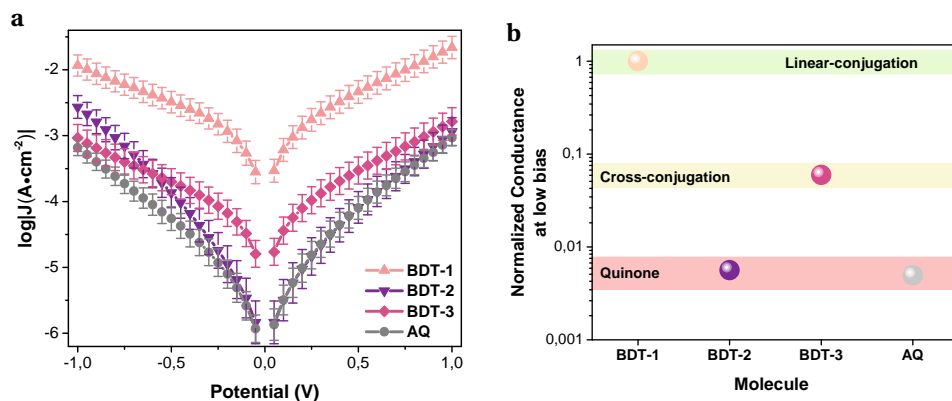
Figure 3.3 (a) Plots of $\log|J(\mathrm{A\,cm^{-2}})|$ versus V of Au/SAM//EGaIn junctions comprising SAMs of **BDT**-1 (salmon up-triangles), **BDT**-2 (purple down-triangles), **BDT**-3 (pink diamonds) and **AQ** (grey circles). Each datum is the peak position of a Gaussian fit of $\log|J|$ for that voltage. The error bars are 95 % confidence intervals taking each junction as a degree of freedom. (b) Normalized low bias conductance, linearly conjugated **BDT**-1 (salmon ball) features the highest values, the quinone **BDT**-2 (purple ball) and **AQ** (grey ball) the lowest and cross conjugated **BDT**-3 (pink ball) is in between.

transmission spectra through isolated molecules in vacuum at zero bias and are useful for predicting trends in conductance. There are three important features of these curves: 1) Only the compounds with cross-conjugation (including quinones) show sharp dips (anti-resonances or QI features)[13, 18] in the frontier orbital gap; 2) the dips occur near E_F only for the two quinones; and 3) the QI features are more pronounced for the molecules in which the cross-conjugation is caused by a quinone moiety as opposed to the carbon-carbon bond topology. When bias is applied to a junction, the x-axis of the transmission plot shifts and E_F broadens such that an integral starting at $E - E_\mathrm{F} = 0\,\mathrm{eV}$ and widening to larger ranges of $E - E_\mathrm{F}$ is a rough approximation of how $T(E)$ translates into current, $I(V)$. This relationship is apparent in the slightly lower conductance of **AQ** compared to **BDT**-2 (Figure 3.3b) and the slightly lower values of $T(E)$ for **AQ** compared to **BDT**-2 across the entire range of $E - E_\mathrm{F}$. The proximities of the QI features to E_F is also apparent in the J/V curves (Figure 3.3a). As the junction is biased, the minimum of the QI feature shifts such that, by 0.5 V, the transmission probabilities are roughly equal for **BDT**-n and **AQ**.

The shape of $T(E)$ near $E - E_\mathrm{F} = 0\,\mathrm{eV}$ is roughly traced by differential conductance plots of $\log|\frac{dJ}{dV}|$ vs. V, allowing QI features near E_F to be resolved experimentally.[18, 41, 52] Figure 3.5 shows heatmap plots of differential conductance of Au/SAM//EGaIn constructed from histograms binned to $\log|\frac{dJ}{dV}|$ for each value of V. (Note that these are histograms of J/V curves with no data-selection, thus, brighter colors correspond to mean values of J and are not related to conductance histograms of single-molecule breakjunctions; More details are discussed in Experimental section.) Both **BDT**-1 and **BDT**-3 exhibit ordinary, U-shaped plots characteristic of non-resonant tunneling. By contrast, both **AQ** and **BDT**-2—the two compounds bearing quinone functionality—show V-shaped plots with negative curvature. These results are in agreement with Figure 3.4, which places the QI features for the quinone moieties, **AQ** and **BDT**-2, much closer to E_F
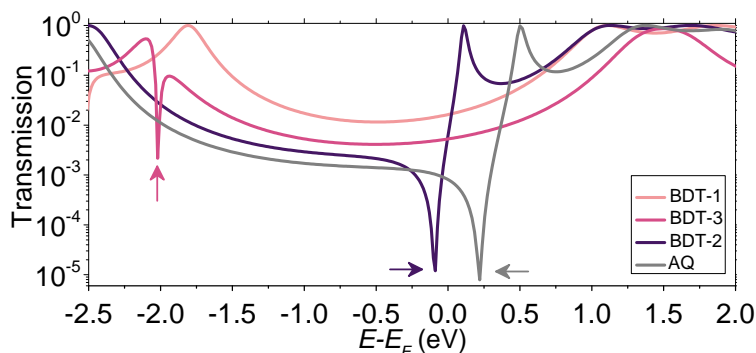
Figure 3.4 Transmission spectra for isolated molecules of **BDT-**n and **AQ**. The spectrum of **BDT-**1 (salmon) is featureless between the resonances ($T(E) \rightarrow 1$) near the frontier orbitals. The sharp dips in the spectra of **BDT-**2 (purple), **BDT-**3 (pink) and **AQ** (grey) indicated with arrows are destructive QI features. The energies on the bottom axis are with respect to the E_F value of -4.3 eV.

than for **BDT-**3. The positions of these features are related to the positions of highest-occupied and lowest-unoccupied π-states (HOPS and LUPS), which are in good agreement between DFT and experiment (Tables 3.3 and 3.4). Thus, the differential conductance heatmaps (experiment) and DFT (simulation) both indicate that cross-conjugation suppresses conductance because it creates a dip in $T(E)$ in the frontier orbital gap, but that the electron-withdrawing nature of the quinone functionality simultaneously pulls the LUPS and the interference features close to E_F such that the J/V characteristics and transmission plots of **AQ** and **BDT-**2 are nearly indistinguishable despite the presence of two thienyl groups in **BDT-**2. These results also suggest that tunneling transport is mediated by the HOPS (hole-assisted tunneling) for **BDT-**1 and **BDT-**3 and by the LUPS (electron-assisted tunneling) for **BDT-**2 and **AQ** because tunneling current is dominated by the resonance(s) closest to E_F.

To further investigate the mechanism of transport, we measured transition voltages, V_{trans} (Table 3.4, Figures 3.22 and 3.23), which provide information about the energy offset between E_F and the dominant frontier orbital.[53, 54] Figure 3.6a shows the levels for the **BDT-**n series calculated by DFT with respect to E_F (-4.3 eV), clearly predicting LUPS-mediated tunneling for **BDT-**2 and **AQ**. Figure 3.6b compares the experimental values of V_{trans} to the energy differences between E_F and the frontier orbitals. The salient feature of Figure 3.6b is that the trend in $|E_{\text{HOPS}} - E_F|$ opposes the trend in V_{trans} such that the trend in experimental values of V_{trans} agrees with DFT only when we compare V_{trans} with $|E_{\text{HOPS}} - E_F|$ for **BDT-**1 and **BDT-**3, and with $|E_{\text{LUPS}} - E_F|$ for **BDT-**2 and **AQ**. Thus, DFT calculations combined with experimental values of V_{trans} predict electron-assisted tunneling for **BDT-**2 and **AQ**. This degree of internal consistency between the experiment and theory is important because, ultimately, the only primary observable is conductance, which we plot as J/V curves, differential conductance heatmaps and Fowler-Nordheim plots (from which we extract V_{trans}). And we find remarkable agreement between these direct and indirect observations and DFT calculations on model junctions comprising single molecules.

74
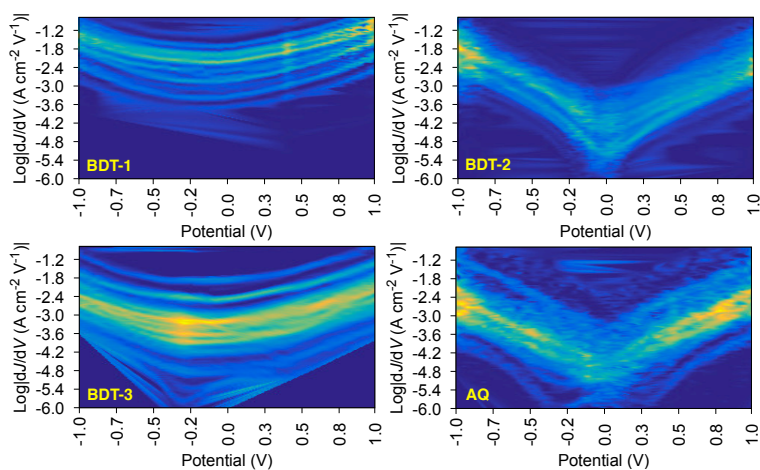
Figure 3.5 Differential conductance heatmap plots of Au/SAM//EGaIn junctions comprising **BDT**-1 (top-left), **BDT**-2 (top-right), **BDT**-3 (bottom-left) and **AQ** (bottom-right) showing histograms binned to $\log|\frac{dJ}{dV}|$ (differential conductance, Y-axis) versus potential (V, X-axis). The colors correspond to the frequencies of the histograms and lighter (more yellow) colors indicate higher frequencies. The bright spots near $\pm 1V$ are due to the doubling of data that occurs in the forward/return J/V traces. The plots for both **BDT**-2 and **AQ**, which contain quinones, are V-shaped at low bias and exhibit negative curvature, indicating a destructive QI feature near E_F, while the plots of **BDT**-1 and **BDT**-3 are U-shaped.
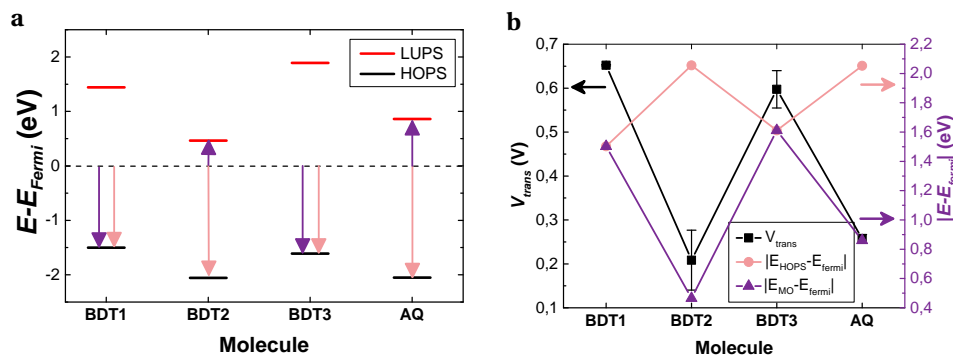
Figure 3.6 (a) Energy offsets of the frontier orbitals calculated using DFT with respect to E_F value of –4.3 eV. (b) The energy offsets (salmon and purple lines, right axis) plotted with the measured values of V_{trans} (black line, left axis). The salmon line plots the energy offsets of the HOPS. The purple line plots the smallest energy difference (purple arrows in Figure 5a); $|E_{HOPS} - E_{Fermi}|$ for **BDT**-1 and **BDT**-3, $|E_{LUPS} - E_{Fermi}|$ for **BDT**-2 and **AQ**. The exact values of V_{trans} and the orbital energies are shown in Table 3.4 and 3.6.

3.3. CONCLUSION

The key question of this work is how cross-conjugation and electronegativity affect QI features.[11, 20, 52, 55, 56] Based on our experimental observations and calculations, we assert that destructive QI induced by cross-conjugation is highly sensitive to the functional groups that induce the cross-conjugation and that quinones are, therefore, a poor testbed for tuning QI effects (beyond switching them on and off[57]) because their strong

electron-withdrawing nature places a deep, destructive feature near E_F irrespective of other functional groups (in our case, two fused thiophene rings barely make a difference). Comparing a quinone to a hydrocarbon also compares HOPS-mediated tunneling to LUPS-mediated tunneling between molecules with significantly different band-gaps and absolute frontier orbital energies. In contrast, **BDT-**1 and **BDT-**3 are heterocyclic isomers with no functional groups, identical molecular formulas, nearly-identical HOPS, identical lengths that translate into SAMs of identical thicknesses, and transport is dominated by the HOPS. They isolate the single variable of conjugation patterns, allowing us to separate bond topology (cross-conjugation) from electronic properties (functional groups), giving experimental and theoretical insight into the relationship between bond topology and QI. Our results suggest that there is a lot of room to tune the conductance of moieties derived from **BDT-**3 by including pendant groups (*e.g.*, halogens, CF_3 groups or acidic/basic sites) that shift the QI feature gradually towards E_F synthetically and/or in response to chemical signals.
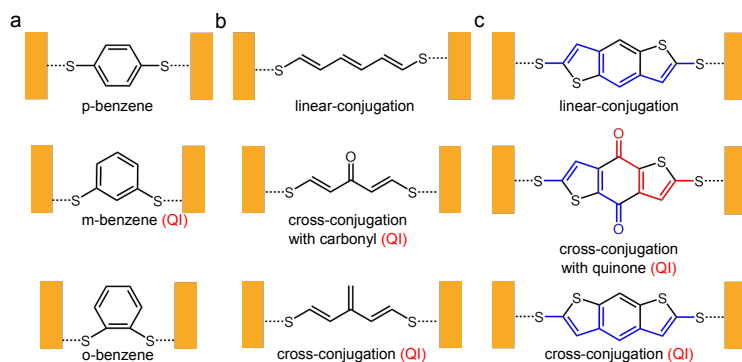
Figure 3.7 A schematic shows a) charge transfer through para-, meta, ortho-benzene between two electrodes (yellow rectangles). The conductance of m-benzene is lower than p- and o-benzene due to QI effects. b) charge transfer through linear-conjugation pattern of unsaturated carbon which has the same topology as **AC** and **BDT-**1, cross-conjugation pattern via carbonyl which has the same topology as **AQ** and **BDT-**2 and cross-conjugation pattern which has the same topology as **BDT-**3. Both cross-conjugation patterns exhibit QI effects. c) charge transfer through the core of **BDT-**1 which is linear-conjugated, the core of **BDT-**2 which is cross-conjugated with quinone and the core of **BDT-**3 which is cross-onjugated.

3.4. Experimental

3.4.1. Synthesis and Characterization

Reagents. All reagents and solvents were commercial and were used as received. Benzo[1,2-b;4,5-b']dithiophene was purchased from TCI. 2,6-dibromobenzo[1,2-b:4,5-b']dithiophene-4,8-dione[61], 2,6-dibromobenzo[1,2-b:5,4-b']dithiophene[62], 4-ethynyl-1-thioacetyl-benzene[63] and 1-tert-butylthio-4-ethynylbenzene[64] were synthesized according to literature procedures.

NMR and Mass Spectra. ^{1}HNMR and ^{13}CNMR were performed on a Varian Unity Plus (400 MHz) instrument at 25 °C, using tetramethylsilane (TMS) as an internal standard. NMR shifts are reported in ppm, relative to the residual protonated solvent signals of CDCl$_3$ (δ = 7.26 ppm) or at the carbon absorption in CDCl$_3$ (δ = 77.0 ppm). Multiplicities are denoted as: singlet (s), doublet (d), triplet (t) and multiplet (m). High Resolution Mass Spectroscopy (HRMS) was performed on a JEOL JMS 600 spectrometer.

General. Unless stated otherwise, all crude compounds were isolated by bringing the reaction to room temperature, extracting with CH$_2$Cl$_2$, washing with saturated NaHCO$_3$, water and then brine. The organic phase was then collected and dried over Na$_2$SO$_4$ and the solvents removed by rotary evaporation.

Synthesis of **BDT**-1
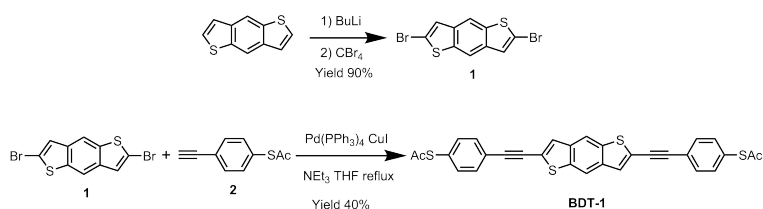
Figure 3.8 Synthetic route for **BDT**-1

2,6-dibromobenzo[1,2-b:4,5-b']dithiophene (1). Benzo[1,2-b;4,5-b']dithiophene (540 mg, 2.84 mmol) were dissolved in 70 mL anhydrous THF under an atmosphere of N$_2$, cooled to −78 °C and *n*-butyllithium (8.5 mmol, 5.3 mL, 1.6 M in hexane) was added drop-wise. The solution was stirred for 30 min in the cold bath before being warmed to room temperature and stirred for and additional 20 min. The mixture was cooled to −78 °C again and a solution of CBr$_4$ (2.8 g, 8.5 mmol) in 5 mL anhydrous THF was added. The solution was stirred for 30 min in the cold bath before being quenched with concentrated sodium bicarbonate solution (10 mL) at −78 °C. The crude solid was purified by recrystallization from CHCl$_3$ to give **1** (890 mg, 90 %) as colorless platelets. ^{1}HNMR (400 MHz, CDCl$_3$) δ: 8.03 (s, 2H); 7.33 (s, 2H). ^{13}CNMR (100 MHz, CDCl$_3$) δ: 138.36, 136.88, 125.63, 116.00, 115.10.

2,6-Bis[(4-acetylthiophenyl)ethynyl]benzo[1,2-b:4,5-b']dithiophene (BDT-1). 2,6-di-bromobenzo[1,2-b:4,5-b']dithiophene (125 mg, 0.36 mmol) and 4-ethynyl-1-thioacetyl-benzene (176 mg, 1 mmol) were dissolved in mixture of fresh distilled Et$_3$N (5 mL) and anhydrous THF (10 mL). After degassing with dry N$_2$, the catalysts Pd(PPh$_3$)$_4$ (58 mg, 0.05 mmol) and CuI (10 mg, 0.05 mmol) were added. The reaction mixture was refluxed

overnight under N_2. The crude solid was purified by column chromatography to give
BDT-1 (78 mg, 40 %). ^{1}HNMR (400 MHz, CDCl$_3$) δ: 8.17 (s, 2H), 7.59 (d, J=8.2, 4H), 7.55 (s,
2H), 7.43 (d, J=8.2, 4H), 2.45 (s, 6H). ^{13}CNMR (100 MHz, CDCl$_3$) δ: 195.88, 140.66, 140.46,
136.90, 134.76, 131.51, 130.89, 126.53, 126.25, 119.27, 97.57, 87.31, 32.97. HRMS(ESI)
calcd. for C$_{30}$H$_{18}$O$_2$S$_4$ [M+H]$^+$: 539,02624, found: 539.02457.
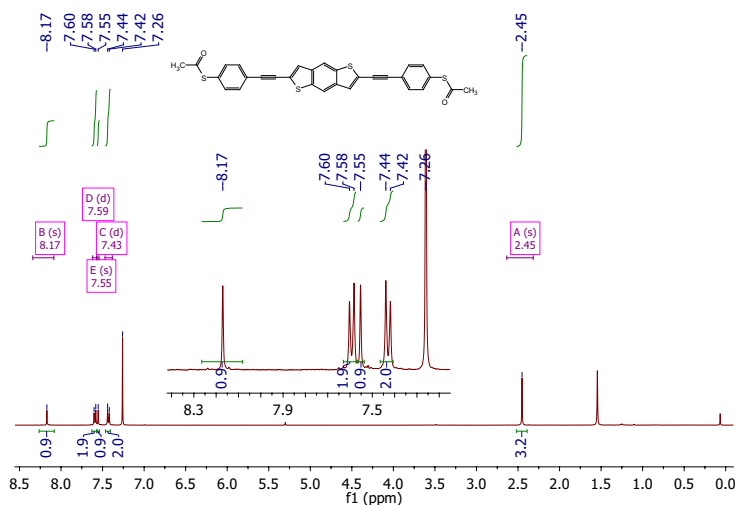
Figure 3.9 ^{1}HNMR spectrum of **BDT**-1
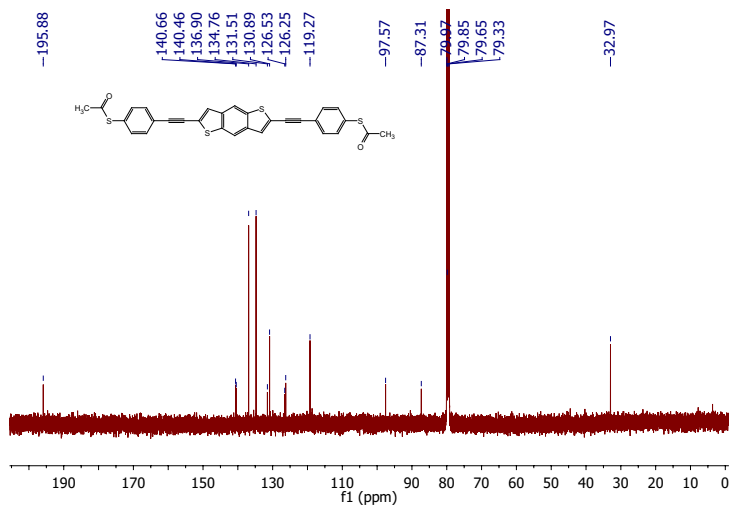
Figure 3.10 ^{13}CNMR spectrum of **BDT**-1

Synthesis of **BDT**-2
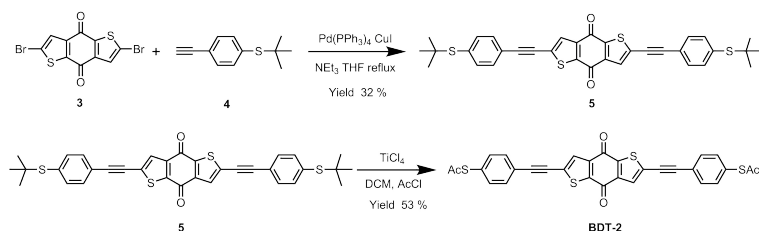
Figure 3.11 Synthetic route for **BDT**-2

2,6-Bis[(4-tert-butylthiophenyl)ethynyl]benzo[1,2-b:4,5-b']dithiophene-4,8-dione (5).
2,6-dibromobenzo[1,2-b:4,5-b']dithiophene-4,8-dione (**3**; 200 mg, 0.53 mmol) and 1-tert-butylthio-4-ethynylbenzene (**4**; 230 mg, 1.21 mmol) were dissolved in mixture of fresh distilled Et_3N (5 mL) and anhydrous THF (10 mL). After degassing, the catalysts $Pd(PPh_3)_4$ (30 mg, 0.03 mmol) and CuI (5 mg, 0.03 mmol) were added. The reaction mixture was re-fluxed for overnight under N_2. The crude solid was purified by column chromatography to give **5** (100 mg, 32 %). ^{1}HNMR (400 MHz, $CDCl_3$) δ: 7.71 (s, 2H), 7.55 (d, J=8.2, 4H), 7.50 (d, J=8.2, 4H), 1.31 (s, 18H). ^{13}CNMR (100 MHz, $CDCl_3$) δ: 173.33, 143.91, 142.55, 137.24, 135.17, 131.73, 131.56, 130.31, 121.70, 98.14, 82.55, 46.81, 31.02.

2,6-Bis[(4-acetylthiophenyl)ethynyl]benzo[1,2-b:4,5-b']dithiophene-4,8-dione (BDT-2).[65] TiCl$_4$ (0.04 mL, 0.364 mmol) was added drop-wise to a solution of compound **5** (100 mg, 0.167 mmol) and $CH_3C(O)Cl$ (0.03 mL, 0.377 mmol) in CH_2Cl_2 at 0 °C. The resulting mixture was stirred at room temperature for 1 h and the conversion was monitored by TLC (hexanes/CH_2Cl_2, 2:1). Upon completion, the reaction was quenched with water (10 mL). The crude solid was purified by column chromatography to give **BDT-**2 (50 mg, 53 %). ^{1}HNMR (400 MHz, $CDCl_3$) δ: 7.73 (s, 2H), 7.59 (d, J=8.2, 4H), 7.45 (d, J=8.2, 4H), 2.46 (s, 6H). ^{13}CNMR (100 MHz, $CDCl_3$) δ: 195.59, 175.96, 145.20, 136.95, 134.87, 134.20, 133.15, 132.57, 132.50, 125.24, 100.42, 85.49, 33.01. HRMS(ESI) calcd. for $C_{30}H_{17}O_4S_4$ [M+H]$^+$: 569,00042, found: 568.99887.

Synthesis of **BDT**-3

2,6-Bis[(4-tert-butylthiophenyl)ethynyl]benzo[1,2-b:5,4-b']dithiophene (7). 2,6-dibro-mobenzo[1,2-b:5,4-b']dithiophene (**6**; 50 mg, 0.143 mmol) and 1-tert-butylthio-4-ethynyl-benzene (**4**; 68 mg, 0.358 mmol) were dissolved in mixture of fresh distilled Et_3N (5 mL) and anhydrous THF (10 mL). After degassing, the catalysts $Pd(PPh_3)_4$ (16 mg, 0.014 mmol) and CuI (2.7 mg, 0.014 mmol) were added. The reaction mixture was refluxed overnight under N_2. The crude solid was purified by column chromatography to give **7** (40 mg, 49 %). ^{1}HNMR (400 MHz, $CDCl_3$) δ: 8.16 (s, 1H), 8.14 (s, 1H), 7.56 (s, 2H), 7.54 (d, J=4, 4H), 7.51 (d, J=4, 4H), 1.31 (s, 18H). ^{13}CNMR (100 MHz, $CDCl_3$) δ: 141.35, 140.05, 139.89, 136.77, 134.10, 131.29, 125.64, 125.38, 120.85, 117.39, 97.51, 86.99, 49.30, 33.67.

2,6-Bis[(4-acetylthiophenyl)ethynyl]benzo[1,2-b:5,4-b'] dithiophene (BDT-3).[65] TiCl$_4$ (0.042 mL, 0.388 mmol) was added drop-wise to a solution of compound **(7)** (100 mg, 0.176 mmol) and $CH_3C(O)Cl$ (0.03 mL, 0.397 mmol) in CH_2Cl_2 at 0 °C. The resulting mix-ture was stirred at room temperature for 10 min and the conversion was monitored by

3

3
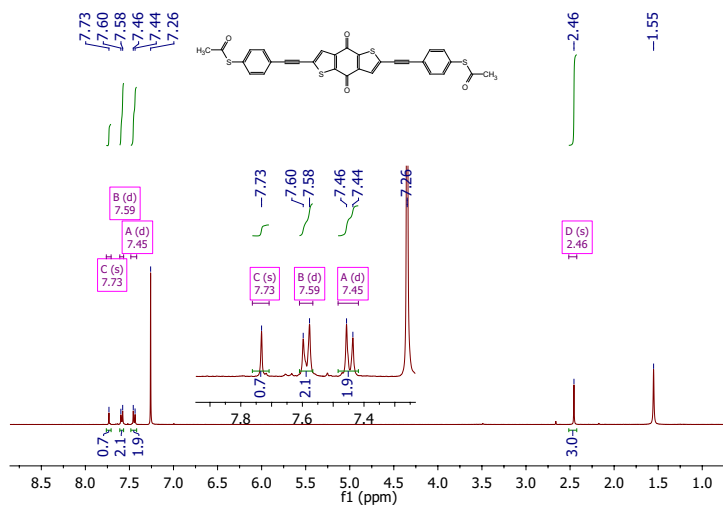
Figure 3.12 ^{1}HNMR spectrum of **BDT**-2
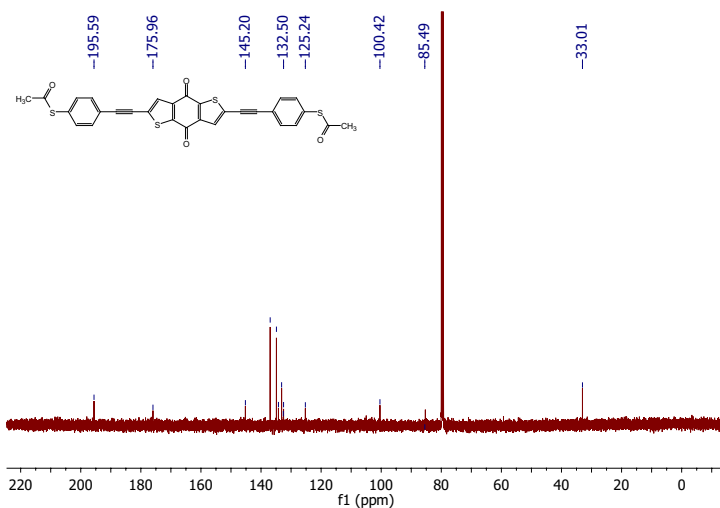
Figure 3.13 ^{13}CNMR spectrum of **BDT**-2

TLC (hexanes/CH$_2$Cl$_2$ 2:1). Upon completion the reaction was quenched with water
(10 mL). The crude solid was purified by column chromatography to give **BDT**-3 (25 mg,
26 %). ^{1}HNMR (400 MHz, CDCl$_3$) δ: 8.17 (s, 1H), 8.15 (s, 1H), 7.59 (d, J=7.2, 4H), 7.58
(s, 2H), 7.43 (d, J=8.2, 4H), 2.45 (s, 3H). ^{13}CNMR (100 MHz, CDCl$_3$) δ: 195.88, 141.43,
140.03, 136.90, 134.76, 131.51, 131.48, 126.27, 126.50, 120.94, 117.42, 97.22, 87.15, 32.97.
HRMS(ESI) calcd. for C30H18O2S4 [M+H]$^+$: 539,02624, found: 539.02476.

Figure 3.14 Synthetic route for **BDT**-3

Figure 3.15 ^{1}HNMR spectrum of **BDT**-3

3.4.2. SELF-ASSEMBLED MONOLAYERS

The SAMs of **BDT**-n were formed via *in situ* deprotection[41, 51] on template-stripped Au substrates[66]. Freshly template-stripped substrates were immersed into 3 mL of 50 μM solutions of the thioacetate precursors in freshly distilled toluene inside a nitrogen-filled glovebox and sealed under a nitrogen atmosphere. The sealed vessels were kept inside a nitrogen flow box[67] (O_2 below 3 %, RH below 15 %) overnight; all subsequent handling and EGaIn measurements were performed inside the flowbox. 1.5 h prior to measurement, 0.05 mL of 17 mM diazabicycloundec-7-ene(DBU) in toluene was added to the precursor/substrate solution. The substrates were then rinsed with toluene and allowed to dry for 30 min before performing the measurements. The SAM of **AQ** was prepared according to the reported methods[16] in dichloromethane (DCM) on Au^{Mica}.

3.4.3. CHARACTERIZATION

The SAMs of **BDT**-n were characterized by XPS (laboratory and synchrotron), NEXAFS, UPS and water contact angles. In some cases, SAMs of $CH_3(CH_2)_{15}SH$ or $CH_3(CH_2)_{17}SH$ on Au were used as a reference.

Figure 3.16 ^{13}CNMR spectrum of **BDT**-3

UV-Vis

UV-Vis measurements were carried out on a Jasco V-630 spectrometer, in 1 cm fused quartz cuvettes with concentrations of 10^{-5} mol/L in toluene. The calculated optical band gaps are summarized in Table 3.3.
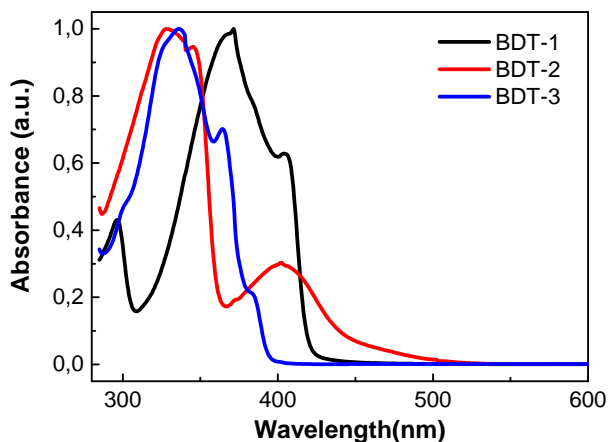
Figure 3.17 Normalized UV-Vis absorption spectra for **BDT-1**(black), **BDT-2**(red), **BDT-3**(blue).

WATER CONTACT ANGLES

Contact Angles were measured under ambient conditions on a SCA20 Dataphysics instrument. Contact angles were obtained by applying 3 μL water droplets on SAMs modified Au substrates using the sessile drop method. The contact angles were measured at

two different samples for each molecule, three different locations on each sample and the results were averaged with the standard deviation as the error.

Ultraviolet Photoelectron Spectroscopy

UPS measurements were performed using a VG microtech clam 100 spectrometer and an ultraviolet (He I, 21.2 eV) light source. Samples of SAMs were prepared as described in the Experimental and quickly transferred into the entry lock of the vacuum system. The base pressure of the measurement chamber was $<5 \times 10^{-9}$ mbar. A bias of -4 V was applied to the sample holder to obtain the secondary electron cut-off (SEC). HOPS onsets were found by fitting multiple Gaussian functions

$$He^{-\frac{(x-\mu)^2}{2\sigma^2}}$$

to the spectra, on top of the linear slope of the Fermi edge. The onset for the HOPS is found at $\mu + 2\sigma$ for the peak at the highest kinetic energy. The vacuum levels for the two samples are found by adding the photon energy, 21.2 eV, to the SEC. The binding energy scale is in reference to these vacuum levels.
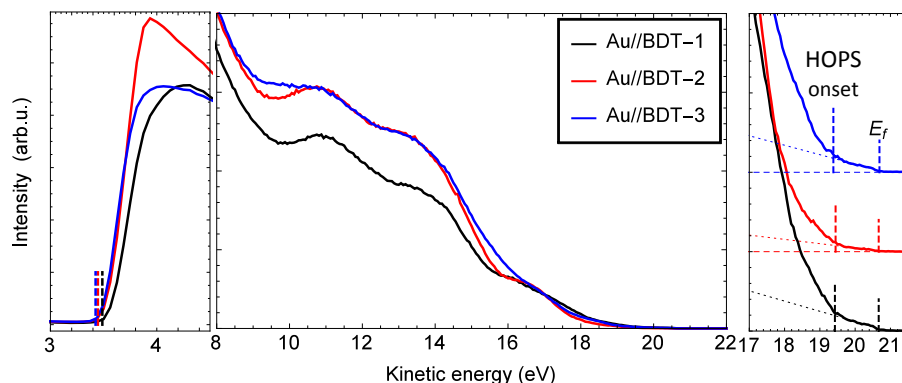
Figure 3.18 UPS spectra for **BDT-1** (black), **BDT-2** (red), **BDT-3** (blue).

Table 3.3 Tabulated energy level data from calculations (DFT) and experiments (CV, UPS, UV-Vis).

	CV		UPS		DFT (gas-phase)		UV-Vis
	HOMO	**LUMO**	**HOPS**[a]	**E$_f$**	**HOMO**	**LUMO**	**E$_g$**
BDT-1	-	-	-5.4	-4.2	-5.38	-2.33	2.95
BDT-2		-3.79	-5.4	-4.2	-5.95	-3.56	2.79
BDT-3	-	-	-5.6	-4.1	-5.59	-2.12	3.15
AQ	-	-3.56[64]	-6.1[51]	-4.5[51]	-5.98	-3.24	2.88[20]

[a] HOPS (from UPS) is the onset of HOPS feature, corrected for instrument resolution.

XPS and NEXAFS

NEXAFS The **BDT-***n* SAMs were characterized by X-ray photoelectron spectroscopy (XPS) and angle-resolved near-edge X-ray absorption fine structure (NEXAFS) spectroscopy. The measurements were performed at the HE-SGM beamline (bending magnet) of the synchrotron storage ring BESSY II in Berlin, Germany using a custom-made experimental station equipped with a SCIENTA SES200 electron energy analyzer and a partial electron yield (PEY) detector.[68]

The spectra acquisition in XPS was carried out in normal emission geometry with an energy resolution of ∼ 0.3 eV at an excitation energy of 350 eV and somewhat lower resolution at higher excitation energies. The binding energy (BE) scale of the XPS spectra was referenced to the Au $4f$7/2 emission at 84.0 eV.[69] The spectra were fitted by symmetric Voigt functions and a Shirley-type background. To fit the S $2p_{3/2,1/2}$ doublets we used two peaks with the same full width at half-maximum (fwhm), a standard[69] spin-orbit splitting of ∼ 1.2 eV (verified by fit), and a branching ratio of 2 (SÊ$2p_{3/2}$/SÊ$2p_{1/2}$). The fits were performed self-consistently: the same fit parameters were used for identical spectral regions.

The intensity values derived within the fitting procedure were used to calculate the effective thicknesses of the **BDT-***n* SAMs. They were estimated on the basis of the CÊ $1s$/Au $4f$ intensity ratio,[70] assuming a standard exponential attenuation of the photoelectron signal[71] and using the attenuation lengths typical of densely packed SAMs.[72] The spectrometer specific constants were determined using the $CH_3(CH_2)_{17}S$ (C18) monolayer of well-defined thicknesses as a reference. In addition, molecular packing densities in the **BDT-***n* SAMs were calculated, based on the S $2p$/Au $4f$ intensity ratio, relying on the established procedure[73] using the same assumptions as in the case of the CÊ$1s$/Au $4f$ evaluation. Only the part of the S $2p$ signal related to the thiolate was used. The C18 monolayer served as a reference; it has a molecular density of 4.63×10^{14} cm^{-2}, which corresponds a molecular footprint of 21.6 Å^2.[74] The NEXAFS spectra were acquired at the C K-edge in the PEY acquisition mode with a retarding voltage of –150 V. Linear-polarized synchrotron light with a polarization factor of 91 % was used. The energy resolution was ∼ 0.3 eV. The incidence angle of the primary X-ray beam was varied from 90° (**E** vector in surface plane) to 20° (**E** vector nearly parallel to surface normal) in few steps to monitor the orientational order in the SAMs. This approach is based on the dependence of the cross-section of the resonant photoexcitation process on the orientation of the electric field vector of the synchrotron light with respect to the molecular orbital of interest (so-called linear dichroism in X-ray absorption).[75] Raw NEXAFS spectra were normalized to the incident photon flux by dividing a spectrum of a clean, freshly sputtered gold sample and were reduced to the standard form by subtracting linear pre-edge background and normalizing to the unity edge jump (determined by a nearly horizontal plateau 40 eV to 50 eV above the respective absorption edges). The photon energy scale was referenced to the most intense $\pi*$ resonance of highly oriented pyrolytic graphite at 285.38 eV.[76]

The C $1s$ and S $2p$ XPS spectra of the **BDT-***n* SAMs are presented in Figure 3.19, along with the spectra for SAMs of $CH_3(CH_2)_{17}S$ (C18) for reference. The C1s spectra of the **BDT-***n* SAMs exhibit a strong peak at 284.7 eV to 285.0 eV assigned to the molecular backbone. The binding energy of this peak is higher for **BDT-**2 monolayer (285.0 eV) as

compared to the **BDT-**1 and **BDT-**2 SAMs (284.7 eV to 284.8 eV), which can be explained by the effect of the oxygen atoms in the quinone core of **BDT-**2. For all **BDT-***n* SAMs, the peak is noticeably broader than that for C18/Au, since it contains contributions of several different functional groups such as oligophenylenes,[77–79] phenyl,[80, 81] and thiophene.[82] In addition, there are much weaker signals at higher binding energies, which can be partly associated with the thiophene moieties[82] and partly stem from contamination (which could not be avoided completely). The S 2p XPS spectra of the **BDT-***n* SAMs exhibited characteristic signals of thiolate (**1**)[81] at 162.0 eV (S $2p_{3/2}$) and a joint signal of the thiophene moieties (**2**) and unbound SAc groups (**3**) at higher binding energies. For the **BDT-**1 and **BDT-**3 SAMs the positions of the latter signals are very close, in agreement with literature reports,[82, 83] merging to a joint doublets at 163.8 eV to 163.9 eV (S $2p_{3/2}$). For the **BDT-**2 SAMs, the position of the thiophene-related doublet (**3**) is shifted to 164.5 eV (S $2p_{3/2}$) due to the effect of the oxygen atoms in the quinone group.

For all **BDT-***n* SAMs, the intensity of the joint thiophene-thioacetate feature is much higher than that of the thiolate groups, which can only be explained by the differences in the attenuation, typical for an upright orientation of thiol-terminated molecules[83] and molecules with sulfur-containing groups in the molecular backbone.[84] This observation suggests that the molecules in the **BDT-***n* SAMs are assembled upright, in the expected SAMs fashion, with one of the terminal (deprotected) thioacetate groups bound to the substrate and the another (partially deprotected) one exposed to the SAMs-ambient interface,[51] where it can be contacted by the top electrodes. Also of interest is the fact that the intensities of the thioacetate- and thiophene-related doublets in the S 2p spectrum of the **BDT-**2 SAMs are almost equal, in spite of two S atoms in the thiophene-based core as compared to only one in the thioacetate group, which can only be explained by the attenuation effects, once more suggesting upright molecular orientation.

We computed the packing densities and effective thicknesses based on the intensities of the XPS peaks and doublets. The effective thickness values correlate coarsely between synchrotron- and laboratory-XPS experiments; these results are compiled in Table 3.2. In agreement with the S 2p data, the derived values of the effective thickness suggest upright molecular orientation in all **BDT-***n* SAMs, even though with a certain tilt. These results are summarized in Table 3.2.

The NEXAFS spectra of the **BDT-***n* SAMs are presented in Fig. 3.20. The 55° spectra, characteristic of the electronic structure only,[75] exhibit a superposition of the characteristic absorption resonances of the OPE compounds[79] and thiophene moieties. The dominant, slightly asymmetric π^* resonance at ~ 285.0 eV is dominated by the π_1^* resonance of OPE (at 285.0 eV as well)[79] with a minor contribution from the π_1^* resonance of thiophene at 285.6 eV.[82] Another prominent π^*-like resonance resonance at 288.5 eV stems presumably from the π_2^* resonance of OPE (at 285.6 eV).[79] Further resonances in the edge region are presumably related to the conjugated orbitals; the resonances at higher binding energies stems from the σ^*-orbitals, with contributions from all functional groups within the molecular backbones. No traces of contamination, above all a very pronounced resonance of carboxyl (most frequent contamination) at 288.8 eV,[85] are observed, revealing that its portion is relatively low (in agreement with the XPS data).

The difference of the NEXAFS spectra acquired at the normal (90°) and the grazing (20°) incidence represent a fingerprint of molecular orientation in terms of linear dichroism in X-ray absorption. The difference spectra of the **BDT-***n* SAMs exhibit very small linear dichroism, as demonstrated by the 90° to 20° spectrum of the **BDT-**1 monolayer shown in Fig. 3.20, representative of the entire series. The most likely interpretation of this observation is that the average tilt angle of the molecules in the **BDT-***n* SAMs is close to 35°, corresponding to a magic tilt angle (55°) for the most relevant π^*-like orbitals. Considering that the difference spectra for the **BDT-**2 and **BDT-**3 SAMs exhibit small positive and negative peak, respectively, at the position of the dominant π^* resonance, one can assume a smaller molecular inclination ($\sim 30°$) for the **BDT-**2 monolayer and a larger ($\sim 40°$) - for the **BDT-**3 monolayer, which correlate with the effective thicknesses of these SAMs (Table 3.2).
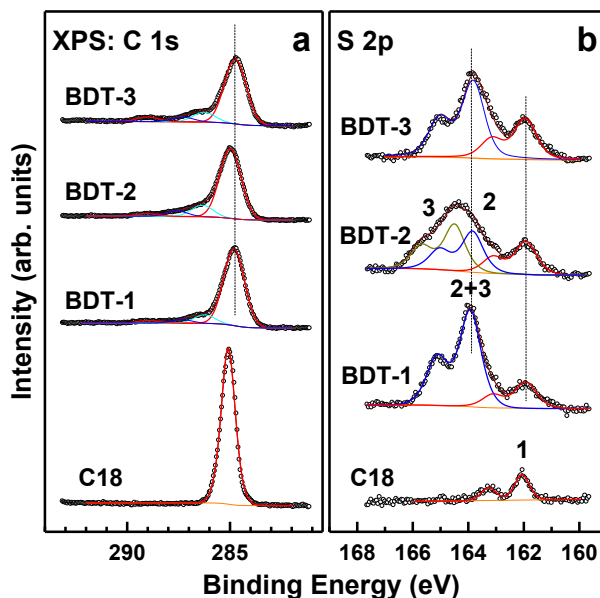
Figure 3.19 C 1s (a) and S 2p (b) synchrotron XPS spectra of the SAMs of **BDT-***n* and C18 for reference. The spectra were acquired at a photon energy of 350 eV. The spectra are decomposed in the component peaks (C 1s) and doublets (S 2p); (see text for details).

There is also a general correlation between the XPS and NEXAFS data (Figure 3.20). The C K-edge NEXAFS spectra of all **BDT-***n* SAMs are quite similar, exhibiting absorption structure that can be associated with the individual functional groups of these molecules, with the dominance of the OPE-stemming resonances. We found negligible (**BDT-**1) or quite small (**BDT-**2 and **BDT-**3) linear dichroism. Taken together with all other data and analysis of the dichroism data, this result suggests that the tilt angle of the molecules in these SAMs is close to 35°, with a slightly smaller and larger molecular inclination for the SAMs of **BDT-**2 and **BDT-**3, respectively, which correlates to the effective thicknesses.
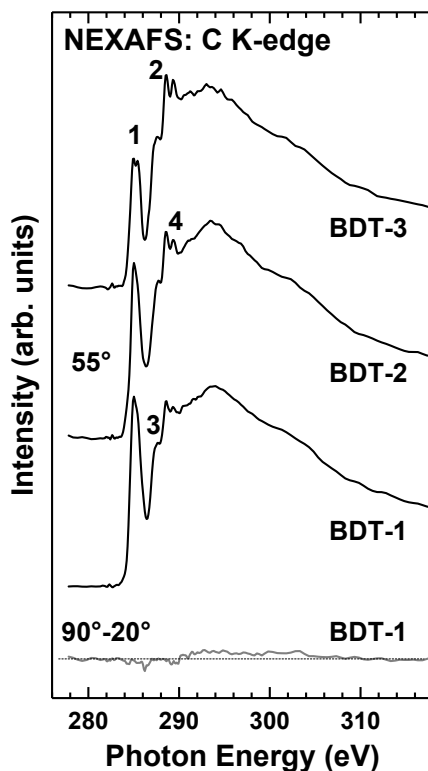
NEXAFS: C K-edge

Figure 3.20 C K-edge NEXAFS spectra of the BDT SAMs. The 55° spectra are exclusively representative of the electronic structure of the monolayers.[75] The 90° to 20° spectra, given on the **BDT**-1 SAM only, representative of the entire series, are representative of the molecular orientation.

CYCLIC VOLTAMMETRY

Cyclic voltammetry (CV) was carried out with a Autolab PGSTAT100 potentiostat in a three-electrode configuration where the working electrode was platinum electrode, the counter electrode was a platinum wire, and the pseudo-reference was an Ag wire that was calibrated against ferrocene (Fc/Fc$^+$). **BDT**-2 with the concentration of 0.001 M in ODCB-CH$_3$CN (9:1) solution containing Bu$_4$NPF$_6$ (0.1 M) was scanned at a rate of 100 mV/s. The first half-wave reduction potential appears at -1.01 V and second one appears at -1.51 V. The LUMO of **BDT**-2 is determined from the first half-wave reduction potential, with E_{HOMO} of ferrocene at -4.8 eV (LUMO = -($E_{1/2}^{red1}$ + 4.8) eV).

3.5. ELECTRICAL MEASUREMENTS

3.5.1. EGAIN

The details of the EGaIn setup are described elsewhere.[16, 41] Briefly, EGaIn measurements were carried in the nitrogen flowbox. For each SAM, at least 10 junctions were measured on each of three different substrates by applying a bias from $0.00\,\text{V} \rightarrow 1.00\,\text{V} \rightarrow$
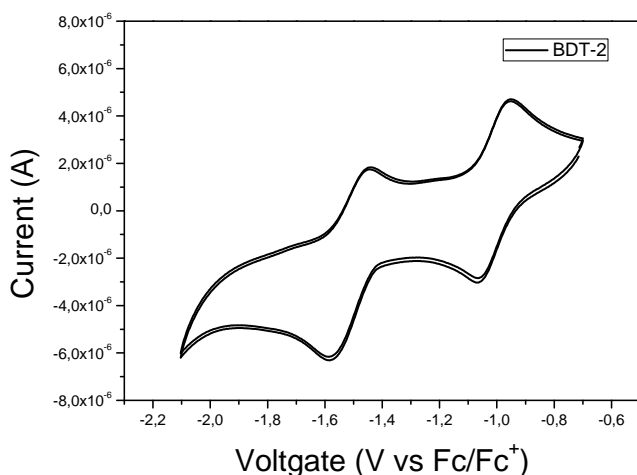
Figure 3.21 Cyclic voltammetry of **BDT**-2 with a scan rate of 100mV/s.

$-1.00\,\text{V} \rightarrow 0.00\,\text{V}$ with steps of 0.05 V. At least 20 trace/re-trace cycles were measured for each junction; only junctions that did not short over all 20 cycles were counted as "working junction" for computing yields. A new EGaIn tip was prepared every 4 junctions.

J-V Data Processing: Data was acquired as described above and then parsed in a "hands-off" manner using Scientific Python to produce histograms of J for each value of V and the associated Gaussian fits (using a least-squares fitting routine). The confidence intervals for μ_{logJ} (Gaussian mean) depicted as error bars in the J/V plots were calculated using $\alpha = 0.95$ from σ_{logJ} (standard deviation) taken from Gaussian fits and a number of degree of freedom equal to the $N_{\text{junctions}} - 1$. The value of t chosen for **BDT**-1 and **BDT**-3 is 2.04 (degree of freedom is 31) and **BDT**-2 is 2.05 (degree of freedom is 29).

Differential Conductance Heatmap: The J-V plots were smoothed by the polynomial model and the derivative of the current density (J) relative to the voltage (dJ/dV) were computed individually from each J-V plot. Then we constructed a 2D histogram of these dJ/dV values by logarithmically binning them for each bias voltage and plotting them, resulting in a heatmap with on the x-axis the bias voltage, on the y-axis the log (dJ/dV) and on the z-axis (in colour scale) the number of counts.

Table 3.4 Summary of Transition Voltage of **BDT**-1, **BDT**-2, **BDT**-3 and **AQ** obtained from EGaIn measurements

	BDT-1	BDT-2	BDT-3	AQ
$V_{\text{trans+}}$	0.652 ± 0.002	0.209 ± 0.068	0.597 ± 0.042	0.257 ± 0.010
$V_{\text{trans-}}$	-0.776 ± 0.054	-0.200 ± 0.059	-0.689 ± 0.068	-0.299 ± 0.099

The asymmetry of J/V plots: We calculated R by dividing each value of J at positive bias into the corresponding value at negative bias for each value of $|V|$ and then fitting a Gaussian to the resulting histogram of $\log|R|$ and expressing the error as the standard
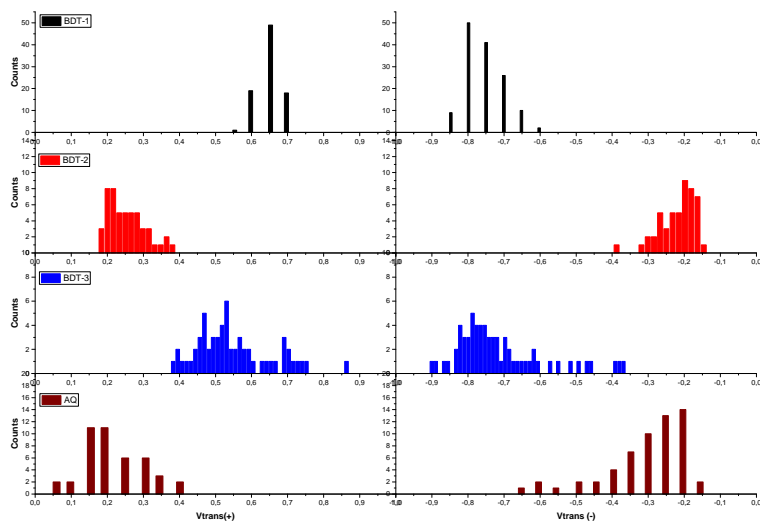
Figure 3.22 Transition Voltage Histogram of junctions comprising Au/**BDT-**1,2,3 and **AQ**//EGaIn. (**BDT-**1:Black, **BDT-**2:Red, **BDT-**3:Blue and **AQ**: Dark red.)
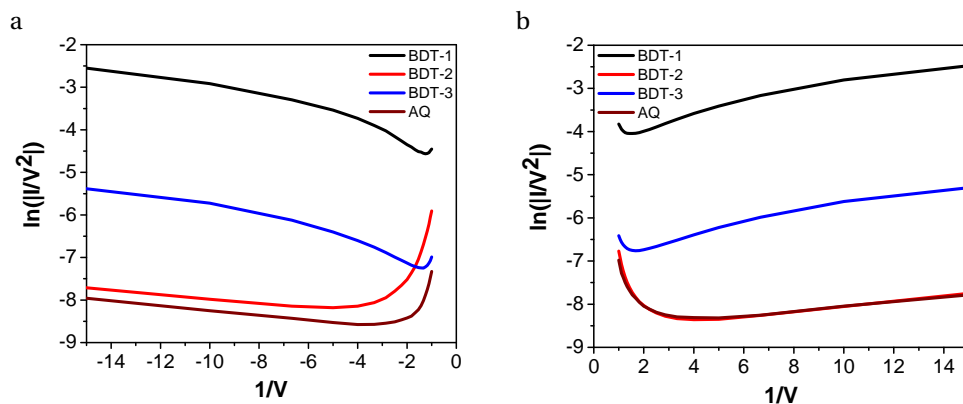
Figure 3.23 Transition voltage spectroscopy of Au/SAM//EGaIn junctions from Gaussian fitted J-V curves obtained by EGaIn: a) negative bias b) positive bias.

deviation of the fit (see Fig. 3.27). In EGaIn junctions, we usually do not consider junctions with $\log|R|$ below ± 1 as exhibiting rectifying behavior. Instead, we refer to it just as "asymmetry". The direction of asymmetry of **BDT-**2 is different from the other three molecules above 0.2 V. One well-known cause of asymmetry is molecular states moving closer to E_F at one sign of bias, which happens when the molecule is strongly asymmetrically coupled to two different electrodes. For the BDT-series, the LUMO of **BDT-**2 is lower in energy than for any other molecule. We hypothesize that the LUMO of **BDT-**2 is sufficiently close to E_F that it comes close to resonance around –0.2 V, causing an increase in current-density. Presumably we would observe a jump in asymmetry for the
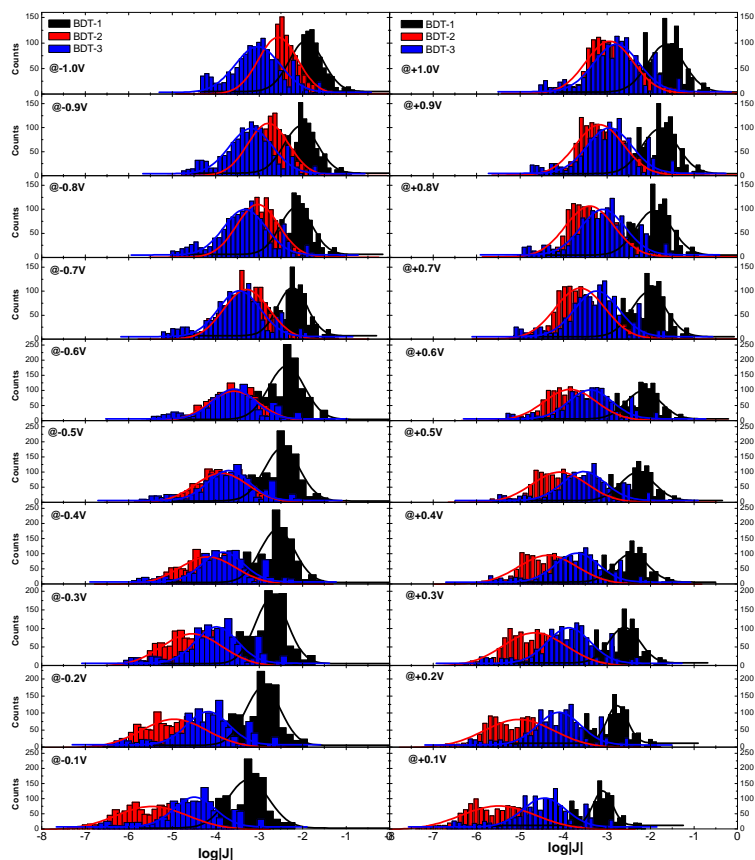
Figure 3.24 log $|J(\text{Acm}^{-2})|$ Histogram of junctions comprising Au$^{\text{TS}}$/**BDT-**1,2,3//EGaIn at at different bias: Left panel top to bottom starting from -1.0 V to -0.1 V and right panel top to bottom starting +1.0 V to +0.1 V.

other molecules if we were able to scan past ±1 V. In fact, **AQ** already shows signs of bending towards negative values of log$|R|$ around 0.8 V in the plot below.

3.5.2. CP-AFM

I-V measurements were performed on a Bruker AFM Multimode MMAFM-2 equipped with a Peak Force TUNA Application Module (Bruker.) The SAMs were contacted with a Au-coated silicon nitride tip with a nominal radius of 30 nm (NPG-10, Bruker, tip A: resonant frequency: 65 kHz, spring constant: 0.35 N/m; tip B: resonant frequency: 23 kHz, spring constant: 0.12 N/m; tip C: resonant frequency: 56 kHz, spring constant: 0.24 N/m; tip D: resonant frequency: 18 kHz, spring constant: 0.06 N/m. Tip A was chosen in this work) in TUNA mode. The AFM tip was grounded and the samples were biased from -1.0 V to $+1.0$ V and from $+1.0$ V to -1.0 V on Au$^{\text{Mica}}$ to record the I-V curves. The
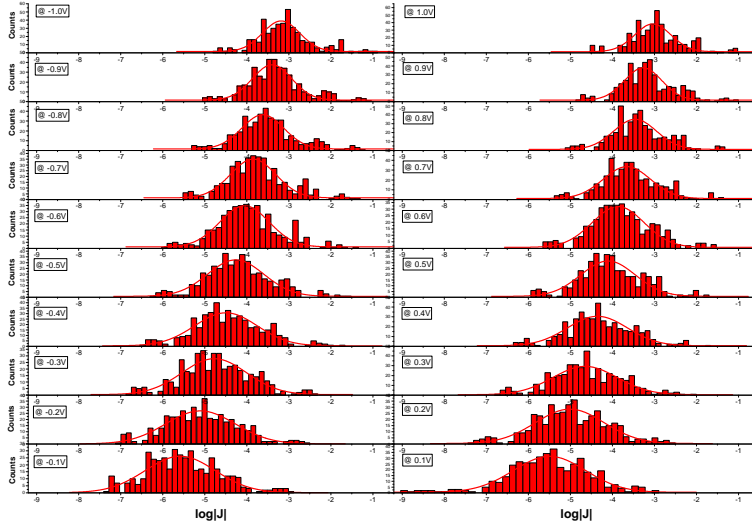
Figure 3.25 log $|J(Acm^{-2})|$ Histogram of junctions comprising Au-on-mica/**AQ**//EGaIn at at different bias: Left panel top to bottom starting from -1.0 V to -0.1 V and right panel top to bottom starting +1.0 V to +0.1 V.
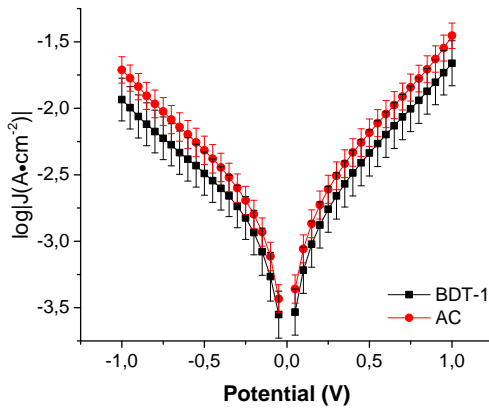
Figure 3.26 log plots of $|J(Acm^{-2})|$ vs. V of Au^{TS}/SAM//EGaIn junctions of **BDT-1** (black) and **AC**(red) (reported somewhere else[41]). Each data point is the peak of a Gaussian fit of log$|J|$ for that voltage and error bars are 95% confidence intervals.

samples of **BDT-**2 were bias from -1.8 V to $+1.8$ V, since the current of **BDT-**2 is on the magnitude of pA from -1.0 V to $+1.0$ V. We plotted **BDT-**2 from the region of -1.0 V to $+1.0$ V for easy comparison with **BDT-**1 and **BDT-**3. 11 trace/re-trace cycles per junction were performed and the top electrode was removed from SAMs between junctions. New tips were replaced between samples. The total number of I-V traces recorded by CP-AFM is summarized in Table 3.5.
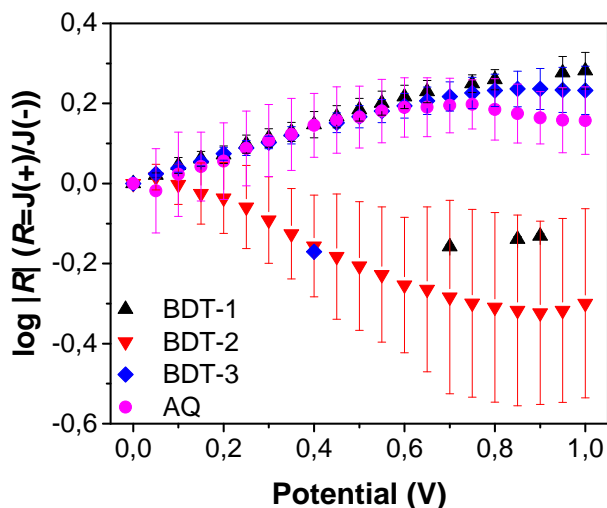
Figure 3.27 $\log|R|$ versus $|V|$ plots of Au/SAM//EGaIn junctions comprising **BDT**-1, **BDT**-2, **BDT**-3 and **AQ**. The error bars are the standard deviation of the Gaussian fit.

Processing. All raw data were processed algorithmically using Scientific Python to generate histograms, Gaussian fits, extract transition voltages and construct differential conductance heatmap plots.
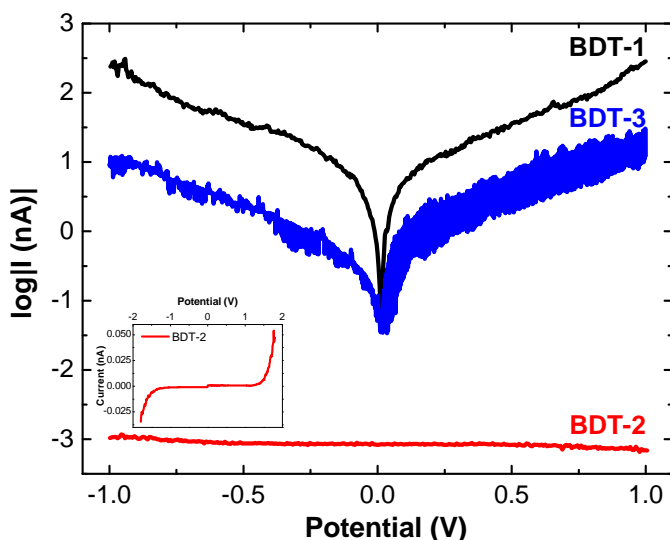
Figure 3.28 Plots of $\log|I(nA)|$ versus V of Au-on-mica/SAM//Au^{AFM} junctions comprising SAMs of **BDT**-1 (black), **BDT**-2 (blue) and **BDT**-3 (red) without error bars. Each datum is the peak of a Gaussian fit of $\log|I|$ for that voltage. The inset shows the Gaussian fitted I/V trace for **BDT**-2 on linear scale to ± 1.8V.

The current of **BDT-**2 was below the detection limit of our CP-AFM setup in the low-bias regime, however, at ±1 V, the difference between **BDT-**1 and **BDT-**2 is 10^5 larger for CP-AFM than for EGaIn.

a

b
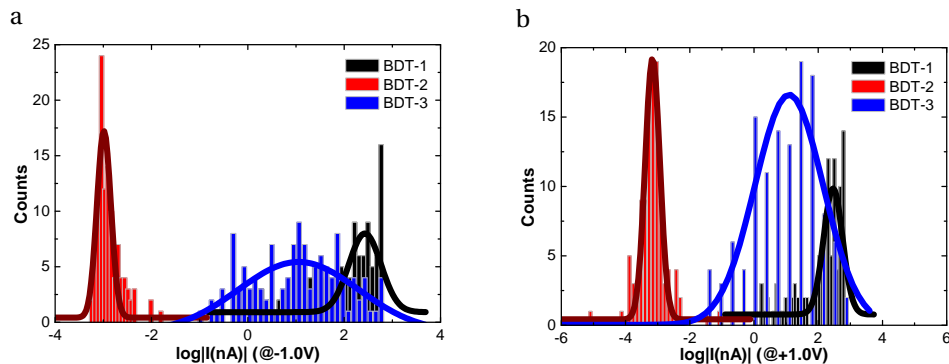
Figure 3.29 $\log|I(\text{nA})|$ Histogram of $\text{Au}^{\text{Mica}}/\text{SAM}//\text{Au}^{\text{AFM}}$ junctions at a) -1.0 V, b) +1.0 V.

Table 3.5 Summary of I-V traces recorded by CP-AFM.

SAMs	Number of junctions	Number of traces
BDT-1	10	110
BDT-2	10	110
BDT-3	12	136

3.6. COMPUTATIONAL METHODOLOGY

We performed the calculations using the *Orca 4.0.0.1* software package[86, 87] and the *Artaios-030417* software package.[88, 89] The procedure is described below step-by-step.

3.6.1. MOLECULAR GEOMETRY OPTIMIZATION

We optimized all the four molecules terminating with dithiols. We used ORCA DFT package and utilized the default Ahlrichs $def2-SVP$ basis sets (ORCA option *Acc-Opt,* that calls the BP functional).[90] This optimized gas-phase geometry was then used for all the following steps.

3.6.2. SINGLE POINT ENERGY CALCULATIONS

GAS-PHASE ENERGIES

We used the ORCA DFT package also for calculating the gas-phase energies for all the four molecules. We used the minimized geometries terminating with thiols to calculate the single-point gas-phase energies using $B3LYP/GLANL2DZ$. The HOMO-LUMO energies obtained from these gas-phase energy calculations are tabulated in Table 3.3.

Attaching Electrodes

We attached the minimized geometries to two 18-atom Au standard electrode clusters after manually deleting the terminal thiols' hydrogen atoms. The geometries of the electrode clusters used in these calculations consisted of 18 Au atoms per electrode, with two layers arranged in a hexagonal close-packed fcc Au-111 surface. The Au-Au distance was set to 2.88 Å, from the experimental lattice values of the bulk gold[91]. This is all similar to previously reported work[92]. S-Au distance was maintained at a value of 2.48 Å and S is attached to the center of the hexagonal close-pack hollow site, taken from literature.[93] We kept these geometrical parameters of the electrodes and the electrode material same throughout all these calculations, so that qualitative comparisons could be drawn. This junction geometry of the molecule attached via the Sulphur linker to the two Au metal clusters as electrodes was used for the next step.

Single Point Energy Calculations with Electrodes

After attaching the cores of the four molecules to the electrodes, we then calculated the single-point energies using the standard SCF convergence criteria using the ORCA DFT package. $B3LYP/G$ hybrid functional was applied and $LANL2DZ$ basis set was used. The energy values of the frontier π-states of the junction, *i.e.*, the HOPS (Highest Occupied π-state) and the LUPS (Lowest Unoccupied π-state) are tabulated in Table 3.6. The HOPS and LUPS were found by manually looking at the electron density of the different energy levels until we found the orbitals with electron density spanning through the molecule's π backbone. The HOMO energy values of the four molecular junctions, for which the electron density was localized on the Au atom clusters, are also tabulated in the Table 3.6. Finally, to calculate the energy differences E_F-E_{HOPS} or $E_{LUPS}-E_F$ in Fig. 3.6, E_F value of EGaIn was taken to be -4.3 eV.

	DFT		
	HOPS	LUPS	HOMO of Au clusters
BDT-1	-5.80	-2.86	-4.84
BDT-2	-6.35	-3.84	-4.88
BDT-3	-5.91	-2.41	-4.83
AQ	-6.35	-3.44	-4.93

Table 3.6 HOPS and LUPS from DFT for the four molecules when in the Au/Molecule/Au model junction along with the HOMO energy values (E_F) of Au clusters in the junction.

3.6.3. Transport Properties

For computing the electron transmission probability plots as function of energy of electron, we first ran single point energy calculations on structures terminating with only sulfur atoms, *i.e.*, by manually deleting the hydrogen atoms from the dithiols. Same basis sets were used as described above for the single point energy calculation. The hamiltonian and overlap matrices were generated from the output of these energy calculations, which served as the input for the *Artaios-030417* software tool for generating the transmission curves.[88, 89] Thus, we used the input geometry of these four molecules

without the terminal hydrogen atoms, computing the transmission of only the gas-phase molecule without the electrode clusters.

The reason for using the molecular system without electrode clusters is that we are only interested in the transmission of the molecule. These calculations are not simulations of an assembled junction; their purpose is to give insight into how the electronic structure affects transmission, not to predict level-alignment. We plotted HOPS for **BDT**-1 and **BDT**-3 and LUPS for **BDT**-2, *i.e.*, the orbitals that dominate the contribution to the electron transmission. The use of electrode clusters in these junctions is to identify the position of Fermi level of EGaIn junctions is physically realistic. Thus, we use the E_F of –4.3 eV for scaling the energy axis of the transmission curve in the Fig. 3.4. It is known that the literature value for workfunction of clean gold is about –5.2 eV to –5.3 eV but the assembly of alkanethiolates atop the gold surface reduces this value by 0.85 eV (–4.32 eV to –4.4 eV) [95]; further, the assembly of conjugated molecules result in a shift of 0.98 eV[96, 97]. Finally, the E_F of EGaIn has been reported as –4.3 eV in the literature[94] Thus, we use the value of –4.3 eV for E_F which is close to the cumulative E_F value for the junctions comprising SAMs with EGaIn as top electrode and Au as bottom electrode. This value is also close to the experimentally measured value of E_F using UPS. The use of this E_F value was also justified in the Fig. 3.6 where the differences of the energies of HOPS and LUPS from the E_F value of EGaIn qualitatively reproduced the trend in the transition voltages obtained from the EGaIn experiments.

BIBLIOGRAPHY

[1] Ayelet Vilan, Dinesh Aswal, and David Cahen. Large-area, ensemble molecular electronics: Motivation and challenges. *Chem. Rev.*, 117(5):4248–4286, 2017.

[2] Na Xin and Xuefeng Guo. Catalyst: The renaissance of molecular electronics. *Chem*, 3(3):373–376, 2017.

[3] Emanuel Lörtscher. Reaction: Technological aspects of molecular electronics. *Chem*, 3(3):376–377, 2017.

[4] Liang-Yan Hsu, Bih-Yaw Jin, Chun-hsien Chen, and Shie-Ming Peng. Reaction: New insights into molecular electronics. *Chem*, 3(3):378–379, 2017.

[5] C J Lambert. Basic concepts of quantum interference and electron transport in single-molecule electronics. *Chem. Soc. Rev.*, 44(4):875–888, 2015.

[6] R. a. Webb, S. Washburn, C. P. Umbach, and R. B. Laibowitz. Observation of he aharonov-bohm oscillations in normal-metal rings. *Phys. Rev. Lett.*, 54(25):2696–2699, 1985.

[7] P. Sautet and C. Joachim. Electronic interference produced by a benzene embedded in a polyacetylene chain. *Chem. Phys. Lett.*, 153(6):511–516, 1988.

[8] Liang-Yan Hsu and Bih-Yaw Jin. An investigation of quantum transport by the free-electron network model: Resonance and interference effects. *Chemical Physics*, 355(2):177–182, 2009.

[9] David M Cardamone, Charles A Stafford, and Sumit Mazumdar. Controlling Quantum Transport through a Single Molecule. *Nano Letters*, 6(11):2422–2426, 2006.

[10] Gemma C Solomon, David Q Andrews, Richard P Van Duyne, and Mark A Ratner. When things are not as they seem: Quantum interference turns molecular electron transfer "rules" upside down. *J. Am. Chem. Soc.*, 130(25):7788–7789, 2008.

[11] Gemma C. Solomon, David Q. Andrews, Randall H. Goldsmith, Thorsten Hansen, Michael R. Wasielewski, Richard P. Van Duyne, and Mark a. Ratner. Quantum interference in acyclic systems: Conductance of cross-conjugated molecules. *J. Am. Chem. Soc.*, 130(18):17301–17308, 2008.

[12] David Q Andrews, Gemma C Solomon, Randall H Goldsmith, Thorsten Hansen, Michael R Wasielewski, Richard P Van Duyne, and Mark A Ratner. Quantum interference: The structural dependence of electron transmission through model systems and cross-conjugated molecules. *J. Phys. Chem. C*, 112(43):16991–16998, 2008.

[13] Gemma C Solomon, Carmen Herrmann, Thorsten Hansen, Vladimiro Mujica, and Mark A Ratner. Exploring local currents in molecular junctions. *Nat. Chem.*, 2(3):223–228, 2010.

[14] Emanuele Maggio, Gemma C Solomon, and Alessandro Troisi. Exploiting quantum interference in dye sensitized solar cells. *ACS Nano*, 8(1):409–418, 2014.

[15] Kim G L Pedersen, Anders Borges, Per Hedegård, Gemma C Solomon, and Mikkel Strange. Illusory connection between cross-conjugation and quantum interference. *J. Phys. Chem. C*, 119(48):26919–26924, 2015.

[16] Davide Fracasso, Hennie Valkenier, Jan C Hummelen, Gemma C Solomon, and Ryan C Chiechi. Evidence for quantum interference in sams of arylethynylene thiolates in tunneling junctions with eutectic ga-in (egain) top-contacts. *J. Am. Chem. Soc.*, 133(24):9556–9563, 2011.

[17] Wenjing Hong, Hennie Valkenier, Gábor Mészáros, David Zsolt Manrique, Artem Mishchenko, Alexander Putz, Pavel Moreno García, Colin J Lambert, Jan C Hummelen, and Thomas Wandlowski. An mcbj case study: The influence of π-conjugation on the single-molecule conductance at a solid/liquid interface. *Beilstein J. Nanotechnol.*, 2:699–713, 2011.

[18] C M Guedon, H Valkenier, T Markussen, K S Thygesen, Jan C. Hummelen, and Sense Jan Van Der Molen. Observation of quantum interference in molecular charge transport. *Nat. Nanotechnol.*, 7(March):305–309, 2012.

[19] Veerabhadrarao Kaliginedi, Pavel Moreno-García, Hennie Valkenier, Wenjing Hong, Víctor M García-Suárez, Petra Buiter, Jelmer L H Otten, Jan C Hummelen, Colin J Lambert, and Thomas Wandlowski. Correlations between molecular structure and single-junction conductance: A case study with oligo(phenylene-ethynylene)-type wires. *J. Am. Chem. Soc.*, 134(11):5262–5275, 2012.

[20] Hennie Valkenier, Constant M Guedon, Troels Markussen, Kristian S Thygesen, Sense J van der Molen, and Jan C Hummelen. Cross-conjugation and quantum interference: A general correlation? *Phys. Chem. Chem. Phys.*, 16(2):653–662, 2014.

[21] Max Koole, Jos M Thijssen, Hennie Valkenier, Jan C Hummelen, and Herre S J van der Zant. Electric-field control of interfering transport pathways in a single-molecule anthraquinone transistor. *Nano Lett.*, 15(8):5569–5573, 2015.

[22] Justin P Bergfield, Henry M Heitzer, Colin Van Dyck, Tobin J Marks, and Mark A Ratner. Harnessing quantum interference in molecular dielectric materials. *ACS Nano*, 9(6):6412–6418, 2015.

[23] Troels Markussen, Robert Stadler, and Kristian S. Thygesen. The relation between structure and quantum interference in single molecule junctions. *Nano Lett.*, 10:4260–4265, 2010.

[24] C Salhani, M L Della Rocca, C Bessis, R Bonnet, C Barraud, P Lafarge, A Chevillot, P Martin, and J. C. Lacroix. Inelastic electron tunneling spectroscopy in molecular junctions showing quantum interference. *Phys. Rev. B*, 95(16):165431, 2017.

3

[25] Marcel Mayor, Heiko B Weber, Joachim Reichert, Mark Elbing, Carsten von Hänisch, Detlef Beckmann, and Matthias Fischer. Electric current through a molecular rod—relevance of the position of the anchor groups. *Angew. Chem., Int. Ed.*, 42(47):5834–5838, 2003.

[26] Masateru Taniguchi, Makusu Tsutsui, Ryoji Mogi, Tadashi Sugawara, Yuta Tsuji, Kazunari Yoshizawa, and Tomoji Kawai. Dependence of single-molecule conductance on molecule junction symmetry. *J. Am. Chem. Soc.*, 133(30):11426–11429, 2011.

[27] Jeffrey S Meisner, Seokhoon Ahn, Sriharsha V Aradhya, Markrete Krikorian, Radha Parameswaran, Michael Steigerwald, Latha Venkataraman, and Colin Nuckolls. Importance of direct metal π coupling in electronic transport through conjugated single-molecule junctions. *J. Am. Chem. Soc.*, 134(50):20440–20445, 2012.

[28] Carlos R Arroyo, Simge Tarkuc, Riccardo Frisenda, Johannes S Seldenthuis, Charlotte H M Woerde, Rienk Eelkema, Ferdinand C Grozema, and Herre S J van der Zant. Signatures of quantum interference effects on charge transport through a single benzene ring. *Angew. Chem., Int. Ed.*, 52(11):3152–3155, 2013.

[29] Jordan R Quinn, Frank W Foss, Latha Venkataraman, Mark S Hybertsen, and Ronald Breslow. Single-molecule junction conductance through diaminoacenes. *J. Am. Chem. Soc.*, 129(21):6714–6715, 2007.

[30] Manabu Kiguchi, Hisao Nakamura, Yuuta Takahashi, Takuya Takahashi, and Tatsuhiko Ohto. Effect of anchoring group position on formation and conductance of a single disubstituted benzene molecule bridging au electrodes: Change of conductive molecular orbital and electron pathway. *J. Phys. Chem. C*, 114(50):22254–22261, 2010.

[31] Sriharsha V. Aradhya, Jeffrey S. Meisner, Markrete Krikorian, Seokhoon Ahn, Radha Parameswaran, Michael L. Steigerwald, Colin Nuckolls, and Latha Venkataraman. Dissecting contact mechanics from quantum interference in single-molecule junctions of stilbene derivatives. *Nano Lett.*, 12:1643–1647, 2012.

[32] David Zsolt Manrique, Cancan Huang, Masoud Baghernejad, Xiaotao Zhao, Oday a Al-Owaedi, Hatef Sadeghi, Veerabhadrarao Kaliginedi, Wenjing Hong, Murat Gulcur, Thomas Wandlowski, Martin R Bryce, and Colin J Lambert. A quantum circuit rule for interference effects in single-molecule electrical junctions. *Nat. Commun.*, 6:6389, 2015.

[33] Jianlong Xia, Brian Capozzi, Sujun Wei, Mikkel Strange, Arunabh Batra, Jose R. Moreno, Roey J. Amir, Elizabeth Amir, Gemma C. Solomon, Latha Venkataraman, and Luis M. Campos. Breakdown of interference rules in azulene, a nonalternant hydrocarbon. *Nano Lett.*, 14:2941–2945, 2014.

[34] Florian Schwarz, Michael Koch, Georg Kastlunger, Heinz Berke, Robert Stadler, Koushik Venkatesan, and Emanuel Lörtscher. Charge transport and conductance

switching of redox-active azulene derivatives. *Angew. Chem., Int. Ed.*, 55(39):11781–11786, 2016.

[35] Guogang Yang, Sara Sangtarash, Zitong Liu, Xiaohui Li, Hatef Sadeghi, Zhibing Tan, Ruihao Li, Jueting Zheng, Xiaobiao Dong, Jun-Yang Liu, Yang Yang, Jia Shi, Zongyuan Xiao, Guanxin Zhang, Colin Lambert, wenjing Hong, and Deqing Zhang. Protonation tuning of quantum interference in azulene-type single-molecule junctions. *Chem. Sci.*, 8:7505–7509, 2017.

[36] Roi Baer and Daniel Neuhauser. Phase Coherent Electronics: A Molecular Switch Based on Quantum Interference. *J. Am. Chem. Soc.*, 124(16):4200–4201, 2002.

[37] Gemma C Solomon, Carmen Herrmann, Josh Vura-Weis, Michael R Wasielewski, and Mark A Ratner. The chameleonic nature of electron transport through π-stacked systems. *J. Am. Chem. Soc.*, 132(23):7887–7889, 2010.

[38] Aleksey A. Kocherzhenko, Ferdinand C. Grozema, and Laurens D A Siebbeles. Charge transfer through molecules with multiple pathways: Quantum interference and dephasing. *J. Phys. Chem. C*, 114:7973–7979, 2010.

[39] Nelson F Phelan and Milton Orchin. Cross conjugation. *J. Chem. Educ.*, 45(10):633–637, 1968.

[40] Peter a. Limacher and Hans P. Lüthi. Cross-conjugation. *Wiley Interdiscip. Rev.: Comput. Mol. Sci.*, 1(August):477–486, 2011.

[41] Marco Carlotti, Andrii Kovalchuk, Tobias Wächter, Xinkai Qiu, Michael Zharnikov, and Ryan C Chiechi. Conformation-driven quantum interference effects mediated by through-space conjugation in self-assembled monolayers. *Nat. Commun.*, 7:13904, 2016.

[42] Anders Borges, Jianlong Xia, Sheng Hua Liu, Latha Venkataraman, and Gemma C Solomon. The role of through-space interactions in modulating constructive and destructive interference effects in benzene. *Nano Lett.*, 17(7):4436–4442, 2017.

[43] Sara Sangtarash, Hatef Sadeghi, and Colin J Lambert. Exploring quantum interference in heteroatom-substituted graphene-like molecules. *Nanoscale*, 8:13199–13205, 2016.

[44] Xunshan Liu, Sara Sangtarash, David Reber, Dan Zhang, Hatef Sadeghi, Jia Shi, Zong-Yuan Xiao, Wenjing Hong, Colin J Lambert, and Shi-Xia Liu. Gating of quantum interference in molecular junctions by heteroatom substitution. *Angew. Chem., Int. Ed.*, 56(1):173–176, 2017.

[45] Yuta Tsuji, Thijs Stuyver, Suman Gunasekaran, and Latha Venkataraman. The Influence of Linkers on Quantum Interference: A Linker Theorem. *J. Phys. Chem. C*, 121(27):14451–14462, 2017.

3

[46] Henriette Lissau, Riccardo Frisenda, Stine T Olsen, Martyn Jevric, Christian R Parker, Anders Kadziola, Thorsten Hansen, Herre S J van der Zant, Mogens Brøndsted Nielsen, and Kurt V Mikkelsen. Tracking molecular resonance forms of donor–acceptor push–pull molecules by single-molecule conductance experiments. *Nat. Commun.*, 6:10233, 2015.

[47] Zongrui Wang, Huanli Dong, Tao Li, Rune Hviid, Ye Zou, Zhongming Wei, Xiaolong Fu, Erjing Wang, Yonggang Zhen, Kasper Norgaard, Bo W Laursen, and Wenping Hu. Role of redox centre in charge transport investigated by novel self-assembled conjugated polymer molecular junctions. *Nat Commun*, 6:7478, 2015.

[48] Parisa Pourhossein, Ratheesh K Vijayaraghavan, Stefan C J Meskers, and Ryan C Chiechi. Optical modulation of nano-gap tunnelling junctions comprising self-assembled monolayers of hemicyanine dyes. *Nat. Commun.*, 7:11749, 2016.

[49] Sohyeon Seo, Eunhee Hwang, Yunhee Cho, Junghyun Lee, and Hyoyoung Lee. Functional molecular junctions derived from double self-assembled monolayers. *Angew. Chem., Int. Ed.*, 56(40):12122–12126, 2017.

[50] Ryan C Chiechi, Emily A Weiss, Michael D Dickey, and George M Whitesides. Eutectic gallium–indium (egain): A moldable liquid metal for electrical characterization of self-assembled monolayers. *Angew. Chem., Int. Ed.*, 120(1):148–150, 2008.

[51] Hennie Valkenier, Everardus H. Huisman, Paul A. van Hal, Dago M. de Leeuw, Ryan C. Chiechi, and Jan C. Hummelen. Formation of high-quality self-assembled monolayers of conjugated dithiols on gold: Base matters. *J. Am. Chem. Soc.*, 133 (13):4930–4939, 2011.

[52] Jacob Lykkebo, Alessio Gagliardi, Alessandro Pecchia, and Gemma C Solomon. Iets and quantum interference: Propensity rules in the presence of an interference feature. *J. Chem. Phys.*, 141(12):124119, 2014.

[53] Jeremy M Beebe, BongSoo Kim, C Daniel Frisbie, and James G Kushmerick. Measuring relative barrier heights in molecular electronic junctions with transition voltage spectroscopy. *ACS Nano*, 2(5):827–832, apr 2008.

[54] Yanxi Zhang, Xinkai Qiu, Pavlo Gordiichuk, Saurabh Soni, Theodorus L Krijger, Andreas Herrmann, and Ryan C Chiechi. Mechanically and electrically robust self-assembled monolayers for large-area tunneling junctions. *J. Phys. Chem. C*, 121 (27):14920–14928, 2017.

[55] Kim G L Pedersen, Mikkel Strange, Martin Leijnse, Per Hedegard, Gemma C Solomon, and Jens Paaske. Quantum interference in off-resonant transport through single molecules. *Phys. Rev. B*, 90(12):125413, 2014.

[56] Gemma C Solomon. Cross-conjugation and quantum interference. In *Cross Conjugation*, pages 397–412. Wiley-VCH Verlag GmbH & Co. KGaA, 2016.

[57] Masoud Baghernejad, Xiaotao Zhao, Kristian Baruël Ørnsø, Michael Füeg, Pavel Moreno-García, Alexander V. Rudnev, Veerabhadrarao Kaliginedi, Soma Vesztergom, Cancan Huang, Wenjing Hong, Peter Broekmann, Thomas Wandlowski, Kristian S. Thygesen, and Martin R. Bryce. Electrochemical control of single-molecule conductance by fermi-level tuning and conjugation switching. *J. Am. Chem. Soc.*, 136(52):17922–17925, 2014.

[58] Vincent Rabache, Julien Chaste, Philippe Petit, Maria Luisa Della Rocca, Pascal Martin, Jean-Christophe Lacroix, Richard L McCreery, and Philippe Lafarge. Direct observation of large quantum interference effect in anthraquinone solid-state junctions. *J. Am. Chem. Soc.*, 135(28):10218–10221, 2013.

[59] Mickael L Perrin, Riccardo Frisenda, Max Koole, Johannes S Seldenthuis, GilJose A Celis, Hennie Valkenier, Jan C Hummelen, Nicolas Renaud, Ferdinand C Grozema, Joseph M Thijssen, Diana Dulić, and van der ZantHerre S J. Large negative differential conductance in single-molecule break junctions. *Nat. Nanotech.*, 9(10):830–834, 2014.

[60] Markus Gantenbein, Lin Wang, Alaa A Al-jobory, Ali K Ismael, Colin J Lambert, and Martin R Bryce. Quantum interference and heteroaromaticity of para- and meta-linked bridged biphenyl units in single molecular conductance measurements. *Sci. Rep.*, 7:1794, 2017.

[61] Cheng-Yu Kuo, Wanyi Nie, Hsinhan Tsai, Hung-Ju Yen, Adytia D Mohite, Gautam Gupta, Andrew M Dattelbaum, Darrick J William, Kitty C Cha, Yang Yang, Leeyih Wang, and Hsing-Lin Wang. Structural design of benzo[1,2-b:4,5-b']dithiophene-based 2d conjugated polymers with bithienyl and terthienyl substituents toward photovoltaic applications. *Macromolecules*, 47(3):1008–1020, 2014.

[62] Ralph Rieger, Dirk Beckmann, Alexey Mavrinskiy, Marcel Kastler, and Klaus Müllen. Backbone curvature in polythiophenes. *Chem. Mater.*, 22(18):5314–5318, 2010.

[63] Zi-Fa Shi, Le-Jia Wang, Hong Wang, Xiao-Ping Cao, and Hao-Li Zhang. Synthesis of oligo(phenylene ethynylene)s with dendrimer "shells" for molecular electronics. *Org. Lett.*, 9(4):595–598, 2007.

[64] Elisabeth H van Dijk, Daniel J T Myles, Marleen H van der Veen, and Jan C Hummelen. Synthesis and properties of an anthraquinone-based redox switch for molecular electronics. *Org. Lett.*, 8(11):2333–2336, 2006.

[65] Thomas C Pijper, Jort Robertus, Wesley R Browne, and Ben L Feringa. Mild ti-mediated transformation of t-butyl thio-ethers into thio-acetates. *Org. Biomol. Chem.*, 13(1):265–268, 2015.

[66] Emily A Weiss, George K Kaufman, Jennah K Kriebel, Zhefeng Li, Richard Schalek, and George M Whitesides. Si/SiO2-templated formation of ultraflat metal surfaces on glass, polymer, and solder supports: Their use as substrates for self-assembled monolayers. *Langmuir*, 23(19):9686–9694, 2007.

[67] Marco Carlotti, Maarten Degen, Yanxi Zhang, and Ryan C Chiechi. Pronounced environmental effects on injection currents in egain tunneling junctions comprising self-assembled monolayers. *J. Phys. Chem. C*, 120(36):20437–20445, 2016.

[68] A Nefedov and C Wöll. Advanced applications of nexafs spectroscopy for functionalized surfaces. *Surface Science Techniques*, 2013.

[69] D. Briggs, C. D. Wanger, W. M. Riggs, L. E. Davis, J. F. Moulder, and G. E.Muilenberg. *Handbook of X-Ray Photoelectron Spectroscopy*, volume 3. Heyden & Son Ltd., Perkin-Elmer Corp., Physical Electronics Division, Eden Prairie, Minnesota, USA, 1981.

[70] J. Thome, M. Himmelhaus, M. Zharnikov, and M. Grunze. Increased lateral density in alkanethiolate films on gold by mercury adsorption. *Langmuir*, 14(26):7435–7449, 1998.

[71] Buddy D. Ratner and David G. Castner. Electron spectroscopy for chemical analysis. In *Surface Analysis - The Principal Techniques*, pages 47–112. John Wiley & Sons, Ltd, 1997.

[72] Christine L. A. Lamont and John Wilkes. Attenuation length of electrons in self-assembled monolayers of n-alkanethiols on gold. *Langmuir*, 15(6):2037–2042, 1999.

[73] Tarek Abu-Husein, Swen Schuster, David A Egger, Martin Kind, Tobias Santowski, Adrian Wiesner, Ryan C Chiechi, Egbert Zojer, Andreas Terfort, and Michael Zharnikov. The effects of embedded dipoles in aromatic self-assembled monolayers. *Adv. Funct. Mater.*, 25(25):3943–3957, 2015.

[74] Frank Schreiber. Structure and growth of self-assembling monolayers. *Prog. Surf. Sci.*, 65(5–8):151–257, 2000.

[75] Joachim Stohr. *NEXAFS Spectroscopy*. Springer-Verlag Berlin Heidelberg, 1992.

[76] P. E. Batson. Carbon 1s near-edge-absorption fine structure in graphite. *Phys. Rev. B*, 48(4):2608–2610, 1993.

[77] Joshua J Stapleton, Philipp Harder, Thomas A Daniel, Michael D Reinard, Yuxing Yao, David W Price, James M Tour, and David L Allara. Self-assembled oligo(phenylene-ethynylene) molecular electronic switch monolayers on gold: structures and chemical stability. *Langmuir*, 19(20):8245–8255, 2003.

[78] Daniel Nilsson, Somsakul Watcharinyanon, Mattias Eng, Liqian Li, Ellen Moons, Lars S O Johansson, Michael Zharnikov, Andrey Shaporenko, Bo Albinsson, and Jerker Må rtensson. Characterization of self-assembled monolayers of oligo(phenyleneethynylene) derivatives of varying shapes on gold: effect of laterally extended π-systems. *Langmuir*, 23(11):6170–6181, 2007.

[79] Hicham Hamoudi, Ping Kao, Alexei Nefedov, David L Allara, and Michael Zharnikov. X-ray spectroscopy characterization of self-assembled monolayers of nitrile-substituted oligo(phenylene ethynylene)s with variable chain length. *Beilstein J. Nanotechnol.*, 3:12–24, 2012.

[80] S Frey, V Stadler, K Heister, W Eck, M Zharnikov, M Grunze, B Zeysing, and A Terfort. Structure of thioaromatic self-assembled monolayers on gold and silver. *Langmuir*, 17(8):2408–2415, 2001.

[81] Michael Zharnikov. High-resolution x-ray photoelectron spectroscopy in studies of self-assembled organic monolayers. *J. Electron Spectrosc. Relat. Phenom.*, 178–179: 380–393, 2010.

[82] E O Sako, H Kondoh, I Nakai, A Nambu, T Nakamura, and T Ohta. Reactive adsorption of thiophene on au(111) from solution. *Chem. Phys. Lett.*, 413(4-6):267–271, 2005.

[83] Y. Tai, A. Shaporenko, H.-T. Rong, M. Buck, W. Eck, M. Grunze, and M. Zharnikov. Fabrication of thiol-terminated surfaces using aromatic self-assembled monolayers. *J. Phys. Chem. B*, 108(43):16806–16810, 2004.

[84] K Heister, S Frey, A Ulman, M Grunze, and M Zharnikov. Irradiation sensitivity of self-assembled monolayers with an introduced "weak link". *Langmuir*, 20(4):1222–1227, 2004.

[85] A Shaporenko, K Adlkofer, LSO Johansson, and M Tanaka. Functionalization of gaas surfaces with aromatic self-assembled monolayers: A synchrotron-based spectroscopic study. *Langmuir*, 2003.

[86] F. Neese. The orca program system. *Wiley Interdiscip. Rev.: Comput. Mol. Sci.*, 2(2): 73–78, 2012.

[87] Frank Neese. Software update: the orca program system, version 4.0. *Wiley Interdisciplinary Reviews: Computational Molecular Science*. ISSN 1759-0884.

[88] Carmen Herrmann, Lynn Gross, Torben Steenbock, Michael Deffner, Bodo Alexander Voigt, and Gemma C. Solomon. Artaios - a transport code for post-processing quantum chemical electronic structure calculations, available from https://www.chemie.uni-hamburg.de/ac/herrmann/software/index.html, 2016.

[89] Carmen Herrmann, Gemma C. Solomon, Joseph E. Subotnik, Vladimiro Mujica, and Mark A. Ratner. Ghost transmission: How large basis sets can make electron transport calculations worse. *J. Chem. Phys.*, 132(2):024103, 2010.

[90] Florian Weigend and Reinhart Ahlrichs. Balanced basis sets of split valence{,} triple zeta valence and quadruple zeta valence quality for h to rn: Design and assessment of accuracy. *Phys. Chem. Chem. Phys.*, 7(18):3297–3305, 2005.

[91] J.H. Fishman and M. Yarish. Gold-palladium electrocatalysts. *Electrochim. Acta*, 12 (5):579–581, 1967.

[92] Hendrik Schlicke and Carmen Herrmann. Controlling molecular conductance: Switching off π sites through protonation. *ChemPhysChem*, 15(18):4011–4018, 2014.

[93] Ante Bilić, Jeffrey R. Reimers, and Noel S. Hush. The structure, energetics, and nature of the chemical bonding of phenylthiol adsorbed on the au(111) surface: Implications for density-functional calculations of molecular-electronic conduction. *J. Chem. Phys.*, 122(9):094708, 2005.

[94] Nisachol Nerngchamnong, Li Yuan, Dong-Chen Qi, Jiang Li, Damien Thompson, and Christian a Nijhuis. The role of van der waals forces in the performance of molecular diodes. *Nat. Nanotechnol.*, 8(2):113–118, 2013.

[95] Orlando M. Cabarcos, Swen Schuster, Iris Hehn, Peng Peng Zhang, Masato M. Maitani, Nichole Sullivan, Jean-Benoit Giguère, Jean-François Morin, Paul S. Weiss, Egbert Zojer, Michael Zharnikov, and David L. Allara. Effects of embedded dipole layers on electrostatic properties of alkanethiolate self-assembled monolayers. *The Journal of Physical Chemistry C*, 121(29):15815–15830, 2017.

[96] Andrii Kovalchuk, Tarek Abu-Husein, Davide Fracasso, David A. Egger, Egbert Zojer, Michael Zharnikov, Andreas Terfort, and Ryan C. Chiechi. Transition voltages respond to synthetic reorientation of embedded dipoles in self-assembled monolayers. *Chem. Sci.*, 7:781–787, 2016.

[97] Tarek Abu-Husein, Swen Schuster, David A. Egger, Martin Kind, Tobias Santowski, Adrian Wiesner, Ryan Chiechi, Egbert Zojer, Andreas Terfort, and Michael Zharnikov. The effects of embedded dipoles in aromatic self-assembled monolayers. *Advanced Functional Materials*, 25(25):3943–3957, 2015.

4

THE FABRICATION OF MOLECULAR JUNCTIONS USING NANOSKIVING

Abstract: *Nanoskiving, a form of edge lithography, is a powerful tool to fabricate ultra-thin objects in size of the nanometer. In this chapter, we demonstrate our approaches in the fabrication of molecular junctions and gating them. Further, we discuss the remaining challenges.*
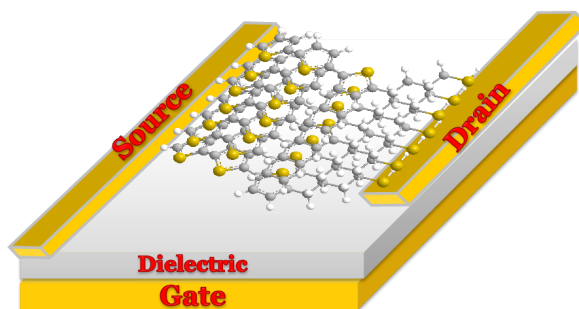
4.1. INTRODUCTION

Nowadays we are looking for the balance between performance and cost in all aspects of the semiconducting silicon technology, which provides numerous opportunities for molecular electronics (ME), with the goal of embedding the molecules into circuits as electronic components.[1] The panoply of molecular structure makes it possible to modulate charge transport by rational organic synthesis. In ME, we investigate charge transport through molecules bound between two electrodes and are developing these molecular junctions with various functions, such as diodes[2, 3], thermoelectrics[4], and switches[5].

Self-assembled monolayers (SAMs) based large-area molecular junctions, the bottom-up approach, are promising for the fabrication of solid-state devices. However, most techniques are limited to the vertical configuration of two terminals (electrodes), like EGaIn, CP-AFM or graphene-based top contacts. The transistors comprise three terminals, including the source, drain and gate electrodes. It is technically difficult to apply a third electrode to gate molecular junctions in a vertical, two-terminal geometry. Nanoskiving is an unconventional approach to nanofabrication able to produce structures on the order of tens of nanometers.[6–8] SAM-templated Addressable Nanogaps (STANs), fabricated by nanoskiving, are two-terminal molecular junctions in a parallel configuration in which the molecules are parallel to an inert substrate.[5, 9] It is relatively easy to gate molecules in STAN electrodes by placing an ionic liquid on top of the junction or transferring the STANs on a silicon wafer with a layer of SiO_2. Making molecular transistors using nanoskiving is the motivation of the work described in this chapter.

4.2. METHOD / EXPERIMENTAL / FABRICATION
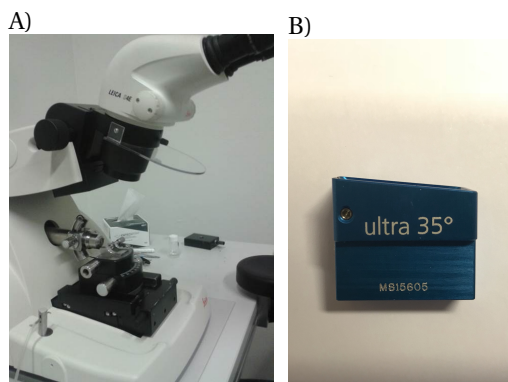
Figure 4.1 The tools for nanoskiving: A) The ultramicrotome. B) The diamond knife (4 mm Diatome Ultra 35°).

We used two types of polymer resins as the embedding materials: 1) The commercial, thermoset epoxy resin Epofix, purchased from Electron Microscopy Sciences and designed for microtome sectioning. The curing process takes three hours at 60 °C. 2) A thiolene resin of our own design. Figure 4.2 shows the chemical structures of the monomers, PETMP, TATATO and the initiator. This material is cured via photopolymer-

ization using a UV lamp for 200 s.

| Pentaerythritol tetrakis(3-mercaptopropionate) **PETMP** | Triallyl-1,3,5-triazine-2,4,6-trione **TATATO** | 2,2-Dimethoxy-2-phenylacetophenone (Light Initiator) |
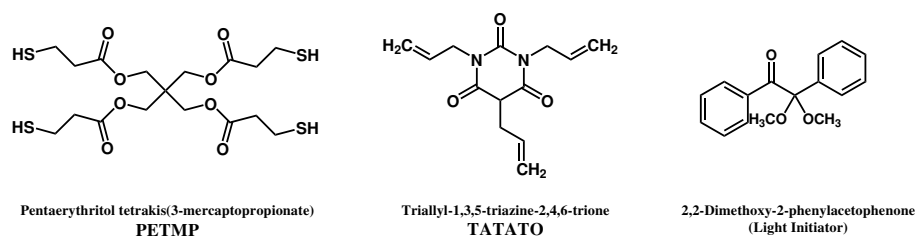
Figure 4.2 The chemical structures of the thiolene monomers: PETMP, TATATO and the initiator.

To form STANs, SAMs must be grown in the presence of the embedding resin. Thus, we tested the tolerance of the polymer resins in toluene and THF, two common solvents for π-conjugated molecular wire-like compounds. We first cured the epoxy and the thiolene (with different weight ratios of PETMP/TATATO for the latter) and immersed them in toluene or THF. We then checked the hardness after 30 minutes, 2 or 3 hours and overnight. The results are shown in Figure 4.3. We found that toluene has almost no impact on both the epoxy and the thiolene, overnight. The thiolene with a weight ratio of 3:4 of PETMP/TATATO was damaged by THF after 30 mins and completely disintegrated overnight. The thiolene with the weight ratio of 3:2 and 1:1 became softer after 2 hours, while the epoxy was apparently ok in THF. All polymer resins, however, were severely damaged after overnight contact with THF.

The properties of two embedding polymer resins, epoxy and the thiolene, are summarized in Table 4.1. The hardness of the resins and their adhesion to metal will affect the quality of the nanoskived sections. We discuss these issues in more detail in the discussion of STANs below.

Table 4.1 A summary that compares the properties of two embedding polymer resins: the epoxy and the thiolene.

Material	Epoxy	Thiolene
Curing Method	Heat	UV
Curing Speed	Slow (3 h)	Quick (100 s)
Hardness	Hard	Soft
Sectioning	Easy	Difficult
Binding to Au	Poor (Delamination)	Good (No Delamination)

The sectioning process of nanoskiving is shown in Figure 4.4. We used an ultramicrotome (Figure 4.1A) equipped with a diamond knife (Figure 4.1B) to cut the ultra-thin slabs from a sample block made by a polymer resin containing the embedded structures. Figure 4.4B and C are the 150 nm and 200 nm thick sections floating on top of the water, respectively. The sections with different thicknesses reflect different colors (yellow for 100 nm, purple for 150 nm and blue for 200 nm) due to thin-film interference.

	Toluene			THF		
	30 minutes	3 hours	Overnight	30 minutes	2 hours	Overnight
Epofix					Looks the same as 30 min	
PETMP:TATATO 3:2					Looks the same as 30 min	
PETMP:TATATO 3:3					Looks the same as 30 min	
PETMP:TATATO 3:4						

Figure 4.3 The results of testing the tolerance of the polymer resins in organic solvents with different immersion time.
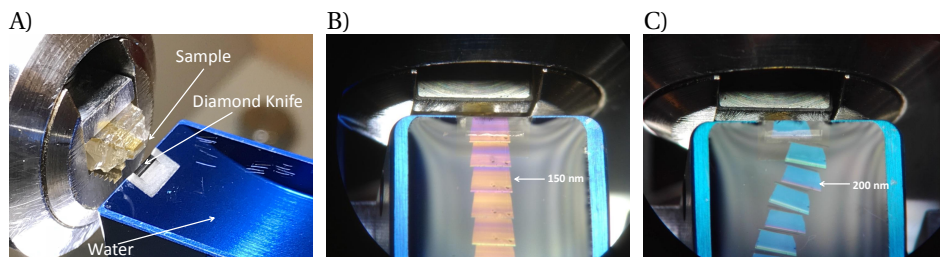
Figure 4.4 A) A side view of the sample chuck, the diamond blade and the water-filled trough. B) A top view of the nanoskived 150 nm thick sections. C) A top view of the nanoskived 200 nm thick sections.

4.3. Au Nanowires (Au NWs)

Gold nanowires (Au NWs; Figure 4.5) are among the simplest nanostructures that can be obtained using nanoskiving. They are transferred to the targeted substrates (usually glass or a Si wafer) using a transfer loop or dipping the substrate into the trough of the diamond knife and lifting it up. Here we discuss the properties of Au NWs prepared by nanoskiving. Figure 4.6A shows representative I/V characteristics of Au NWs, which exhibit ordinarily, ohmic contact. The yield of working Au NWs is 90.9% (30 out of 33). One possible reason for the failure of Au NWs is shown in Figure 4.6B. Scanning electron
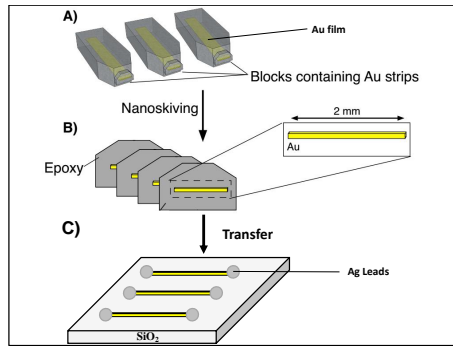
Figure 4.5 A schematic represents the fabrication of the Au nanowires using nanoskiving.[10]

microscopy (SEM) images show a defect in the fabrication process that leads to a discontinuity in the Au NWs. It is common to observe this type of defects in nanoskived structures made from evaporated metallic films. Several possibilities could result in these defects such as pinholes on the deposited film, dust on the silicon wafer or mechanical stress introduced during either the fabrication of sample blocks or nanoskiving.
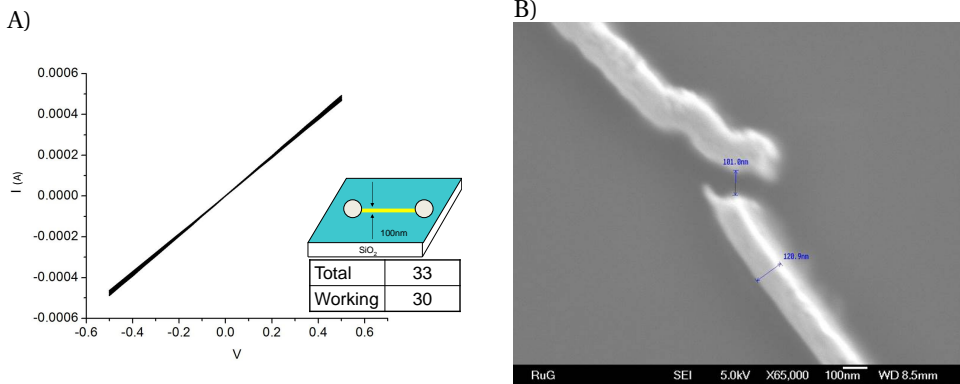
Figure 4.6 A) The I/V characterization of one Au NW. B) The SEM image shows a fracture on one Au NW.

We have found another failure mode of the Au NWs that is due to thermally-assisted electromigration. When applying electric current to a metallic wire, the effects of Joule heating are enhanced by the large surface-area:volume ratio of the NWs, leading to excessive heating. Mobile metal atoms, driven by the electric field, begin to move, particularly at nicks and constrictions. This process is generally described as electromigration. In Figure 4.7, we increased the applied bias on the Au NW until the current decreased dramatically, indicating that the Au NW became discontinuous. The current where the wire broke was 7.8 mA, which was calculated by dividing the potential by the resistance (this experiment was done with Gerard A. Kalkman).

To further investigate the failure of Au NWs, we examed the Au NWs using scanning electron microscopy (SEM). We applied a high potential (10 V) to break the Au NWs.
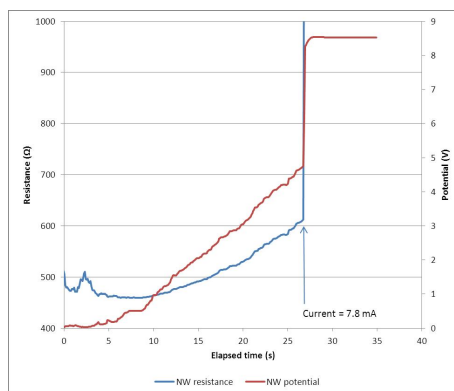
Figure 4.7 The plot of the resistance of a Au NW versus time with increasing the applied potential until the resistance increased dramatically (recorded by Gerard A. Kalkman).

Afterward, we checked with SEM along the Au NWs until we found the failure point. Figure 4.8 shows a failure point of a Au NW with a ~ 10 μm gap.
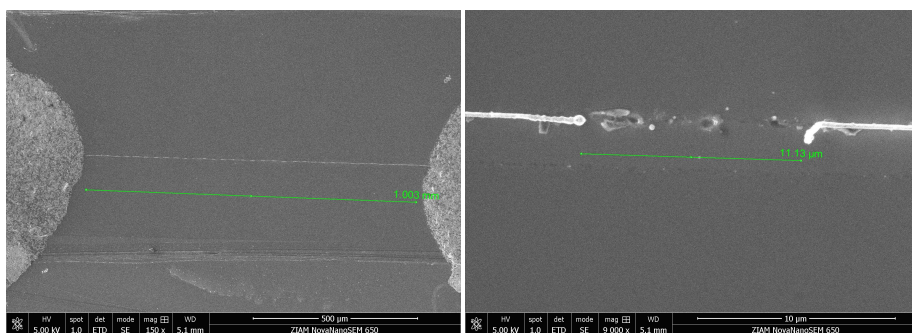
Figure 4.8 The SEM images of the Au NW after applying a high bias (10 V) to break down the conductivity of the Au NW. A big gap (~ 10 μm) was observed (Right).

The Patterned Au Nanowires Besides the conventional fabrication of the rectangular Au NWs, we also seek better ways to pattern the Au NWs in different geometries, such as a "trench-like" Au NWs, of which the central part is thinner than two sides. Figure 4.9 shows the fabrication steps. First, we deposited 100 nm of Au through a stainless steel mask. After this step, we placed an Au wire with a diameter of 250 μm (normally used for STM) in the center of the mask and deposited a second, 100 nm layer of Au. The Au wire in the middle of the mask blocks the evaporated Au resulting in a trench-like patterned Au NW (the middle part of the Au NW, ~100 nm, is thinner than two ends of Au NW, ~200 nm). Figure 4.10 shows the SEM images of the obtained Au NW.
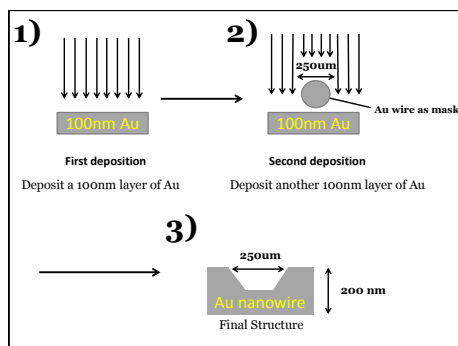
Figure 4.9 The fabrication process of patterned Au nanowires.
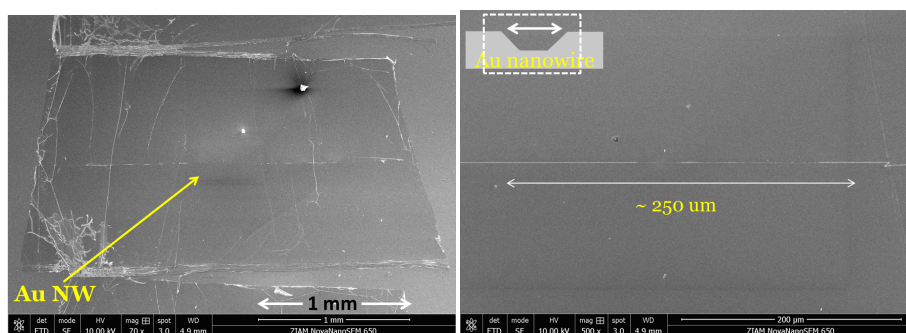
Figure 4.10 The SEM image of one patterned Au nanowire. The central part (~100nm) is thinner than two sides (~200nm).

4.4. SAM-TEMPLATED ADDRESSABLE NANOGAP ELECTRODES (STANs)

In the previous section, we discussed the fabrication of single Au NWs. Here we discuss our efforts to use nanoskiving to construct molecular junctions comprising molecules sandwiched by two electrodes.[1]
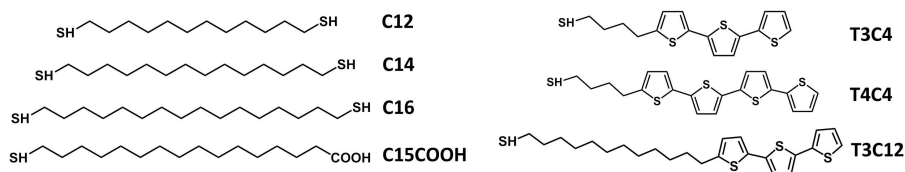
Figure 4.11 The chemical structures of molecules for STANs.

The fabrication of STANs

Figure 4.12A illustrates the steps to fabricate sample blocks containing Au/SAM/Au sandwich structures (*i.e.*, STANs), which was first reported by Pourhossein et al.[5, 9] First, we evaporated 100 nm Au or 200 nm Ag on a Si wafer through a Teflon mask and then we passivated the entire wafer by exposing it to trichloro(1H,1H,2H,2H-perfluorooctyl)silane vapor for one hour inside a desiccator. After that, we covered the entire wafer with a polymer resin (either the thiolene or epoxy). For the epoxy polymer resin, we used ~ 8.5 mL of Epofix (monomer:harder=7.5:1 in volume ratio) and cured it for three hours at 60 °C. And for the thiolene polymer resin, we used a weight-ratio of PETMP:TATATO=3:2 with 0.1 weight % of initiator and cured it under UV light for 200 s. In the next step, we template-stripped the metal layer (Au/Ag) by carefully peeling the polymer resin from the wafer. In this way, we transferred the Au/Ag layer to the cured polymer resin. We passivated the Si wafer after the deposition of metal to keep the metal surface ultra flat. After cleaving the polymer resin from the wafer, we immediately immersed the template-stripped Au/Ag in a 1 mM solution of an alkanedithiol/16-mercaptohexadecanoic acid in ethanol overnight or a 0.5 mM solution of oligothiophene derivatives in toluene for three hours in a closed desiccator purged with nitrogen. We used the SAM as the active layer for molecular junctions; after it formed, we removed the polymer resins from solution and rinsed the samples with ethanol or toluene and dried them with nitrogen. We placed the Teflon mask back on the polymer substrates with a lateral offset of ~ 80% of the Au/Ag strips and deposited the second layer of metal, for example, 100 nm Au or 200 nm Ag. After evaporating the second electrode, we covered the polymer resin substrate with the same material and cured it. In the final step, we cut out the individual strips of metal/SAM/metal with a jeweler's saw and placed them into the wells in an embedding mold (purchased from Electron Microscopy Sciences) for microtomy, topped it off with uncured polymer resin and cured them again to complete the sample blocks (the final step of Figure 4.12 shows the completed sample block). The chemical structures used to form the gap in STANs are shown in Figure 4.11.
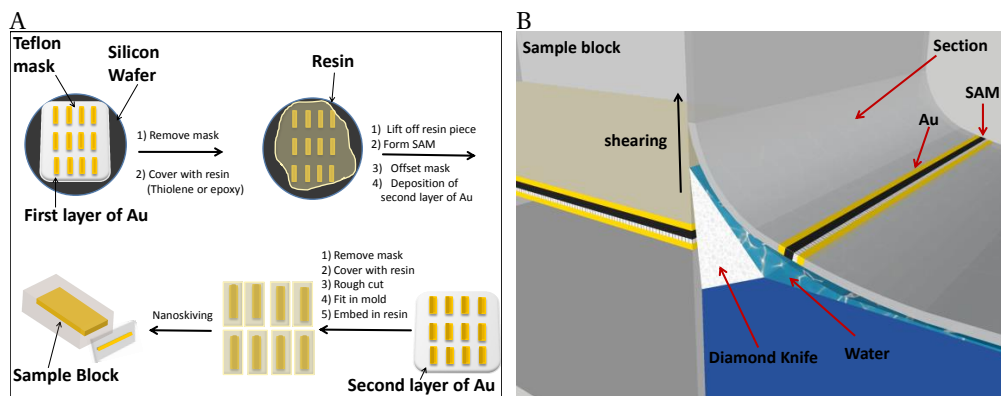
Figure 4.12 A) A schematic shows the fabrication steps of the sample blocks. B) A schematic represents the process of nanoskiving. (By H. H. Mellema)

The sectioning process The sectioning process is shown in Figure 4.4. After fabricat-
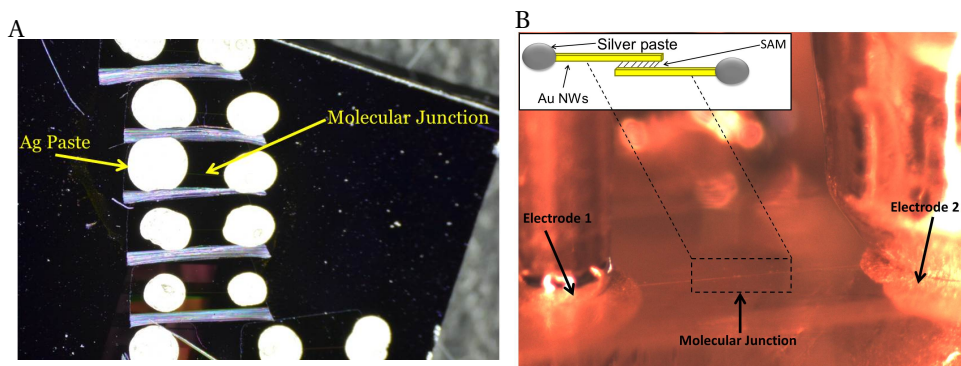
Figure 4.13 A) The transferred sections on the Si wafer with Ag paste at the ends. B) The image of I/V characterization of a STAN with two probes.

ing the sample blocks, we used a saw to chop part of the block away to expose one side of the embedded structures. We then mounted the blocks, one at a time, in the sample holder of the microtome. Before sectioning, we trimmed the block into a trapezoid shape commensurate with the width of the diamond knife (4 mm Diatome Ultra 35°). The trapezoid shape makes the sectioning stable and reduces the mechanical stress on the block. Before sectioning with the diamond knife, we used a glass knife to rough cut the block to get a smooth surface, which can reduce the damage to the diamond knife and extend its operational lifetime. We then placed a diamond knife in a Petri dish filled with water for at least 10 min to wet the face of the knife. To produce the final sections, we replaced the glass knife with the wet diamond knife, cleaned the edge with a polystyrene block soaked in ethanol and aligned the edge of diamond knife parallel to the bottom side of the block. We sectioned the block in the speed of either 100 nm at 1 mm/s or 200 nm at 1.2 mm/s. The schematic in Figure 4.12B shows the process of sectioning a polymer block with a diamond knife.[11] The fresh-cut sections were transferred to glass or a Si wafer using a loop or by placing substrate under the water and lifting it. We dried the sections at 60 °C in the oven for 15 mins to remove all traces of liquid water and promote adhesion to the substrate. For electrical measurements, we applied silver paste at two ends of STANs. Figure 4.13A is the image of the transferred sections on the Si wafer with Ag paste at the ends, under an optical microscope. To measure tunneling currents through the molecular junctions, we applied probes on the Ag paste at the ends of STANs, scanned the voltage and recorded the current. Figure 4.13B is an image of STANs with two probes for I/V characterization.

CHARACTERIZATION OF STANs

We characterized STANs in two ways: 1) electrical measurements. 2) Scanning Electron Microscopy (SEM). We discussed the epoxy and thiolene resin separately.

The epoxy resin We measured "non-contact" I/V traces for most STANs, which were characterized by non-ohmic, unstable current in the pA regime. To examine the quality of the nanoskived STAN electrodes, we imaged them at high magnification using a SEM. We observed the gaps defined by SAMs of alkanedithiol in STANs which are shown in
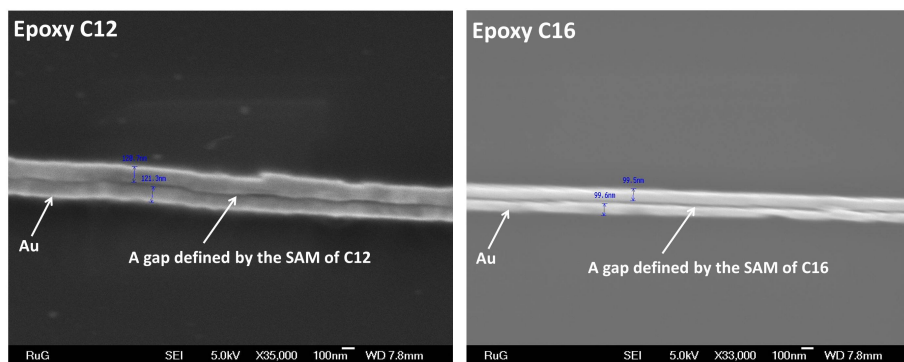
Figure 4.14 Left: The SEM image of STANs using C12dithiol. Right: The SEM image of STANs using C16dithiol.

Figure 4.14. The width of Au electrodes is approximately 100 nm, which is the same as the thickness of deposited Au film. However, we found a general issue that the delamination between Au and the epoxy occurred everywhere, as shown in Figure 4.15, indicating that the binding between Au and the epoxy is poor. The delaminated epoxy tears STANs, which breaks the Au electrodes and leads to non-contact traces in I/V measurements. We think this is the primary failure of STANs embedded in the epoxy resin.
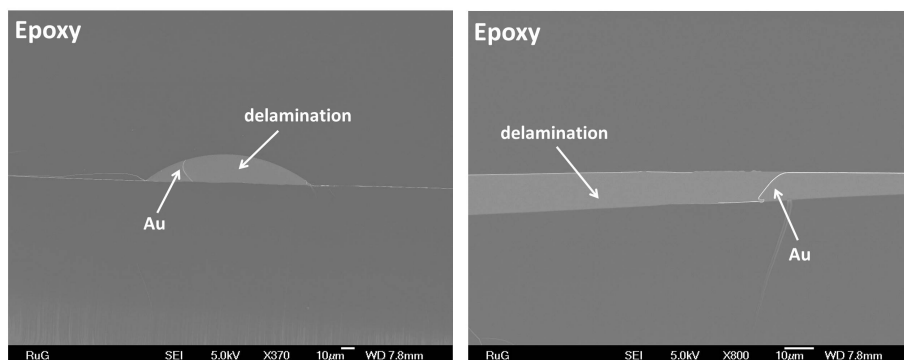
Figure 4.15 The SEM images show the delaminated region in an epoxy slab containing Au electrodes.

Besides the delamination issues, we also observed fractures on Au electrodes of STANs (Figure 4.16 Left), which have been found in Au NWs before. There are two possibilities for the fractures: 1) the pinholes on Au film deposition. 2) Mechanical stress during template-stripping that introduces cracks in deposited Au film. Moreover, we observed that there were the wrinkles on sections that developed while transferring the sections from water to the substrates and during the subsequent drying, which broke STANs (Figure 4.16 Right).

It is also possible that nicks in the edge of the diamond knife could damage the sections. Figure 4.17 shows exemplary images of damaged sections. The leading edge of the diamond knife is nearly atomically sharp as-received, but nicks develop from nor-
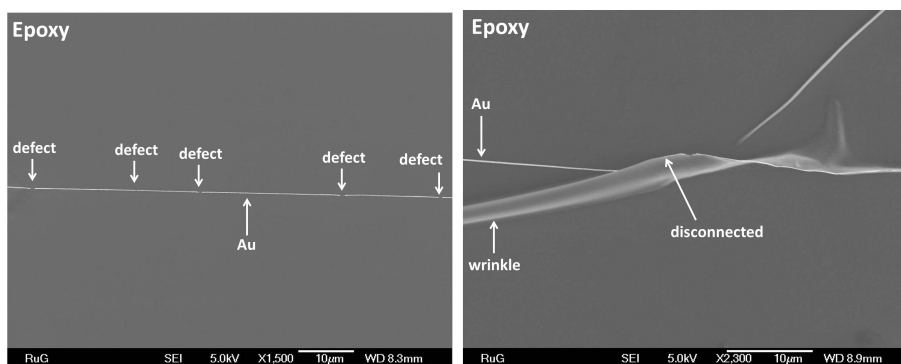
Figure 4.16 Left: The SEM image shows the multiple defects in the Au electrodes. Right: The SEM image shows the wrinkle introduced by the drying process of the section.

mal wear-and-tear and, in particular, from improper handling or sectioning of very hard materials. It is difficult to resolve the nicks directly under an optical microscope. However, their presence is apparent in the cut sections. A nick on the diamond knife scars the entire section (from bottom to top) during nanoskiving and scratches or nicks the embedded metallic structures. We could easily observe this damage, which appears in optical micrographs as white lines parallel to the cutting direction (which is perpendicular to the Au electrodes) on the sections during nanoskiving or after drying of sections. In Figure 4.17 left, we observed a trace on the section from the nick, which tore the epoxy section. Further, we zoomed in the region of the Au electrode (Figure 4.17 right) to check if the Au electrode was damaged, which is clearly the case.
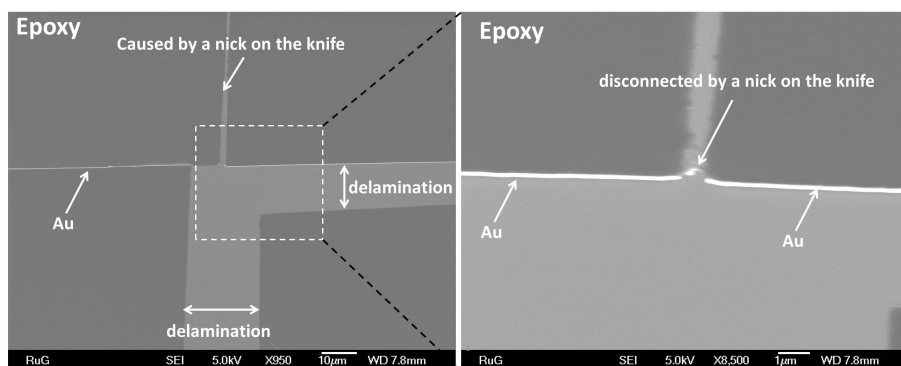
Figure 4.17 The SEM images show the damages on the epoxy caused by the nicks on the diamond knife.

The thiolene resin We switched to the thiolene resin as the embedding material for nanoskiving due to the binding/delamination issue of the epoxy. The thiolene resin binds more strongly to Au because it contains free thiol groups (Figure 4.2.) Indeed, there was no delamination apparent during fabrication. Thus, by using the thiolene resin, we were able to overcome the delamination issue. Figure 4.18 and 4.19 are the SEM images

of STANs prepared from alkanes (C12dithiol and C16dithol) and oligothiophene (T3C4 and T4C4). We observed gaps between the Au NWs that are approximately the size of the thickness of the SAMs. For STANs fabricated from C15COOH and T3C12, we observed a large separation between the two Au NWs (from hundreds of nanometers to micrometers) in Figure 4.20. The separation indicates that the adhesion of the two Au layers is poor, which means the functional groups—carboxylic acid and thiophene—may block the penetration of Au atoms during the deposition of Au, but fail to form a stable interface.
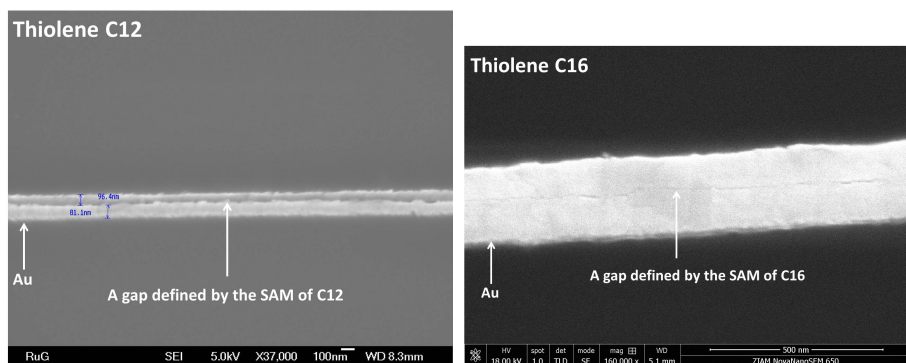
Figure 4.18 Left: The SEM image shows the gap of STANs formed using C12dithiol in thiolene. Right: The SEM image shows the gap of STANs formed using C16dithiol in thiolene.
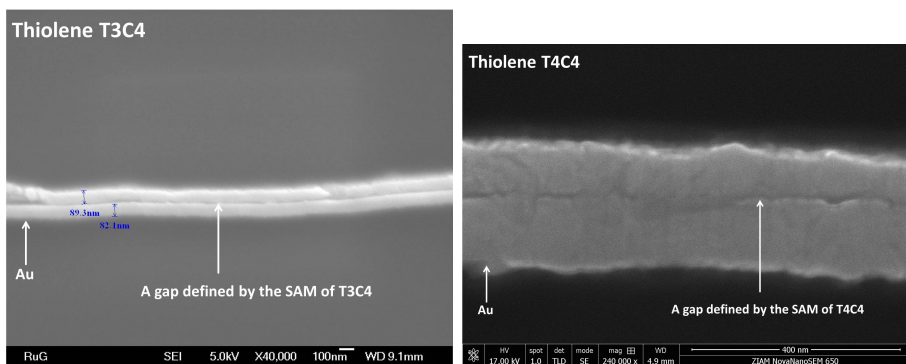
Figure 4.19 Left: The SEM image shows the gap of STANs formed using T3C4 in thiolene. Right: The SEM image shows the gap of STANs formed using T4C4 in thiolene.

So far we have been unable to fabricate working molecular junctions from STANs. They either shorted or showed non-contact. Several factors resulted in the failure of STANs in the thiolene resin. First, we observed the same fractures on the Au electrodes in the thiolene resin as in the epoxy, shown in Figure 4.21. These fractures interrupt the contact of the Au electrodes. We were eventually able to image the STANs and NWs with a modern SEM with improved resolution. We observed many nanoscopic fractures in the
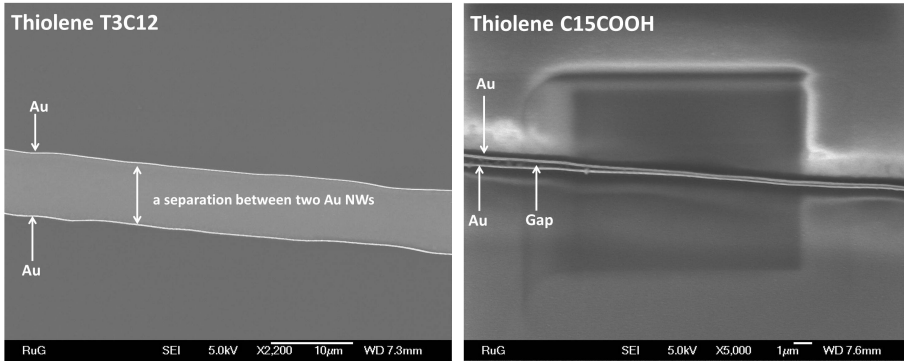
Figure 4.20 Left: The SEM image shows the gap of STANs formed using T3C12 in thiolene. Right: The SEM image shows the gap of STANs formed using C15COOH in thiolene.

whole top Au electrode (Figure 4.22), indicating that the second deposition of Au electrode was perturbed, possibly due to outgassing of the thiolene resin. We also found that microscopic air bubbles trapped during the curing of the resin broke nearby NWs (Figure 4.23). Air is trapped while mixing the monomers, but apparently enough remains after degassing to rupture the NWs in ultra-high vacuum during metal deposition. Moreover, the nicks on the diamond knife could damage STANs as well. In Figure 4.24, we observed the traces on the thiolene which was caused by the nick on the diamond knife.
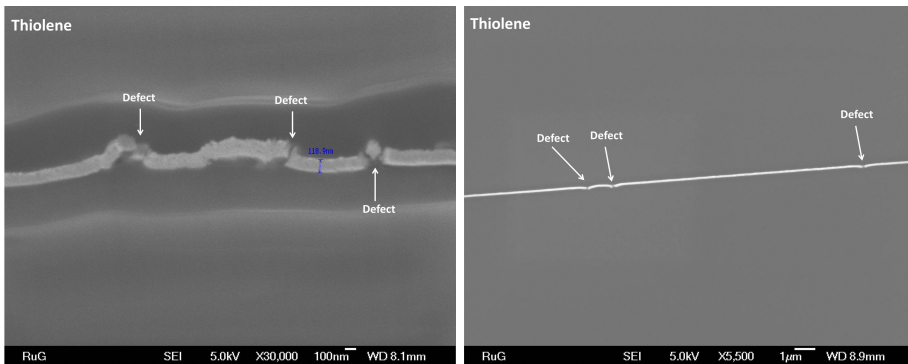
Figure 4.21 The SEM images show the fractures of the Au electrodes in the thiolene resin.

4.5. Reduced Graphene Oxide (rGO) defined sub-10 nm Nanogaps

In addition to using SAMs to fabricate nanogap devices, we also tried to manufacture the sub-10 nm nanogaps defined by the reduced graphene oxide (rGO). The rGO films were prepared in University of Copenhagen following reported methods.[12] Figure 4.25 left shows the rGO suspension, prepared from graphite. We spin-coated the rGO on the

117
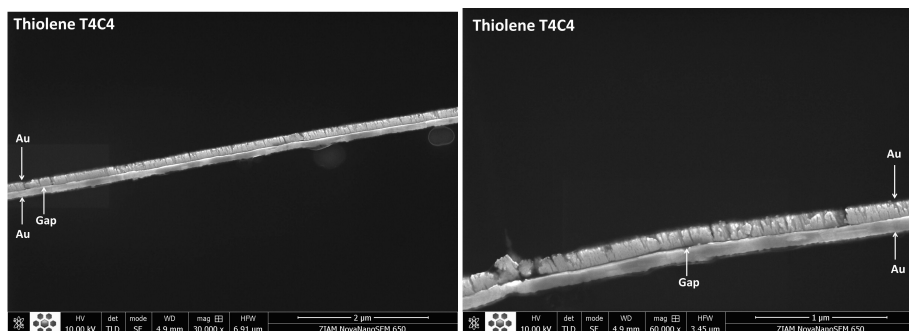
Figure 4.22 The SEM images show the fractures on the top Au electrode of STANs of T4C4.
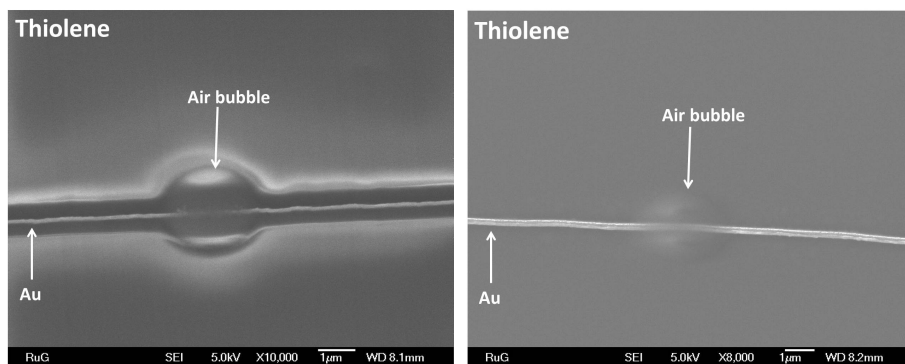
Figure 4.23 The SEM images show the air bubbles trapped inside the thiolene resin that destroyed the Au electrodes.
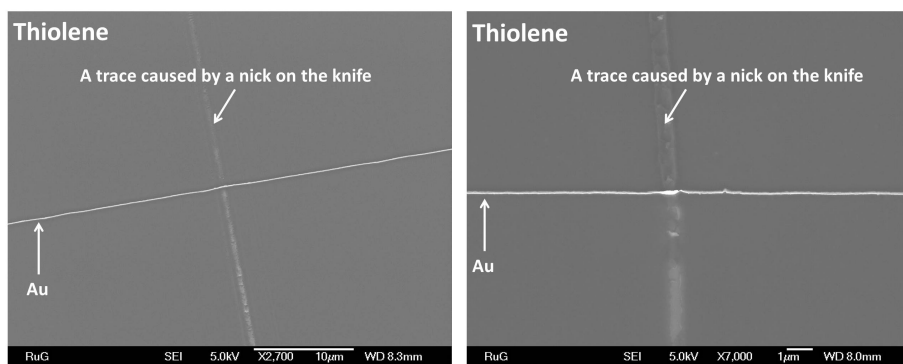
Figure 4.24 The SEM images show the traces on the sections of the thiolene caused by the nicks on the diamond knife.

glass slide, annealed overnight under N_2 and then released the film of rGO on the water (Figure 4.25). We then placed the substrate (the epoxy resin) under the water and raised
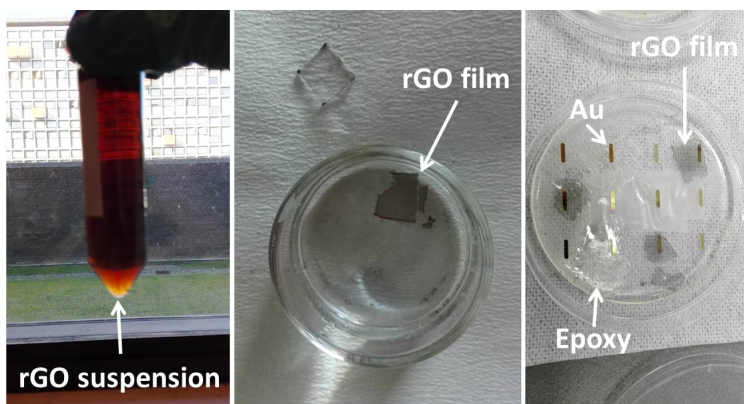
Figure 4.25 Left: The picture of the rGO suspension in the mixture solvent of $H_2O/MeOH$. Middle: The picture shows that a rGO film was floating on the water. Right: The picture shows that the rGO films were transferred to the bottom layer of Au electrodes.

it carefully to transfer rGO to the Au strips on the resin shown in Figure 4.25 right. Afterwards, we evaporated the top Au electrodes and finished the samples as the steps for STANs.
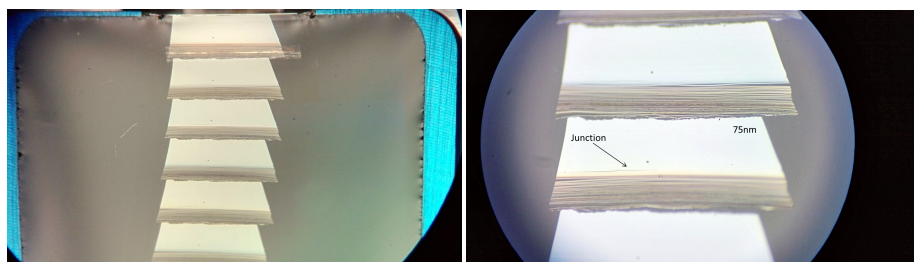
Figure 4.26 The photos show the nanoskived 100 nm thick sections embedding with Au-rGO-Au structures.

We nanoskived the sections with a thickness of 100 nm. As shown in Figure 4.26, the sections look nice. We didn't observe any nicks under the optical microscope. We characterized the rGO-defined gap using SEM and atomic force microscopy (AFM). Both the SEM images (Figure 4.27) and the AFM images (Figure 4.28) show a clear ~10nm rGO gap sandwiched by two Au electrodes.

In the next step, we tried to gate the rGO layer using an ionic liquid; we built three-terminal transistors, as shown in Figure 4.29. One Au electrode acts as the source in the transistor, and the other is the drain. We applied Ag paste on one end of both two Au electrodes for the probe contacts in the electrical measurements. We placed ionic liquid on the top of the Au-rGO-Au junctions as the gate dielectric and used an Au wire as the gate electrode to complete the devices.

We characterized the gating effect of the rGO transistors using a three-probe station controlled by semiconductor characterization system (KEITHLEY 4200-SCS). We placed
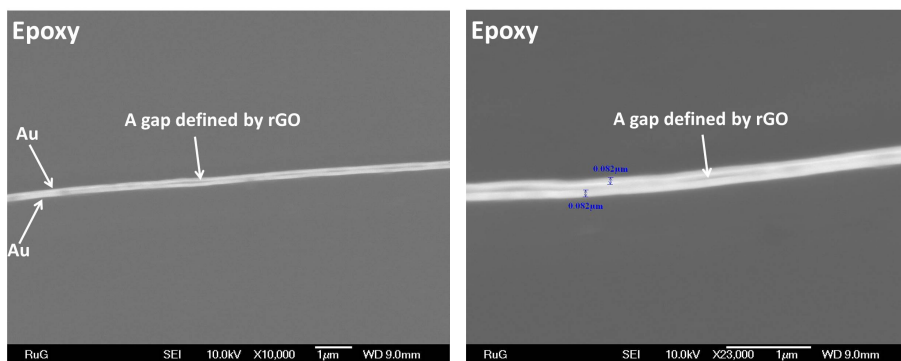
Figure 4.27 The SEM images show the rGO defined gap between two gold electrodes.
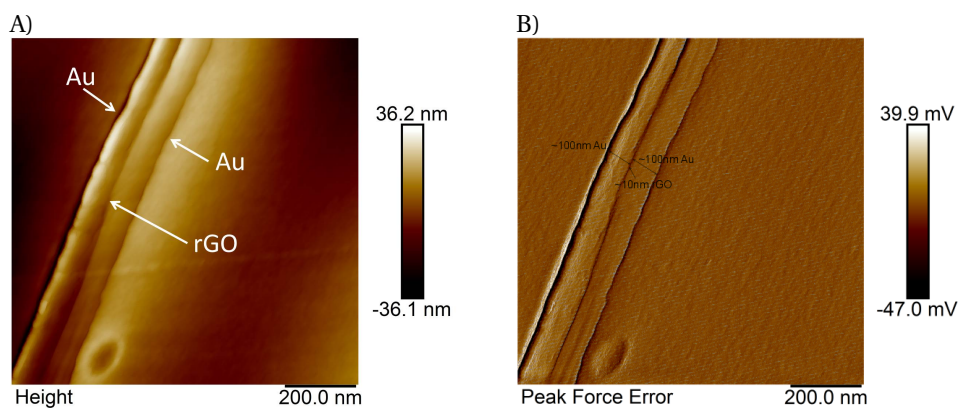
Figure 4.28 A) The AFM height map of rGO sandwiched by two Au electrodes. B) The AFM peakforce error map of rGO sandwiched by two Au electrodes. (ScanAsyst-Air mode, performed by Xinkai Qiu)

the devices inside a cryo-chamber, and measured them in the vacuum at −55 °C. We characterized the devices at low temperature to avoid gate-leakage current (the current from the source electrode to the gate electrode). Figure 4.30A shows the output curve of one working device. We applied 5 steps of gate voltage from 0 V to −10.0 V, each step was −2.5 V to the device. And we scanned the drain voltage from −10.0 V to 10.0 V at each gate voltage. The drain current increased with increasing gate voltage. We also collected the transfer curve, which is shown in Figure 4.30B. In the transfer curve, we fixed the drain voltage to −2.0 V and scanned the gate voltage from −8.0 V to 8.0 V. The on-off ratio was about 4 (The highest drain current (4nA) divided by the lowest drain current (1nA)). In this working device, we observed a weak gating effect on the rGO transistor. So far we only characterized one working device. The low yield is due to the same delamination and defect issues that we discussed above for the epoxy resin.

120
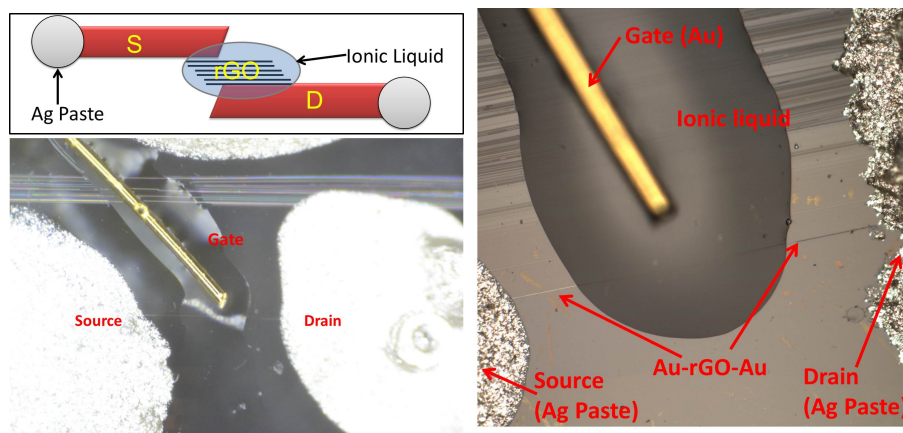
Figure 4.29 The optical images of a ionic liquid gated rGO transistor. The schematic on the left top represents the geometry of the device.

A)

B)
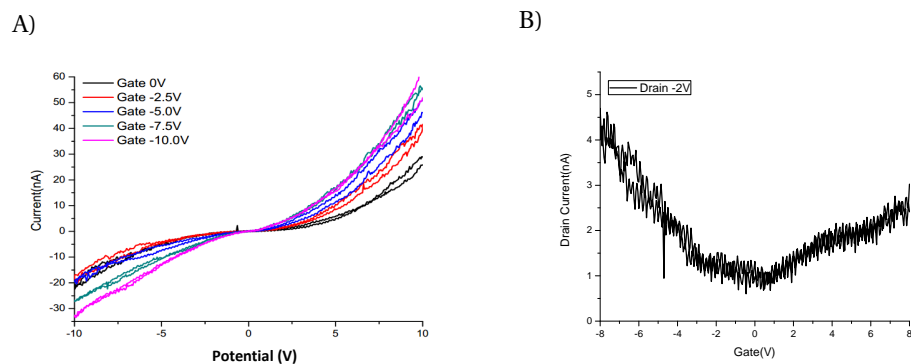
Figure 4.30 A) The output curve of a IL gated sub-10 nm rGO device. B) The transfer curve of a IL gated sub-10 nm rGO device.

4.6. CONCLUSION

In this chapter, we set out to fabricate gaps on the order of single nanometers, defined by either SAMs or rGO using nanoskiving. We characterized the nanoskived sections using I/V measurements and SEM. The SEM results show that the gaps were fabricated successfully using both SAMs and rGO. However, there are remaining challenges in making working molecular junctions, getting electrical contact and improving the yield. Overall, it is more difficult than we expected. Several factors lead to the failure of STANs, like the fractures on Au electrodes, delamination between Au and the epoxy resin and nicks on the diamond knife. Going forward great care must be taken in each step of the fabrication, including the metal deposition, the formation of SAMs, the curing of polymer resins, nanoskiving and the handling of the sections. Once we overcome these difficulties, it will be possible to gate molecular junctions prepared by nanoskiving, as

we demonstrated using rGO.

BIBLIOGRAPHY

[1] Yanxi Zhang, Zhiyuan Zhao, Davide Fracasso, and Ryan C. Chiechi. Bottom-up molecular tunneling junctions formed by self-assembly. *Is. J. Chem.*, 54(5-6):513–533, 2014.

[2] Brian Capozzi, Jianlong Xia, Olgun Adak, Emma J Dell, Zhen-Fei Liu, Jeffrey C Taylor, Jeffrey B Neaton, Luis M Campos, and Latha Venkataraman. Single-molecule diodes with high rectification ratios through environmental control. *Nat. Nanotechnol.*, 10(6):522–527, 2015.

[3] Xiaoping Chen, Max Roemer, Li Yuan, Wei Du, Damien Thompson, Enrique del Barco, and Christian A Nijhuis. Molecular diodes with rectification ratios exceeding 105 driven by electrostatic interactions. *Nat. Nanotechnol.*, 12:797, 2017.

[4] Nico Mosso, Ute Drechsler, Fabian Menges, Peter Nirmalraj, Siegfried Karg, Heike Riel, and Bernd Gotsmann. Heat transport through atomic contacts. *Nat. Nanotechnol.*, 12:430, 2017.

[5] Parisa Pourhossein, Ratheesh K Vijayaraghavan, Stefan C J Meskers, and Ryan C Chiechi. Optical modulation of nano-gap tunnelling junctions comprising self-assembled monolayers of hemicyanine dyes. *Nature Communications*, 7:11749, 2016.

[6] Qiaobing Xu, Robert M Rioux, Michael D Dickey, and George M Whitesides. Nanoskiving: a new method to produce arrays of nanostructures. *Accounts of chemical research*, 41(12):1566–77, 2008.

[7] Darren J Lipomi, Filip Ilievski, Benjamin J Wiley, Parag B Deotare, Marko Loncar, and George M Whitesides. Integrated fabrication and magnetic positioning of metallic and polymeric nanowires embedded in thin epoxy slabs. *ACS nano*, 3 (10):3315–25, 2009.

[8] Darren J Lipomi, Ramses V Martinez, Robert M Rioux, Ludovico Cademartiri, William F Reus, and George M Whitesides. Survey of materials for nanoskiving and influence of the cutting process on the nanostructures produced. *ACS applied materials & interfaces*, 2(9):2503–14, 2010.

[9] Parisa Pourhossein and Ryan C Chiechi. Directly addressable sub-3 nm gold nanogaps fabricated by Nanoskiving using self-assembled monolayers as templates. *ACS nano*, 6(6):5566–73, 2012.

[10] Gerard A Kalkman, Yanxi Zhang, Enrico Monachino, Klaus Mathwig, Machteld E Kamminga, Parisa Pourhossein, Pieter E Oomen, Sarah A Stratmann, Zhiyuan Zhao, Antoine M van Oijen, Elisabeth Verpoorte, and Ryan C Chiechi. Bisecting Microfluidic Channels with Metallic Nanowires Fabricated by Nanoskiving. *ACS Nano*, 10 (2):2852–2859, 2016.

4

[11] Darren J Lipomi, Ramses V Martinez, and George M Whitesides. Use of Thin Sectioning (Nanoskiving) to Fabricate Nanostructures for Electronic and Optical Applications. *Angewandte Chemie International Edition*, 50(37):8566–8583, 2011.

[12] Martin Kühnel, Søren V Petersen, Rune Hviid, Marc H Overgaard, Bo W Laursen, and Kasper Nørgaard. Monolayered Graphene Oxide as a Low Contact Resistance Protection Layer in Alkanethiol Solid-State Devices. *The Journal of Physical Chemistry C*, 122(18):9731–9737, 2018.

4

5

BISECTING MICROFLUIDIC CHANNELS WITH METALLIC NANOWIRES FABRICATED BY NANOSKIVING

Abstract: *This paper describes the fabrication of millimeter-long gold nanowires that bisect the center of microfluidic channels. We fabricated the nanowires by nanoskiving and then suspended them over a trench in a glass structure. The channel was sealed by bonding it to a complementary poly(dimethylsiloxane) structure. The resulting structures place the nanowires in the region of highest flow, as opposed to the walls, where it approaches zero, and expose their entire surface area to fluid. We demonstrate active functionality, by constructing a hot-wire anemometer to measure flow through determining the change in resistance of the nanowire as a function of heat dissipation at low voltage ($< 5V$). Further, passive functionality is demonstrated by visualizing individual, fluorescently labelled DNA molecules attached to the wires. We measure rates of flow and show that, compared to surface-bound DNA strands, elongation saturates at lower rates of flow and background fluorescence from nonspecific binding is reduced.*
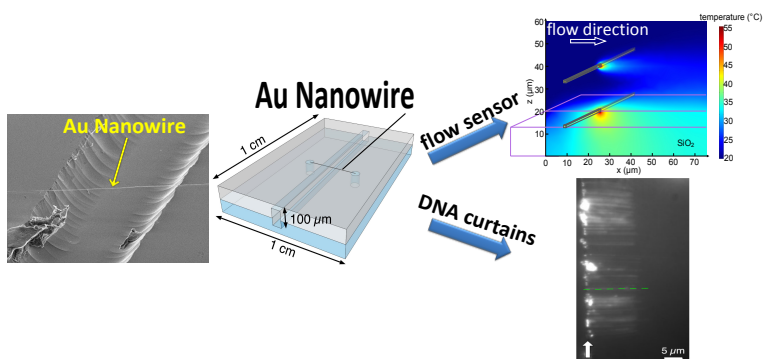
5.1. INTRODUCTION

Nanotechnology necessarily involves creating (or co-opting) and manipulating widgets or patterns with dimensions on the nanoscale. Creating nanoscale widgets can be done by constructing them from smaller components, *e.g.*, synthesizing molecules or growing colloids, or by fabricating them from bulk materials, *e.g.*, lithography. The latter approach falls generally within the purview of nanofabrication, which enables three important advantages of nanotechnology; the ability to interact with micro-scale objects (*e.g.*, cells), the miniaturization of macroscale functionality (*e.g.*, microelectronics) and access to very high surface area to volume ratios (*e.g.*, nanowires). Most nanofabrication is confined to a surface, which acts both as a substrate for lithographic processes and as an interface between the macroscopic world and the nanoscopic world.

Nanoskiving, a form of edge lithography in which planar structures are sectioned into thin slabs,[1, 2] circumvents some of these limitations by forming nanostructures inside a host matrix (usually a cross-linked polymer[3]) that can be manipulated one or several at a time. Compatibility of materials with nanoskiving is defined by mechanical properties,[4] and soft, organic materials that cannot tolerate typical photolithographic processing may be used,[5] such as, molecular and graphene templates to define dimensions with subnanometer precision.[6–8] While nanoskiving can be used to fabricate arbitrary shapes,[9–11] it can also be used to form nanowires directly from thin films embedded in polymer matrices[12] and planar crystals.[13, 14] The simplest case, sectioning thin metal films, produces metallic nanowires with control over all three dimensions, that can be millimeters long.[15, 16] These wires can be transported, positioned, and aligned directly under a light microscope *via* the (sacrificial) host matrix.[17] This combination of properties is unique to nanoskiving, directly coupling macro- and nano-regimes and affording access to the entire surface area of the resulting nanowires.

Although nanowires fabricated by nanoskiving are produced serially, this does not have to be a limitation for applications that exploit the functionality of single nanowires, such as microfluidics.[18] Placing nanowires on the floor of a microchannel, however, confines them to a surface and does not take advantage of their discrete nature; there is little functional difference between a thin, photolithographically patterned strip of metal or a nanowire lying flat on a surface. In microfluidic devices viscous forces tend to dominate, leading to laminar flow. The flow profile in this case is zero at the solid/liquid interface and at a maximum in the center of the channel. In sufficiently small channels with large surface-to-volume ratios, this profile is confined such that flow is near-zero over a large portion of the channel. Therefore, experiments or measurements that utilize flow, but involve structures anchored to a surface in the channel for flow interaction in regions that are near or at zero flow, will yield results that are not fully representative of the flow profile. A common example of this problem arises in the *in situ* measurement of rates of flow. Planar lithography confines metallic features to two dimensions and anchors them to a surface, requiring two sensing elements and a heating element to measure flow resistively.[19] Micro-electromechanical systems (MEMS) can measure flow mechanically *e.g.*, using external optics, [20] but at the expense of sensitivity and the simplicity of resistive measurements. Another example of an experiment requiring flow in a passive microfluidic system is the study of flow elongation in which long macromolecules (e.g., DNA molecules) are confined to a microfluidic channel and pulled

taut by flow for visualization by single-molecule fluorescence.[21–23] If macromolecules are attached to the surface of the bottom of a channel, they are placed in a region of near-zero flow and require high flow rates to achieve elongation. Moreover, non-specific binding of, in particular, biological molecules to surfaces can significantly lower the recorded signal-to-background ratio of the bound macromolecules of interest. Both of these examples—one active and one passive—would benefit from the (nanoscale) objects of interest being elevated from the surface and held in the center of the channel where the flow is the highest. However, to do so requires the ability to place discrete, three-dimensional nano-objects at arbitrary positions inside of a microchannel, exposing the entire surface area to the fluid environment.
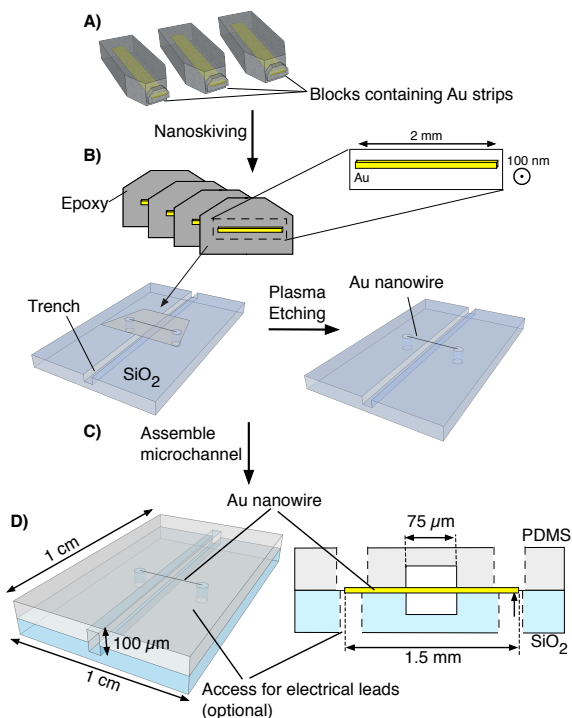
Figure 5.1 Fabrication scheme and schematics of a microfluidic channel bisected by a gold nanowire. A) Epoxy blocks containing strips of Au are mounted in an ultramicrotome. B) The blocks are sectioned to produce epoxy slabs containing Au nanowires from the cross-section of the Au films. C) The slabs are placed over a pre-etched trench in a glass substrate and the epoxy is removed by plasma etching to leave a free-standing Au nanowire (see Figure 5.2). D) Left: Schematic of an intact device with access ports for electric leads. Right: Cross-section of the channel showing the positioning of the nanowire.

We bisected microfluidic channels with millimeter-long gold nanowires fabricated by nanoskiving. A schematic of the device architecture is shown in Fig 5.1. We used glass and PDMS for the rigidity and ease of fabrication, respectively. Holes can be made through the top or bottom layers to access the ends of the nanowires. Because the nanowires extend sufficiently far from the channel, these holes can be drilled or punched

by hand and filled with conductive paste to connect the wires to macroscopic leads. The fabrication process is extraordinarily simple due to the discrete nature of nanowires formed by nanoskiving; they are not formed in templates, grown from surfaces, or captured from a liquid suspension. They can be placed one-at-a-time or in arrays as part of a convergent fabrication, that is, the channels are fabricated independently and therefore can be combined with wires of arbitrary compositions and dimensions without requiring alteration. This simple, convergent fabrication also enables control over the rotation (about the axis normal to the bottom of the channel), height (relative to the bottom of the channel), spacing (of multiple wires), and position (with respect to the inlet and outlet). To demonstrate the utility of integrating discrete nanowires into microfluidic channels, we designed experiments using two device architectures, one active and one passive. The active device demonstrates a two-terminal, hot-wire anemometer that samples flow in the center of the channel in which the entire surface area of the wire is in contact with the fluid being measured. The passive device uses the nanowires as substrates for the attachment of long DNA molecules for the study of elongation.

5.2. RESULTS AND DISCUSSION

5.2.1. FABRICATION

Au nanowires were fabricated by using nanoskiving. A 200 or 400 nm thick gold film was embedded in a block of epoxy from which 200 nm thick slabs were cut and floated onto a water bath using an ultramicrotome. These slabs containing nanowires were transferred from the water and positioned over 30 μm deep trenches etched in glass substrates. The epoxy matrix was then removed by etching with O_2 plasma to yield freestanding nanowire(s) spanning the trench in the etched glass. The yield of the wires (when using a well maintained knife) was 100%. The devices were completed by sealing a complementary PDMS channel, also 30 μm deep, to the glass to form a closed channel. By stacking Au films, several wires can be installed with arbitrary separation and composition in one channel in a single fabrication step. A detailed description of the entire fabrication procedure is provided in the Experimental section.

The microfluidic devices were characterized at all stages of fabrication using a combination of optical microscopy, scanning electron microscopy (SEM) and electrical measurement. An image of the finished device is shown in the Figure 5.12. To verify that the gold nanowires are suspended freely over the channel, SEM images of the etched glass/nanowire assembly were acquired at a 45° angle (after etching the epoxy). An example of a 200 × 200 nm square nanowire spanning the entire width of a 70 μm wide trench etched in glass is shown in Figure 5.2. The wire is completely suspended and does not contact the surface of the glass inside the trench. The angle of the wire with respect to the channel is controlled by rotating the epoxy section containing the wire while the carrier water from the ultramicrotome boat dries. We found it possible, but difficult to achieve perfectly parallel wires, however, the angle had a negligible impact on the subsequent experiments.
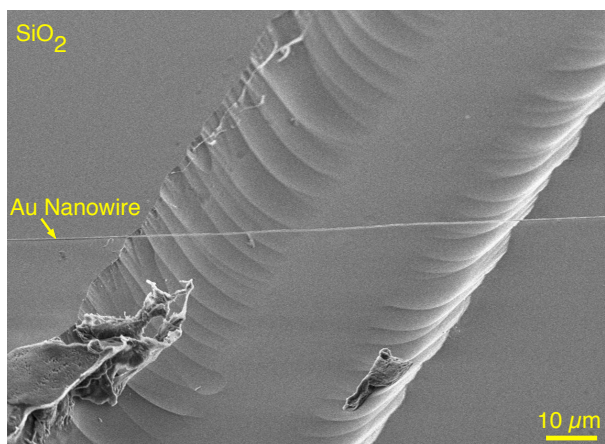
Figure 5.2 Scanning electron micrograph of 1.5 mm × 200 nm × 200 nm Au nanowire suspended over a 70 μm wide, 20 μm deep trench etched into a glass substrate.

5.2.2. Hot-wire Anemometry

Sensors that utilize the principle of heat dissipation can be classified as hot-wire, hot-film, or calorimetric. In microfluidics, the rate of flow can be determined by measuring changes in conductivity affected by changes in temperature as the carrier liquid flows past a metallic conductor. To avoid the risk of physically changing flows in microchannels by the insertion of relatively bulky structures to measure flow rates, the heating and sensing elements (*e.g.*, "nanowires" in the form of thin strips of metal) are placed at the bottom of the channel where the flow is near zero. This precludes simple hot-wire anemometry and necessitates more complex, multi-wire architectures that include separate heating and sensing elements. Nanowires are small enough that they will not disrupt flow and so can be placed directly in the center of the channel without affecting it. To demonstrate the utility of bisecting microfluidic channels with nanowires fabricated by nanoskiving, we constructed a simple hot-wire anemometer using only a single wire as both the heating and sensing element.

The dimensions of the microfluidic channel test-bed are shown in Figure 5.1. Ethanol was injected continually into the channel using a syringe pump, and the current response monitored as a function of flow rate at 0.5, 1.0, 1.5 and 2.0 V (the raw data and a calibration curve are shown in Figure 5.14, 5.15 and 5.16). Joule heating causes the resistance of the nanowire to increase, which is counteracted by the transport of heat away from the wire by the carrier liquid. Higher rates of flow cool the wire more, and higher voltages give higher sensitivity. Thus, the current at a fixed voltage rises to a plateau as the rate of flow is increased. In order to relate the conductance of the nanowire to flow rates, we replotted these plateaus as relative conductance G/G_0 *versus* pump flow rate, where G is the conductance at a plateau and G_0 is the conductance at zero flow. These data are shown in the left plot of Figure 5.3 over a range of 0 μL/min to 30 μL/min with increases of 10 μl/min in each step. Data acquired for a nanoskived nanowire placed at the bottom of a channel are shown in red for comparison. These plots clearly show that

G/G_0 varies with the rate of flow when the nanowire is freely suspended in the channel, but not when it is placed on the floor. Increasing the voltage increases the sensitivity (and the magnitude of G/G_0) for the suspended nanowire, but not sufficiently to detect the rate of flow when the nanowire is placed on the bottom of the channel. Ramping the flow rate up and then back down has no effect on the initial value of G/G_0, indicating that there is no hysteresis associated with this approach. Although we only report data up to 30 μL/min, the wires are mechanically stable to sufficiently high rates of flow to rupture the devices; we were unable to break the wires from shear alone.
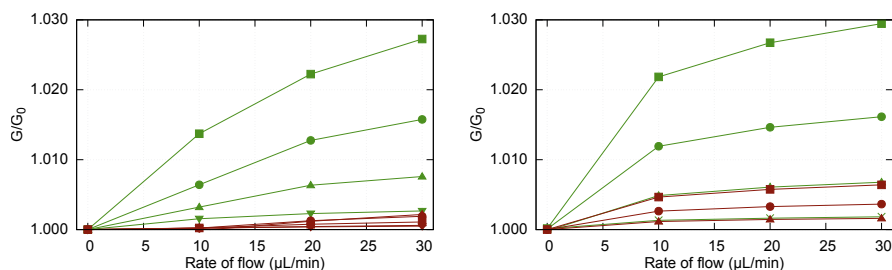
Figure 5.3 Plots of flow sensor data (left) and simulation (right) from hot-wire anemometers formed by bisecting microfluidic channels with Au wires (green) and placing the wires on the floor of the channel (red). The data show the conductance *versus* rate of flow at 2.0 V (squares), 1.5 V (circles), 1.0 V (triangle), 0.5 V (upside-down triangle) and 0 V (exes).

5.2.3. SIMULATIONS

To gain further insight into the effect of the position of the wire on the sensitivity of the hot-wire anemometry, we modeled the change in the conductivity of the nanowire numerically using a three-dimensional finite-element simulation and the details are described in Experimental section. The right plot of Figure 5.3 shows simulated data based on the geometry and materials used in the actual device. The simulation agrees qualitatively with the experimental data and is in very close numerical agreement when the wire is bisecting the channel, but overestimates the response when the wire is placed on the floor of the channel. The probable origin of this discrepancy and the dependence of the sensitivity on the position of the nanowire can be seen in the heatmap plots shown in Figure 5.4. The temperature distribution in the center of the microchannel is comparable for both nanowire positions, and, as predicted, the bisecting wire is in the region of highest flow, while the flow velocity approaches zero at the floor. However, the dominant effect is the proximity of the wire to the glass substrate, which acts as a heat sink, effectively masking the relatively small changes in heat dissipation from the carrier liquid. That is, when the nanowire is suspended freely in the microchannel, the entire surface is in contact with the carrier fluid, and therefore heat dissipation is dominated by the fluid. When the wire is placed on the floor, however, one surface is in contact with the relatively enormous mass of the glass substrate, which dominates heat dissipation; that is, the wire just equilibrates with the glass.

The simulation results confirm that the operation of the hot-wire anemometer is
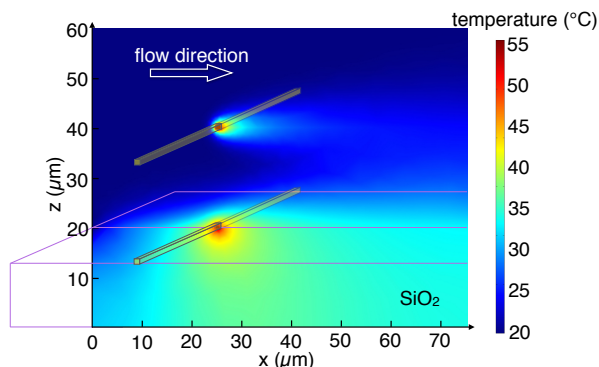
Figure 5.4 Comparison of the simulated temperature distribution in the center of the microchannel for nanowires positioned at the channel floor and at a height of 20 μm for a rate of flow of 30 μL/min.

5

contingent upon the entire surface area of the portion of the wire that spans the channel contacting the carrier fluid. Thus, this method of flow-sensing is nanoscopic in origin and relies on the ability of nanoskiving to produce discrete, three-dimensional nanowires that can be positioned arbitrarily. It is also simple, requiring only the ability to apply voltage and measure current. For potential applications beyond this proof-of-concept, the choice of nanowire dimensions and composition is limited only by the loose constraints of nanoskiving.

5.2.4. SUSPENDED DNA CURTAINS

The observation of protein-DNA interactions at the single-molecule level represents a powerful approach to understand the molecular mechanisms that are responsible for the copying, reading, and repairing of the genetic information stored in DNA.[21–23] A frequently used method relies on the fluorescence imaging of long, stretched DNA molecules and the proteins interacting with it. A common requirement for such techniques is the coupling of one end of a long, linear DNA molecule to a planar surface[24] and its stretching by a laminar flow.[25, 26] However, a major drawback of this approach is that the DNA molecule and proteins bound to it are susceptible to nonspecific interactions with the surface.[22, 24, 27–29] Further, stretching surface-tethered DNA molecules by flow is challenging because of the low rate of flow close to the surface in a laminar, Poiseuillian flow. By binding DNA molecules to a gold nanowire bisecting a flow cell (microfluidic channel), we anchor DNA molecules far away from the four walls of the channel, thereby preventing any interaction of the DNA with the surface. Furthermore, being attached to an elevated nanowire, the DNA molecules experience a more uniform flow and higher rate of flow than if they were tethered to a surface, allowing a lower overall rate of flow.

The attachment of many linear DNA molecules to a suspended nanowire results in a pattern that is defined as a "DNA curtain."[30] A curtain of DNA molecules grants the possibility of recording several single-molecule events at the same time and allows the study of DNA-protein interactions at high local DNA concentration. These curtains are

usually formed by planar lithography, using e-beam writing and etching to define barriers that interrupt a passivating lipid layer. Defining this passivating layer is a critical step in the formation of the curtains and for imaging the DNA. Bisecting microfluidic channels simplifies the formation of curtains by eliminating the planar lithography steps and obviating the need for passivation of a surface. In principle, these advantages come without any significant loss in the quality of the recorded images as compared to fluorescence imaging approaches visualizing proteins interacting with long DNA molecules.
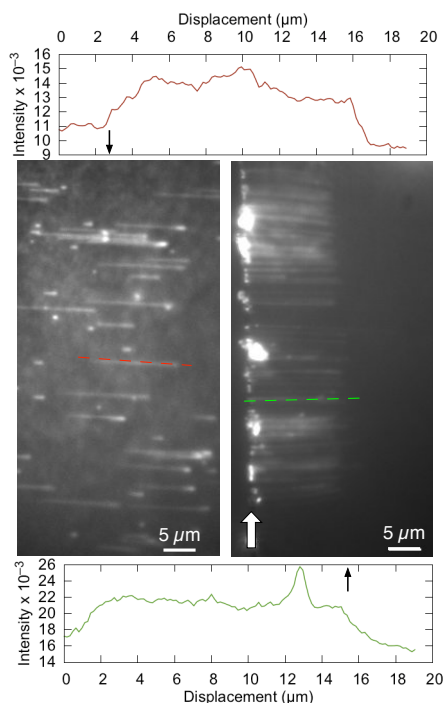
Figure 5.5 Averaged fluorescence images of immobilized DNA elongated by flow. Intercalating dye (SYTOX Orange) was present in solution to specifically stain and visualize double-stranded DNA. Left; Typical experiment in which the DNA is bound to random positions on the bottom surface of a microfluidic channel. Right; Typical experiment in which the DNA is bound to a Au nanowire bisecting the microfluidic channel at the midpoint. The position of the nanowire is indicated with a white arrow. A curtain of DNA extends outward from the wire in the direction of flow (from left to right). Intensity profiles corresponding to the green and red dashed lines are shown above and below the images; the x-axis is the displacement along the dashed lines. In the surface-bound experiment (left, top) there is significant background from nonspecific binding and lower signal intensity. In the nanowire-bound experiment (right, bottom) there is no nonspecific binding, leading to a significantly reduced level of background and a higher signal intensity.

Using a similar channel geometry as shown in Figure 5.1, we coupled DNA molecules to the suspended nanowires using standard Au-S chemistry to attach biotin/streptavidin followed by the introduction of biotinylated DNA. By specifically coupling one end of linear lambda-phage DNA (48.5 kilobases of double-stranded DNA; contour length 16.3 μm) to the nanowire, we obtained a curtain of DNA molecules that can be stretched by flow. Stable attachment at only the biotinylated end of the DNA was confirmed by revers-

ing the flow direction. The DNA density on the nanowire was controlled by varying the DNA concentration and the time of incubation. At sufficiently low densities, single molecules could easily be resolved. Figure 5.5 shows a DNA curtain attached to a nanowire (in the presence of intercalating dye to stain the double-stranded DNA fluorescently) alongside an image of surface-bound DNA molecules. Other than the obvious difference between DNA molecules arranged along a nanowire and molecules randomly-bound to a surface, the experiment using the nanowire results in less image artifacts due to non-specific binding (visible as diffuse shapes between isolated DNA molecules in the left image). Intensity profiles along the lengths of DNA molecules (Figure 5.5 top and bottom) show that the signal intensity is indeed slightly higher and more uniform in the curtain than in the randomly-bound surface case. We ascribe this difference to the complete lack of background signal from the separation of the curtain from the floor of the channel; *i.e.*, non-specific binding still occurs, but it is far removed from the focal plane.
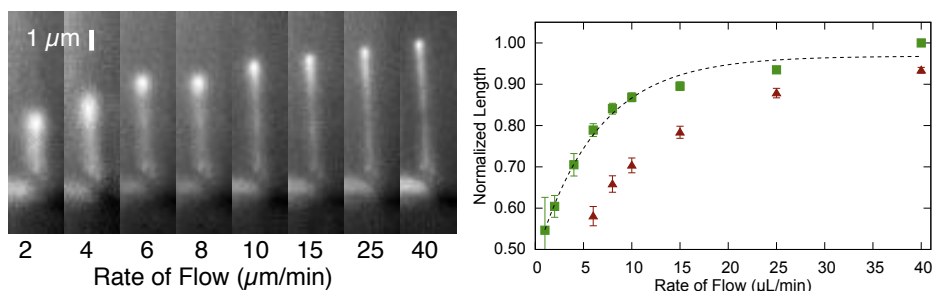
Figure 5.6 Left; sequential images of the elongation of lambda-phage DNA bound to a Au nanowire bisecting the microfluidic channel at the midpoint. Right; extension-force curve of lambda-phage DNA showing the normalized length averaged from six DNA molecules bound to nanowires (green squares) and from twelve DNA molecules bound to the surface of the same device (red triangles) *versus* rate of flow. It shows the influence of the different flow velocities at the nanowire and the surface. The dashed lines are exponential fit to guide the eye.

The ability to image individual, nanowire-coupled and flow-stretched DNA molecules at high signal-to-background ratios allowed the determination of the length of the DNA molecule as a function of rate of flow, ranging between 1 and 40 μl/min (measured at the pump). These flow-extension data are shown in Figure 5.6. At low rates of flow, large DNA fluctuations orthogonal to the flow direction were visible and the total DNA extension was measured to be significantly less than the contour length. This behavior represents the entropic collapse of the long DNA molecule at low stretching forces.[31] At high rate of flow, such fluctuations were no longer visible and the hydrodynamic force increased the mean extension of the DNA molecules. The relation between a force applied to the DNA and its extension has been extensively studied and well described by the worm-like chain (WLC) model.[31–34] In our setup, the tension along the DNA molecule decreases as one moves from the tethered end to the free end, instead of being uniformly applied to the end as assumed in the WLC model. However, even in this case the length will asymptotically approach the contour length (0.34 nm per basepair).[24] The lengths of six DNA molecules at various rates of flow were measured, and their average length was normalized by their average length at 40 μL/min (Figure 5.6). At relatively low rates

of flow, 5 μL/min, the DNA reaches 75% of its contour length. By contrast, DNA bound to the floor of the same microchannel did not reach 75% extension until 15 μL/min. The origin of this difference is the higher rate of flow experienced by the nanowire-bound DNA, demonstrating that the presence of the nanowire does not interfere significantly with laminar flow in the center of the channel. Although we do not have experimental evidence that the wires have no effect on laminar flow at all, this observation is important, as the apparent noninterference with the laminar flow is a crucial prerequisite for the further application of these nanowires to flow-based measurements.

5.3. CONCLUSIONS

Applications of microfluidic devices that take advantage of flow, but that are constrained to the solid-liquid interface at the walls of the channel, require high rates of flow and must compete with nonspecific binding. Measurements of flow upstream or downstream of an experiment are often limited to sampling the rate of flow at the walls, where it is lowest. Bisecting a microfluidic channel with a gold nanowire allows experiments to be performed in the center of the channel, where the rate of flow is the highest. Measurements of flow can then be conducted at the region of the highest rate of flow and directly at a point of interest. However, forming the discrete, millimeter-long gold nanowires necessary to bisect microfluidic channels is prohibitively complex using standard lithographic techniques. Nanoskiving enables the fabrication of these ultralong nanowires and facilitates the implementation of the wires, which are simply scooped off of the surface of a water bath directly onto a channel as they are formed. While it is possible to place very thin (micrometer-sized) wires in a microfluidic channel, true nanoscale wires benefit from a very large surface-to-volume ratio, low drag, and minimized effects on laminar flow.

Methods of flow sensing based on heat dissipation rely on a heating element and a downstream sensor to achieve a temperature gradient sufficient to measure a change in conductivity. However, a single nanowire is sensitive enough to serve both as the heating and sensing element if it is suspended in a microfluidic channel. Finite-element analysis reveals that this sensitivity arises from having the entire surface area of the wire in contact with the carrier liquid, eliminating the mass of the substrate as a heat sink. Binding DNA molecules to nanowires similarly exposes the entire surface of the nanowire-DNA assembly to the carrier fluid, eliminating background signal from nonspecific binding in fluorescence experiments and forming a curtain of DNA along the length of the nanowire. Flow-elongation measurements reveal that the DNA reaches maximum extension at lower rates of flow (measured at the pump) because the rate of flow within the channel is highest away from the walls of the channel.

This fabrication technique provides the ability to place a nanoscale object directly in the center of a microfluidic channel, gaining access to the peak rate of flow. We demonstrate the technique with gold nanowires, but nanoskiving is compatible with virtually any nonbrittle material. Any experiment or measurement that utilizes flow across a stationary widget can therefore potentially benefit from this technique.

5.4. EXPERIMENTAL

5.4.1. GENERAL

Au nanowires were fabricated by nanoskiving. First, 200 or 400 nm thick gold films were deposited onto a silicon wafer (used as-received) through a Teflon mask by thermal evaporation. The gold films were then covered with a layer of Epofix epoxy (Catalog #1232, Electron Microscope Sciences) and, after curing, the epoxy was separated from the wafer mechanically. The gold films remained attached to the epoxy. The epoxy was rough cut with a jeweler's saw into small enough pieces to fit into a "coffin mold" used to form standard blocks for ultramicrotomy. The mold was filled with more epoxy and then cured at 60 °C overnight. The result was a 200 nm or 400 nm thick gold film embedded in a block of epoxy. The 200 nm thick slabs were sectioned and floated onto a water bath using an ultramicrotome (Leica UC-6). These slabs, containing nanowires, were transferred from the water onto the appropriate substrate (*e.g.*, etched glass). Nanowires were liberated from the epoxy matrix by O_2 plasma dry etching for 1 hour at 100 mTorr, 30 W, using a Harrick Plasma Cleaner. Figure 5.7 shows the process of nanoskiving of Au nanowires and Figure 5.8 shows the image of a section containing one Au nanowire on the Si wafer.
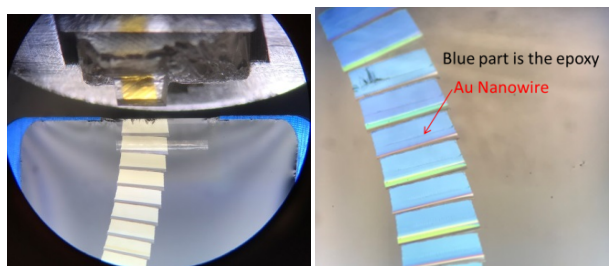
Figure 5.7 Left; An optical image of a ribbon of nanoskived 100 nm thick sections floating on top of the water (Yellow). Right; An optical image of nanoskived 200 nm thick sections floating on top of the water (Blue). The sections with different thicknesses exhibit the different colors in the image.

For the glass substrates, a prefabricated 4 ft square borofloat wafer coated with chromium and photoresist (Telic, USA, MED027021P) was exposed to a UV light source through a semitransparent mask. Developer (AZ 351 B Developer, AZ Electronic Materials, Germany) was used to remove the exposed photoresist. Chrome etch (Chrome Etch 18, OSC-OrganoSpezialChemie, Germany) was used to remove the chrome layer beneath. The exposed glass was etched using HF. After etching the unexposed photoresist and chrome were removed using acetone and chrome etch.

Soft lithography was preformed using a 40 μm-high SU-8 master fabricated on a glass borofloat wafer (10 cm diameter, 0.7 mm thick). The wafer was cleaned following standard wet cleaning protocols and dried on a hot plate. A spin coater was used to coat the wafer with a 40 μm-thick layer of SU-8 50 (Microchem). After a baking step to evaporate the solvent in the SU-8, the wafer was exposed to UV light through a semi-transparent mask. After exposure a baking step was preformed to cross-link the exposed SU-8. Developer (md-Dev 600, Micro Resist Technology, Germany) was used to remove the unexposed SU-8. PDMS monomer (Sylgard 184, Dow Corning) was mixed with PDMS curing
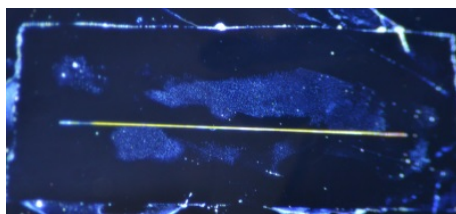
Figure 5.8 An optical image of a section of Au nanowire on the Si wafer.

agent in a 10:1 (w/w) ratio and the mixture was placed under a vacuum for 30 minutes to remove any bubbles. The uncured PDMS was poured over the wafer and cured on a hot-plate for 3 hours at 60 °C. After curing, the desired patterns were cut from the PDMS slab using a sharp razor blade. To create fluid inlets and outlets, a biopsy puncher with a diameter of 1.2 mm was used.

For flow-sensing measurements the nanowire was connected with a Keithley 2400 SourceMeter. The I-V plots of the nanowire suspended in microfluidic channel before and after the injection of the ethanol were recorded before the flow measurements. The current through the nanowire at different voltages was recorded with step size of 0.1 V. After that, a series of voltages (0.5V, 1.0V, 1.5V, 2V) was applied to the nanowire and the resulting current was measured over time at different rates of fluid flow. The fluid inlet of the nanowire device was connected to a 10 ml syringe (Terumo Syringe) with a diameter of 15.8 mm, and the fluid outlet was coupled to a waste beaker. Polyethylene tubing (PE60, 0.76 mm inner diameter, 1.22 mm outer diameter, Bioseb) was used to make the fluid connections. The inlet rates of the flow were set manually by a syringe pump (Spritzenpumpe LA-100, Landgraf Laborsysteme HLL GmbH). The used fluid was ethanol.

We used a finite-element simulation (COMSOL Multiphysics) to model a simplified three dimensional geometry of a microchannel with a 75 μm (width) by 60 μm (height) rectangular cross section and a length of 70 μm. A nanowire with a quadratic cross section of 200 nm by 200 nm bisects the microchannel at 20 μm channel height 25 μm downstream of the inlet, or is positioned at the floor of the microchannel, respectively. (See Figure 5.4.)

The stationary flow profile in the channel was calculated by evaluating the Stokes equation for an incompressible fluid (using the viscosity and density of ethanol). No-slip conditions were chosen for all boundaries except for an outlet (0 Pa exit pressure) and an inlet with a laminar inflow rate ranging from 0 to 30 μL/min (at a constant inflow temperature of 293 K). The electrical current through the nanowire was modeled by using the boundary conditions of a potential difference applied at both ends of the nanowire (electrical conductivity of gold) separated by 75 μm. In the experiment, the nanowire extends beyond the width of the microchannel and, thus, the potential difference is applied effectively over a wire length of several hundred micrometers. In the simulation, identical potential drops *per wire length* were used. For better comparability, in Figure 5.3 (right), the simulated potentials are stated as values corresponding to the equivalent longer *experimental* wire lengths.

To simulate heat transfer caused by the electrical current, the nanowire was coupled to the surrounding liquid by employing a heat equation for convective and conductive heating. As boundary conditions, thermal isolation was chosen for the side walls and ceiling of the microchannel; heat dissipation at the microchannel floor was modeled by a borosilicate block of 20 μm height underneath.

Flow cells were constructed to allow the incorporation of a suspended nanowire. Glass coverslips (Marienfeld-Superior) were cleaned by successive sonication in 2% (v/v) Hellmanex III (Hellma Analytics), in 100% ethanol (Avantor), and in 1 M KOH (Sigma-Aldrich). After each step, the slides were rinsed thoroughly with milli-Q water. The coverslips were 60 mm long, 24 mm wide, and 0.13-0.16 mm thick. On each slide, two strips of 50 μm thick double-sided tape (3M) were deposited so that a 40 x 4 mm sized channel was obtained. A 0.7 mm thick, 5 x 45 mm sized borofloat glass (TELIC) was used as flow chamber top. A 60 μm wide and 20 μm deep channel was excavated in this slide by HF etching (see above). Two holes 40 mm apart were made in the channel for the inlet and outlet tubing.

Subsequently, an array of gold nanowires was deposited across the channel. The gold nanowires had a diameter of 400 nm and a length of 1.5 mm. With the nanowires on the bottom face, the etched slide was positioned on the two tape strips while taking care that the etched channel was centered. The assembled flow cell was sealed with epoxy (Bison). Two homemade ports (3d printed in ABS) were glued with epoxy on top of the inlet/outlet holes. They were used as support for the polyethylene tubing (PE60, 0.76 mm inner diameter, 1.22 mm outer diameter, Bioseb). After placing the flow cell on the microscope sample stage, the outlet tube was connected to a syringe pump (New Era Pump Systems Inc.) used to control the flow of buffer.

The gold nanowires were modified with DNA molecules tethered through Au-S bond and biotin-streptavidin-biotin linkages. First, the suspended gold nanowires in the flow cell were incubated with 10 mM cysteamine (cysteamine hydrochloride from Sigma-Aldrich) in ethanol for at least two hours, functionalizing the surface with primary amines *via* the formation of a self-assembled monolayer. After washing the ethanol solution out, the modified gold nanowires were incubated with 0.3 mg/ml NHS-biotin (Thermo Scientific) in PBS (pH=8.2) for 1 hour to functionalize them with surface-bound biotin. Subsequently, they were incubated with 0.2 mg/ml streptavidin (Sigma-Aldrich) in PBS (pH=8.2) for 30 minutes to bind the biotin resulting in nanowires modified with surface-bound streptavidin. Finally, forked lambda-phage DNA molecules, biotinylated at the 5' end of the fork (3), were flowed into the chamber in 20 mM Tris (pH=7.5), 2 mM EDTA, 50 mM NaCl, 1 mg/ml bovine serum albumin (BSA), and 0.025% Tween20. Excess DNA was removed by washing with the same buffer. 100 nM SYTOX Orange (Invitrogen) was used to stain the DNA molecules. The Sytox-stained DNA molecules were excited with a 532 nm solid-state laser (Coherent Sapphire 532-200 CW) at 25 Wcm^{-2} in epifluorescence mode. The resulting fluorescent signal was collected through a 100x oil-immersion TIRF objective (Olympus, 1.49 NA) and recorded on an EM-CCD camera (Hamamatsu).

5.4.2. SEM

Scanning electron microscope images of the single Au nanowires were acquired using a field emission SEM (Jeol JSM 7000F) operating at 5 kV. SEM analysis was undertaken for

visual characterization of nanowires and determination of the dimensions of the wires. A nanowire (or array of nanowires) was placed on the etched glass substrate and a thin layer of gold was sputtered on the top to avoid charging artifacts. Figure 5.9 shows a SEM image of a 200 nm x 200 nm Au nanowire (Left) and a top-down image of a 200 x 200 nm Au nanowire suspended over a trench etched into glass (Right).
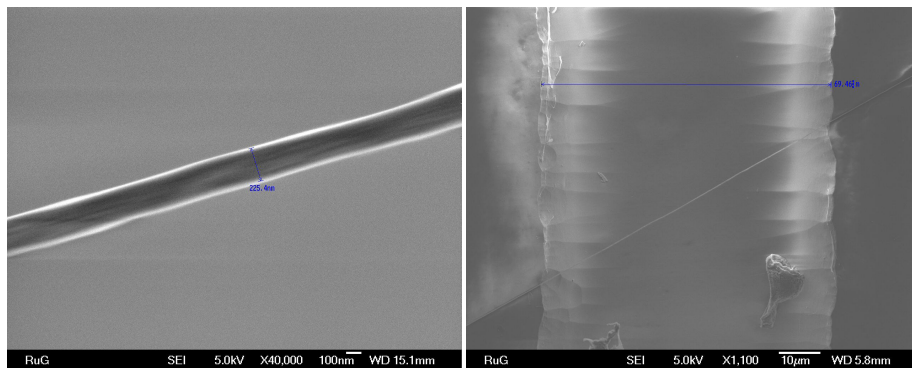

Figure 5.9 Left; SEM image of a gold nanowire with the width of 200 nm. Right; An SEM image of a nanoskived nanowire suspended over a trench with the width of 70 μm on glass substrate

5.4.3. CHOICE OF FLUID

All of the flow sensing data are from channels filled with ethanol. We chose ethanol for experimental convenience because the surface tension of water is sufficient to break the nanowires upon introduction to the channel. However, we were able to use pure water by first filling the channels with ethanol and then introducing water as long as no bubbles were introduced. The DNA stretching experiments described below were performed in PBS and Tris buffer using this method.

5.4.4. FLOW SENSOR

DEVICE FABRICATION

Figure 5.10 shows a schematic overview of the steps in the device fabrication. The device consists of a glass bottom part and a PDMS top part, each containing a channel structure. Both parts are bonded together with the structures facing each other and the nanowire positioned in between. The bottom part was first etched in glass as described above (Figure 5.10A). A sand blaster (Sandmaster FG 2-94) was used to create holes for contacting wires. The holes were positioned approximately 2 mm from the center of the channel. Next, two contact wires were added (0.1 mm tin wires) through the holes and the glass was mounted on a microscope slide using epoxy glue for easy handling and mechanical stability (Figure 5.10B and C). A nanoskived epoxy section containing a 200 x 200 nm Au nanowire (or an array of wires) was transferred to the glass bottom of the device, over the center of the channel (Figure 5.10D and E). The top PDMS part was then fabricated as described above. A 3 mm-diameter biopsy puncher was used to create two holes in the PDMS top part, one on either side of the center of the channel, approximately 0.5 mm

from the sides of the channel. These holes are later filled with silver paste to connect
each end of the nanowire electrically with a contact wire. The epoxy matrix was then
removed using oxygen plasma etching (Figure 5.10F). The glass and PDMS parts of the
device were then irreversibly bonded. This was done by briefly exposing both parts to
oxygen plasma and then bringing both surfaces in contact with each other. A custom-
built aligner (Figure 5.11) was used to align both parts prior to bonding. The aligner
consists of a bottom and top stage that can be moved independently. The bottom stage
has a trench in which a standard microscope slide (~2.6 cm width) can be placed. The
top stage consists of an 8 x 8 cm glass plate that can be moved vertically. The bottom
stage can be rotated and moved parallel to the top stage. To align two parts, one part
is placed on the bottom stage and the second part is attached to the top stage. The top
stage is then lowered until both parts are in close proximity. Alignment can be accurately
performed by manipulating the bottom stage. Since the top part and the top stage are
both transparent, the alignment can be done while observing both parts simultaneously
from the top using a microscope. When the parts are properly aligned, we lowered the
top stage further until both parts were in contact with each other. In the last step the
nanowire was electrically connected to the contact wires by adding a drop of silver paste
into the two contact holes. The total dimensions of the top and bottom parts of the
device are roughly 2 x 1 cm, which was mounted on a microscope slide with dimensions
of approximately 2.5 x 2.5 cm. The length of the channel was 1.0 cm. Devices with glass
and PDMS channels of respectively 60 μm and 80 μm in width were designed. The PDMS
channels have a depth of 20-40 μm (defined by the spin speed during SU-8 film forma-
tion). The width of the channels in the mask used for HF etching were 20 μm wide. This
should yield glass channels with a depth of 20 μm. The resulting width of a glass channel
is around 70 μm measured by SEM. Figure 5.12 shows a microfluidic channel device for
flow sensing.

Figure 5.13 is an optical micrograph showing two Au nanowires before the epoxy is
etched, placed over a trench etched into glass. It shows how far the wires extend past
the trench on both sides. The nanowires are labeled in red and are only visible as thin
lines from the index mismatch between epoxy and Au (they are too small to visualize
at that magnification). The colorful lines are the result of interference from wrinkles in
the epoxy. The dimensions of these devices is such that several wires can bisect a single
channel allowing for multiple experiments in a single channel and fabrication proced-
ure.

5.4.5. Resistance versus temperature measurements
The influence of a change in temperature on the resistance of a gold nanowire was meas-
ured. A nanoskived gold nanowire (200 x 200 nm) was placed on a piece of glass and con-
nected to two metal contact wires (0.1 mm diameter, tin) using silver paste. The wires
were connected to a multimeter (Fluke 10). The nanowire was placed on a hot plate with
a digital temperature display. The temperature was set to different values and the resist-
ance was recorded when the temperature stabilized. The resistance of a nanowire as a
function of temperature is shown in Figure 5.14 Left. The resistance of Gold Nanowires
shows linear relationship with the temperature. The relation between temperature and
resistivity is described by the Temperature Coefficient of Resistivity (TCR) equation (5.1).
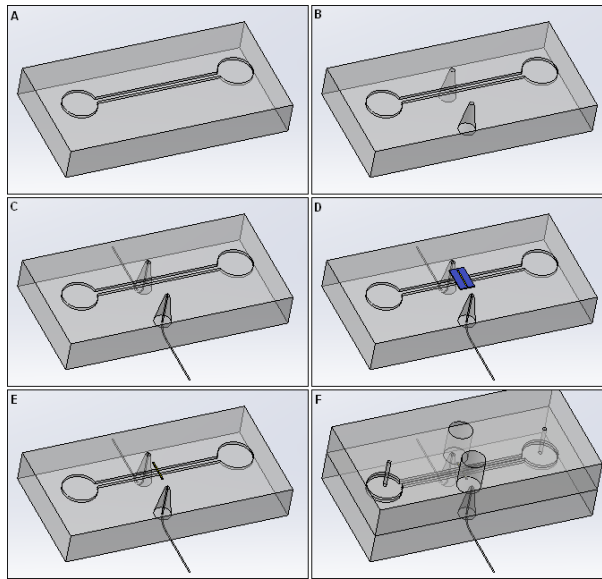
Figure 5.10 A schematic overview of the device fabrication. A) The bottom half of the channel is etched in glass. B) Contact holes are created using a sand blaster. C) Metal contact wires are added. D) A nanoskived section containing a gold nanowire is added. E) The epoxy from the section is removed using an oxygen plasma, leaving the nanowire behind. F) The PDMS top is bonded to the glass bottom, sealing the channel. The PDMS top contains two holes that each overlap with a contact wire and one end of the nanowire.
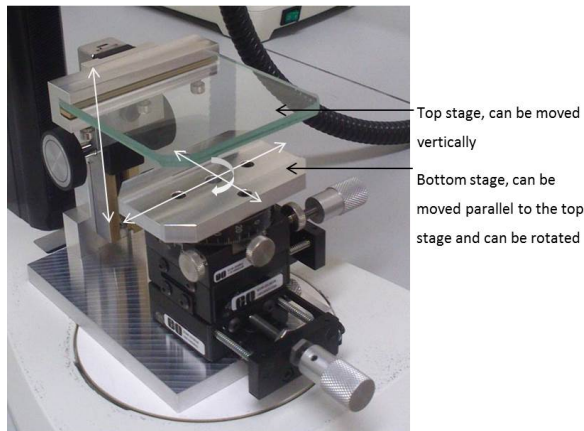
Figure 5.11 An image of the custom-built aligner used to accurately align both parts of the device. The image shows the aligner positioned on the base plate of a microscope. The gray arrows indicate the different ways in which the stages can be manipulated. The top stage contains a transparent piece of glass so that both parts of the device can be viewed simultaneously through the microscope.

In this equation $\rho(T)$ is the resistivity in Ω at temperature T in ^{o}C, ρ_0 is the resistivity in Ωm at reference temperature T_0 in $^\circ$C and α_0 is the TCR in $^\circ$C^{-1}. The electrical charac-

Figure 5.12 An image of fabricated microfluidic channel device for flow sensing.
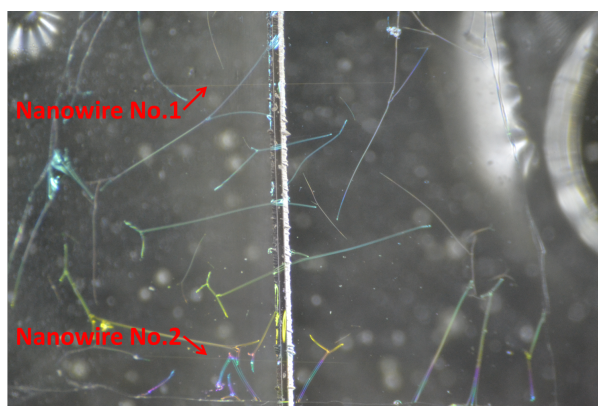
Figure 5.13 An optical image of a nanoskived section containing two gold nanowires

terization using standard I-V plots was performed in the voltage range of 0 to +1 V. The I-V measurement displayed Ohmic linear responses and exhibited low resistance 400-500 Ω (Shown in Figure 5.14 Right). This temperature is probably an over estimation of the real temperature of the nanowire since the temperature sensor in the hot place is located closer to the heat element than the nanowire. For control purpose, further, we plotted the I-V curve before and after the injection of ethanol in the channel. However, there is no significant difference, also shown in Figure 5.14 Right.

The TCR can be explained as the change in resistivity per unit of temperature, expressed as a fraction of the resistivity at a reference temperature. The reference temperature is usually $0\,°C$. The TCR at $0\,°C$ from Figure 5.14 is $2.60 \times 10^{-3}\,°C^{-1}$ and was calculated by dividing the slope of the trend line by the (extrapolated) resistance at $0\,°C$. This value is roughly in agreement with a value found for 145 nm gold nanowires ($1.34 \times 10^{-3}\,°C^{-1}$) and the value for bulk gold ($3.9 \times 10^{-3}\,°C^{-1}$).

$$R(T) = R(T_0)[1 + \alpha(T - T_0)] \tag{5.1}$$

142
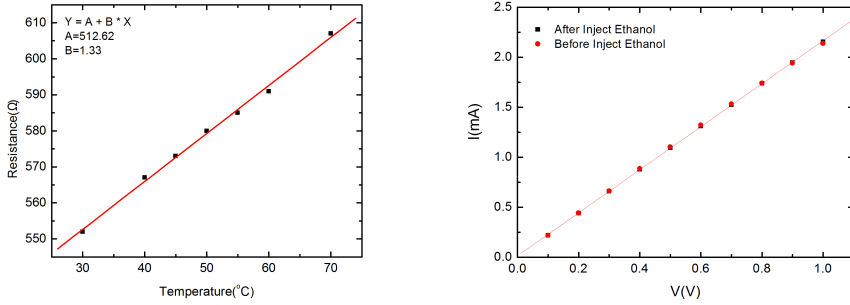
Figure 5.14 Left; The resistance of a nanowire as a function of temperature. Right; I-V plot before and after the injection of ethanol in the microfluidic channel.

5.4.6. Resistance versus flow measurements

The raw I/V data are shown in Figures 5.15 and 5.16.
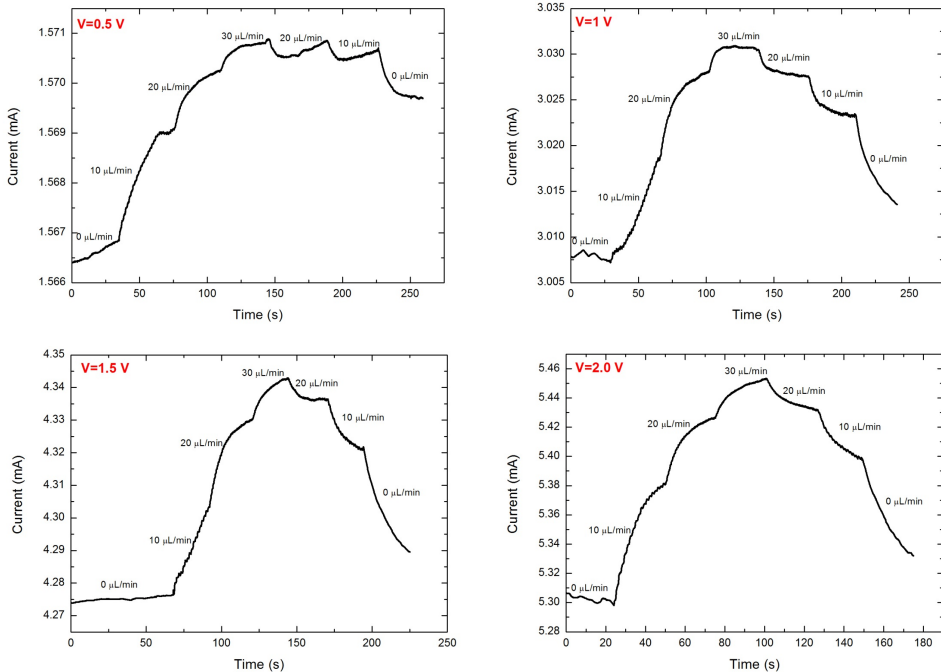
Figure 5.15 The current passed the nanowire centered in the microfluidic channel response to the different rates of flow over time at different voltages: 0.5V, 1V, 1.5V, 2.0V

5
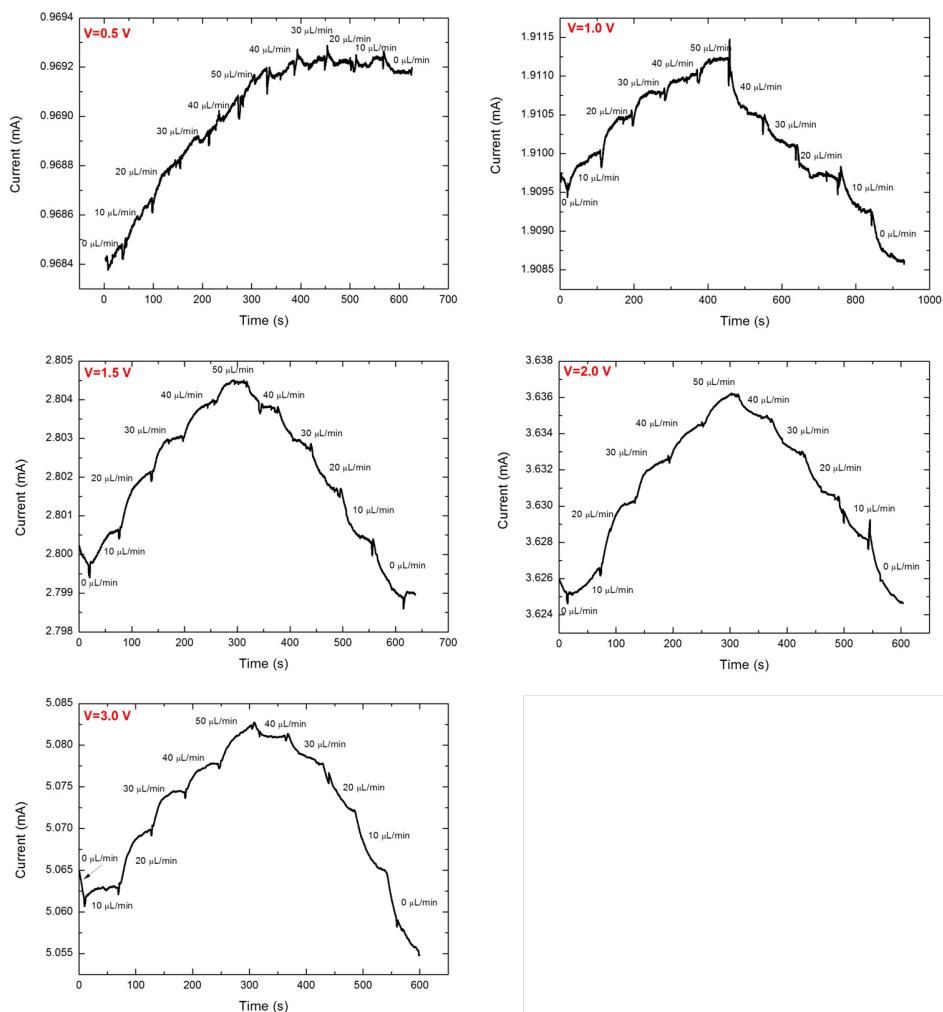
Figure 5.16 The current passed the nanowire placed at the floor of microfluidic channel response to the different rates of flow over time at different voltages: 0.5V, 1V, 1.5V, 2.0V, 3.0V

5.4.7. Simulations

To further illustrate the applicability of the bisecting nanowire as a flow sensor and to test the validity of the experimental results, we numerically modeled the nanowire conductivity as a function of flow rate and applied potential.

We determined the change in nanowire resistance by sampling the temperature in the wire and then multiplying it by the experimentally determined resistance–temperature dependence (see Fig. 5.14).

The corresponding numerical relative conductances are shown in Fig. 5.3 (right) as

a function of flow rate and potential for a bisecting nanowire as well as a wire positioned at the microchannel floor.

In Fig. 5.4, the temperature distribution is shown for a flow rate of 30 μL/min and a potential drop of 0.25 V over 75 μm for both wires.

5

BIBLIOGRAPHY

[1] Qiaobing Xu, Robert M. Rioux, Michael D. Dickey, and George M. Whitesides. Nanoskiving: A new method to produce arrays of nanostructures. *Acc. Chem. Res.*, 41(12):1566–1577, 2008.

[2] Darren J. Lipomi, Ramses V. Martinez, and George M. Whitesides. Use of thin sectioning (nanoskiving) to fabricate nanostructures for electronic and optical applications. *Angew. Chem. Int. Ed.*, 50(37):8566–8583, 2011.

[3] Robin L Mays, Parisa Pourhossein, Dhanalekshmi Savithri, Jan Genzer, Ryan C Chiechi, and Michael D Dickey. Thiol-Containing Polymeric Embedding Materials for Nanoskiving. *J. Mater. Chem. C*, 1(1):121–130, 2013.

[4] Darren J Lipomi, Ramses V. Martinez, Robert M Rioux, Ludovico Cademartiri, William F Reus, and George M Whitesides. Survey of Materials for Nanoskiving and Influence of the Cutting Process on the Nanostructures Produced. *ACS Appl. Mat. Interf.*, 2(9):2503–2514, 2010.

[5] Darren J. Lipomi, Ryan C. Chiechi, Michael D. Dickey, and George M. Whitesides. Fabrication of conjugated polymer nanowires by edge lithography. *Nano Let.*, 8(7):2100–2105, 2008.

[6] Aliaksandr V Zaretski, Brandon C Marin, Herad Moetazedi, Tyler J Dill, Liban Jibril, Casey Kong, Andrea R Tao, and Darren J Lipomi. Using the Thickness of Graphene to Template Lateral Subnanometer Gaps between Gold Nanostructures. *Nano Letters*, 15(1):150105140507005–640, 2015.

[7] Parisa Pourhossein and Ryan C Chiechi. Fabricating Nanogaps by Nanoskiving. *J. Vis. Exp.*, 75:e50406–e50406, 2013.

[8] Parisa Pourhossein and Ryan C Chiechi. Directly Addressable Sub-3 nm Gold Nanogaps Fabricated by Nanoskiving Using Self-Assembled Monolayers as Templates. *ACS Nano*, 6(6):5566–5573, 2012.

[9] Qiaobing Xu, Raquel Perez-Castillejos, Zhefeng Li, and George M. Whitesides. Fabrication of High-Aspect-Ratio metallic nanostructures using nanoskiving. *Nano Let.*, 6(9):2163–2165, 2006.

[10] Qiaobing Xu, Robert M. Rioux, and George M. Whitesides. Fabrication of complex metallic nanostructures by nanoskiving. *ACS Nano*, 1(3):215–227, 2007.

[11] Darren J. Lipomi, Mikhail A. Kats, Philseok Kim, Sung H. Kang, Joanna Aizenberg, Federico Capasso, and George M. Whitesides. Fabrication and replication of arrays of single- or multicomponent nanostructures by replica molding and mechanical sectioning. *ACS Nano*, 4(7):4017–4026, 2010.

[12] BJ Wiley, DI Lipomi, J Bao, F Capasso, and GM Whitesides. Fabrication of surface plasmon resonators by nanoskiving single-crystalline gold microplates. *Nano Let.*, 8(9):3023–3028, 2008.

146

[13] Darren J. Lipomi, Ryan C. Chiechi, William F. Reus, and George M. Whitesides. Laterally ordered bulk heterojunction of conjugated polymers: Nanoskiving a jelly roll. *Adv. Func. Mater.*, 18(21):3469–3477, 2008.

[14] Albert Wan, Tao Wang, Tingting Yin, Anran Li, Hailong Hu, Shuzhou Li, Ze Xiang Shen, and Christian A. Nijhuis. Plasmon-modulated photoluminescence of single gold nanobeams. *ACS Photonics*, 2(9):1348–1354, 2015.

[15] Qiaobing Xu, Byron D Gates, and George M Whitesides. Fabrication of Metal Structures with Nanometer-Scale Lateral Dimensions by Sectioning Using a Microtome. *J. Am. Chem. Soc.*, 126(5):1332–1333, 2004.

[16] Qiaobing Xu, Jiming Bao, Federico Capasso, and George M Whitesides. Surface Plasmon Resonances of Free-Standing Gold Nanowires Fabricated by Nanoskiving. *Angew. Chem.*, 118(22):3713–3717, 2006.

[17] Darren J. Lipomi, Filip Ilievski, Benjamin J. Wiley, Parag B. Deotare, Marko Lončar, and George M. Whitesides. Integrated fabrication and magnetic positioning of metallic and polymeric nanowires embedded in thin epoxy slabs. *ACS Nano*, 3(10): 3315–3325, 2009.

[18] Karen Dawson, Jörg Strutwolf, Ken P Rodgers, Grégoire Herzog, Damien W M Arrigan, Aidan J Quinn, and Alan O'Riordan. Single Nanoskived Nanowires for Electrochemical Applications. *Anal. Chem.*, 83(14):5535–5540, 2011.

[19] L Schöler, B Lange, K Seibel, H Schäfer, M Walder, N Friedrich, D Ehrhardt, F Schönfeld, G Zech, and M Böhm. Monolithically Integrated Micro Flow Sensor for Lab-On-Chip Applications. *Microelectronic Engineering*, 78-79:164–170, 2005.

[20] Mohammad Sadegh Cheri, Hamid Latifi, Jalal Sadeghi, Mohammadreza Salehi Moghaddam, Hamidreza Shahraki, and Hasan Hajghassem. Real-Time Measurement of Flow Rate in Microfluidic Devices Using a Cantilever-Based Optofluidic Sensor. *Analyst*, 139(2):431–438, 2013.

[21] David Dulin, Jan Lipfert, M Charl Moolman, and Nynke H Dekker. Studying Genomic Processes at the Single-Molecule Level: Introducing the Tools and Applications. *Nat Rev Genet*, 14(1):9–22, 2013.

[22] Boyang Hua, Kyu Young Han, Ruobo Zhou, Hajin Kim, Xinghua Shi, Sanjaya C Abeysirigunawardena, Ankur Jain, Digvijay Singh, Vasudha Aggarwal, Sarah A Woodson, and Taekjip Ha. An Improved Surface Passivation Method for Single-Molecule Studies. *Nat Meth*, 11(12):1233–1236, 2014.

[23] Andrew Robinson and Antoine M van Oijen. Bacterial Replication, Transcription and Translation: Mechanistic Insights from Single-Molecule Biochemical Studies. *Nat Rev Micro*, 11(5):303–315, 2013.

[24] Annette Granéli, Caitlyn C Yeykal, Tekkatte Krishnamurthy Prasad, and Eric C Greene. Organized Arrays of Individual DNA Molecules Tethered to Supported Lipid Bilayers. *Langmuir*, 22(1):292–299, 2006.

5

[25] Nathan A Tanner, Joseph J Loparo, Samir M Hamdan, Slobodan Jergic, Nicholas E Dixon, and Antoine M van Oijen. Real-Time Single-Molecule Observation of Rolling-Circle DNA Replication. *Nucleic Acids Research*, 37(4):e27–e27, 2009.

[26] Nathan A Tanner and Antoine M van Oijen. Chapter Eleven - Visualizing DNA Replication at the Single-Molecule Level. In Nils G Walter B T Methods in Enzymology, editor, *Single Molecule Tools, Part B:Super-Resolution, Particle Tracking, Multiparameter, and Force Based Methods*, volume Volume 475, pages 259–278. Academic Press, 2010.

[27] Teresa Fazio, Mari-Liis Visnapuu, Shalom Wind, and Eric C Greene. DNA Curtains and Nanoscale Curtain Rods: High-Throughput Tools for Single Molecule Imaging. *Langmuir*, 24(18):10524–10531, 2008.

[28] Taekjip Ha, Ivan Rasnik, Wei Cheng, Hazen P Babcock, George H Gauss, Timothy M Lohman, and Steven Chu. Initiation and Re-Initiation of DNA Unwinding by the Escherichia coli Rep Helicase. *Nature*, 419(6907):638–641, 2002.

[29] Ivan Rasnik, Sua Myong, Wei Cheng, Timothy M Lohman, and Taekjip Ha. DNA-Binding Orientation and Domain Conformation of the E. coli Rep Helicase Monomer Bound to a Partial Duplex Junction: Single-molecule Studies of Fluorescently Labeled Enzymes. *J. Mol. Bio.*, 336(2):395–408, 2004.

[30] Bridget E Collins, Ling F Ye, Daniel Duzdevich, and Eric C Greene. In Quantitative Imaging in Cell Biology. Jennifer C Waters and Torsten Wittman B T Methods; Editors, *Academic Press*, Vol.123:217–234, 2014.

[31] Carlos Bustamante, Steven B Smith, Jan Liphardt, and Doug Smith. Single-Molecule Studies of DNA Mechanics. *Cur. Op. Struct. Bio.*, 10(3):279–285, 2000.

[32] Christoph G Baumann, Steven B Smith, Victor A Bloomfield, and Carlos Bustamante. Ionic effects on the elasticity of single DNA molecules. *Proc. Natl. Acad. Sci. USA*, 94(12):6185–6190, 1997.

[33] C Bustamante, J F Marko, E D Siggia, and S Smith. Entropic Elasticity of Lambda-Phage DNA. *Science*, 265(5178):1599–1600, 1994.

[34] John F Marko and Eric D Siggia. Stretching DNA. *Macromolecules*, 28(26):8759–8770, 1995.

SUMMARY

The goal of this thesis is to investigate the tunneling properties of large-area molecular junctions comprising self-assembled monolayers of conjugated, organic molecules with different conjugation patterns and to incorporate them into three-terminal junctions to modulate the tunneling charge transport via gating with electric fields.

In **Chapter 2**, we studied the mechanical and electrical properties of SAMs comprising an oligothiophene-quaterthiophene with a flexible butanethiol chain (**T4C4**) using CP-AFM and EGaIn. Oligothiophenes are π-conjugated molecules with superior electrical properties and of interest in electronics. We investigated the structure-property relationship between mechanical deformation and electrostatics in SAMs of **T4C4**. By varying the loading force applied to the AFM probe, we found that the SAM of **T4C4** is more mechanically robust than SAMs of alkanes over a range of pressures. Combining density functional theory (DFT) calculations and transition voltage spectroscopy, we concluded that the tunneling current of **T4C4** increases at high pressures because of changes to the electronic structure, not the physical structure. Further, we found the correlation between mechanical stability and breakdown voltages in large-area junctions using EGaIn. The mechanically robust SAM of **T4C4** can withstand higher breakdown voltage than those of alkanes, which indicates that the mechanical properties of the SAM play the critical role rather than the electrochemical stability. This study could be useful for the potential application of large area molecular junctions.

In **Chapter 3**, we set out to investigate the influence of conjugation patterns in large area molecular junctions. We designed and synthesized three benzodithiophenes based molecular wires with different conjugation patterns but the same molecular length: one linearly-conjugated, one cross-conjugated and one cross-conjugated quinone. Then we studied the tunneling charge transport of the large-area molecular junctions comprising these benzodithiophenes derivatives and compared the results to a well-known anthraquinone. We found that the quinone functional group doesn't only introduce cross-conjugation but also suppresses tunneling transport due to its electronegativity. In the end, we showed that the presence of an interference feature and its position could be manipulated via bond topology and electronegativity synthetically.

We are investigating the potential of molecular electronics and the fabrication of solid-state devices comprising molecular tunneling junctions. In **Chapter 4**, we tried to incorporate organic molecules into nano-gap tunneling junctions using nanoskiving that we call SAM-templated addressable nanogap electrodes (STANs). During the fabrication process, we encountered several difficulties such as the binding issue between metals and the embedding polymer resin, fractures in fabricated electrodes and lots of short circuits. We discussed the related fabrication issues in detail in this chapter and addressed the remaining challenges.

In **Chapter 5**, we fabricated the 1.5 mm x 200 nm x 200 nm ultra-long, free-standing gold nanowires (Au NWs) using nanoskiving. We bisected microfluidic channels with

these Au NWs and showed two applications: A hot-wire anemometer to monitor the rate of the flow of ethanol inside the microfluidic channels; And stretching DNA molecules in the flow to visualize them by single-molecule fluorescence imaging. By attaching the DNA to a suspended Au nanowire, we reduced the background noise from non-specific binding in the fluorescence imaging and showed that the DNA extends at lower rates of the flow because it is located in the center of the channel where flow is highest, compared todirect binding to the bottom of microfluidic channels.

5

Nederlandse samenvatting

Het doel van dit proefschrift is om de tunnelingeigenschappen van grote-oppervlakte moleculaire juncties bestaande uit zelforganiserende monolagen van geconjugeerde, organische moleculen met verschillende conjugatiepatronen the onderzoeken en om deze te integreren in drie-terminale juncties met als doel het transport van lading middels tunneling via sturing met elektrische velden.

In **hoofdstuk 2** hebben we de mechanische en elektrische eigenschappen van zelforganiserende monolagen (self-assembled monolayers, SAMs) bestaande uit oliothiopheen-quarterthiopheen met een flexibele butaanthiolstaart (**T4C4**) bestudeerd met behulp van CP-AFM en EgaIn. Oligothiophenen zijn π-geconugeerde moleculen met superieure electrische eigenschappen en zijn daarom interessant voor toepassing in electronica. Wij hebben het verband tussen structuur en eigenschap bestudeerd tussen mechanische deformatie en elektrostaticiteit in SAMs bestaande uit **T4C4**. Door de aangebrachte kracht op de AFM-sonde te variëren hebben we gevonden dat de SAM uit T4C4 mechanisch robuster is dan SAMs uit alkanen. Dit gaat op bij een verscheidenheid aan drukken. Door density functional theory (DFT)-berekeningen en transition voltage spectroscopie te combineren, kwamen we tot de conclusie dat de tunnelingstroom van **T4C4** toeneemt bij hogere drukken door veranderingen in de electronische en niet in de fysische structuur. Tevens vonden we de correlatie tussen mechanische stabiliteit en doorslagspanning in grote-oppervlakte juncties met bebruik van EgaIn. De mechanisch robuuste SAM uit **T4C4** kan een hogere doorbraakspanning doorstaan dan SAMs uit alkanen, wat aangeeft dat de mechanische eigenschappen van de SAM belangrijker zijn dan de elektrochemische stabiliteit. Deze studie kan bijdragen aan de mogelijke toepassing van grote-oppervlakte moleculaire juncties.

In **hoofdstuk 3** hebben we de invloed van conjugatiepatronen op grote-oppervlakte moleculaire juncties onderzocht. Drie moleculaire draden gebaseerd op benzodithiopheen werden gesynthetiseerd, elk met dezelfde lengte maar een ander conjugatiepatroon: lineair geconjugeerd, kruisgeconjugeerd en kruisgeconjugeerd quinone. We hebben het tunneling-ladingstransport van de grote-oppervlakte moleculaire juncties bestaande uit deze benzodithiopheenderivaten bestudeerd en vergeleken met het bekende anthraquinone. De quinone functionele groep introduceert niet alleen kruisconjugatie, maar remt ook het tunneling transport vanwege zijn elektronegativiteit. Uiteindelijk konden we aantonen dat de aanwezigheid van een interferentiefunctie en de positie daarvan synthetisch gemanipuleerd kan worden via bindingstopologie en elektronegativiteit.

We zijn het potentieel van moleculaire elektronica en de fabricatie van solid-stateapparaten bestaande uit moleculaire tunneling juncties aan het onderzoeken. In **hoofdstuk 4** wordt beschreven hoe organische moleculen in nano-gap tunneling juncties ingebouwd kunnen worden met behulp van nanoskiving. We noemen deze SAM-templated addressable nanogap electrodes (STANs). Tijdens de fabricatie liepen we tegen een aantal moeilijkheden aan, zoals de gebrekkige hechting tussen metalen en de omgevende

polymeerhars, fracturen in de gefabriceerde elektrodes en vele kortsluitingen. In dit hoofdstuk hebben we deze kwesties gedetailleerd beschreven en andere uitdagingen aangepakt.

In **hoofdstuk 5** hebben we met behulp van nanoskiving uiterst lange, vrijstaande gouden nanodraden (Au NWs) gemaakt. Deze nanodraden zijn gebruikt om microfluide kanalen in twee te delen. Mogelijke toepassingen zijn: een hetedraads anemometer om de stroomsnelheid van ethanol in microfluide kanalen te meten; en het oprekken van DNA moleculen in de stroom om ze te visualiseren met fluorescentiemicroscopie. Door een DNA molecuul aan een gouden nanodraad vast te maken konden we de achtergrondruis van niet-specifieke binding verminderen en aantonen dat DNA uitrekt bij lagere stroomsnelheden doordat het zich in het midden van het kanaal bevindt, daar waar de stroming het hoogst is.

5

BIOGRAPHY

Yanxi ZHANG

Yanxi Zhang was born in Xiamen, P. R. China (1988). He obtained his Bachelor's degree in polymer chemistry at the University of Science and Technology of China (**USTC**) in 2010, under the supervision of Prof. Shiyong Liu. Then he earned his Master's degree (2012) in chemical engineering, at the Åbo Akademi University, Finland, under the supervision of Prof. Carl-Eric Wilén. His master was awarded "with distinction." In December 2013, he joined Prof. Dr. Ryan C. Chiechi's group and became a Ph.D. student at the University of Groningen. His Ph.D. is funded by the ERC Starting Grant - MOLECSYN-CON. His research interests include organic and molecular electronics, nanofabrication and device physics.

LIST OF PUBLICATIONS

1. **Y. Zhang, G. Ye, S. Soni, X. Qiu, T. L. Krijger, H. T. Jonkman, M. Carlotti, E. Sauter, M. Zharnikov and R. C. Chiechi**, *Controlling Destructive Quantum Interference in Tunneling Junctions Comprising Self-assembled Monolayers via Bond Topology and Functional Groups*, Chemical Science, back cover, **9**, 4414 (2018).

2. **Y. Zhang, X. Qiu, P. Gordiichuk, S. Soni, T. L. Krijger, A. Herrmann and R. C. Chiechi**, *Mechanically and Electrically Robust Self-Assembled Monolayers for Large-Area Tunneling Junctions*, The Journal of Physical Chemistry C, **121**, 14920 (2017).

3. **G. Kalkman, Y. Zhang, E. Monachino, K. Mathwig, M. E. Kamminga, P. Pourhossein, P. E. Oomen, S.A. Stratmann, Z. Zhao, A. M. van Oijen, E. Verpoorte and R. C. Chiechi**, *Bisecting Microfluidic Channels with Metallic Nanowires Fabricated by Nanoskiving*, ACS Nano **10**, 2852 (2016). **(Equal contribution as first author.)**

4. **Y. Zhang, Z. Zhao, D. Fracasso and R. C. Chiechi**, *Bottom-Up Molecular Tunneling Junctions Formed by Self-Assembly*, Israel Journal of Chemistry, **54**, 513 (2014). **Review Article.**

5. **Y. Zhang, S. Soni, T. L. Krijger, P. Gordiichuk, X. Qiu, G. Ye, H. T. Jonkman, A. Herrmann, K. Zojer, E. Zojer and R. C. Chiechi**, *Tunneling Probability Increases with Distance in Junctions Comprising Self-assembled Monolayers of Oligothiophenes*, submitted.

6. **P. E. Oomen, Y. Zhang,, R. C. Chiechi and K. Mathwig**, *Electrochemical Sensing with a Suspended Single Nanowire*, Lab on a Chip, just accepted.

7. **L. Qiu, Y. Zhang, T. L. Krijger, X. Qiu, P. van't Hof, J.C. Hummelen and R. C. Chiechi**, *Rectification of current responds to incorporation of fullerenes into mixed-monolayers of alkanethiolates in tunneling junctions*, Chemical Science, **8**, 2365 (2017).

8. **M. Carlotti, M. Degen, Y. Zhang, and R. C. Chiechi**, *Pronounced Environmental Effects on Injection Currents in EGaIn Tunneling Junctions Comprising Self-Assembled Monolayers*, The Journal of Physical Chemistry C, **120**, 20437 (2016).

9. **Y. Ai, A. Kovalchuk, X. Qiu, Y. Zhang,, S. Kumar, X. Wang, M. Kühnel, K. Nørgaard and R. C. Chiechi**, *In-Place Modulation of Rectification in Tunneling Junctions Comprising Self-Assembled Monolayers*, submitted.

ACKNOWLEDGEMENTS

Life is a journey, and it is not easy. Without the support from all the people around me, I could not finish my Ph.D.. I would like to thank all of you sincerely and wish you all the best.

First and foremost, I would especially like to thank my dear supervisor Prof. Dr. Ryan C. Chiechi who offered me the great opportunity to study and carry out research in Groningen. I still remember clearly the first time we talked via the Internet, the first time I arrived in Groningen, and the first time we met. I feel these just happened yesterday. You are not only a great supervisor but also a good friend to me. You supported me in all aspects in the past four years, including funding, guidance. You guided me to achieve all the important results in my research. And you help me to complete my Ph.D. with your knowledge. I love to discuss science with you. You have tremendous knowledge and are always enthusiastic. You always inspired me with fruitful discussion and managed to create an innovative research environment. Besides, we had lots of interesting discussions and conversations about culture, history and other aspects of life. I enjoyed it very much. I feel that I am fortunate to have a supervisor like you. I am very grateful. I want to say sincerely "Thank you, Ryan." I will be back for your retirement ceremony. I would also like to thank our lovely visiting researchers-Leo Chiechi and Camille Chiechi for the joy that they have brought to the group. I wish you have a happy childhood and pursue your dream in the future.

I also would like to thank Prof. Dr. Jan C Hummelen who always supports and encourages me in the past four years. The conversations with you are interesting. Your brilliance always influences me.

I would like to thank all the members of the assessment committee Prof. Dr. W. Hong, Prof. Dr. M. S. Pchenitchnikov and Prof. Dr. E. van der Giessen for your time to read my thesis and suggestions.

Moreover, I would like to thank all the members of the "CMMD" group. First, I would like to thank our dear secretary Renate for the help in all the daily life-related issues. I would like to thank our technician Reinder and Rick for all the help in solving the problems in the lab. I also would like to thank Dr. Harry T. Jonkman, Alfred, Hennie, Davide, Parisa, Olga, Zhiyuan, Wenqiang, Difei, Mehrnoosh, Jenny, Oleg, Thijs, Andrew, Marco, Gang, Xinkai, Victor, Gongbao, Saurabh, Sumit, Yong, Sylvia, Yuru, Bouke, Eva, Ellen, Roza and Dr. Li Qiu. And I would like to express my thank to Silang, Tian, Harm and Eelco for their contributions to the projects.

I would also express my gratitude to all the collaborators. I would like to thank Dr. Pavlo Gordiichuk, Prof. Dr. Andreas Herrmann, Gerard A Kalkman, Enrico Monachino, Dr. Klaus Mathwig, Dr. Machteld E Kamminga, Dr. Pieter E Oomen, Dr. Sarah A Stratmann, Prof. Dr. Antoine M van Oijen, Prof. Dr. Elisabeth Verpoorte for their contributions to the joint projects and discussions. I would like to thank Dr. Qihong Chen, Prof. Dr. Justin Ye for the collaboration and discussions. I would like to thank Eric Sauter and

5